

# Documentation Report for SSHAC level 2: Site Response

Date Published: November 2021

Prepared by:

A. Rodriguez-Marek  
Department of Civil and Environmental Engineering  
Virginia Tech

E. Rathje  
Department of Civil, Architectural and Environmental Engineering  
The University of Texas at Austin

J. Ake, NRC

C. Munson, NRC

S. Stovall, NRC  
NRC Project Manager

T. Weaver, NRC

K. Ulmer  
Center for Nuclear Waste Regulatory Analyses

M. Juckett  
Center for Nuclear Waste Regulatory Analyses  
CNWRA Project Manager

## **Disclaimer**

Legally binding regulatory requirements are stated only in laws, NRC regulations, licenses, including technical specifications, or orders; not in Research Information Letters (RILs). A RIL is not regulatory guidance, although NRC's regulatory offices may consider the information in a RIL to determine whether any regulatory actions are warranted



## **ABSTRACT**

In 1997, the U.S. Nuclear Regulatory Commission (NRC) issued NUREG/CR-6372 entitled, "Recommendations for Probabilistic Seismic Hazard Analysis: Guidance on Uncertainty and the Use of Experts" (NRC, 1997). The document prepared by the Senior Seismic Hazard Analysis Committee (SSHAC) focused on the way uncertainties in probabilistic seismic hazard analysis (PSHA) should be addressed when expert judgments are necessary. That report and subsequent more detailed guidance (NUREG-2117 and NUREG-2213) is referred to as the SSHAC process. The SSHAC process has been consistently applied to the seismic source characterization (SSC) and ground motion characterization (GMC) components of PSHAs performed for critical facilities for more than 15 years. However, because site response analyses (SRA) have often been conducted outside of the SSHAC process it has not benefitted from the systematic evaluation of alternative data, models, and methods within a structured and logical framework. Following the process described in NUREG-2213, capturing the center, body, and range (CBR) of the technically defensible interpretations (TDI) is achieved through a disciplined execution of the evaluation and execution phases of the SSHAC methodology. This report documents work sponsored by the NRC that applied the SSHAC process for systematically identifying and propagating epistemic uncertainties in the SRA as has been previously applied to the SSC and GMC analyses. The process was tested at two example sites, the resulting epistemic uncertainty in elements of the SRA at both sites were found to be as large or larger than those of the SSC and GMC models. This finding supports the rationale for implementing a structured process such as SSHAC to capture and document the uncertainties in the SRA. This report also documents the efficacy of alternative methods for incorporating the results of the SRA into the final PSHA hazard calculations.



# **DOCUMENTATION REPORT FOR SSHAC LEVEL 2: SITE RESPONSE**

*Prepared for*

**Participatory Peer Review Panel and  
U.S. Nuclear Regulatory Commission  
Contract No. 31310018D0002  
Task Order No. 31310019F0030**

*Prepared by*

**Dr. Adrian Rodriguez-Marek (Consultant, TI Team Lead)  
Dr. Jon Ake (NRC, TI Team)  
Dr. Cliff Munson (NRC, TI Team)  
Dr. Ellen Rathje (Consultant, TI Team)  
Dr. Scott Stovall (NRC, Hazard Analyst)  
Dr. Thomas Weaver (NRC, Hazard Analyst)  
Dr. Kristin Ulmer (CNWRA, Hazard Analysis Support)  
Miriam Juckett (CNWRA, Project Manager)**

**Center for Nuclear Waste Regulatory Analyses  
San Antonio, Texas**

**September 2021**



# Table of Contents

<b>ABSTRACT .....</b>	<b>iii</b>
<b>LIST OF FIGURES .....</b>	<b>xi</b>
<b>LIST OF TABLES .....</b>	<b>xviii</b>
<b>Abbreviations and Acronyms .....</b>	<b>xix</b>
<b>1 Introduction .....</b>	<b>1-1</b>
1.1 Background and Objective.....	1-1
1.2 Overview of SSHAC Process .....	1-2
1.3 Project Organization .....	1-3
1.4 Project Process Description.....	1-10
1.5 References.....	1-11
<b>2 Site Response Analysis Framework and Evaluation of Key Issues.....</b>	<b>2-1</b>
2.1 Overview of Approaches for Incorporating Site Response into PSHA.....	2-1
2.2 Workshop Summary .....	2-2
2.3 Identification of Key Issues .....	2-8
2.4 References.....	2-9
<b>3 Site Response Models for Incorporation into PSHA.....</b>	<b>3-1</b>
3.1 Approaches to Develop Site Response Adjustments .....	3-1
3.2 Epistemic Uncertainty and Aleatory Variability in Site Response .....	3-3
3.3 Philosophy for Developing Weights .....	3-9
3.4 Implementation into PSHA.....	3-9
3.5 Capturing the Center, Body, and Range of the Technically Defensible Interpretations .....	3-14
3.6 References.....	3-15
<b>4 Project Study Sites.....</b>	<b>4-1</b>
4.1 Factors Considered in Site Selection .....	4-1
4.2 Savannah River Site .....	4-2
4.2.1 Geologic Setting .....	4-2
4.2.2 Geotechnical and Geophysical Data.....	4-3
4.2.3 Source Characterization and Ground Motion Models.....	4-4
4.3 Garner Valley Site .....	4-15
4.3.1 Geologic Setting .....	4-15
4.3.2 Geotechnical and Geophysical Data.....	4-16
4.3.3 Source Characterization and Ground Motion Models.....	4-17

4.4	References .....	4-24
<b>5</b>	<b>Description of Site Response Logic Trees .....</b>	<b>5-1</b>
5.1	Introduction .....	5-1
5.2	Shear-Wave Velocity .....	5-1
5.2.1	Issues Related to Developing $V_S$ Logic Tree .....	5-1
5.2.2	$V_S$ Components of the Logic Tree for SRS .....	5-3
5.2.3	$V_S$ Components of Logic Tree for GVDA .....	5-9
5.3	Kappa .....	5-15
5.3.1	Issues Related to Developing Kappa Logic Tree .....	5-15
5.3.2	Kappa Components of the Logic Tree for SRS .....	5-16
5.3.3	Kappa Components of Logic Tree for GVDA .....	5-19
5.3.4	Depth Partitioning of Kappa and Damping .....	5-20
5.4	Modulus Reduction and Damping .....	5-23
5.4.1	Issues Related to Developing a Logic Tree for Modulus Reduction and Damping Curves .....	5-23
5.4.2	Modulus Reduction and Damping Curve Components of the Logic Tree for the SRS Study Site .....	5-25
5.4.3	Modulus Reduction and Damping Curve Components of Logic Tree for GVDA .....	5-28
5.5	Site Response Analysis Method .....	5-29
5.6	Summary of Final Logic Trees .....	5-33
5.7	References .....	5-40
<b>6</b>	<b>Site Adjustment Factor Results .....</b>	<b>6-1</b>
6.1	SRS Study Site .....	6-2
6.1.1	Site Adjustment Factor Branches .....	6-2
6.1.2	Sensitivity Studies .....	6-5
6.2	GVDA Study Site .....	6-18
6.2.1	Site Adjustment Factor Branches .....	6-18
6.2.2	Empirical Site Term .....	6-29
6.3	References .....	6-31
<b>7</b>	<b>Control Point Hazard Results .....</b>	<b>7-1</b>
7.1	Background .....	7-1
7.2	Ground Motion Hazard Results .....	7-1
7.2.1	SRS Hazard Results and Sensitivity .....	7-2
7.2.2	GVDA Hazard Results and Sensitivity .....	7-14
7.2.3	Conclusions from Multiple Hazard Implementations .....	7-23
7.3	References .....	7-23
<b>8</b>	<b>Conclusions .....</b>	<b>8-1</b>
8.1	Summary .....	8-1
8.2	Technical Lessons Learned and Research Opportunities .....	8-2

8.2.1	Shear-Wave Velocity Characterization .....	8-3
8.2.2	Kappa 8-4	
8.2.3	Kappa Correction and Site Response Analysis Methods .....	8-4
8.2.4	One-Step Approach for Development of Site Adjustments Factors .....	8-5
8.2.5	Input Motion Specification.....	8-5
8.2.6	Variance Contributions .....	8-5
8.2.7	Model Error.....	8-6
8.2.8	Lower Bound Adjustment Factors.....	8-6
8.2.9	Empirical Validation .....	8-6
8.2.10	Implementation of Site Response into PSHA.....	8-6
8.2.11	Downstream Applications That Utilize PSHA Results .....	8-7
8.3	Conclusions.....	8-8
8.4	References.....	8-8
<b>APPENDIX A</b>	.....	<b>1</b>
<b>APPENDIX B</b>	.....	<b>30</b>
<b>APPENDIX C</b>	.....	<b>1</b>
<b>APPENDIX D</b>	.....	<b>1</b>



## LIST OF FIGURES

Figure 1-1	Flowchart for the SSHAC Level 2 site response analysis study, with time running from top to bottom (modified from NUREG–2213).....	1-4
Figure 1-2	Organizational structure of this SSHAC Level 2 study.....	1-5
Figure 3-1	Schematic of the GMM reference condition and the site-specific reference condition + near-surface profile.....	3-1
Figure 3-2	(a) Two-step method and (b) one-step method to develop <i>SAF</i> .....	3-3
Figure 3-3	Example illustrating an approach to capture epistemic uncertainties using three <i>VS</i> profiles. (a) Stratigraphic profiles (left) and best-estimated and alternative upper- and lower-case <i>VS</i> profiles (right) considered for this study, (b) Linear <i>SAF</i> corresponding to these three profiles. The arrows point to oscillator periods where the three <i>SAFs</i> cross over and the resulting epistemic uncertainty is low (from Rodriguez-Marek et al., 2020). .....	3-6
Figure 3-4	(a) Median <i>SAF</i> (light gray lines) for full logic tree profiles capturing all sources of uncertainty for the site shown in Figure 3-3 along with the <i>SAF</i> for the median, upper, and lower profiles in Figure 3-3, (b) the resampled, five-point discrete representation of the full logic tree, and (c) the standard deviation of the <i>SAF</i> from the logic tree ( $\sigma_{ep}$ ) compared with the minimum epistemic uncertainty. ....	3-8
Figure 4-1	SRS location map relative to the Coastal Plain and Piedmont physiographic provinces. The location of the map inset showing F-Area is indicated by small rectangle within the SRS boundary. ....	4-3
Figure 4-2	Stratigraphic column beneath SRS-FA.....	4-4
Figure 4-3	CEUS-SSC model sources for SRS (red triangle). Three alternative Charleston RLME configurations are depicted. Dotted circle shows 320 km radius used for the ECC-AM and PEZ-N source zones. ....	4-6
Figure 4-4	Reference condition hazard curves (light blue) from implementing all of the 24 alternative recurrence rates with their associated beta values compared to the reference hazard curves (tan) from the implementation of the 5 recurrence rates and an average beta value for each of the distributed seismicity source zone cells.....	4-7
Figure 4-5	M6 rupture sources for CEUS-SSC ECC-AM source zone. SRS location is shown as a green triangle. The large Gulf Coast zone used for NGA-East GMM, which is below the ECC-AM source, is shown in green. ....	4-10
Figure 4-6	(a) 1 Hz mean (red) and fractile (dashed, 0.05, 0.10, 0.16, 0.50, 0.84, 0.90, and 0.95) reference condition hazard curves for ECC-AM source and (b) 10 Hz mean (red) and fractile (dashed, 0.05, 0.10, 0.16, 0.50, 0.84, 0.90, and 0.95) reference condition hazard curves for ECC-AM source.....	4-11
Figure 4-7	Mean 10 <sup>-4</sup> AFE tornado plot for ECC-AM source and NGA-East GMM. Parameters from top to bottom are ECC-AM magnitude recurrence rate (purple), ECC-AM maximum magnitudes (green), ECC-AM	

	seismotectonic thickness (blue), NGA-East median GMMs (red), and NGA-East aleatory variability (logarithmic standard deviations; brown). Circle size for each of the parameter values scales with the logic tree weight. ....	4-12
Figure 4-8	(a) 1 Hz mean hazard curves for SRS. Total hazard (black), Charleston RLME (blue), ECC-AM (red), and PEZ-N (green) hazard curves are shown and (b) 10 Hz mean hazard curves for SRS. Total hazard (black), Charleston RLME (blue), ECC-AM (red), and PEZ-N (green) hazard curves are shown.....	4-13
Figure 4-9	(a) 1 Hz $10^{-4}$ AFE deaggregation plot for SRS. Charleston RLME source dominates the hazard and (b) 10 Hz $10^{-4}$ AFE deaggregation plot for SRS. The host zone ECC-AM controls the local hazard and the Charleston RLME source dominates the distant hazard.....	4-14
Figure 4-10	Response spectra for $10^{-3}$ (green), $10^{-4}$ (blue), and $10^{-5}$ (red) AFE, for 1 and 10 Hz deaggregation mean controlling earthquake magnitude and distance pairs. Each response spectrum is scaled (small circles) to either the 1 or 10 Hz UHRS value, as appropriate. ....	4-15
Figure 4-11	Location of GVDA with respect to the San Andreas Fault and San Jacinto Fault.....	4-16
Figure 4-12	Stratigraphic column beneath the GVDA site .....	4-17
Figure 4-13	Simplified San Jacinto Fault Zone source model (thin black line). GVDA site is shown as red triangle and is about 7 km from the San Jacinto Fault at the closest approach. ....	4-18
Figure 4-14	(a) 1 Hz mean and fractile (0.16, 0.50, and 0.84) hazard curves for the GVDA site and (b) 10 Hz mean and fractile (0.16, 0.50, and 0.84) hazard curves for the GVDA site.....	4-21
Figure 4-15	Mean UHRS for the GVDA site. Shown are UHRS for $10^{-3}$ , $10^{-4}$ , and $10^{-5}$ AFE levels.....	4-22
Figure 4-16	(a) 1 Hz deaggregation results for $10^{-3}$ AFE and (b) 10 Hz deaggregation results for $10^{-3}$ AFE. ....	4-23
Figure 4-17	Response spectra (solid line) from deaggregation controlling earthquake mean magnitude and distance pairs. Each response spectrum is scaled to the appropriate UHRS (dashed line) at either 1 or 10 Hz. ....	4-24
Figure 5-1	SRS shear-wave velocity test locations.....	5-4
Figure 5-2	SRS shear-wave velocity profiles from tests and the base-, upper-, and lower-case profiles .....	5-6
Figure 5-3	Shear-wave velocity distribution at ~34 m depth from shear-wave velocity measurements (data), and from random velocity profiles developed using the site-specific correlation model for the SRS study site. ....	5-6
Figure 5-4	Standard deviation of $VS$ (in natural log units) for the SRS study site.....	5-8
Figure 5-5	SRS correlation model for normalized $VS$ residuals of two consecutive layers. The dots correspond to the sample correlation values from the $VS$ data and the dotted lines are the fitted model. Numbers above each dot	

	represent the number of depth pairs that were used to obtain the sample correlation values.....	5-8
Figure 5-6	SRS random shear-wave velocity profiles using the site-specific correlation model for the (a) lower case, (b) base case, and (c) upper case epistemic profiles.....	5-10
Figure 5-7	Host profile for the SWUS ground motion model (left). Upper 300 m of the SWUS profile (right). .....	5-10
Figure 5-8	(a) Downhole, <i>P-S</i> suspension logging and SASW profiles for GVDA, (b) Comparison of linear transfer functions for the downhole and <i>P-S</i> suspension logging with the mean empirical transfer function. ....	5-12
Figure 5-9	Location of MAM arrays used by Teague et al. (2018) to characterize the GVDA site .....	5-12
Figure 5-10	Inverted MASW/MAM profiles from dispersion data collected at GVDA's central location for each layering ratio.....	5-13
Figure 5-11	Forward-modeled dispersions of 60 randomized shear-wave velocity profiles (green) generated using a $\sigma_{InvS}$ of 0.15. Black error bars represent two standard deviations of the bounded experimental dispersion data across the north, south and central locations. ....	5-15
Figure 5-12	Example combining MASW/MAM profiles (colored lines) with SWUS host profile (black line). Left shows the upper 300 m. Right shows how each inverted profile is connected into the SWUS host profile at a depth where the shear-wave velocity of the host profile equals that of the last layer in an individual inverted profile.....	5-16
Figure 5-13	Logic tree used to develop cumulative kappa distribution and representative five-point distribution for use in site response logic tree for SRS. Values below branches are the branch weights. ....	5-18
Figure 5-14	Comparison of surface versus downhole (150 m depth) $\kappa r$ slopes computed from frequency bands of 25 Hz to 35 Hz (top) and 25 Hz to 45 Hz (bottom) .....	5-21
Figure 5-15	Cumulative distribution of weighted $\kappa 0$ values and representative five-point distribution values from Miller and Rice (1983). ....	5-22
Figure 5-16	Illustration of the effects of strength correction on the modulus reduction curve, (a) Example 1 where shear strength is less than the curve large strain stress and (b) Example 2 where the strength is greater than the large-strain stress. ....	5-25
Figure 5-17	SRS-specific MRD curves .....	5-27
Figure 5-18	Comparison of site-specific and generic MRD curves used to capture epistemic uncertainty in dynamic material properties for SRS .....	5-28
Figure 5-19	Comparison of stress-dependent modulus reduction curves (Darendeli 2001) and GVDA site-specific modulus reduction curves developed by Stokoe and Darendeli (1998). ....	5-30
Figure 5-20	Comparison of stress-dependent damping curves (Darendeli, 2001) and GVDA site-specific damping curves developed by Stokoe and Darendeli, (1998). ....	5-31

Figure 5-21	Illustration of the different approaches to the kappa correction applied to a FAS from EQL analysis.....	5-33
Figure 5-22	SRS site response logic tree. Values under branches represent branch weights. Kappa values are provided in Table 5-3. ....	5-35
Figure 5-23	GVDA site response logic tree. Values under branches represent branch weights. Kappa values are provided in Table 5-5. ....	5-36
Figure 5-24	Epistemic uncertainty in shear-wave velocity versus depth for (a) the SRS study site and (b) the GVDA study site. For the SRS, the left plot shows the alternative base case profiles. For the GVDA, the black lines in the left two plots are alternative median velocity profiles. ....	5-37
Figure 5-25	Epistemic uncertainty in MRD for (a) the SRS and (b) the GVDA site .....	5-38
Figure 5-26	Base case shear strength profiles and associated epistemic uncertainty for (a) SRS and (b) GVDA.....	5-39
Figure 6-1	Site adjustment factors ( <i>SAF</i> ) for seven re-sampled epistemic branches for the SRS and mean of the log standard deviations (aleatory variability) for (a) 0.5 Hz, (b) 5 Hz, (c) 10 Hz, and (d) 100 Hz.....	6-3
Figure 6-2	Epistemic standard deviation of natural <i>SAF</i> for the SRS study site as a function of frequency for reference rock PGA of (a) 0.01 g, (b) 0.43 g, and (c) 1.2 g. ....	6-4
Figure 6-3	<i>SAF</i> for 1 Hz as a function of <i>Saref</i> at the SRS site with and without imposing minimum epistemic uncertainty. ....	6-5
Figure 6-4	Input reference rock spectral acceleration for five hazard levels using PSM and CMS conditioned at a frequency ( $f^*$ ) of 25 Hz. ....	6-8
Figure 6-5	<i>SAF</i> developed from PSM and CMS input motions. ....	6-8
Figure 6-6	Surface FAS and response spectra for input motions derived from (a) point source model and (b) conditional mean spectra conditioned at an oscillator frequency ( $f^*$ ) of 25 Hz. ....	6-9
Figure 6-7	Numbers in parentheses indicate the value of the transition frequency ( $f_{tr}$ ) for the kappa2 approach. ....	6-10
Figure 6-8	Spectral amplification for NL DeepSoil analysis and EQL RVT and EQL analyses using RVT and kappa-corrected RVT.....	6-10
Figure 6-9	<i>SAF</i> for a target site kappa of 0.036 s where the small strain damping curves are modified at depths deeper than 3 m, deeper than 50 m, and deeper than 153 m to achieve the target site kappa.....	6-12
Figure 6-10	Effective strain profiles with a target site kappa of 0.036 s where small strain damping was modified at depths below 3 m, 50 m, and 153 m to achieve the target site kappa. ....	6-13
Figure 6-11	<i>SAF</i> as a function of frequency for reference rock PGA of (a) 0.43 g, and (b) 1.2 g. The colored lines show <i>SAF</i> for the EQL and kappa-corrected analysis methods. ....	6-14

Figure 6-12	<b>SAF</b> as a function of frequency for reference rock PGA of (a) 0.43 g, and (b) 1.2 g. The colored lines show <b>SAF</b> for the lower-, base-, and upper-case velocity profiles. ....	6-14
Figure 6-13	<b>SAF</b> as a function of frequency for reference rock PGA of (a) 0.43 g, and (b) 1.2 g. The colored lines show <b>SAF</b> for the profile kappa values ranging from 0.021 to 0.076 s. ....	6-15
Figure 6-14	<b>SAF</b> as a function of frequency for reference rock PGA of (a) 0.43 g, and (b) 1.2 g. The colored lines show <b>SAF</b> for the two MRD curve models. ....	6-15
Figure 6-15	<b>SAF</b> as a function of frequency for reference rock PGA of (a) 0.43g, and (b) 3g. The colored lines show <b>SAF</b> for the lower-, base- and upper-shear strength cases. ....	6-16
Figure 6-16	<b>SAF</b> as a function of frequency for reference rock PGA of (a) 0.01 g, and (b) 3 g. The colored lines show amplification for when layer thickness is not randomized and when layer thickness is randomized assuming a lognormal distribution. ....	6-16
Figure 6-17	Variance contribution for a reference rock PGA of (a) 0.01 g, (b) 0.12 g (c) 0.43 g (d) 1.2 g. ....	6-17
Figure 6-18	Tornado plots for reference rock PGA of 1.2 g. The open square symbols represent mean branch amplification. ....	6-19
Figure 6-19	<b>SAF</b> for seven epistemic branches and the log standard deviations (aleatory variability) for (a) 1 Hz, (b) 5 Hz, (c) 10 Hz, and (d) 100 Hz. ....	6-20
Figure 6-20	Epistemic standard deviation of natural log spectral acceleration as a function of frequency for input reference rock PGA of (a) 0.01 g, (b) 0.39 g, and (c) 1.0 g. ....	6-21
Figure 6-21	100 Hz amplification with and without imposing minimum epistemic uncertainty. ....	6-21
Figure 6-22	<b>SAF</b> as a function of frequency for reference rock PGA of (a) 0.39 g and (b) 1.0 g. The colored lines show <b>SAF</b> for the EQL and kappa-corrected analysis methods. ....	6-24
Figure 6-23	<b>SAF</b> as a function of frequency for reference rock PGA of (a) 0.39 g and (b) 1.0 g. The colored lines show <b>SAF</b> for the alternative velocity profiles. ....	6-24
Figure 6-24	<b>SAF</b> as a function of frequency for reference rock PGA of (a) 0.39 g and (b) 1.0 g. The colored lines show <b>SAF</b> for the profile kappa values ranging from 0.013 to 0.028 s. ....	6-25
Figure 6-25	<b>SAF</b> as a function of frequency for reference rock PGA of (a) 0.39 g, and (b) 1.0 g. The colored lines show <b>SAF</b> for the two MRD curves models. ....	6-25
Figure 6-26	<b>SAF</b> as a function of frequency for reference rock PGA of (a) 0.39 g and (b) 1.0 g. The colored lines show <b>SAF</b> for the lower-, base- and upper-shear strength cases. ....	6-26
Figure 6-27	Variance contribution for a reference rock PGA of (a) 0.01 g, (b) 0.14 g, (c) 0.39 g, and (d) 1.0 g. ....	6-27

Figure 6-28	Tornado plots for reference rock PGA of 1.0 g. The open square symbols represent mean branch <i>SAF</i> , where the size of the symbol represents the relative weight for a branch. ....6-28
Figure 6-29	Empirical site term with respect to the site-specific condition (solid black line) with 95% confidence intervals (black bars).....6-31
Figure 7-1	(a) Reference condition 1 Hz hazard curves for seismic sources implemented for SRS-FA. Mean hazard curves for each source are shown (dashed red curves) as well as the total hazard (black curve). (b) SRS median site adjustment factors and logarithmic standard deviation for 1 Hz. (c) Control point 1 Hz hazard curves for seismic sources implemented for SRS-FAZ. Mean hazard curves for each source are shown (dashed red curves) as well as the total hazard (black curve). ....7-4
Figure 7-2	(a) Reference condition 10 Hz hazard curves for seismic sources implemented for SRS-FA. Mean hazard curves for each source are shown (dashed red curves) as well as the total hazard (black curve). (b) SRS median site adjustment factors and logarithmic standard deviation for 10 Hz. (c) Control point 10 Hz hazard curves for seismic sources implemented for SRS-FA. Mean hazard curves for each source are shown (dashed red curves) as well as the total hazard (black curve). ....7-5
Figure 7-3	(a) 1 and 10 Hz total mean hazard for reference condition and control point elevation and (b) Uniform hazard response spectra for reference condition and control point (surface). ....7-6
Figure 7-4	GMRS for seismic design category 3, 4, and 5 structure.....7-7
Figure 7-5	Total control point hazard curve fractiles (dashed red curves) and mean (green curve) developed for SRS using repeated sampling approach.....7-9
Figure 7-6	(a) 1 Hz control point total mean (dashed) and fractile (solid) hazard curves for the Hazard Integral Approach 3 compared to Approach 4 and (b) 10 Hz control point total mean (dashed) and fractile (solid) hazard curves for Hazard Integral Approach 3 compared to Approach 4. ....7-10
Figure 7-7	Mean control point UHRS for the Hazard Integral Approach 3 versus Approach 4 .....7-11
Figure 7-8	(a) Comparison of the 10 Hz control point fractile hazard curves for the two different Approach 3 implementations for the 10th and 90th percentiles, SRS study site and (b) Comparison of the 10 Hz control point fractile hazard curves for the two different Approach 3 implementations for the 16th and 84th percentiles, SRS study site.....7-12
Figure 7-9	(a) 1 Hz tornado plot for mean 10-4 AFE and (b) 10 Hz tornado plot for mean 10-4 AFE.....7-13
Figure 7-10	(a) Reference condition 1 Hz hazard curves for modified San Jacinto fault for GVDA, (b) GVDA median site adjustment factors and logarithmic standard deviation for 1 Hz, and (c) control point 1 Hz hazard curves for modified San Jacinto fault for GVDA. ....7-15
Figure 7-11	(a) Reference condition 10 Hz hazard curves for modified San Jacinto fault for GVDA, (b) GVDA median site adjustment factors and logarithmic

	standard deviation for 10 Hz, and (c) control point 10 Hz hazard curves for modified San Jacinto fault for GVDA. ....	7-16
Figure 7-12	(a) 1 and 10 Hz total mean hazard for reference condition and control point elevation and (b) UHRS for reference condition and control point (surface). ....	7-17
Figure 7-13	GMRS for seismic design category 3, 4, and 5 structures. ....	7-18
Figure 7-14	(a) 1 Hz control point total mean (dashed) and fractile (solid) hazard curves for Hazard Integral Approach 3 compared to Approach 4 and (b) 10 Hz control point total mean (dashed) and fractile (solid) hazard curves for Hazard Integral Approach 3 compared to Approach 4. ....	7-19
Figure 7-15	Mean control point UHRS for Hazard Integral Approach 3 versus Approach 4. ....	7-20
Figure 7-16	(a) Comparison of the 10 Hz control point fractile hazard curves for the two different Approach 3 implementations for the 10th and 90th percentiles, GVDA study site and (b) comparison of the 10 Hz control point fractile hazard curves for the two different Approach 3 implementations for the 16th and 84th percentiles, GVDA study site. ....	7-21
Figure 7-17	(a) 1 Hz tornado plot for mean 10-4 AFE and (b) 10 Hz tornado plot for mean 10-4 AFE. ....	7-22
Figure 8-1	Tornado plot for mean 10 Hz spectral acceleration at 10-4 AFE for (a) SRS and (b) GVDA sites. ....	8-3

## LIST OF TABLES

		Page
Table 1-1	Roles and responsibilities for the SSHAC Level 2 .....	1-6
Table 1-2	Presentations and interviews for workshop .....	1-8
Table 1-3	Workshop attendees .....	1-9
Table 3-1	Nomenclature for subjective weights .....	3-9
Table 3-2	Alternative versions of approaches 3 and 4 .....	3-13
Table 4-1	Controlling earthquake mean magnitude and distance pairs for spectral frequencies .....	4-14
Table 4-2	Controlling earthquake mean magnitude and distance pairs .....	4-23
Table 5-1	Parameters for the correlation model for normalized $VS$ residuals of two consecutive layers .....	5-8
Table 5-2	Site kappa ( $\kappa_0$ ) from empirical models using the base case $VS$ profile .....	5-18
Table 5-3	Re-sampled kappa branch values and weights for SRS site response logic tree .....	5-18
Table 5-4	Summary of approach used to quantify epistemic uncertainty in $\kappa_0$ .....	5-21
Table 5-5	Five-point distribution of $\kappa_0$ using the Miller and Rice (1983) approach .....	5-22
Table 5-6	SRS site-specific MRD curves .....	5-27

## Abbreviations and Acronyms

1D	one-dimensional
2D	two-dimensional
ADAMS	Agencywide Documents Access and Management System
AFE	annual frequency of exceedance
CBR of TDI	center, body, and range of technically defensible interpretations
CCDF	complementary cumulative distribution function
CDF	cumulative distribution function
CENA	Central and Eastern North America
CEUS	central and eastern United States
CLS	Charleston Local Source
CMS	conditional mean spectra
CNWRA <sup>®</sup>	Center for Nuclear Waste Regulatory Analyses
COV	coefficient of variation
CNS	Charleston Narrow Source
CRP	Charleston Regional Source–Parallel
CRR	Charleston Regional Source–Perpendicular
DCPP	Diablo Canyon Power Plant
dB	decibels
DOE	U.S. Department of Energy
ECC-AM	Extended Continental Crust – Atlantic Margin
EQL	equivalent linear
EQL-FD	equivalent linear with frequency dependence
FAS	Fourier amplitude spectra
FD	frequency dependent
FIRS	foundation input response spectrum

FFT	fast Fourier transform
ft <sub>r</sub>	transition frequency
GMM	ground motion model
GMPE	ground motion prediction equation
GMRS	ground motion response spectra
GVDA	Garner Valley Downhole Array
HID	Hazard Input Document
H/V	horizontal-to-vertical
Hz	hertz
km	kilometers
kPa	kilopascals
MAM	microtremor array measurements
MASW	multi-channel analysis of surface waves
MCMC	Markov chain Monte Carlo
MRD	modulus reduction and damping
MSL	mean sea level
NEES	Network for Earthquake Engineering Simulations
NGA	Next Generation Attenuation
NL	non-linear
NRC	U.S. Nuclear Regulatory Commission
OCR	overconsolidation ratio
OLS	ordinary least squares
PEZ-N	Paleozoic Extended Crust – Narrow Geometry
PGA	peak ground acceleration
PGV	peak ground velocity
PSM	point source models

PMF	probability mass functions
PPRP	participatory peer review panel
PSHA	probabilistic seismic hazard analyses
PSM	point source models
RC	resonant column
RG	Regulatory Guide
RLME	repeated large-magnitude earthquakes
RP	return periods
RVT	Random Vibration Theory
S <sub>a</sub>	spectral acceleration
<i>SAF</i>	site adjustment factor
SASW	spectral analysis of surface wave
SJFZ	San Jacinto Fault Zone
SM	silty sand
SNR	signal to noise ratio
SPIP	screening, prioritization, and implementation details
SRA	site response analysis
SRS	Savannah River Site
SRS-FA	Savannah River Site-F Area
SSC	seismic source characterization
SSE	safe shutdown earthquake
SSHAC	Senior Seismic Hazard Analysis Committee
SSI	soil-structure interaction
SWUS	Southwest United States
TI Team	Technical Integration Team
TS	torsional shear

UHRS	uniform hazard response spectrum
UHS	uniform hazard spectra
U.S.	United States
V <sub>s</sub>	Velocity
WUS	Western United States

# 1 Introduction

## 1.1 Background and Objective

In the earliest seismic hazard assessments for nuclear facilities, site response analyses were rarely performed. Deterministic seismic hazard assessments produced a single estimate of high-frequency [ $>30$  Hertz (Hz)] ground shaking, which was used to anchor a site-independent smooth broad-banded ground response spectrum. This spectrum was derived by analyzing a limited number of empirical recordings from a broad range of site conditions. Subsequently, United States (U.S.) Nuclear Regulatory Commission (NRC) and U.S. Department of Energy (DOE) guidance began focusing on probabilistic seismic hazard analyses (PSHA) and requiring an evaluation of the seismic wave transmission characteristics of the site. The response of the soil deposit (the seismic wave transmission characteristics) was typically characterized by a single mean deterministic amplification function derived by driving a small number of seismograms through an equivalent-linear model of the site column using best estimate properties. The desired hazard at the ground surface was obtained by multiplying either a uniform hazard spectrum or hazard curves by the deterministic amplification function. These site response analyses were typically performed independently of the PSHA. By the late 1990's, the NRC published regulatory guidance (a Regulatory Guide, or RG) for the determination of the safe shutdown earthquake ground motion (SSE) (RG 1.165; NRC, 1997), which provided a consistent approach for determining the seismic design basis ground motion for a site. Fully probabilistic methodologies were then developed to account for potential non-linear soil response and the associated uncertainties, resulting in hazard-consistent spectra on soil (Bazzurro et al., 1999; Lee et al., 1998; McGuire et al., 2001).

By its very nature, site response analysis is site-specific and depends on several factors, including the site strata (material type, stiffness, and thickness) and response of the site strata to dynamic loading. Because it is site-specific, the ability to accurately model site response depends on the quantity and quality of available site-specific geologic and geotechnical data and the interpretation and use of that data to develop input models that assess amplification (or de-amplification) of ground motions. The results of the site response analysis are used to develop site adjustment (or amplification) factors. The site adjustment factors are assessed for a wide range of input ground motions as part of understanding the changes in the soil and rock responses as the input ground motions increase.

The development of the site adjustment factors also requires the characterization of significant uncertainties, particularly epistemic uncertainties. The challenges in properly characterizing these uncertainties have been described in previous studies—in particular, the report of the Senior Seismic Hazard Analysis Committee, or SSHAC (Budnitz et al., 1997), later updated in NUREG-2117 (NRC, 2012). The most recent NRC guidance for conducting SSHAC studies is NUREG-2213 (NRC, 2018).

As noted above, in previous seismic hazard evaluations, site response analyses typically occurred after the implementation and/or development of a seismic source characterization (SSC) model, ground motion models (GMM), and the subsequent PSHA calculations for the reference conditions specified by the GMM. Because site response analyses have often been conducted outside of the SSHAC process used to develop SSCs and GMMs for the site, site response analysis has not benefitted from the SSHAC process of systematically evaluating data, models, and methods within a structured and logical framework. Based on experiences gained by conducting many SSAHC studies, the NRC staff, along with experts in academia and

industry, have determined that site response analysis would benefit from the standardized SSHAC practices that are applied in the development of SSC models and GMMs. This process will ensure that associated technical judgments and decisions are properly justified and documented and are consistent with the SSHAC goal to capture the center, body, and range of technically defensible interpretations (commonly referred to as the CBR of TDI) and are thoroughly reviewed by a Participatory Peer Review Panel (PPRP).

The purpose of this project is to apply the SSHAC process to the conduct of site response analyses at two sites to develop a consistent, scalable framework that can be applied in future site response analyses. This framework will provide a set of practical tools and methods for future studies, and it will enable practitioners to systematically identify and propagate epistemic uncertainties. This report documents the Technical Integration (TI) Team's site response analyses for the two study sites, which were performed using the SSHAC guidance as documented in NUREG-2213 (NRC, 2018) and the most current methods and models that are consistent with recent state of practice for nuclear facilities. The SSHAC guidance describes four levels of study (Levels 1-4) of increasing scope and rigor (see NUREG-2213 Sections 2.5 and 3.2). For the purposes of the current demonstration project, the NRC staff determined that this project should be performed as a Level 2 study.

The NRC staff continues to evaluate the most appropriate methods for incorporating site response results into the PSHA calculations and the subsequent use of the PSHA hazard curves to derive ground motion response spectra (GMRS) and the foundation input response spectra (FIRS). Thus, a secondary objective of this study is to compare hazard results computed using alternative methods for incorporating the site response results into the hazard calculations.

## **1.2 Overview of SSHAC Process**

As described in NUREG-2213, the essence of the SSHAC process is the structured interaction among experts to produce a well-documented hazard study that captures the CBR of TDI. There are five key features that are indispensable to the SSHAC process and that distinguish all SSHAC studies from non-SSHAC projects:

1. Clearly defined roles for all participants, including the responsibilities and attributes associated with each role.
2. Objective evaluation of all available data, models, and methods that could be relevant to the characterization of the hazard at the site.
3. Integration of the outcome of the evaluation process into models that reflect both the best estimate of each element of the hazard input with the current state of knowledge and the associated uncertainty.
4. Documentation of the study with sufficient detail to allow reproduction of the hazard analyses. The documentation must identify all the data, models, and methods considered in the evaluation, and justify in detail the technical interpretations that support the hazard input models.
5. Independent participatory peer review is required to confirm that the evaluation considered relevant data, models, and methods, and that the evaluation was conducted objectively and without bias. The peer review is conducted following a "participatory" or continual process throughout the entire project. The peer review is also required to

confirm that the study did capture the CBR of TDIs and that the technical bases for all elements of the models are adequately documented. For the peer review process to be considered complete, it must be documented in the form of a closure letter from the PPRP.

These five features are essential for all SSHAC studies, regardless of the SSHAC Level at which the study is performed.

The flow chart shown in Figure 1-1, which was modified from NUREG-2213, illustrates how this specific SSHAC Level 2 study was conducted by the TI Team. Although the general SSHAC process was followed in this study, the focus is on the site response, so no separate GMMs were developed or reviewed. For the SSC models, the TI Team developed and implemented a simplified model for one of the study sites and implemented a limited portion of an existing SSC model for the other study site. Review of SSC models and GMMs was limited to a determination of whether they are suitable for the purposes of this study. As such, the final hazard resulting from the implementation of the site adjustment factors into the PSHA should not be considered a complete hazard characterization that would typically be conducted for a critical facility. Instead, the focus of this project is on the implementation of the SSHAC methodology for performing the site response analysis and incorporating the results into the PSHA. In addition, the TI Team also evaluated and compared the different variants of Approaches 3 and 4 (McGuire et al., 2001 and Bazzurro and Cornell, 2004) for the development of the final hazard results.

Consistent with NUREG-2213, this study included all the roles and responsibilities needed to meet the expectations of a SSHAC Level-2 study, including a PPRP. Although this study was not for a specific regulatory action, the PPRP was included in the study to ensure that the results achieved the SSHAC goal to capture the CBR of TDIs. In addition, the study included one SSHAC Workshop with resource and proponent experts, and two PPRP briefings were held to discuss progress and elicit feedback. All the specific SSHAC roles are described more fully in the next section of this document.

### **1.3 Project Organization**

This project followed the personnel structure described for a SSHAC study consistent with the guidance in NUREG-2213 (Figure 1-2). This included a TI Team and oversight by a PPRP. The TI Team was composed of four members, all of whom are technical experts with previous experience in applying the SSHAC guidance. The TI Team was supported by three senior technical experts who performed many of the analyses. The PPRP had three members (one of whom served as chair of the panel), all of whom are also technical experts with experience in applying the SSHAC guidance. A Project Manager provided coordination, liaison, and contractual support. The roles and responsibilities of the project participants are summarized in Table 1-1.

As previously noted, the study included one formal Workshop, during which additional resource and proponent experts made presentations to provide information on existing data sets, alternative models, and subsequent uses of the site response analysis results. A summary of the Workshop is provided in Section 2 of this report and a list of presenters and attendees are provided in Tables 1-2 and 1-3, respectively. Presentations from the Workshop are contained in a package in the NRC's online document library (ADAMS) at ML21272A001.

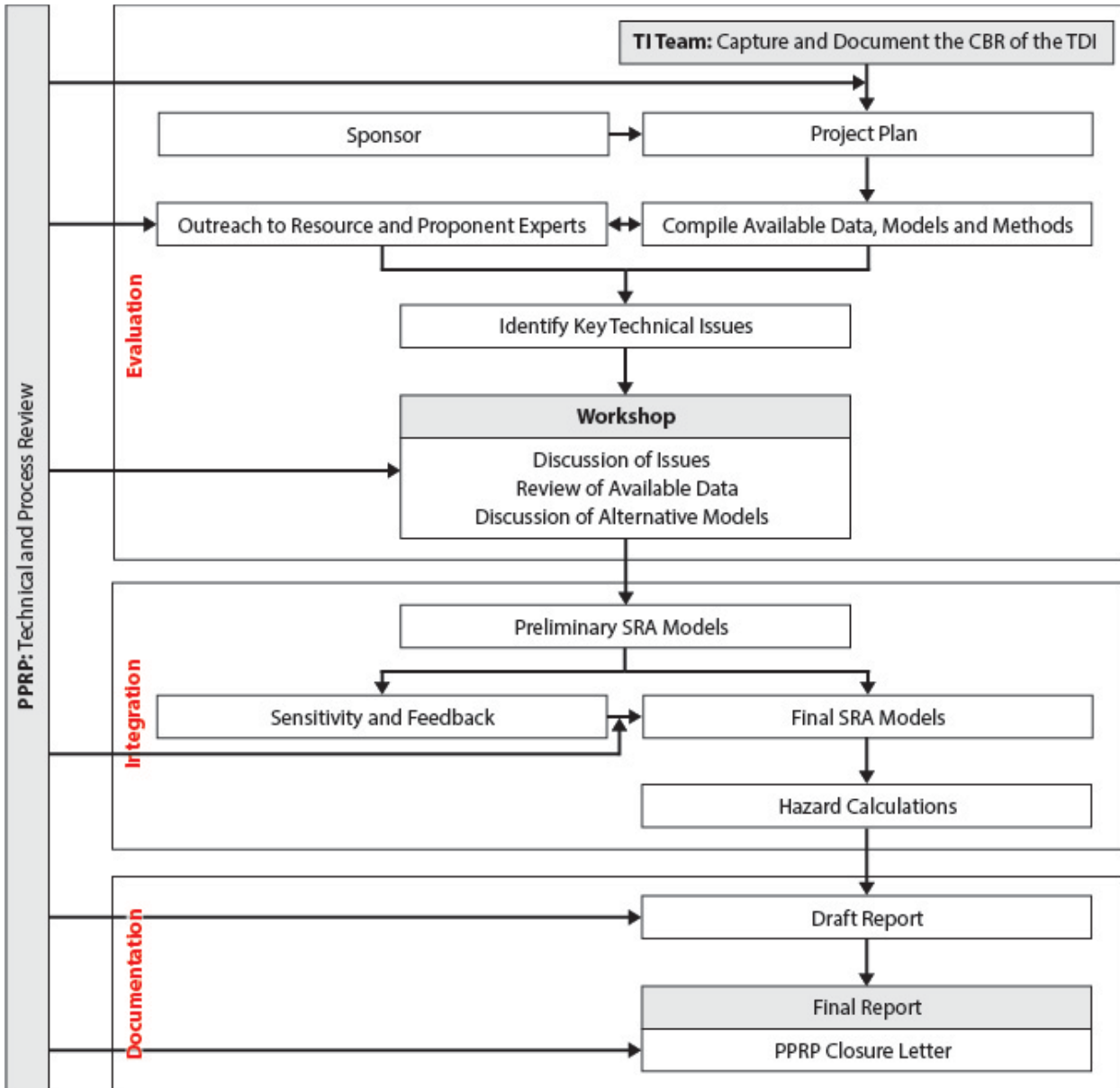


Figure 1-1 Flowchart for the SSHAC Level 2 site response analysis study, with time running from top to bottom (modified from NUREG-2213)

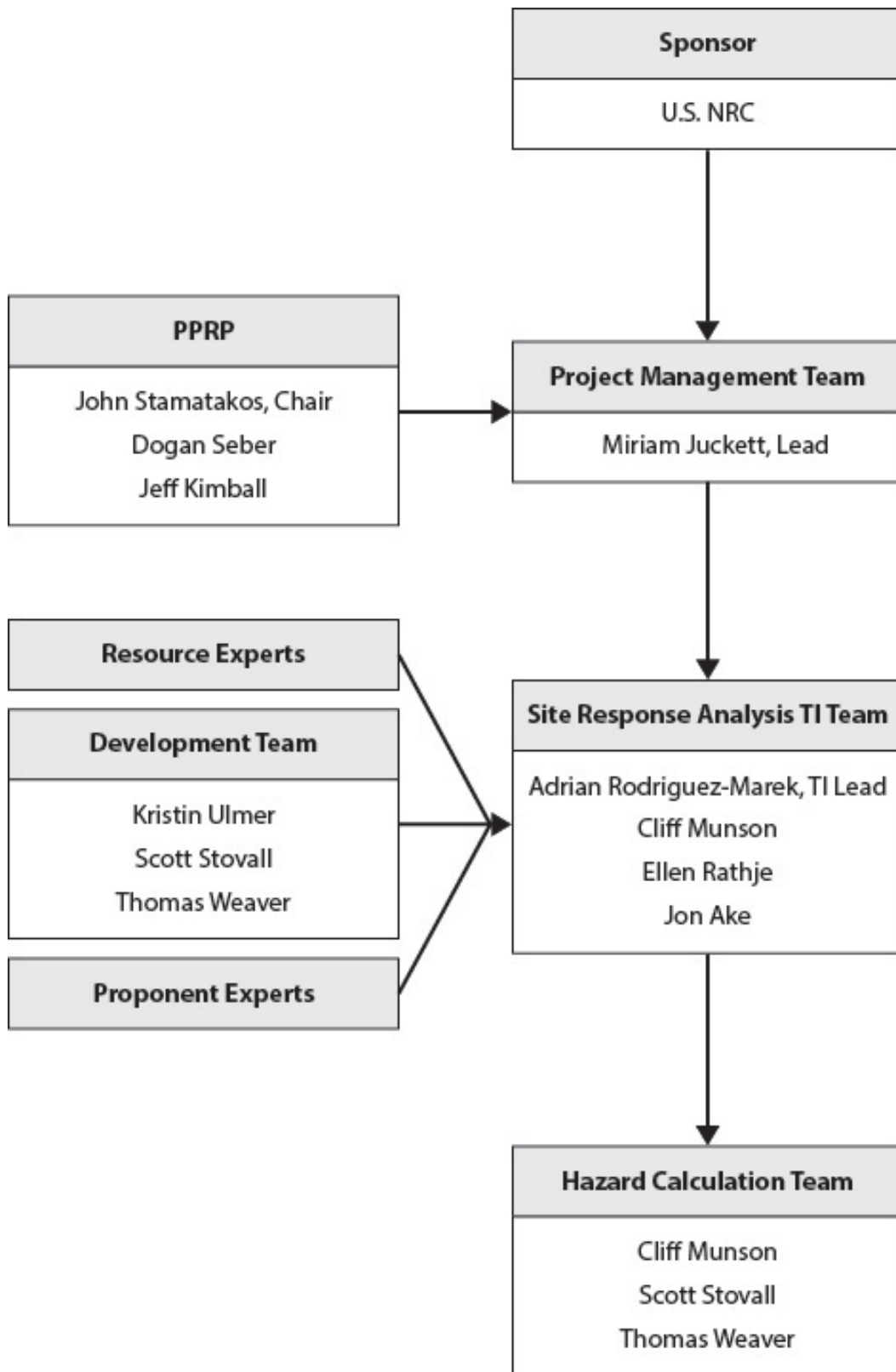


Figure 1-2 Organizational structure of this SSHAC Level 2 study

<b>Table 1-1 Roles and responsibilities for the SSHAC Level 2</b>		
<b>Role</b>	<b>Participant (Organization)</b>	<b>Responsibilities</b>
Project Manager	Miriam Juckett (CNWRA®)	Provides overall coordination and responsibility for organizational and administrative aspects of the project. Is the liaison between the Sponsor and the project participants, as needed.
Technical Integration Team (TI Team) Lead and Members	Dr. Adrian Rodriguez-Marek (TI Lead; Independent Consultant) Dr. Jon Ake (NRC) Dr. Cliff Munson (NRC) Dr. Ellen Rathje (Independent Consultant)	Responsible for developing the models and final recommendations for performing site response analysis following the SSHAC process and incorporating the site response results into PSHA hazard computations. As the <i>Evaluator</i> experts, TI Team members objectively examine available data, diverse models, challenge their technical bases and underlying assumptions, and, where possible, test the models against observations. They also identify the hazard-significant issues and the applicable data to address those issues, compile the available data (where practicable), and evaluate data relative to their quality and relevance for constructing models. They also identify the full range of data, models, and methods that exist in the technical community. The TI Team relies on available data and literature to make their evaluations. In light of their evaluations of the data, models, and methods in the professional literature, TI Team members as <i>integrators</i> build models that capture their assessments of knowledge and uncertainties. If existing models and methods are not judged to be adequate or viable, the integrators may develop their own models and methods, or they may refine or enhance existing models and methods. The TI Team also has the responsibility of developing inputs for use by the Hazard Analysts.
Hazard Analysts and Development Team (TI Team Support)	Dr. Scott Stovall (NRC) Dr. Thomas Weaver (NRC)	Responsible for establishing and managing necessary data sets and maintaining them in a Team-accessible location. Responsible for executing calculations and sensitivity studies and documenting the final results according to the inputs developed by the TI Team.
Hazard Analysis Support (Development Team)	Dr. Kristin Ulmer (CNWRA)	Assists the hazard analysts and TI Team with supplemental analyses, as requested.
Sponsor	Represented by NRC Contracting Officer's Representative,	Funds the study and provides input as requested on the Project Plan; works with Project Manager to ensure that the purpose,

<b>Table 1-1 Roles and responsibilities for the SSHAC Level 2</b>		
<b>Role</b>	<b>Participant (Organization)</b>	<b>Responsibilities</b>
	Dr. Scott Stovall (NRC)	process, and outcomes of the study will meet Sponsor goals.
Resource and Proponent Experts	Dr. Youssef Hashash Dr. Gabriel Toro Dr. Brady Cox Dr. Tom Houston Dr. Ken Stokoe Dr. Bob Youngs Dr. Katerina Ziotopoulou Dr. Jon Stewart Dr. Walt Silva	Provides input via presentations and teleconference interviews on site response models and incorporation of site response into the hazard.
Participatory Peer Review Panel (PPRP)	Dr. John Stamatakos (CNWRA), PPRP Chair  Jeff Kimball (Independent Consultant)  Dr. Dogan Seber (NRC)	Responsible for technical and process reviews to ensure the SSHAC approach is implemented per regulatory guidance. For the technical reviews, the PPRP will ensure that the full range of data, models, and methods have been duly considered in the assessment as appropriate for this study, and all technical decisions are adequately justified and documented. They also ensure adequate oversight and assurance that the evaluation and integration aspects of the TI Team's assessments have been performed appropriately. Through their participation at meetings, conference calls, and webinars, the PPRP addresses TI Team concerns, guides selection of sensitivity analyses, reviews inputs to calculations as appropriate, reviews calculation and sensitivity analysis results, and reviews all draft and final documentation. At the end of the study, if acceptable, documents approval in a closure letter.
<p>NRC—U.S. Nuclear Regulatory Commission; CNWRA®—Center for Nuclear Waste Regulatory Analyses; SSHAC—Senior Seismic Hazard Analysis Committee; PSHA—probabilistic seismic hazard analyses; TI—Technical Integration.</p>		

•

<b>Table 1-2 Presentations and interviews for workshop</b>		
<b>• Title of Presentation</b>	<b>• Name</b>	<b>• Affiliation</b>
• Introduction: Project description, scope, and objectives	• Jon Ake • Miriam Juckett	• NRC • CNWRA
• Epistemic uncertainty in ground motion characterization and site response analyses	• Adrian Rodriguez-Marek	• Independent Consultant/Virginia Tech
• Western United States (WUS) Data	• Scott Stovall	• NRC
• Central and Eastern United States (CEUS) data	• Thomas Weaver	• NRC
• Sources and ground motion models	• Cliff Munson	• NRC
• Uncertainty in laboratory characterization of soils – non-linear behavior	• Ken Stokoe	• Independent Consultant/University of Texas
• Uncertainty in site characterization – surface wave and borehole studies	• Ken Stokoe	• Independent Consultant/University of Texas
• Uncertainty in site characterization – surface wave and borehole studies	• Brady Cox	• Independent Consultant/University of Texas
• Propagation of epistemic uncertainty and aleatory variability in site response analyses to include randomization approaches	• Gabriel Toro	• LCI
• Issues with site response at large strains	• Ellen Rathje	• Independent Consultant/University of Texas
• 1D site response – sources of epistemic uncertainty	• Youssef Hashash	• Independent Consultant/University of Illinois
• How to capture 2D spatial variability in 1D site response analyses	• Katerina Ziotopoulou	• University of California Davis

<b>• Title of Presentation</b>	<b>• Name</b>	<b>• Affiliation</b>
• Approaches to include uncertainty of site response into hazard calculations, including host to target approaches	• Bob Youngs	• Wood
• Downstream uses	• Tom Houston	• Independent Consultant
• Response to questions from SwRI/NRC site response TI Team (Phone interview, 3/27/2020)	• Jon Stewart	• University of California at Los Angeles
• Site response (Phone Interview, 3/27/2020)	• Walt Silva	• Pacific Engineering

•

<b>• Name</b>	<b>• Affiliation</b>	<b>• Role</b>
• Jon Ake	• NRC	• TI Team
• Laurel Bauer	• NRC	• Observer (Regulator)
• Brady Cox	• Independent Consultant/University of Texas	• Resource/Proponent Expert
• Vladimir Graizer	• NRC	• Observer (Regulator)
• Youssef Hashash	• Independent Consultant/University of Illinois	• Resource/Proponent Expert
• Tom Houston	• Independent Consultant	• Resource Expert
• Miriam Juckett	• CNWRA	• Project Manager
• Jeff Kimball	• Independent Consultant	• PPRP
• Albert Kottke	• PG&E	• Observer
• Steve McDuffie	• DOE	• Observer
• Cliff Munson	• NRC	• TI Team
• Ellen Rathje	• Independent Consultant/University of Texas	• TI Team
• John Richards	• EPRI	• Observer
• Adrian Rodriguez-Marek	• Independent Consultant/Virginia Tech	• TI Team Lead

<b>Table 1-3 Workshop attendees</b>		
<b>Name</b>	<b>Affiliation</b>	<b>Role</b>
• Lisa Schleicher	• DNFSB	• Observer
• Dogan Seber	• NRC	• PPRP
• John Stamatakos	• NRC	• PPRP Chair
• Ken Stokoe	• University of Texas	• Resource/Proponent Expert
• Scott Stovall	• NRC	• TI Team Support/Hazard Analyst
• Gabriel Toro	• LCI	• Resource/Proponent Expert
• Kristin Ulmer	• CNWRA	• Technical and Project Management Support
• Thomas Weaver	• NRC	• TI Team Support/Hazard Analyst
• Rucker Williams	• SRNS	• Observer
• Bob Youngs	• Wood	• Resource/Proponent Expert
• Katerina Ziotopoulou	• University of California, Davis	• Resource/Proponent Expert

#### **1.4 Project Process Description**

The process followed to perform this study began with the development of a draft Project Plan by the Sponsor (the NRC). The Sponsor identified a TI Team Lead and Project Manager, and then chose the additional potential members of the TI Team and PPRP. Once participation by the team members was confirmed, the TI Team, Project Manager, and Sponsor developed a final draft of the Project Plan and provided it to the PPRP for comment. After engaging with the PPRP on comments, the TI Team finalized the Project Plan, which is included as Appendix B to this document.

To comport with the SSHAC guidance, the project was conducted with an initial evaluation phase followed by an integration phase.

The evaluation phase began with the TI Team identifying specific criteria that were important in the selection of study sites. Once those criteria were identified (described in more detail in Section 2) and sites selected, the TI Team also identified specific key technical issues for investigation during the Workshop and appropriate resource and proponent experts to address those issues. A few experts were unable to participate in the Workshop in person and instead provided presentations or information via phone interviews. Immediately following the Workshop, the TI Team received feedback from the PPRP on the conduct and content of the Workshop.

Subsequently, the TI Team and supporting technical staff began the integration phase by holding frequent working meetings, some of which had PPRP members participate as observers. Initial site response analyses and hazard calculations were performed to assess the hazard sensitivity of certain factors prior to the model-building activity. Then, preliminary site response analysis logic trees were constructed. The TI Team and technical support staff

conducted additional sensitivity studies, performed final calculations, and developed documentation. A draft report was developed and provided to the PPRP for comment. [PENDING: After interaction with the PPRP and resolution of comments, this final report was developed. The closure letter from the PPRP is included as Appendix A of this report.]

The remainder of this report is composed of the following sections: Section 2 describes the approaches for incorporating the site response analyses into the PSHA and provides a summary of the project Workshop and the key issues identified. Section 3 summarizes the approaches for developing site adjustment factor models, the use of site response logic trees, and the implementation of the site adjustment factors into the PSHA. Section 4 describes the motivation for selecting each of the two demonstration sites and provides a description of the geological settings, available geotechnical data, the SSC models and GMMs, and the reference condition hazard for the two sites. Section 5 provides a detailed explanation and technical justification for the site response logic trees and associated weights for each of the two demonstration sites. Section 6 presents the results of the site response analyses in terms of the site adjustment factors for the two sites and describes the contributions of different parts of the logic tree to the variability in the site adjustment factors. Section 7 presents the surface hazard curves for each of the sites along with hazard sensitivities. Conclusions and recommendations are contained in Section 8.

## **1.5 References**

Bazzurro, P., C. A. Cornell, and F. Pelli (1999). Site- and soil-specific PSHA for nonlinear soil sites, in Proc. of 2nd International Symposium on Earthquake Resistant Engineering Structures—ERES99, Catania, Italy, 15–17 June 1999, WIT Press, Southampton, U.K., Paper No. 27214.

Bazzurro, P. and C.A. Cornell. “Nonlinear Soil-site Effects in Probabilistic Seismic-hazard Analysis.” *Bulletin of the Seismological Society of America*. Vol. 94, Issue 6. pp. 2,110–2.123. 2004.

Budnitz, R.J., G. Apostolakis, D.M. Boore, L.S. Cluff, K.J. Coppersmith, C.A. Cornell, P.A. Morris. NUREG/CR–6372, “Recommendations for Probabilistic Seismic Hazard Analysis: Guidance on Uncertainty and Use of Experts.” Washington, DC: U.S. Nuclear Regulatory Commission. 1997.

Lee, R.C., W.J. Silva, and C.A. Cornell. “Alternatives in Evaluating Soil- and Rock-Site Seismic Hazard.” *Seismological Research Letters*. Vol. 69, p. 81. 1998.

McGuire, R.K., W.J. Silva, and C.J. Costantino. NUREG/CR-6728, “Technical Basis for Revision of Regulatory Guidance on Design Ground Motions: Hazard- and Risk-Consistent Ground Motion Spectra Guidelines.” Washington, DC: U.S. Nuclear Regulatory Commission. ML013100232. 2001.

NRC. NUREG–2213, “Updated Implementation Guidelines for SSHAC Hazard Studies.” ML18282A082. Washington, DC: U.S. Nuclear Regulatory Commission. 2018.

NRC. NUREG–2117, “Practical Implementation Guidelines for SSHAC Level 3 and 4 Hazard Studies.” Washington, DC: U.S. Nuclear Regulatory Commission. 2012a.

NRC. Regulatory Guide 1.165, "Identification and Characterization of Seismic Sources and Determination of Safe Shutdown Earthquake Ground Motion." Washington, DC: U.S. Nuclear Regulatory Commission. March 1997

## 2 Site Response Analysis Framework and Evaluation of Key Issues

### 2.1 Overview of Approaches for Incorporating Site Response into PSHA

The properties and parameters that control the soil and rock dynamic response can affect the amplitude, frequency content, and duration of the ground motion at a site. The extent of these effects depends on the properties of the subsurface materials, site topography, and input motion characteristics. However, these properties and parameters are often not known with certainty (i.e., they are uncertain). Previously, the state of practice in calculating a site-specific ground motion was to calculate probabilistic bedrock ground motion and then multiply it by a deterministic site-amplification factor (often a single mean or median value). If site amplification were truly single-valued, this would then imply that there is no uncertainty in its calculation, and the resulting site-specific ground motion would still be a probabilistic result. However, there is uncertainty in estimating the site amplification. Thus, the resulting ground motion produced by this process is a hybrid result that is no longer truly probabilistic.

To produce a truly probabilistic estimate of seismic hazard at the soil surface (or any arbitrary elevation), both the epistemic uncertainties and aleatory variability of the soil dynamic response need to be estimated and propagated through the calculations (Lee et al., 1998; Lee et al., 1999, Cramer, 2003; Bazzurro and Cornell, 2004). Two basic types of procedures to incorporate uncertainties in soil dynamic response have been discussed for estimating “soil” uniform hazard spectra (UHS) (McGuire et al., 2001). One approach uses the rock UHS at a given annual frequency of exceedance (AFE) to derive a soil UHS at the same annual frequency. The mean site adjustment factors (*SAFs*) are used in this procedure. The second approach integrates over all “rock” amplitudes to compute soil hazard (probability or frequency of exceedance versus amplitude). UHS can then be derived directly from the soil hazard curves. This procedure integrates over the full distribution of uncertainty in *SAFs*. Following the nomenclature used in McGuire et al. (2001), the procedures that utilize a rock UHS to derive a soil UHS are collectively referred to as Approach 2. The procedures that integrate over rock amplitudes to compute soil hazard are Approach 3. Approach 4 is also an integration method, but it relies on deriving a site-specific ground motion prediction equation (GMPE) or modifying an existing GMPE with the *SAFs* and their associated uncertainties (derived either empirically or analytically) prior to performing the hazard integration.

Approach 2 has been previously used in commercial nuclear power plant applications in the United States (U.S.). Approach 2 was used for some early site permits and combined operating license applications because the applications focused on defining a design spectrum consistent with the expectations from RG 1.165 and 1.208, rather than hazard curves at plant grade. The application of Approach 2 uses an enveloping step to mitigate some of the potential un-conservatism inherent in the approach. However, several recent studies have applied Approaches 3 or 4 [Bommer et al. (2013), Coppersmith et al. (2014), EPRI (2013), Spain (unpublished)<sup>1</sup>]. There are several reasons for the increased application of the integration approaches. First, they allow the full transparent propagation of uncertainty into the soil hazard results. Second, the soil hazard curves and associated uncertainties (usually expressed as fractiles) are an important product for risk analysis purposes. Third, it is an open question

---

<sup>1</sup> Several members of the Technical Integration (TI) Team and Participatory Peer Review Panel (PPRP) for this project also participated in the Senior Seismic Hazard Analysis Committee (SSHAC) studies conducted in Spain and Taiwan. Results from these studies are not currently published or publicly available; thus, no specific citation is provided.

whether the soil UHS derived from Approach 2 is a full representation of the center, body, and range of technically defensible interpretations (CBR of TDIs), as described in NUREG–2213 (NRC, 2018). Finally, because the soil UHS can be derived simply from the soil hazard results, there is nothing provided by Approach 2 that cannot be developed from the Approach 3 or 4 results.

The challenge in performing all state-of-the-practice site response analysis studies remains the identification of the significant sources of uncertainty and the consistent characterization of them as either epistemic or aleatory. This challenge provides the framework for the Senior Seismic Hazard Analysis Committee (SSHAC) Workshop convened for this project and subsequent discussions among the Technical Integration (TI) Team during the conduct of the present study. The remainder of this section presents a summary of the Workshop followed by a detailed description of the key issues that the TI Team considered in developing the site response logic trees for the two sites.

## **2.2 Workshop Summary**

Collectively, the TI Team has extensive experience conducting and reviewing site response analysis studies for critical facilities. Based upon that experience and knowledge of the applicable literature, the TI Team identified several topics of interest prior to the Workshop. These topics were determined to be important to the characterization of uncertainty and influenced the choice of invited experts and the questions provided to them. The invited experts are listed in Section 1.3 and Tables 1-1 and 1-2. The following paragraphs summarize some of these topics, the questions posed to the speakers, and the insights provided by the resource and proponent experts during the Workshop.

Prior to the Workshop, the TI and Project Development Teams had identified two study sites to be used for application of the SSHAC process in site response analysis, one in the western U.S. (WUS) and one in the eastern U.S. A detailed description of the two study sites and their relevant attributes is provided in Section 4. Several of the resource experts had direct experience with these two sites and some of the discussions during the Workshop were related to characteristics of the sites and how best to characterize the uncertainties. The Workshop agenda and complete presentations of the invited experts are contained in a package in NRC's document management system (ADAMS) at ML21272A001.

### **Topic 1: Uncertainty in Laboratory and Field Characterization**

One of the key elements of uncertainty in predicting soil response to ground shaking is the characterization of the properties of the subsurface material. Some of these properties are measured in the field and some in the laboratory. Two experts were invited to discuss this topic during the Workshop (Professors Ken Stokoe and Brady Cox). Specific questions (in bold) and composite summary responses are given below:

- **Compare and contrast the available  $V_S$  measurement approaches, in terms of maximum depth of investigation and layer resolution, for commonly used  $V_S$  techniques. Discuss how to differentiate (and, if possible, quantify) epistemic uncertainty and aleatory variability (i.e., spatial variability) in those techniques.**
  - To compare results between different  $V_S$  measurement techniques, it is important to consider the wavelength and the volume of soil/rock being sampled with each technique. Depth resolution depends on the frequency/wavelength of the bandwidth

- of dispersion data [for multi-channel analysis of surface waves (MASW) and microtremor array measurements (MAM) techniques], which depends on receiver array geometry, frequency content, and amplitude of noise. The ability to resolve thin layers decreases with increasing depth.
- The uncertainty in the experimental dispersion data is both aleatory and epistemic. For areas with common parent material, a coefficient of variation (COV) of 0.1 to 0.2 is reasonable. Measured COVs in  $V_S$  for placed and compacted material is  $\sim 0.05$  and should be viewed as a lower bound for native material. Analyst-to-analyst variability in MASW processing is  $\sim 10\%$ .
  - Concerns were raised with the blind application of generic uncertainties in  $V_S$ ; the resulting profiles may be inconsistent with the site signature (i.e., fundamental mode dispersion curve). The recommendation is to constrain randomized profiles to fit (to some degree) observed dispersion results.
  - **Should epistemic uncertainty in modulus reduction and damping (MRD) curves be captured via the use of alternative families of curves?**
    - No, the epistemic uncertainty should be small (at least at small strains). The variability in published MRD curves results from using test results of materials from all over the world.
    - Soils with the same index properties from different sites generally have some differences, but these differences are likely small.

Topic 2: Propagation of Aleatory/Epistemic Variability from Site Characterization into Site Response Analysis Calculations

After the properties of the subsurface materials and their associated uncertainties have been estimated, the question of how to partition the total uncertainty into aleatory and epistemic components and propagate those uncertainties into the site response calculations becomes important. The TI Team invited Dr. Gabriel Toro to discuss these issues as a resource expert. Specific questions (in bold) and responses are below:

- **Discuss approaches for differentiating epistemic uncertainty and aleatory variability in the inputs to site response analyses.**
  - Recent studies (EPRI, 2013) recommend treating spatial variability over the typical scale of nuclear facilities [ $\sim 100$  to 200 meters (m)] as aleatory variability. Dr. Toro recommended treating profile uncertainty as an aleatory variability because footprint variability cannot be handled within the framework of commonly used one-dimensional (1D) analyses. Randomization is often used to compensate for the limitations in current approaches to site response analysis, usually to smooth sharp peaks in computed amplification functions. These sharp peaks are not observed in empirical data.
  - The COVs obtained from generic category-based analyses are large ( $\sim 0.35$ ), but these values are not relevant to the aleatory “footprint” situation.

- **Address the differentiation of epistemic uncertainty and aleatory variability in consideration of different elements of site response, including shear-wave velocity profiles, shear modulus reduction and damping curves.**
  - It is important to recognize there are method-to-method and analyst-to-analyst differences that contribute to total uncertainty. Uncertainty that is explicitly recognized and incorporated by a given stochastic model is aleatory. Uncertainty on the model and its parameters is epistemic. Hence, the aleatory/epistemic split of the total uncertainty is a model-dependent issue.
  - It is important to focus on the aleatory/epistemic partition because insights can be gained from these considerations. However, the primary focus should be on getting the total uncertainty correct. The mean hazard is still the most widely used product of probabilistic seismic hazard analysis (PSHA), and it only depends on the total uncertainty.
- **Discuss the choice of reference horizon and the resulting uncertainty related to uncertainty in the reference horizon.**
  - Uncertainty arises from the choice of reference horizon. This uncertainty depends on the approach taken; for example, starting the site response calculations at the reference horizon or at the source depth results in different uncertainties. Modeling uncertainty in this choice should be treated explicitly.
  - The reference horizon should be defined to be consistent with the GMPEs. The uncertainties in the reference horizon properties should be captured by the uncertainty in the rock/reference GMPE.

### Topic 3: Incorporating Spatial Variability

Current practice in site response analysis assumes a 1D condition with plane-wave input. A two-dimensional (2D) representation will likely result in a more realistic representation of actual site conditions. The TI Team was interested in assessing the impact of the 1D assumption on the characterization of spatial variability in site response. To address this question, the Team invited Professor Katerina Ziotopoulou. Specific questions (in bold) and responses are provided below:

- **Discuss the impacts of 2D spatial variability, both random and systematic, on site amplification.**
  - The results from 1D analyses should not be exceeded by 2D analyses. Randomization of 1D profiles suppresses amplitude in the response (referred to as “Pseudo-Damping”)
- **Discuss approaches to capture 2D spatial variability in response using 1D site response analyses.**
  - To address this, a 2D response exercise was conducted using plane-wave input. The mean of the 2D analyses is different from the 1D randomization: the differences are in both frequency and amplitude. Less discrepancy is observed as  $V_s$  increases,

but there is more discrepancy for deeper profiles – the differences should be a function of wavelength.

- In the long-term, approaches should be to move towards 2D analyses.

#### Topic 4: Bias and Uncertainty in 1D Site Response Analysis

The current practice in site response modeling assumes a 1D system (flat layers that extend infinitely in the horizontal direction). Commonly used analysis techniques include equivalent linear (EQL) and non-linear (NL) methods. The TI Team wished to evaluate the potential bias that might exist between alternative analysis methods and whether including alternative methods was justified based on the state-of-the-practice and maturity in these models. To address this topic, the TI Team requested that Professors Ellen Rathje and Yousef Hashash respond to a set of questions acting as resource/proponent experts. Specific questions (in bold) and composite summary responses are below:

- **Discuss the validity of EQL and NL analyses at large strains.**
  - Rathje: Based upon analyses of empirical downhole data, both EQL and NL analysis methods underpredict motions for shear strains  $> 0.1\%$  and frequencies greater than  $\sim 2$  Hertz (Hz). Implementing EQL with frequency dependent (FD) properties (EQL-FD) improves the comparison with empirical data relative to both EQL and NL methods.
  - Rathje: Applying a strength correction for the  $G/G_{\max}$  curves improves results somewhat but does not entirely remove bias relative to observations.
  - Hashash: NL generally works well. For existing NL models, there are some that are older and have issues (Rayleigh damping, implementation of unload-reload rules, and computational efficiency) and should no longer be used.
- **Discuss approaches to more accurately capture large strain site response (EQL-FD and site kappa-scaling).**
  - Rathje: Comparison of empirical downhole data to EQL-FD predictions indicate an overprediction by the EQL-FD model for frequencies  $> 5$  Hz due to the use of small-strain damping at high frequencies.
  - Rathje: Agreement between small-strain and large-strain site kappa (also referred to as  $\kappa_0$ ) indicates that at high frequencies, damping should remain at  $D_{\min}$  for large strain motions. This implies that it is reasonable to scale results of EQL response analyses to a target, small-strain  $\kappa_0$ . Comparison of residuals using kappa-corrected EQL to EQL-FD and strength-corrected EQL shows significant reduction in bias with kappa-correction.
  - Hashash: Strength is a fundamental parameter in NL modeling – constraining mean and uncertainty in strength is important. Caution should be exercised about base isolation effect (which can lead to severe underestimation in the predicted motions).
  - Hashash: Even for NL analyses, shear strain limits of 0.3 to 1.0% should be respected.

## Topic 5: Incorporating Site Amplification into Hazard Calculations

Another important issue is related to how the site response results are incorporated into a computational framework for the final PSHA calculations. Based on experience on other projects, the TI Team identified several issues that justified additional consideration. Dr. Robert Youngs was invited to participate as a resource expert and provide insights based on his considerable experience in this area. Specific questions (in bold) and responses are provided below:

- **Discuss different approaches for accounting for epistemic uncertainty and aleatory variability in site response analyses, including which elements of aleatory variability in site response should be excluded from the uncertainty in site response to avoid double-counting of uncertainty.**
  - There are two approaches to performing site response analyses in current use: one applies reference rock motions at a specified depth (often called the geotechnical approach); another utilizes the full crustal profile in a “host-to-target” adjustment. In terms of implementation in hazard calculations, there are no differences between the two approaches. Typically, uncertainties in the reference profiles are not explicitly included, although these are expected to be small.
  
- **Discuss approaches for obtaining hazard fractiles that include epistemic uncertainty in site response, including issues of Approach 3 versus Approach 4.**
  - *SAFs* enter the hazard calculations differently depending upon the approach. The convolution, post reference hazard version of Approach 3 (Bazzurro and Cornell, 2004) can be implemented in two ways. In one method, the *SAF* epistemic alternatives are combined into a single composite mean and sigma. In the other method, a soil hazard for each mean *SAF* epistemic alternative is developed, and these are combined using the appropriate logic tree weights. Conceptually, the two should produce the same mean hazard. However, this is true only if uncertainties in  $V_S$  and MRD curves are considered to follow lognormal distributions. It is not true when a lognormal distribution can't be assumed. This is an advantage of the second approach.
  - Using the second alternative described above, it is possible to produce an estimate of soil fractiles by convolution of *SAF* with multiple rock fractiles. Fractiles of rock hazard can be generated using a discrete representation of the distribution of rock hazard and then convolved with the *SAF* fractiles to develop equally weighted fractiles (generally 100+ required). Representative rock hazard curves could be built by applying cluster analysis, but one must reproduce the covariance structure of all hazard curves. Difficulties arise if there is significant magnitude dependence of *SAF*. An alternative is to insert *SAF* into the hazard integral.
  - Both methods compare well except at low mean AFE—differences get smaller as the site gets stiffer.
  - To expedite computations, entire distribution of *SAFs* (many hundreds) can be collapsed into a small number of branches (7 for example). We are interested in capturing CBR of the *SAF* distributions.

- Proponent view: Single station phi (phi-ss) already includes variability that results from randomization in *SAF* for the linear range. To avoid double-counting in the linear range, turn the uncertainty in *SAF* (sigma- $\ln SAF$ ), “on” at some intensity level to account for additional uncertainty at larger strains, but ignore at low strains.
- **Discuss approaches for developing input motions for site response analyses.**
  - There are two methods in current use. One uses stochastic input motions (Random Vibration Theory, or RVT)—this method is computationally faster but requires specification of duration. The second uses multiple time series which are conditioned on target spectra (generally loosely matching). An advantage to this approach exists if time histories might be needed in subsequent analyses.
  - Spectral shape matters for nonlinearity; in some situations, it may also be important in the linear range. The concept of deaggregating earthquakes was developed for this purpose. Bimodal scenarios suggest the use of two target frequencies or perhaps the use of conditional mean spectra (CMS).

#### Topic 6: Site Response Outputs Needed for Soil-Structure Interaction Analyses

The TI Team concluded it was important to consider input from an expert who represented the community of downstream users of the final soil hazard/site response results (e.g., structural engineers). The objective was to ensure that the final product produced by the site response process would be useful for that community. Based on his extensive experience in the soil-structure interaction (SSI) field, the Team invited Dr. Tom Houston to participate in the Workshop as a resource expert. Specific questions (in bold) and responses are provided below:

- **Provide a brief description of the current process for integrating or utilizing the results of the site response analysis into the SSI analysis.**
  - Current practice utilizes a deterministic representation of profiles and properties to develop SSI inputs. The strain-compatible properties are defined for both surface conditions (GMRS) and at depth (foundation input response spectrum, or FIRS).
  - Three columns are usually specified based on PSHA and site response analysis results. The best-estimate column is usually derived from the mean of the PSHA, consistent with strain levels of GMRS. The lower-bound profile is developed from the 16<sup>th</sup>-percentile  $V_S$  and 84<sup>th</sup>-percentile soil damping. The upper-bound profile is based on 84<sup>th</sup>-percentile  $V_S$  and 16<sup>th</sup>-percentile soil damping properties. The results of the three columns are enveloped.
  - Uncertainty in site response analysis affects SSI response in these areas; (1) estimate of mean and standard deviation in strain compatible properties, and (2) spatial variability of soil properties and ground motions.
- **What is the expectation for future directions in site response analysis-SSI analysis?**
  - If we base sigma (uncertainty in properties) on adjustment factors rather than  $V_S$ , a mapping scheme to get SSI properties consistent with code objectives will be needed.

## 2.3 Identification of Key Issues

Based upon the Workshop presentations and subsequent internal discussion, the TI Team developed a general framework for the site response analysis logic trees (see Section 5). Important issues raised in the Workshop that informed the TI Team's development of the logic trees are presented below.

- The interface with the GMM provides a starting point for the framework, as the approach used to develop the *SAFs* determines the different profiles that must be analyzed.
- Epistemic uncertainty in the  $V_S$  profiles (including the need for potential alternative base cases), as well as the aleatory variability about any individual base case, should be assessed for each site.
- The TI Team will need to assess how the relevant uncertainties should be partitioned into epistemic and aleatory components, and how they can be constrained based on the available information at each site. Establishing the correct total uncertainty was identified as an essential task.
- The  $\kappa_0$  should be used to constrain the small strain damping in the profiles. The uncertainty in this parameter should also be captured through the site response logic trees, although the approach to estimate  $\kappa_0$  will be quite different for the two sites.
- Modulus reduction curves may produce biased shear stress estimates at large strain since the available testing is limited to small to moderate strain levels (typically <0.3%). To address this issue, the TI Team will use multiple sets of MRD curves to capture the epistemic uncertainty, modify the modulus reduction curves at large strains to ensure that the shear stresses were consistent with the soil shear strength, and generate randomized MRD curves to capture aleatory variability.
- Alternative analysis methods were identified that resulted in the addition of downstream nodes. The resulting logic trees could have many branches. Based on recommendations presented in the Workshop, the TI Team elected to implement a process that produces a distribution of the complete set of *SAFs* and represent it with a much smaller discrete distribution that preserves the moments of the larger population.
- The TI Team concluded that it would be informative to produce hazard results for both Approach 3 and 4 as well as alternative implementations of Approach 3. The use of multiple approaches, using the same set of *SAFs*, will provide a comparison of the advantages and disadvantages of each approach as well as the consistency of the resulting hazard curves.

After the Workshop and during TI Team internal meetings, several issues were identified as potentially important, and the TI Team decided to perform sensitivity analyses to understand the hazard significance of these issues. These multiple sensitivity analyses are described throughout this report.

## 2.4 References

Bazzurro, P. and C.A. Cornell. "Nonlinear Soil-Site Effects in Probabilistic Seismic-Hazard Analysis." *Bulletin of the seismological society of America*. Vol. 94, No. 6. pp. 2110–2123. 2004.

Bommer, J.J., K.J. Coppersmith, R.T. Coppersmith, K.L. Hanson, A. Mangongolo, J. Neveling, E.M. Rathje, A. Rodriguez-Marek, F. Scherbaum, R. Shelembe, P. Stafford, and F.O. Strasser. "Probabilistic Seismic Hazard Analysis for the Thyspunt Nuclear Site, South Africa: Final Report, Submitted to ESKOM, South Africa. 2013.

Coppersmith, K., J. Bommer, K. Hanson, R. Coppersmith, J. Unruh, L. Wolf, B. Youngs, L. Al Atik, A. Rodriguez-Marek, G. Toro. "Hanford Sitewide Probabilistic Seismic Hazard Analysis." PNNL-23361. Prepared for the U.S. Department of Energy Under Contract DE-AC06076RL01830, and Energy Northwest, Pacific Northwest National Lab Report. November 2014.

Cramer, C.H. "Site-Specific Seismic-Hazard Analysis that is Completely Probabilistic." *Bulletin of the Seismological Society of America*. Vol. 93, Issue 4. pp. 1,841–1.846. 2003.

EPRI. "Seismic Evaluation Guidance: Screening, Prioritization and Implementation Details (SPID) for the Resolution of Fukushima Near-Term Task Force Recommendation 2.1: Seismic." Technical Report 1025287. Palo Alto, California: Electric Power Research Institute. February 2013.

Lee, R., M.E. Maryak, and J. Kimball. "A Methodology to Estimate Site-Specific Seismic Hazard for Critical Facilities on Soil or Soft-Rock Sites." *Seismological Research Letters*. Vol. 70. p. 230. 1999.

Lee, R., W.J. Silva, and C.A. Cornell. "Alternatives in Evaluating Soil- and Rock-Site Seismic Hazard." *Seismological Research Letters*. Vol. 69. p. 81. 1998.

McGuire, R.K., W.J. Silva, and C.J. Costantino. NUREG/CR-6728, "Technical Basis for Revision of Regulatory Guidance on Design Ground Motions: Hazard- and Risk-Consistent Ground Motion Spectra Guidelines." Washington, DC: U.S. Nuclear Regulatory Commission. ML013100232. 2001.

NRC. NUREG–2213, "Updated Implementation Guidelines for SSHAC Hazard Studies." Washington, DC: U.S. Nuclear Regulatory Commission. 2018.

### 3 Site Response Models for Incorporation into PSHA

#### 3.1 Approaches to Develop Site Response Adjustments

A key component of a probabilistic seismic hazard analysis (PSHA) is the ground-motion model (GMM), which predicts the probability distribution of ground shaking at a site as a function of the seismic source (e.g., earthquake magnitude or style of faulting), site-to-source distance (e.g., distance to rupture, or  $r_{rup}$ ), path effects, and simplified site characteristics [(e.g.,  $V_{S30}$ , the average shear-wave velocity over the top 30 meters (m))]. The effects of the site-specific soil and rock conditions are incorporated through a site adjustment factor ( $SAF$ ) that converts the spectral acceleration (5%-damped pseudo-acceleration response spectra,  $Sa$ ) for the GMM reference condition ( $Sa_{ref}$ ) into the spectral acceleration for the site-specific conditions ( $Sa_s$ ):

$$Sa_s = Sa_{ref} \cdot SAF \quad (\text{Eq. 3-1})$$

There are two components to the  $SAF$  that can be applied to a GMM (Figure 3-1): (1) an adjustment for the site-specific reference condition associated with the deeper velocity structure and site kappa (i.e., the zero-distance spectral decay factor, or  $\kappa_0$ ), and (2) an adjustment for the site amplification associated with the near-surface shear wave velocity ( $V_S$ ) profile and associated nonlinear soil properties (i.e., modulus reduction,  $G/G_{max}$ , and damping,  $D$ , as a function of shear strain).

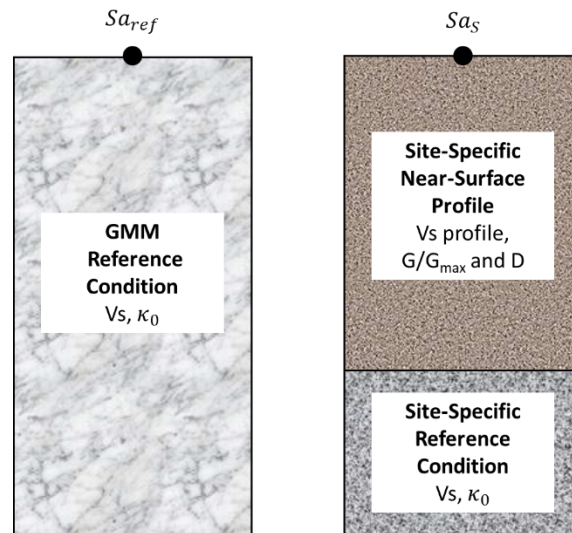


**Figure 3-1 Schematic of the GMM reference condition and the site-specific reference condition + near-surface profile**

#### **Reference Condition Adjustment**

The ground motions predicted by a GMM are associated with a reference site condition (Figure 3-1) that represents a crustal  $V_S$  profile and  $\kappa_0$ . Together, these parameters influence the amplitude and spectral shape of the ground motion. The  $V_S$  profile and  $\kappa_0$  associated with the reference condition of a GMM can be determined via direct measurements in the region for which the GMM was developed, or they can be inferred from the GMM itself (Al Atik and Abrahamson, 2021). The reference condition generally represents a stiff condition where the

GMM models the site amplification as linear (i.e., unaffected by the level of ground shaking). If this is not the case (e.g., if the GMM for the reference condition includes a term for nonlinear behavior or if it has some embedded nonlinearity due to the ground motions used in its development), then the nonlinearity needs to be taken into account in the adjustment to reference conditions.

An important consideration is whether the GMM reference condition is consistent with the site-specific reference condition in terms of the deeper  $V_S$  profile and  $\kappa_0$ . The site-specific reference condition is commonly selected to represent the rock condition below the base of the site-specific soil profile, which is modeled as an elastic half-space in the site response analysis. The reference condition for the GMM may not be appropriate for a site because of regional differences in crustal  $V_S$  and/or  $\kappa_0$ . If the reference condition for the GMM is not appropriate for the site, a  $V_S$ - $\kappa_0$  adjustment is required (Rodriguez-Marek et al., 2014).

### **Near-Surface Site Adjustment**

The site-specific adjustment associated with the near-surface materials is derived from site response analysis. This analysis requires a  $V_S$  profile (and density) along with nonlinear soil properties ( $G/G_{max}$  and  $D$ ), and outcropping input motions appropriate for the site-specific reference condition at the base of the soil column. These motions are propagated through the soil column to compute the site amplification due to the near-surface materials.

The site response analyses may be performed using the equivalent linear (EQL) approach or the fully nonlinear (NL) approach. One advantage of the EQL approach is that random vibration theory (RVT) can be utilized, which eliminates the need to select input time series for analysis (e.g., Silva et al., 1996; Wang and Rathje, 2016). A commonly held belief is that EQL analysis becomes less accurate at larger strains and NL analysis is needed at these strain levels. However, some recent studies using downhole array data (e.g., Kaklamanos et al. 2015; Zalachoris and Rathje, 2015) indicate that improvements provided by NL analysis may be modest at best. Other options for improving site response estimates at large strains include (1) using the small-strain  $\kappa_0$  to scale the high-frequency components of the response (Xu and Rathje 2021) or (2) incorporating strain-dependent soil properties that account for the frequency dependence of the induced strains (e.g., Assimaki and Kausel, 2002).

### **Two-Step Versus One-Step Approach**

The reference condition adjustment and near-surface site adjustment have traditionally been performed separately through a two-step approach (e.g., Rodriguez-Marek et al., 2014). This approach first applies the  $V_S$ - $\kappa_0$  adjustment ( $Adj_{V_S-\kappa_0}$ ) to convert the GMM reference condition ( $Sa_{ref}$ ) into the site-specific reference condition ( $Sa_{sref}$ , Figure 3-2a). The second adjustment is associated with the near-surface site amplification ( $AF_{site}$ ) and converts the site-specific reference condition into the site-specific surface motion. The combined effects of these two adjustments result in the following two-step  $SAF$ :

$$SAF_{two-step} = Adj_{V_S-\kappa_0} \cdot AF_{site} \quad (\text{Eq. 3-2})$$

where  $AF_{site}$  is the ratio of the site spectral acceleration ( $Sa_s$ ) and  $Sa_{sref}$ . Alternatively, the crustal adjustment associated with  $V_S$ - $\kappa_0$  and the near-surface site amplification adjustment can be performed in one step through a single adjustment factor (Figure 3-2b). Here, a common, hard rock input motion ( $Sa_{input}$ ) is used for two separate site response analyses: one for the

reference GMM  $V_S$  profile and one for the combined site-specific reference profile plus near-surface  $V_S$  profile and nonlinear properties. The surface spectra from the two analyses are used to compute the one-step  $SAF$  as:

$$SAF_{one-step} = Sa_s^*/Sa_{ref}^* \quad (\text{Eq. 3-3})$$

where the asterisks indicate that these are not the values of  $Sa$  (spectral acceleration) for the site from the hazard assessment, but rather are associated with the hard rock input motion ( $Sa_{input}$ ). For the one-step adjustment, the differences in  $\kappa_0$  are modeled by assigning appropriate small-strain damping profiles to each  $V_S$  profile to generate the appropriate  $\kappa_0$  (i.e.,  $\kappa_0$  for the reference GMM condition and  $\kappa_0$  for the site-specific reference + near-surface condition). This issue is discussed further in Section 5.

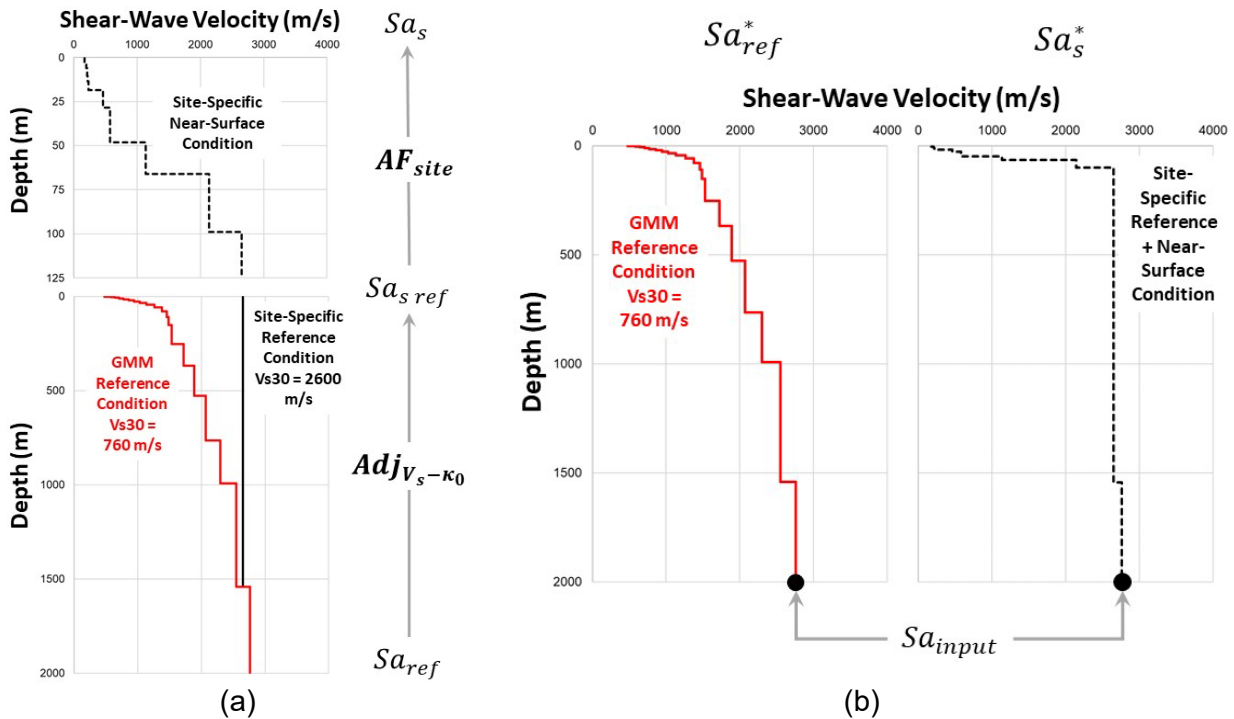


Figure 3-2 (a) Two-step method and (b) one-step method to develop  $SAF$

### 3.2 Epistemic Uncertainty and Aleatory Variability in Site Response

Independent of the approach adopted to compute the site adjustment for a site-specific PSHA, the process must capture the epistemic uncertainty and the aleatory variability<sup>2</sup> that is associated with the estimation of the  $SAF$ . While the separation of epistemic uncertainty and aleatory variability has little impact on the mean hazard, a proper partition of these sources of uncertainty is important whenever hazard fractiles are required as outputs from the PSHA. The correct separation of aleatory variability and epistemic uncertainty is also important because the latter can, at least in principle, be reduced through the acquisition of additional data or by using more appropriate methods and models. Therefore, identifying the reducible components of uncertainty can inform decisions for additional data collection or investments in more complex models (Rodriguez-Marek et al., 2020). A proper capture of the full range of epistemic uncertainty becomes even more important within a partially non-ergodic PSHA approach

<sup>2</sup> In general, “uncertainty” refers to epistemic uncertainty and “variability” refers to aleatory variability.

(Atkinson 2006, Rodriguez-Marek et al., 2013), where the site-to-site variability is excluded from the aleatory variability in the GMM [i.e., the aleatory variability is captured by the single-station sigma ( $\sigma_{ss}$ )]. A precondition to use  $\sigma_{ss}$  is that the uncertainty associated with the site term must be treated as epistemic uncertainty (Rodriguez-Marek et al., 2013).

The separation of aleatory variability and epistemic uncertainty in site response is not straightforward. In principle, epistemic uncertainty can be reduced if additional information (in the form of additional data or improved methods or models) becomes available, while aleatory variability reflects variability that cannot be reduced within the selected modeling approach. From this point of view, uncertainty in the estimation of *SAF* should be counted as epistemic uncertainty. Moreover, uncertainty in  $V_S$  profiles from the use of different measurement techniques or from measurement errors within a single technique should be treated as epistemic uncertainty. On the other hand, uncertainties that reflect spatial variability in soil properties within the footprint of a structure can be considered aleatory, as these cannot be reduced [at least not in the context of a one-dimensional (1D) site response]. This conceptual separation is adopted in this work. Additional discussion of aleatory variability is presented in Section 3.4. The remaining paragraphs in this section propose an approach to capture epistemic uncertainty in site response through a logic tree approach.

### **Site Response Logic Tree**

A common approach to capture epistemic uncertainty in more recent site response analyses for critical facilities has been to include alternative site properties within a logic-tree formulation. The guidelines for the selection of ranges of epistemic uncertainty for site response analyses presented in Electric Power Research Institute (EPRI) (2013) were developed for older nuclear facilities, for which limited site subsurface surveys were performed. Although the logic tree approach recommended in EPRI (2013) is for the seismic hazard reevaluations of older nuclear facilities, more recent and ongoing Senior Seismic Hazard Analysis Committee (SSHAC) projects have also implemented this approach in recognition that it is needed to fully capture the epistemic uncertainty inherent in site response analyses. The development of the logic tree for the site response analysis in terms of the number of branches and their weights is site-specific, in that it depends on the quantity and quality of the data as well as the characteristics of the site itself. Indeed, the aim of this project is to demonstrate the benefits of using the SSHAC process in order to more accurately characterize the epistemic uncertainties in the development of *SAF*.

The EPRI (2013) guidelines include suggestions for a three-branch logic tree to capture uncertainty in  $V_S$  profiles and a similar approach for the nonlinear soil properties ( $G/G_{max}$  and  $D$ ) and  $\kappa_0$ . There are, however, some potential problems associated with this approach. First, the choice of a limited number of logic tree branches (i.e., three branches as specified in EPRI, 2013) can lead to an artificially low spread of resulting *SAF*. An example that illustrates this point was constructed by Rodriguez-Marek et al. (2020) and is shown in Figure 3-3. While this example illustrates an artificially constructed profile, it clearly shows that three base-case  $V_S$  profiles that have a considerable spread in values across all depths can lead to a small range of uncertainty in *SAF* at some periods. The problems illustrated in Figure 3-3 result from the fact that the epistemic uncertainty in soil properties does not necessarily map well into the epistemic uncertainty in *SAF*. The use of a larger number of branches to capture the uncertainty in the  $V_S$  profile can reduce or eliminate this problem, but there are no assurances that this problem is fully addressed until the resulting epistemic uncertainty is evaluated in terms of the epistemic uncertainty in *SAF*.

The problem identified in the previous paragraph can also occur in ground-motion space, where a logic tree populated by alternative GMMs does not necessarily ensure an adequate spread of ground motions for all magnitude and distance combinations. For this reason, recent projects have focused attention on developing schemes to sample GMMs directly from ground-motion space using visualization schemes such as Sammons Maps (proposed for PSHA by Scherbaum et al., 2010; for applications of the approach see GeoPentech, 2015; Goulet et al., 2018). An alternative solution is the “backbone” approach proposed by Atkinson et al. (2014). In this approach, the branches of a logic tree are populated with scaled or adjusted versions of a single GMM, which ensures that the range of predicted ground-motion amplitudes is consistent with the intended range of epistemic uncertainty.

The approach proposed herein is to represent the uncertainty in site properties through a site response logic tree, but then resample the *SAF* into a discrete number of branches (Rodriguez-Marek et al. 2020). This approach is conceptually similar to the backbone approach, whereas the epistemic uncertainty is sampled directly in the parameter space that enters into the PSHA. Directly sampling the results of the site response analysis process (i.e., the *SAF*) avoids the problem of an unintended under-representation of epistemic uncertainty. In addition to this obvious benefit, the proposed approach has two additional benefits. First, the resampling process implies that the computational cost of additional logic tree branches in the site response logic tree does not get transferred to an additional cost in the hazard computation. This can be significant when the site response is considered within the PSHA hazard integral (Section 3.4). A second benefit is that the tools to explore the sensitivity of logic trees in PSHA (i.e., tornado plots, or variance contribution plots) can be used to explore which components of the logic tree have the highest impact on the uncertainty in *SAFs*.

To illustrate the approach, Figure 3-4 shows the results of linear site response analyses conducted for the same profiles shown in Figure 3-3, but now using separate logic tree branches to account for the uncertainties in soil  $V_S$ , rock  $V_S$ , thickness of the rock layer, the gradient in the transition to the weathered rock, and uncertainties in viscous damping, resulting in 1350 logic tree profiles. The resulting range of uncertainty is, not surprisingly, broader than the uncertainty captured by the three representative  $V_S$  profiles (Figure 3-4a). A resampled, five-point, discrete representation of the 1,350 logic tree branches (with appropriate weights) more fully captures the uncertainty in the adjustment factors (Figure 3-4b).

### ***Model Error and Minimum Epistemic Uncertainty***

As mentioned above, one of the components of uncertainty that must be considered is the model error associated with the selected site response approach. In general, the range of epistemic uncertainty that results from the consideration of alternative profiles (e.g., Figure 3-4b) reduces at long oscillator periods. Figure 3-4c, which shows the standard deviation of the *SAF*, demonstrates that even for the example site response analysis that implements a more complete and detailed logic tree, the *SAFs* begin to merge for spectral periods greater than 1 second (s). This is a result of the assumptions of 1D site response, which predicts that the *SAF* reduce to unity for oscillator periods much longer than the site period. The low uncertainty would seem to suggest that the predictions of site response are very accurate for long periods. However, observations from the KiK-net array suggest that this is not the case. Rodriguez-Marek et al. (2011) found that the site-to-site variability for very stiff borehole sites was between 0.15 and 0.2 (in natural log units).

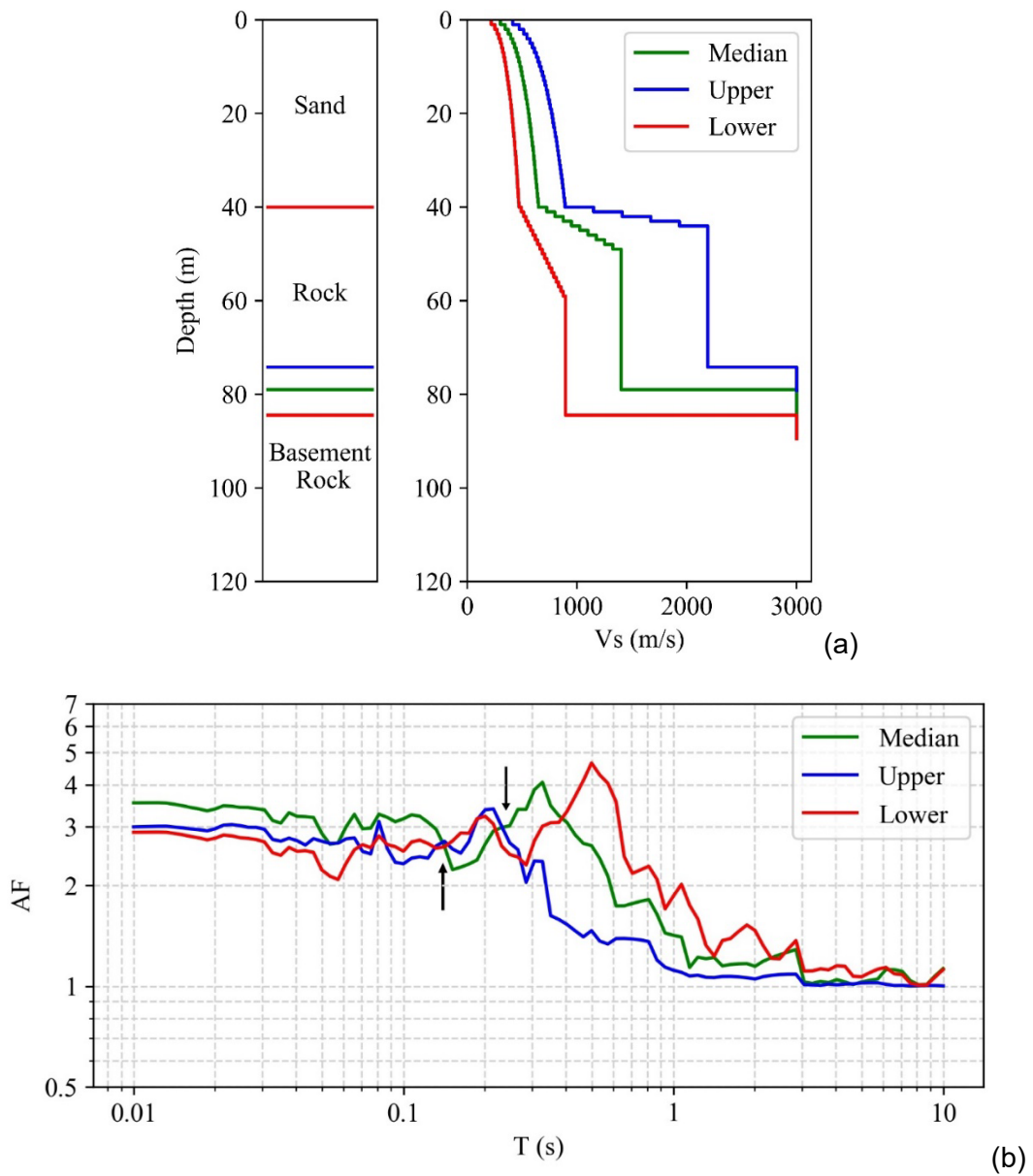


**Figure 3-3** Example illustrating an approach to capture epistemic uncertainties using three  $V_s$  profiles. (a) Stratigraphic profiles (left) and best-estimated and alternative upper- and lower-case  $V_s$  profiles (right) considered for this study, (b) Linear  $SAF$  corresponding to these three profiles. The arrows point to oscillator periods where the three  $SAFs$  cross over and the resulting epistemic uncertainty is low (from Rodriguez-Marek et al., 2020).

The minimum epistemic uncertainty quantified by Rodriguez-Marek et al. (2011) is focused on long periods where 1D site response predicts  $SAF = 1.0$ . Other authors have tried to directly quantify the model error in 1D site response analysis using downhole arrays (Stewart and Afshari, 2020; Kaklamanos et al., 2013, and Silva, 2015). The model error, defined as the standard deviation of the bias-corrected site terms, was reported between 0.2 and 0.4 by Stewart and Afshari (2020), between 0.3 and 0.6 by Kaklamanos et al. (2013), and between 0.1 and 0.15 by Silva (2015). One open question is whether the site properties should be optimized before evaluating the model error in an effort to separate the epistemic uncertainty in the site characterization from the model error. This is the likely reason that the values from Silva (2015) are smaller than the others. For cases where the epistemic uncertainty in the site characterization is captured elsewhere (e.g., via a site response logic tree), estimates of model error should exclude potential errors due to uncertainties in the site characterization.

There are two alternative approaches to capture the epistemic uncertainty that results from the model error; these two approaches imply two different assumptions on the nature of the estimated model error. One approach is to assume that estimates of model error cannot be decoupled from the parametric uncertainty that is built into a site response logic tree (i.e., uncertainties in the  $V_S$  profile, low-strain damping, etc.). In this case, the model error should be considered as a lower bound to the epistemic uncertainty in the computed  $SAFs$ ; that is, a *minimum epistemic uncertainty* for the  $SAFs$ . This approach has been adopted in several SSHAC Level 3 studies (Bommer et al., 2013; Coppersmith et al., 2014). Rodriguez-Marek et al. (2020) discuss how to implement the minimum epistemic uncertainty into the sampling of  $SAFs$ . An alternative approach assumes that the model error is statistically independent from the parametric uncertainty captured in the site response logic tree (Stewart and Afshari, 2020). In such a case, the model error must be added (via sum of variances) to the epistemic uncertainty computed by the proposed logic-tree approach. This can easily be incorporated into a site response logic tree via an additional branch to the logic tree. For this study, the Technical Integration (TI) Team chose to adopt the minimum epistemic uncertainty approach to capture model error. A minimum epistemic uncertainty of 0.15 in natural log units was selected for this study based on the Taiwan SSHAC study (unpublished)<sup>3</sup>.

Justification for this numerical value is given in Section 6. The TI Team's choice of the minimum epistemic uncertainty approach is guided by the consideration that current estimates of model error are unlikely to fully decouple the effects of parametric uncertainty. However, as indicated above, the choice of approach is dictated by how the model error is computed; additional research is needed to improve this quantification.

The application of the proposed approach to capture epistemic uncertainty in the  $SAFs$  is discussed throughout this report. The implementation of site response into the PSHA computations, including considerations of aleatory variability, is discussed in Section 3.4.

---

<sup>3</sup> Several members of the TI Team and PRRP for this project also participated in the SSHAC studies conducted in Spain and Taiwan. Results from these studies are not currently published or publicly available; thus, no specific citation is provided.

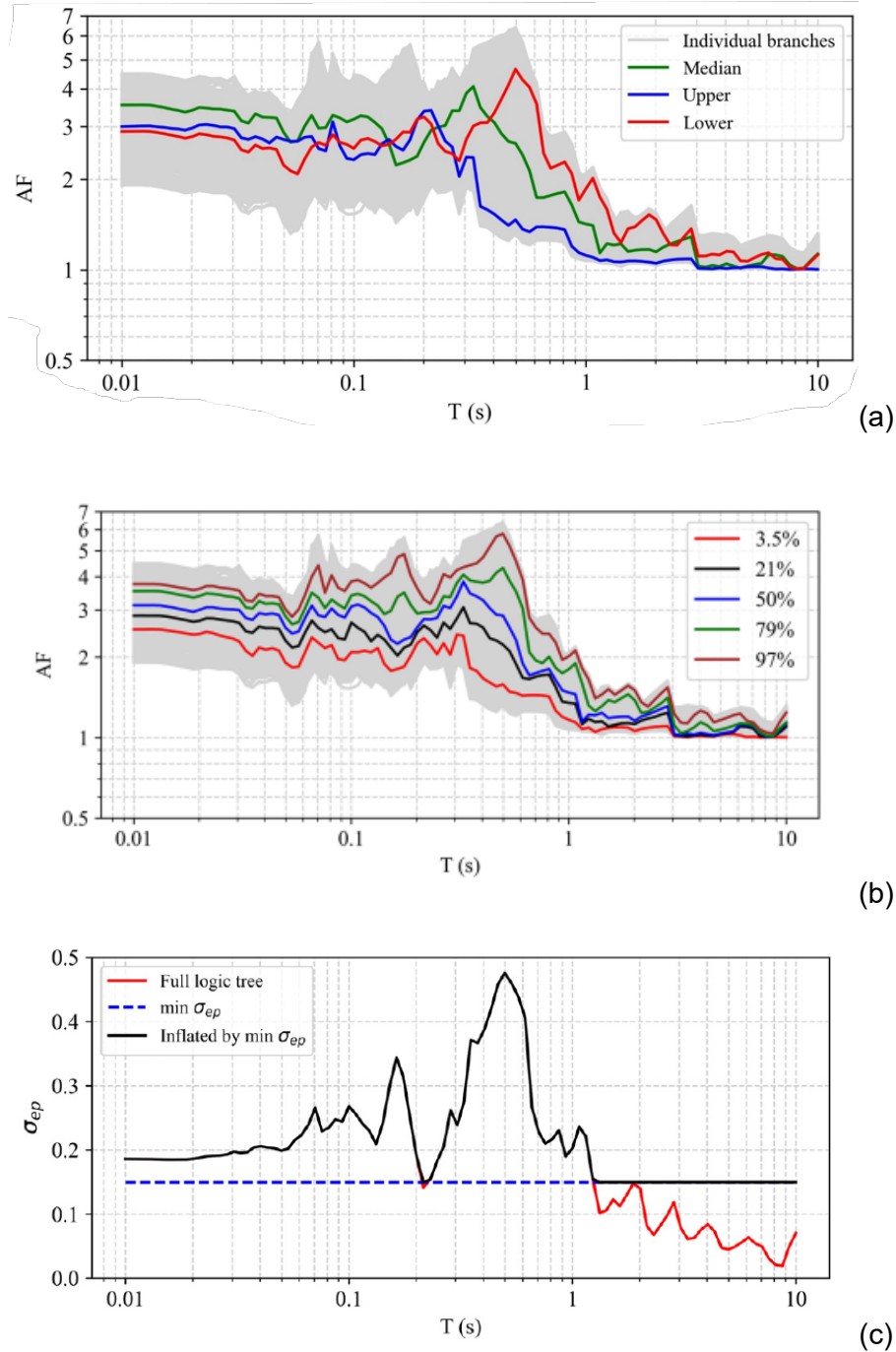


**Figure 3-4** (a) Median *SAF* (light gray lines) for full logic tree profiles capturing all sources of uncertainty for the site shown in Figure 3-3 along with the *SAF* for the median, upper, and lower profiles in Figure 3-3, (b) the resampled, five-point discrete representation of the full logic tree, and (c) the standard deviation of the *SAF* from the logic tree ( $\sigma_{ep}$ ) compared with the minimum epistemic uncertainty.

Section 5 discusses the elements of a site response logic tree and different approaches to fully sample the epistemic uncertainty for each logic tree branch. The remaining sections present

the application of this approach to the selected study sites. Section 6 of this report describes the distribution of *SAF* resulting from the implementation of the site response logic trees for the two study sites, and Section 7 provides the results from implementation of the median *SAF* into the PSHA.

### 3.3 Philosophy for Developing Weights

The goal of the TI Team was, wherever feasible, to let the existing data influence the assignment of weights to alternative branches in the epistemic uncertainty logic tree (see, for example, the discussion of the epistemic uncertainty on  $\kappa_0$  in Section 4.3). However, for many instances, the data was not sufficiently informative to allow the derivation of objective weights. In those cases, subjective (degree-of-belief) weights were assigned to alternative logic tree branches.

To ensure that this process of assigning weights was consistent and transparent to the extent practicable, the TI Team developed a set of verbal descriptors that was used and discussed when assigning subjective weights to elements of the logic tree. The set of descriptive terms that was used in this process is contained in Table 3-1.

The objective of this process was to ensure that all TI Team members had a common understanding of the intent of the weights and that the process was transparent so that subsequent users of the product were also informed of the Team’s intent and assumptions. A small set of subjective weights were used to avoid a false sense of precision in the assignment of weights. If a set of N alternatives were deemed equally likely, then weights of 1/N were assigned to all branches.

### 3.4 Implementation into PSHA

As described in the previous section, the TI Team developed a cumulative distribution of weighted median *SAF* ( $\widehat{SAF}|m, r, x$ ) for each of the two study sites and then selected a seven-point discrete distribution using the percentiles and weights provided in Table 3 of Miller and Rice (1983). Table 3 of Miller and Rice (1983) provides discrete approximations for subjective, continuous probability distributions using Gaussian Quadrature. The TI Team selected a seven-point discrete approximation for the median *SAF* based on a comparison of the control point hazard curves using the full distribution of median *SAF* compared to the hazard curves developed using the seven-point discrete approximation. In his presentation during the Workshop for this SSHAC project (see Section 1.3 and 1.4), Dr. Robert Youngs demonstrated that the seven-point discrete distribution provides a reasonable approximation to the control point hazard results using the full distribution of median *SAFs*. In addition, prior to implementing the *SAFs* into the PSHA for the two project sites, the TI Team evaluated the standard deviation (in natural log units) of the median *SAF* across the entire range of spectral frequencies to ensure that the standard deviation met or exceeded a minimum epistemic uncertainty of 0.15. As recommended by Rodriguez-Marek et al. (2020), the TI Team widened the selected seven-point distribution of median *SAF* for the two study sites to achieve this minimum standard deviation before implementing the *SAF* into the PSHA.

<b>Table 3-1 Nomenclature for subjective weights</b>	
<b>Weights</b>	<b>Verbal Descriptors</b>
1.0/0.0	Certain/Impossible

<b>Table 3-1 Nomenclature for subjective weights</b>	
<b>Weights</b>	<b>Verbal Descriptors</b>
0.95/0.05	Virtually Certain
0.9/0.1	Highly Likely/Highly Unlikely
0.8/0.2	Very Strong Preference/Cannot Preclude
0.7/0.3	Strong Preference
0.6/0.4	Weak Preference
0.5/0.5	Equally Likely/No Preference

To implement the *SAF* into the PSHA, the TI Team used both Approaches 3 and 4 as described in McGuire et al. (2001). The frequency of exceedance ( $v(z)$ ) at which the spectral acceleration ( $Sa_s$ ) at the site exceeds a particular value  $z$  from  $N$  regional seismic sources is given by

$$v(z) = \sum_{n=1}^N \lambda_n(m_{min}) \int_{m_{min}}^{m_{max}} f(m) \left[ \int_0^{\infty} f(r|m) P(Sa_s \geq z|m, r) dr \right] dm \quad (\text{Eq. 3-4})$$

where  $\lambda_n(m_{min})$  is the frequency of earthquakes on source  $n$  above a minimum magnitude of engineering significance,  $m_{min}$ ;  $f(m)$  is the probability density function for event magnitude on source  $n$  between  $m_{min}$  and a maximum event magnitude for the source,  $m_{max}$ ;  $f(r|m)$  is the probability density function for source-to-site distance for ruptures on source  $n$ , which is conditional on earthquake magnitude; and  $P(Sa_s \geq z|m, r)$  is the probability that the site spectral acceleration exceeds a level  $z$ , given a source with magnitude  $m$  at a distance  $r$  from the site. As described in McGuire et al. (2001), the  $P(Sa_s \geq z|m, r)$  is given by

$$P(Sa_s \geq z|m, r) = \int_0^{\infty} P\left(SAF \geq \frac{z}{x} | m, r, x\right) f(x|m, r) dx \quad (\text{Eq. 3-5})$$

where  $P\left(SAF \geq \frac{z}{x} | m, r, x\right)$  is the probability that the *SAF* exceeds the ratio  $\frac{z}{x}$  given a source with magnitude  $m$  at a distance  $r$  that produces a reference condition spectral acceleration level  $Sa_{ref} = x$ ; and  $f(x|m, r)$  is the probability density function for  $Sa_{ref} = x$ , which is conditional on earthquake magnitude  $m$  and source-to-site distance  $r$ . The  $P\left(SAF \geq \frac{z}{x} | m, r, x\right)$  is given by

$$P\left(SAF \geq \frac{z}{x} | m, r, x\right) = 1 - \Phi\left(\frac{\ln\frac{z}{x} - \mu_{\ln SAF|m, r, x}}{\sigma_{\ln SAF|m, r, x}}\right) \quad (\text{Eq. 3-6})$$

where  $\Phi(\cdot)$  is the standard normal cumulative distribution function (CDF);  $\mu_{\ln SAF}$  is the conditional logarithmic mean of the *SAF*; and  $\sigma_{\ln SAF|m, r, x}$  is the conditional logarithmic standard deviation of the *SAF*.

### **Approach 3**

The TI Team used Approach 3 to develop site control point hazard curves by implementing Eq. 3-5 and Eq. 3-6 into Eq. 3-4 and then discretizing Eq. 3-4:

$$v(z) = \sum_{n=1}^N \lambda_n(m_{min}) \sum_{i=m_{min}}^{m_{max}} P[m_i] \left\{ \sum_{j=r_{min}}^{r_{max}} P[r_j|m_i] \sum_{k=x_{min}}^{x_{max}} P\left(SAF \geq \frac{z}{x_k} | m_i, r_j, x_k\right) P[Sa_{ref} = x_k | m_i, r_j] \right\} \quad (\text{Eq. 3-7})$$

where the multiple integrals in Eq. 3-4 to Eq. 3-6 have been replaced by summations and the probability density functions for magnitude, source-to-site distance, and reference condition spectral acceleration ( $Sa_{ref}$ ) have been replaced by their respective probability mass functions (PMF). The PMF for each of these random variables are then determined by differencing their respective CDF or complementary CDF (CCDF), as appropriate. For example, the PMF for the reference condition spectral acceleration is given by differencing its CCDF:

$$P[Sa_{ref} = x_k | m_i, r_j] = P(Sa_{ref} \geq x_{k-1} | m_i, r_j) - P(Sa_{ref} \geq x_k | m_i, r_j) \quad (\text{Eq. 3-8})$$

where  $P(Sa_{ref} \geq x | m, r)$  is given by

$$P(Sa_{ref} \geq x | m, r) = 1 - \Phi\left(\frac{\ln x - \mu_{\ln Sa_{ref}} | m, r}{\sigma_{\ln Sa_{ref}} | m, r}\right) \quad (\text{Eq. 3-9})$$

and the distribution parameters for the reference condition spectral acceleration  $\mu_{\ln Sa_{ref}}$  and  $\sigma_{\ln Sa_{ref}}$  are provided by the GMM.

#### Approach 4

The TI Team implemented Approach 4 to develop site control point hazard curves by discretizing Eq. 3-4:

$$v(z) = \sum_{n=1}^N \lambda_n(m_{min}) \sum_{i=m_{min}}^{m_{max}} P[m_i] \left\{ \sum_{j=r_{min}}^{r_{max}} P[r_j|m_i] P(Sa_s \geq z | m_i, r_j) \right\} \quad (\text{Eq. 3-10})$$

where the CCDF  $P(Sa_s \geq z | m, r)$  is given by

$$P(Sa_s \geq z | m, r) = 1 - \Phi\left(\frac{\ln z - \mu_{\ln Sa_s} | m, r}{\sigma_{\ln Sa_s} | m, r}\right) \quad (\text{Eq. 3-11})$$

In Eq. 3-11 above,  $\mu_{\ln Sa_s} | m, r$  is the conditional logarithmic mean of the site spectral acceleration; and  $\sigma_{\ln Sa_s} | m, r$  is the conditional logarithmic standard deviation of the site spectral acceleration. The conditional logarithmic mean and standard deviation of the site spectral acceleration can be estimated either empirically using site recordings, if available, or through an analytical site response analysis. For the Garner Valley Downhole Array (GVDA) study site, the TI Team implemented the analytical approach and used empirical site recordings to verify the analytical  $SAF$  (Section 5.2). For the Savannah River Site (SRS) study site, the TI Team used the analytical approach (Section 5.1).

To implement the analytical approach to determine the surface ground motion, the TI Team used Bazzurro and Cornell (2004b), which provides an estimate of  $\widehat{Sa}_s$ :

$$\ln \widehat{Sa}_s \approx c_0 + (c_1 + 1) \ln \widehat{Sa}_{ref} \quad (\text{Eq. 3-12})$$

where the coefficients  $c_0$  and  $c_1$  are the piecewise intercept and slope, respectively, in logarithmic space of the median site adjustment factor ( $\widehat{SAF}$ ) as a function of the reference condition spectral acceleration ( $Sa_{ref}$ ). Similarly,  $\sigma_{\ln Sa_s}$  can be estimated by

$$\sigma_{\ln Sa_s} \approx \sqrt{(c_1 + 1)^2 \sigma_{\ln Sa_{ref}}^2 + \sigma_{\ln SAF|x}^2} \quad (\text{Eq. 3-13})$$

For Eq. 3-12 and Eq. 3-13,  $\widehat{Sa_{ref}}$  and  $\sigma_{\ln Sa_{ref}}$  are provided by the GMM. Both GMMs used for this project estimate  $\sigma_{SS}$ , which should be inserted in place of  $\sigma_{\ln Sa_{ref}}$  in Eq. 3-13. Eq. 3-13 assumes that the  $SAF$  depends only on the amplitude of the reference spectral acceleration ( $Sa_{ref}$ ), and that the uncertainty in the  $SAF$  ( $\varepsilon_{\ln SAF}$ ) is uncorrelated with the uncertainty of the  $Sa_{ref}$  ( $\varepsilon_{\ln Sa_{ref}}$ ). The dependence of the  $SAF$  on the amplitude of the  $Sa_{ref}$  and not on earthquake magnitude and source-to-site distance is discussed below.

### **Site Adjustment Factor Conditional Dependence**

For both Approaches 3 and 4 described above, the distribution parameters for the  $SAF$  ( $\mu_{\ln SAF|m,r,x}$  and  $\sigma_{\ln SAF|m,r,x}$ ) are assumed to be conditional on earthquake magnitude, source-to-site distance, and  $Sa_{ref}$ . Bazzurro and Cornell (2004a) demonstrated that (1) the amplitude ( $x$ ) of the reference condition spectral acceleration ( $Sa_{ref}$ ) is the dominant contributor to the  $SAF$ , (2) earthquake magnitude may have a smaller but still significant impact, and (3) source-to-site distance has a negligible impact. For both study sites for this project, the TI Team evaluated whether the  $SAF$  depends on magnitude and source-to-site distance in addition to the amplitude of the  $Sa_{ref}$ . Based on these sensitivity studies for the two study sites, the TI Team found that only the amplitude of the  $Sa_{ref}$  had a significant effect on the  $SAF$ . These two sensitivity studies are described in Section 6 of this report. As such, the CCDF,  $P\left(SAF \geq \frac{z}{x} | m, r, x\right)$ , in Eq. 3-5 above can be replaced by  $P\left(SAF \geq \frac{z}{x} | x\right)$  and the distribution parameters for the  $SAF$  are taken as conditional only on the reference condition spectral acceleration ( $\mu_{\ln SAF|x}$  and  $\sigma_{\ln SAF|x}$ ).

### **Alternative Versions of Approaches 3 and 4**

For its implementation of Approach 3, the TI Team used Equation 3-7 above by simultaneously determining the reference condition hazard and applying the site adjustment factors to determine the control point or surface hazard. In practice, a variation of Approach 3 is often used where the reference condition hazard curve is first determined and then convolved with the CCDF of the  $SAF$  (Bazzurro and Cornell, 2004b). This approach has often been referred to as the “convolution” variation of Approach 3, and it can be advantageous if the hazard for the reference condition is performed independently and prior to the site response analyses. The site control point hazard curves using the “convolution” variation of Approach 3 are given by modifying Eq. 3-7 above:

$$v(z) = \sum_{k=x_{min}}^{x_{max}} P\left(SAF \geq \frac{z}{x_k} | x_k\right) P[Sa_{ref} = x_k] \quad (\text{Eq. 3-14})$$

where the PMF for the reference condition spectral acceleration is given by differencing the predetermined reference condition hazard curves.

The TI Team decided to implement the convolution Approach 3, the more rigorous version of Approach 3 described above in the hazard integral (i.e., Eq. 3-7 to Eq. 3-9), and the analytical version of Approach 4 (i.e., Eq. 3-10 to Eq. 3-13) for the development of the site control point hazard curves for the two sites. To clarify the terminology used to refer to these various approaches with respect to McGuire et al. (2001) and throughout this report, the TI Team developed Table 3-2.

### **Site Adjustment Factor Aleatory Variability**

To account for aleatory (i.e., spatial) variability and to reduce the influence of resonances created by impedance contrasts that result from a site profile with idealized horizontal layers and changes in velocity across layer boundaries, the TI Team randomized about each of the site base case  $V_S$  profiles. In addition, the TI Team applied randomization to the shear modulus reduction and damping curves ( $G/G_{max}$  and  $D$ ). This randomization produced a logarithmic standard deviation of the  $SAF$  ( $\sigma_{\ln SAF|x}$ ) for each terminal branch of the site response logic tree, which the TI Team then implemented into the PSHA. However, for this project, the TI Team assumed that the single-station standard deviation for the GMM ( $\sigma_{SS}$ ) captures the aleatory variability of the spectral acceleration ( $Sa_{ref}$ ) in the linear site response range. This decision by the TI Team is based on the assumption that the ground motion datasets used to develop the two GMMs used for this project adequately capture the aleatory variability of the predicted median ground motions for the lower linear site response range of ground motions. As such, the TI Team decided to separate the  $SAF$  standard deviation ( $\sigma_{\ln SAF|x}$ ) into its linear and nonlinear components and implement only the nonlinear response component of the  $SAF$  standard deviation into the PSHA. The nonlinear component ( $\sigma_{\ln SAF|x}^{NL}$ ) is given by

$$\sigma_{\ln SAF|x}^{NL} = \sqrt{\sigma_{\ln SAF|x}^2 - (\sigma_{\ln SAF|x}^{LS})^2} \quad (\text{Eq. 3-15})$$

where  $\sigma_{\ln SAF|x}^{LS}$  is the low-strain or linear component of the logarithmic standard deviation defined as  $\sigma_{\ln SAF|x}^{LS} = \sigma_{\ln SAF|x}$  at a selected reference condition spectral acceleration value (e.g.,  $x = 0.1g$ ). In Eq. 3-6 and Eq. 3-15 above,  $\sigma_{\ln SAF|x}^{NL}$  is used in place of  $\sigma_{\ln SAF|x}$ . For this project, the TI Team determined an estimate of the linear-nonlinear boundary for each of the GMM spectral frequencies. Below this selected value, the TI Team assumed that the nonlinear component of the  $SAF$  standard deviation ( $\sigma_{\ln SAF|x}^{NL}$ ) is zero.

<b>Table 3-2 Alternative versions of approaches 3 and 4</b>		
<b>McGuire et al., 2001</b>	<b>This Report</b>	<b>Description</b>
Approach 3 McGuire et al. (2001) Eq. 6-2 to Eq. 6-5	Hazard Integral Approach 3	Simultaneously determine reference hazard and implement $SAF$ using Eq. 3-7 to Eq. 3-9 assuming either $SAF m, r, x$ or just $SAF x$

Approach 3A McGuire et al. (2001) Eq. 6-6 to Eq. 6-7	Not used	Convolution approach assuming $SAF m, x$
Approach 3B McGuire et al. (2001) Eq. 6-8 to Eq. 6-9	Convolution Approach 3	Eq. 3-14
Approach 4 McGuire et al. (2001) Eq. 6-1	Analytical Approach 4	Eq. 3-10 to Eq. 3-13 with site response analysis used to estimate $Sa_s$
	Empirical Approach 4 (not used)	Eq. 3-10 to Eq. 3-11 with site recordings used to estimate $Sa_s$

### **3.5 Capturing the Center, Body, and Range of the Technically Defensible Interpretations**

The fundamental goal of the SSHAC process is to produce a probabilistic hazard analysis that captures the center, body, and range of technically defensible interpretations (commonly referred to as the CBR of TDIs). Based on the process described in NUREG–2213 (NRC, 2018), this outcome is achieved through disciplined execution of the two phases of the SSHAC methodology, evaluation and integration, which the project team executed in this Level 2 study. In the first phase, the TI Team evaluated all available data, models, and methods that exist within the larger technical community and are of potential relevance to the site in question. In the second phase, the TI Team integrated these data, models, and methods into the site response analysis model to capture the CBR of TDIs.

As noted in Chapter 1, there are five essential attributes that a SSHAC study must possess:

1. Clearly defined roles and responsibilities for all participants.
2. Objective evaluation of all data, models, and methods.
3. Integration of the results of the evaluation process into models that reflect the best estimate and uncertainty of the model elements (CBR of TDI).
4. Documentation that provides a complete and transparent record of the evaluation and integration process.
5. Independent participatory peer review that confirms the evaluation considered all relevant data, models, and methods and that the technical bases for all elements are adequately documented.

To ensure that all relevant and available data, models, and methods are considered, there must be active engagement between the TI Team and experts prior to and during the SSHAC workshop. Throughout the course of a SSHAC study, the TI Team actively challenged and debated technical issues. It is worth noting that during the model building process, the TI Team avoided including alternatives that had a minimal impact on the final hazard results as demonstrated by the TI Team’s sensitivity studies, described throughout this report.

To ensure that both process and technical issues are addressed, the Participatory Peer Review Panel (PPRP) and TI Team were engaged during project planning, the workshop, and the

evaluation/integration and documentation process. Adherence to the SSHAC process, including broad engagement with outside experts, and the endorsement of the PPRP that the project applied the principles of the SSHAC process.

### **3.6 References**

Al Atik, L. and N.A. Abrahamson. "A Methodology for the Development of 1D Reference Vs Profiles Compatible with Ground Motion Prediction Equations: Applications to NGA-West2 GMPEs." *Bulletin of the Seismological Society of America*. Vol. 111, Issue 4. pp. 1765–1783. 2021.

Assimaki, D. and E. Kausel. "An Equivalent Linear Algorithm with Frequency- and Pressure-dependent Moduli and Damping for the Seismic Analysis of Deep Sites." *Soil Dynamics and Earthquake Engineering*. Vol. 22, Issues 9–12. pp. 959–965. 2002.

Atkinson, G.M. "Single-station sigma." *Bulletin of the Seismological Society of America*. Vol. 96, Issue 2. pp. 446–455. 2006.

Atkinson, G.M., J.J. Bommer, and N.A. Abrahamson. "Alternative Approaches to Modeling Epistemic Uncertainty in Ground Motion in Probabilistic Seismic-Hazard Analysis." *Seismological Research Letters*. Vol. 85, Issue 6. pp. 1,141–1,144. 2014.

Bazzurro, P. and C.A. Cornell. "Ground-motion Amplification in Nonlinear Soil Sites with Uncertain Properties." *Bulletin of the Seismological Society of America*. Vol. 94, Issue 6. pp. 2,090–2,109. 2004a.

Bazzurro, P. and C.A. Cornell. "Nonlinear Soil-site Effects in Probabilistic Seismic-hazard Analysis." *Bulletin of the Seismological Society of America*. Vol. 94, Issue 6. pp. 2,110–2,123. 2004b.

Bommer, J.J., K.J. Coppersmith, R.T. Coppersmith, K.L. Hanson, A. Mangongolo, J. Neveling, E.M. Rathje, A. Rodriguez-Marek, F. Scherbaum, R. Shelembe, P. Stafford, and F.O. Strasser. "Probabilistic Seismic Hazard Analysis for the Thyspunt Nuclear Site, South Africa: Final Report, Submitted to ESKOM, South Africa. 2013.

Coppersmith, K., J. Bommer, K. Hanson, R. Coppersmith, J. Unruh, L. Wolf, B. Youngs, L. Al Atik, A. Rodriguez-Marek, G. Toro. Hanford Sitewide Probabilistic Seismic Hazard Analysis, Prepared for the U.S. Department of Energy Under Contract DE-AC06076RL01830, and Energy Northwest, Pacific Northwest National Lab Report PNNL-23361. November 2014.

EPRI. "Seismic Evaluation Guidance: Screening, Prioritization and Implementation Details (SPID) for the Resolution of Fukushima Near-Term Task Force Recommendation 2.1: Seismic." Technical Report 1025287. Palo Alto, California: Electric Power Research Institute. February 2013.

GeoPentech. "Southwestern United States Ground Motion Characterization SSHAC Level— Technical Report Rev.2." 2015.

Goulet, C. A., Y. Bozorgnia, N. Abrahamson, N. Kuehn, L. Al Atik, R. Youngs, R. Graves, and G. Atkinson. "Central and Eastern North America Ground—Motion Characterization—NGA-East Final report." Pacific Earthquake Engineering Research Center. 2018.

- Kaklamanos, J., L.G. Baise, E.M. Thompson, and L. Dorfmann. "Comparison of 1D Linear, Equivalent-linear, and Nonlinear Site Response Models at Six KiK-net Validation Sites." *Soil Dynamics and Earthquake Engineering*. Vol. 69. pp. 207–219. 2015.
- Kaklamanos J, B.A. Bradley, E.M. Thompson, and L.G. Baise. "Critical Parameters Affecting Bias and Variability in Site-response Analyses Using KiK-net Downhole Array Data." *Bulletin of the Seismological Society of America*. Vol. 103, Issue 3. pp. 1,733–1,749. 2013.
- McGuire, R.K., W.J. Silva, and C.J. Costantino. NUREG/CR-6728, "Technical Basis for Revision of Regulatory Guidance on Design Ground Motions: Hazard- and Risk-Consistent Ground Motion Spectra Guidelines." Washington, DC: U.S. Nuclear Regulatory Commission. ML013100232. 2001.
- Miller III, A.C. and T.R. Rice. "Discrete Approximations of Probability Distributions." *Management Science*. Vol. 29, Issue 3. pp. 352–362. 1983.
- NRC. NUREG-2213, "Updated Implementation Guidelines for SSHAC Hazard Studies." Washington, DC: U.S. Nuclear Regulatory Commission. 2018. ML18282A082.
- Rodriguez-Marek, A., J.J. Bommer, R.R. Youngs, M.J. Crespo, P.J. Stafford, and M. Bahrampouri. "Capturing Epistemic Uncertainty in Site Response." *Earthquake Spectra*. Vol. 37, Issue 2. pp. 921–936. 2020. <https://doi.org/10.1177/8755293020970975>.
- Rodriguez-Marek, A., E.M. Rathje, J.J. Bommer, P.J. Stafford, and F. Scherbaum. "Application of Single-Station Sigma and Site Response Characterization in a Probabilistic Seismic Hazard Analysis for a New Nuclear Site." *Bulletin of the Seismological Society of America*. Vol. 104, Issue 4. pp. 1,601–1,619. 2014. <https://doi.org/10.1785/0120130196>.
- Rodriguez-Marek, A., F. Cotton, N.A. Abrahamson, S. Akkar, L. Al Atik, B. Edwards, G.A. Montalva, and H.M. Dawood. "A Model for Single-station Standard Deviation Using Data from Various Tectonic Regions." *Bulletin of the Seismological Society of America*. Vol. 103, Issue 6. pp. 3,149–3,163. 2013.
- Rodriguez-Marek, A., G.A. Montalva, F. Cotton, and F. Bonilla. "Analysis of Single-station Standard Deviation Using the KiK-net Data." *Bulletin of the Seismological Society of America*. Vol. 101, No. 3. pp. 1,242–1,258. 2011.
- Scherbaum F., N.M. Kuehn, M. Ohrnberger, and A. Koehler. "Exploring the Proximity of Ground-motion Models Using High-dimensional Visualization Techniques." *Earthquake Spectra*. Vol. 26, Issue 4. pp. 1,117–1,138. 2010.
- Silva, W. Modeling uncertainty for site response at INL, Excerpts from Pacific Engineering and Analysis Report, personal communication. 2015.
- Silva, W.J., N. Abrahamson, G. Toro, and C. Costantino. "Description and Validation of the Stochastic Ground Motion Model." Report to Brookhaven National Laboratory, U.S. Nuclear Regulatory Commission, ADAMS Accession Number ML042800294. 1996.
- Stewart, J.P. and K. Afshari. "Epistemic Uncertainty in Site Response as Derived from One-dimensional Ground Response Analyses." *Journal of Geotechnical and Geoenvironmental Engineering*. Accepted for publication. 2020.

Wang, X. and E. Rathje. "Influence of Peak Factors on Site Amplification from Random Vibration Theory Based Site Response Analysis." *Bulletin of the Seismological Society of America*. Vol. 106, Issue 4. pp. 1,733–1,746. 2016. <https://doi.org/10.1785/0120150328>.

Xu, B. and E. Rathje. "The Effect of Soil Nonlinearity on High Frequency Spectral Decay and Implications for Site Response Analysis." *Earthquake Spectra*. Vol. 2021. <https://doi.org/10.1177/8755293020981991>.

Zalachoris, G. and E.M. Rathje. "Evaluation of One-dimensional Site Response Techniques Using Borehole Arrays." *Journal of Geotechnical and Geoenvironmental Engineering*. 141.12: 04015053. 2015.

## 4 Project Study Sites

The Technical Integration (TI) Team and project management (in consultation with the study Sponsor) discussed the selection of sites and identified two study sites for which enough resources were available to implement the Senior Seismic Hazard Analysis Committee (SSHAC) process for site response analysis. The selection of the two sites was made based on the types and quality of site characterization data available, the availability of ground-motion data for evaluating empirical constraints to the site response, and the types of challenges that would be present at potential locations of existing and future nuclear facilities. Because the focus of this project is forward-looking (i.e., for future siting activities) the TI Team concluded that it would not be appropriate to consider sites where the data was limited or consisted only of older legacy information.

Section 4.1 describes the specific factors that were considered in the site selection process. Section 4.2 provides a description of the geologic setting, stratigraphy, available geophysical and geotechnical data, and source and ground-motion models used to develop the reference condition hazard for the study site selected by the TI Team in the central and eastern United States (CEUS). Similarly, Section 4.3 provides an analogous description of the same factors for the study site selected by the TI Team in the western United States (WUS).

### 4.1 Factors Considered in Site Selection

The TI Team identified several factors important to the site selection process that, if satisfied, would maximize the experience gained from conducting this study. The expectation is that this study would influence future analyses for nuclear or other critical facilities. Because current practice for these facilities requires a robust site characterization process, the TI Team concluded it would be necessary for the sites selected for this study to have abundant high-quality geologic and geotechnical data. The TI Team further concluded that it would be useful to have the two sites represent two different types of hazard characterizations. Because this study only uses two study sites, the TI Team concluded that one site should represent a moderate hazard level in the CEUS and the other should represent a higher hazard level in the WUS. The inclusion of a higher-hazard site allows the TI Team to assess and characterize the additional uncertainty that arises if significant non-linear behavior in the near-surface materials is expected to occur. The TI Team further concluded that at least one site should have state-of-the-art surface wave data available, which is becoming a more commonly used tool for characterizing sites. Further, the TI Team believed that at least one site should have site-specific strong motion earthquake recordings that could be used to provide empirical constraints on the various elements of the ground motion characterization. Finally, because the site response analysis is influenced by both the reference site condition of the ground motion model (GMM) and the characteristics of the site, it was decided that the two sites should have different reference conditions for the relevant ground motion prediction model.

Based on these factors, the TI Team considered several potential sites and identified two as satisfying the factors identified above. The first site is located on the Savannah River Site (SRS) U.S. Department of Energy (DOE) facility in South Carolina. This site is representative of many CEUS locations; has abundant geological, geotechnical, and geophysical data; and is located in a moderate hazard setting. The second site is the Garner Valley Downhole Array (GVDA) site, which is located in southern California near the San Jacinto fault. This site has good geological and geotechnical data, recently acquired surface-wave velocity testing data, several earthquake recordings, and is located in a high-hazard setting.

## 4.2 Savannah River Site

### 4.2.1 Geologic Setting

The SRS is in South Carolina along the Savannah River within the Coastal Plain physiographic province and is founded on about 300 meters (m) of sedimentary deposits over either the Mesozoic-age Dunbarton Basin or Paleozoic crystalline rock. As described in Denham (1999), the Savannah River Site occupies approximately 800 square kilometers (km<sup>2</sup>) in portions of Aiken, Allendale, and Barnwell counties. The site is located approximately 40 km southeast of the Fall Line, the boundary between the Coastal Plain and Piedmont provinces. The Coastal Plain province is underlain by a seaward-dipping wedge of unconsolidated and semi-consolidated sediments, which extends from the Fall Line to the edge of the continental shelf and ranges in age from the Cretaceous to the Holocene. The SRS lies within the Aiken Plateau, which is bounded by the Savannah and Congaree Rivers and extends from the Fall Line to the Orangeburg Scarp (Figure 4-1).

The Coastal Plain sequence near the location on the SRS selected for this demonstration project corresponds to what is referred to as the “F-Area.” In this section, we refer to the site as SRS-FA; elsewhere in the report we use SRS for brevity. The SRS-FA site consists of about 167 m of Upper Cretaceous quartz sand, pebbly quartz sand, and kaolinitic clay, overlain by 18 m of Paleocene clayey and silty quartz sand, glauconitic sand, and silt. The Paleocene beds are in turn overlain by about 91 m of Eocene sediments that grade from quartz sand, clay, and limestone into calcareous sand, silt, and clay (Denham, 1999 and DOE, 2003). These Paleocene and Eocene sedimentary layers are divided into three groups: the Barnwell Group, Orangeburg Group, and Black Mingo Group. The Late Cretaceous age sediments beneath these three groups are from the Lumbee Group, which overlies the Cape Fear Formation. Paleozoic crystalline bedrock is located at an elevation of about -174 m below mean sea level (MSL) near the SRS-FA. Figure 4-2, adapted from DOE (2003), shows the stratigraphy of the SRS-FA.

The upper sedimentary layers of the stratigraphic column beneath the SRS-FA consist of the Tobacco Road and Dry Branch Formations, which are from the Barnwell Group. The late Eocene age Tobacco Road Formation, which consists of moderately to poorly sorted, fine to coarse, clayey quartz sand, averages approximately 20 m in thickness near the SRS-FA. Underlying the Tobacco Road Formation is about 18 m of late Eocene sediments (primarily sand and clay) that make up the Dry Branch Formation.

Underlying the Barnwell Group are the early to middle Eocene Santee, Warley Hill, and Congaree Formations from the Orangeburg Group. The Santee Formation, which is about 33 m thick beneath the SRS-FA, consists of moderately sorted sand, calcareous sands and clays, limestones, and clay. The calcareous part of the Santee is missing to the northwest of the SRS near the SRS-FA. Beneath the Santee Formation is a thin layer (about 4 m) of dense clayey sands from the Warley Hill Formation and underlying this layer is a thicker sequence (about 9 m) of fine to coarse quartz sands from the Congaree Formation.

The late Eocene to early Paleocene age Black Mingo Group underlies the Orangeburg Group and consists of quartz sand, silty clay, and clay. Near the SRS-FA, the Fourmile Member of the Fishburne Formation comprises the Black Mingo Group and is primarily sand with a few pebbly zones near the base of the unit. The Fourmile Member is about 25 m beneath the SRS-FA.

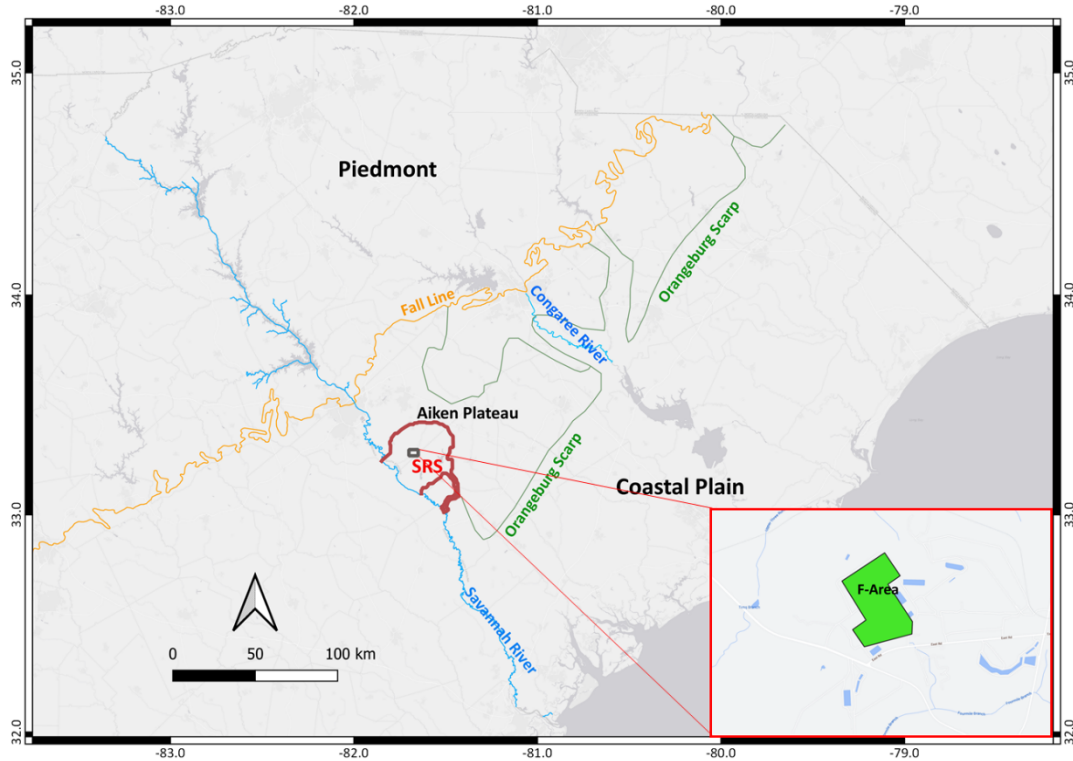


**Figure 4-1 SRS location map relative to the Coastal Plain and Piedmont physiographic provinces. The location of the map inset showing F-Area is indicated by small rectangle within the SRS boundary.**

Beneath the Black Mingo Group are the late Cretaceous sediments from the Steel Creek, Black Creek, and Middendorf Formations, which constitute the Lumbee Group. These sedimentary units are underlain by the Cape Fear Formation, which lies over crystalline bedrock beneath the SRS-FA. These late Cretaceous sediments consist predominantly of clay-rich sand, sandy clay, and gravel and are about 264 m beneath the SRS-FA (Denham, 1999; DOE, 2003).

#### 4.2.2 Geotechnical and Geophysical Data

The geotechnical field investigations within the SRS-FA consisted of drilling and sampling, borings, and cone penetration tests, which included seismic cone penetration tests (DOE, 2003). Borings within the SRS-FA extend to elevations ranging from 55 m to 35 m mean sea level (MSL) and generally reached the dense sands of the Congaree Formation. Cone penetration tests extended to elevations of 53 m to 43 m MSL. Site geology and geophysical characterizations at greater depths at the SRS-FA are based on deep well borings and an ensemble of cross-hole, downhole, and suspension logging shear-wave tests from across the SRS.

Laboratory tests performed on soil samples obtained from the borings within the SRS-FA include moisture content, wet and dry density, specific gravity, particle size analysis, plasticity, consolidation, shear strength, and cyclic triaxial and resonant column tests. The triaxial shear tests used to evaluate static shear strength were performed on clayey sands that are representative of the softer and lower density materials encountered. Consolidation testing also focused on clayey, softer materials within the geologic units.

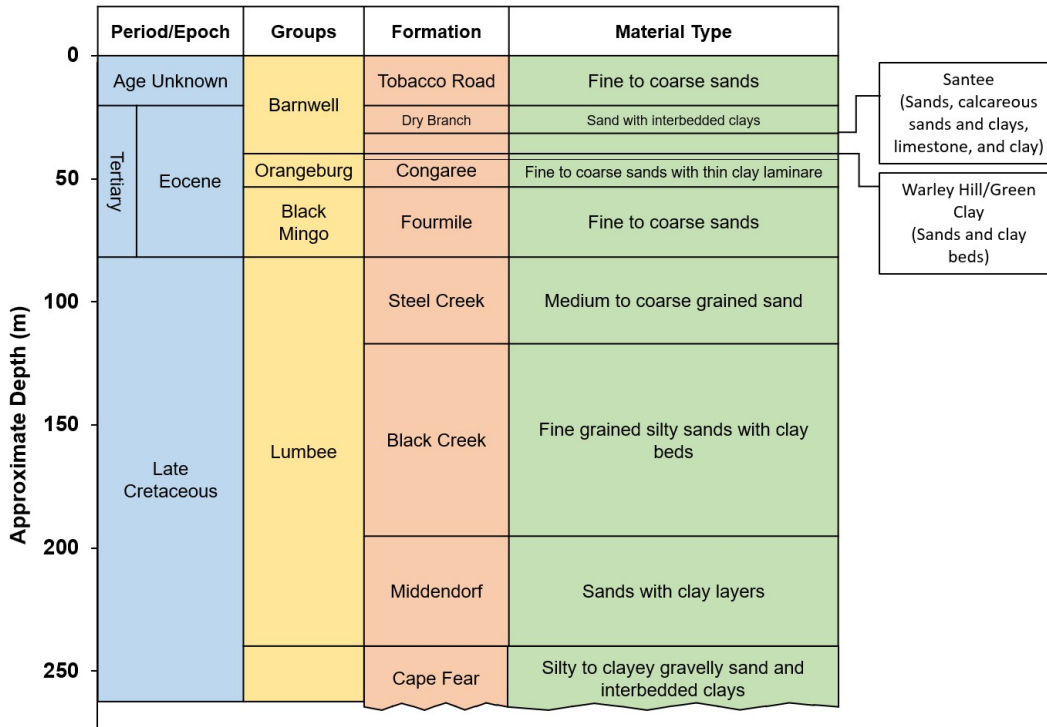


**Figure 4-2 Stratigraphic column beneath SRS-FA**

In addition to resonant column tests performed for the site investigation within the SRS-FA, previous dynamic tests of soils from across the SRS were reported by Stokoe et al. (1995). Modulus reduction curves obtained from test results for the SRS-FA are in good agreement with results reported by Stokoe et al. (1995) for soil across the SRS. Damping ratios reported for the SRS-FA are considerably higher than those reported by Stokoe et al. (1995) for the SRS. These higher damping values are believed to be an overestimation due to the effects of excitation frequency in the resonant column tests at small strains (DOE, 2003). This is likely due to the viscous nature of the pore fluid (Moayerian, 2012). Because the modulus reduction curves from the SRS-FA site investigation are consistent with the SRS results reported by Stokoe et al. (1995), the lower damping ratios are used to characterize damping in the SRS soils.

#### 4.2.3 Source Characterization and Ground Motion Models

To develop the reference rock hazard for the SRS-FA, the TI Team used the Central and Eastern United States Seismic Source Characterization for Nuclear Facilities (CEUS-SSC) model (NRC, 2012) along with the Next Generation Attenuation for Central and Eastern North America (NGA-East) ground motion model (GMM) (Goulet et al., 2018b). Both of these projects were conducted using the SSHAC Level 3 guidelines with the goal of capturing the center, body, and range of the technically defensible interpretations (CBR of TDI) in light of the available data and models. Because this SSHAC Level 2 project is focused on site response analysis, the TI Team decided to use a limited number of seismic sources from the CEUS-SSC model and to implement slightly abbreviated versions of the full CEUS-SSC and NGA-East GMM logic trees. The TI Team's implementation of these two models along with the reference condition hazard for the SRS-FA are described below.

## **Seismic Source Characterization Model**

The CEUS-SSC is a regional model developed to calculate seismic hazard at potential or existing nuclear facilities. As described in Chapter 9 of NUREG–2115 (NRC, 2012b), for site-specific applications, local data sets (including local geologic structures or local seismic sources) that were not captured in the CEUS-SSC model should be reviewed for potential site-specific refinements to the model. However, for the purposes of this project, the TI Team determined that the use of the CEUS-SSC regional model, as published, is adequate.

The CEUS-SSC model defines two types of seismic sources. The first type of seismic source characterizes the contribution to hazard from repeated large-magnitude earthquakes (RLMEs). RLMEs are defined based on paleoseismic evidence for the occurrence of two or more earthquakes with moment magnitudes ( $M$ ) that are greater than or equal to  $M6.5$  that occur in approximately the same location over periods of a few thousand years. The second type of seismic source characterizes the contribution to hazard from distributed seismicity and serves as background zones to the RLME sources. For the distributed seismicity sources, two alternative approaches were implemented by the developers of the CEUS-SSC model. The first approach defines seismic source boundaries based on differences in the degree of Mesozoic crustal extension, which has been interpreted to impact the maximum magnitude ( $M_{max}$ ) that the source can generate. The second approach defines seismic sources based on their different seismotectonic characteristics (e.g., depth of seismicity, style of faulting, and  $M_{max}$ ). For the hazard evaluation used for this project, the TI Team decided to include the Charleston RLME and the seismotectonic sources ECC-AM (Extended Continental Crust – Atlantic Margin) and PEZ-N (Paleozoic Extended Crust – Narrow Geometry). These two areal sources (ECC-AM and PEZ-N) are part of the highest weighted seismotectonic CEUS-SSC source zone configuration. Figure 4-3 shows the SRS-FA location as well as the CEUS-SSC model sources used for this project. For details regarding these three seismic sources, see NUREG–2115 (NRC, 2012b).

As described in the Hazard Input Document (HID) for the CEUS-SSC, the logic trees for the distributed seismicity sources include branches for  $M_{max}$ , seismotectonic thickness, and recurrence rate parameters. In addition, each source has a set of aleatory distributions for characterization of future earthquake ruptures, which captures the source boundary characteristics (leaky or rigid) as well as the relative frequency of the sense of slip, rupture strike, and rupture dip. For this project, the TI Team simplified the CEUS-SSC logic tree by using 5 alternative weighted magnitude recurrence rate values rather than the total of 24 alternative rates (3 cases and 8 smoothing realizations) developed for the full CEUS-SSC model for each of the distributed seismicity source zone cells. To develop the 5 alternative weight magnitude recurrence rates, the TI Team developed a cumulative distribution of the 24 alternative weighted rates and determined 5 fractile rates using Table 3 from Miller and Rice (1983). In addition, the TI Team used the average beta value (where beta is the slope of the recurrence curve) for each of the distributed seismicity source zone cells. Figure 4-4 shows the 10 Hertz (Hz) reference condition hazard for SRS-FA from the ECC-AM seismotectonic source zone. Shown on Figure 4-4 are the reference condition hazard curves (light blue) from implementing all of the 24 alternative recurrence rates with their associated beta values versus the reference hazard curves (tan) from the implementation of the 5 recurrence rates and an average beta value for each of the distributed seismicity source zone cells. By implementing only the 5 recurrence rates and an average beta value for each of the source zone cells, the TI Team broadened the distribution of the reference condition hazard relative to the implementation of all 24 rates and their associated beta values.

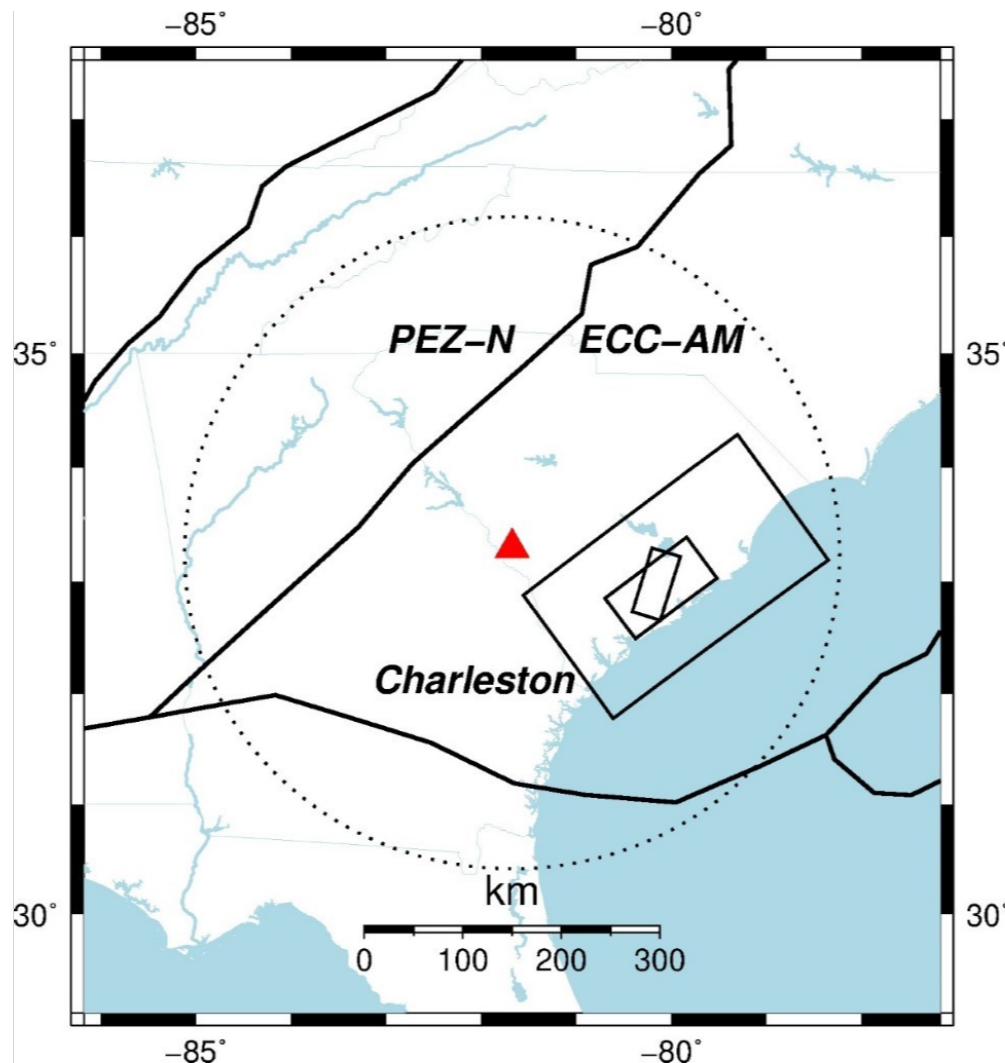


**Figure 4-3 CEUS-SSC model sources for SRS (red triangle). Three alternative Charleston RLME configurations are depicted. Dotted circle shows 320 km radius used for the ECC-AM and PEZ-N source zones.**

In summary, the simplification of the CEUS-SSC logic tree resulted in the same mean but different hazard fractiles than those that would have been computed with the full 24 alternative weighted recurrence rates.

The CEUS-SSC logic tree also generally specifies three alternative seismotectonic thicknesses and five  $M_{max}$  values for each of the distributed seismicity sources. The TI Team for this project initially fully implemented these two sets of alternative branches; however, after evaluating the initial hazard results, the Team decided that seismotectonic thickness did not have a significant impact. As such, only the average seismotectonic thickness was implemented for the source model for this project. Finally, for the aleatory distribution of earthquake ruptures, the TI Team randomly selected for each potential virtual rupture a set of rupture characteristics based on the weighting provided in the CEUS-SSC hazard input document (HID) (NRC, 2012b).

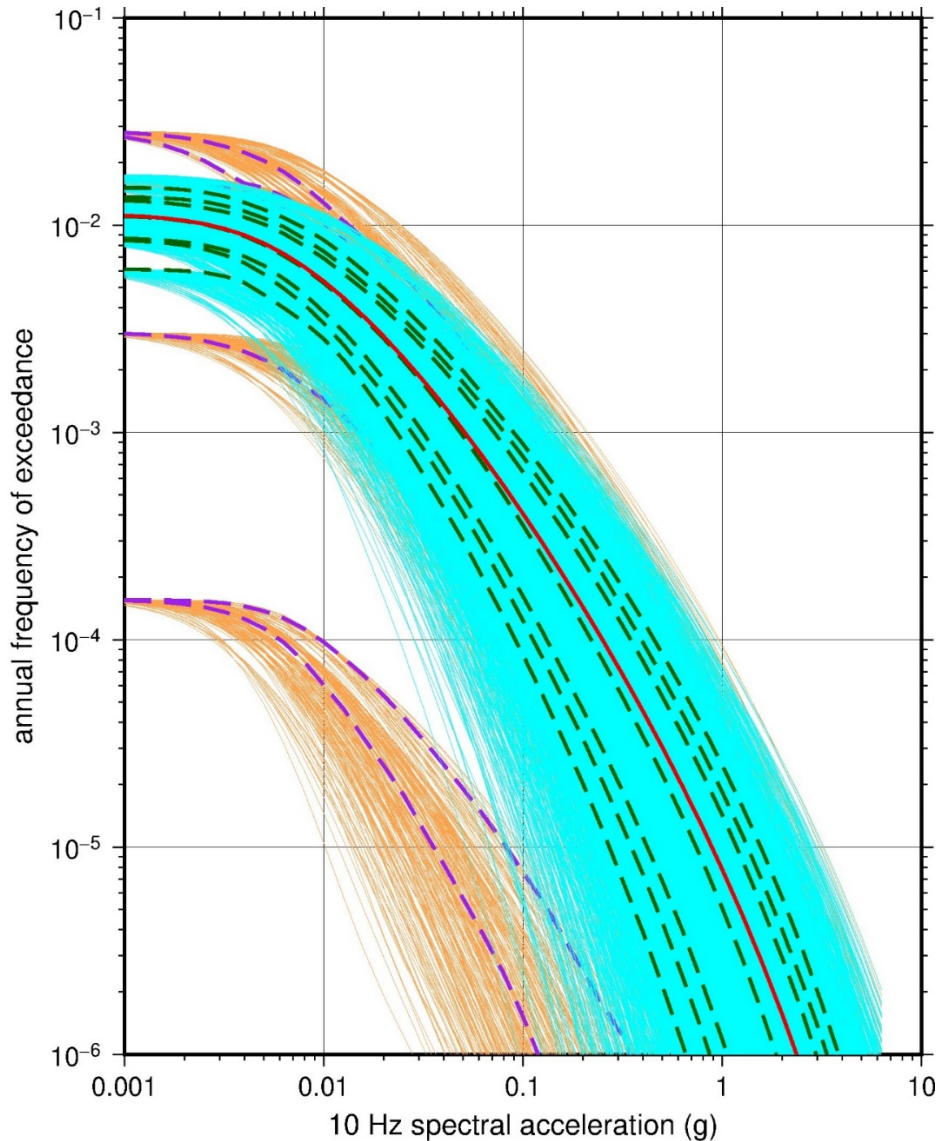


**Figure 4-4** Reference condition hazard curves (light blue) from implementing all of the 24 alternative recurrence rates with their associated beta values compared to the reference hazard curves (tan) from the implementation of the 5 recurrence rates and an average beta value for each of the distributed seismicity source zone cells.

For the Charleston RLME, the CEUS-SSC HID specifies multiple sets of five RLME annual frequency branches based on the earthquake renewal model (Poisson model or Brownian Passage Time renewal model), earthquake count (number of RLMEs that have occurred with the Charleston source), and time period (2,000-year versus 5,000-year paleoliquefaction record). Rather than implement all 20 alternative sets of RLME annual frequency branches, the TI Team for this project determined that a single set of five weighted alternative frequencies was sufficient. In addition, based on an initial hazard run, the TI Team also determined that a single average seismotectonic thickness of 17 km was adequate to capture the entire distribution of reference condition hazard curves. For the remaining portions of the HID logic tree for the Charleston RLME, the TI Team fully implemented each of the alternative  $M_{max}$  values, source zone configurations, rupture strikes, and temporal clustering options.

## **Ground Motion Model**

The NGA-East GMM is a set of GMMs for the median and standard deviation of predicted ground motions and their associated weights to be used in probabilistic seismic hazard analyses (PSHAs) for seismic hazard characterizations of critical facilities located in Central and Eastern North America (CENA) (Goulet et al., 2018b). In particular, the GMM includes a set of 17 median GMMs for the horizontal component of ground motion (5%-damped pseudo-acceleration response spectra) for 23 oscillator frequencies between 0.1 and 100 Hz as well as peak ground acceleration (PGA) and peak ground velocity (PGV). The median GMMs predict spectral acceleration ( $Sa$ ) values as a function of  $M$  and source-to-site rupture distance ( $r_{rup}$ ) and are applicable to hard-rock sites in CENA in the magnitude range of **M**4.0 to **M**8.2 and  $r_{rup}$  distances up to 1500 km. Standard deviation models for each of the spectral frequencies, which depend on  $M$ , are also provided for site-specific analysis (single-station standard deviation,  $\sigma_{SS}$ ) and for general PSHA applications (ergodic standard deviation). Adjustment factors are provided for source-depth effects (depth to top of rupture), hanging-wall effects, and for hazard computations at sites in the Gulf Coast region (alternative Gulf Coast regions and median adjustments). The reference condition parameter values for the NGA-East GMM are a  $V_{S30}$  of 3 km/sec and a site kappa of 0.006 sec, where  $V_{S30}$  is the average shear-wave velocity over the top 30 m and the site kappa refers to the zero-distance spectral decay factor,  $\kappa_0$ .

The full logic tree for the NGA-East GMM, as described in the HID, consists of 17 branches for the median predictions, two branches for alternative Gulf Coast regions (large and small), and two branches for alternative Gulf Coast median adjustments (Goulet et al., 2018a). For the aleatory variability models, the logic tree consists of three branches for the standard deviation (low, medium, and high) and two branches for the aleatory variability distribution (mixture and lognormal). For this project, the TI Team decided to implement the full logic tree for the median ground motion predictions as well as the hanging-wall and depth to top of rupture median adjustments. Because the SRS-FA, as well as the two CEUS-SSC source zones (ECC-AM and PEZ-N) and the Charleston RLME, fall outside of the two Gulf Coast regions, the TI Team did not implement the NGA-East Gulf Coast median adjustment factors. For the aleatory variability logic tree, the TI Team implemented the three-alternative  $\sigma_{SS}$  estimates (low, medium, and high), but used only the mixture model for the aleatory variability distribution. The TI Team concluded that because the mixture model is more heavily weighted than the lognormal distribution (0.8 versus 0.2), the epistemic uncertainty of the hazard curve for the reference condition would not be impacted by implementing just the mixture model.

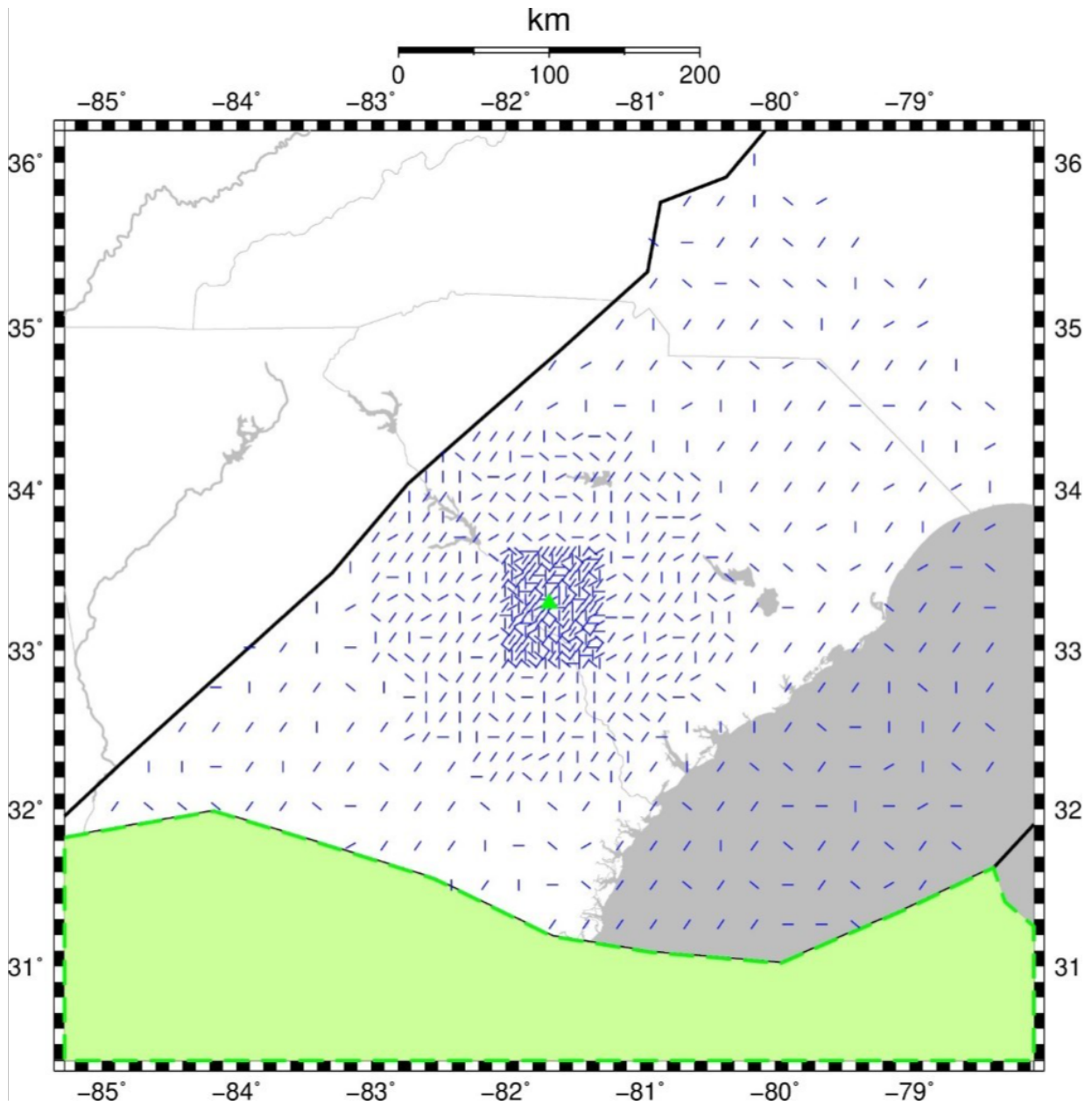
## **Reference Condition Hazard**

The TI Team developed the reference condition hazard model for the SRS-FA by implementing three CEUS-SSC sources and the NGA-East GMM. For each of the CEUS-SSC sources, the TI Team included the five-alternative weighted  $M_{max}$  values, a single average seismotectonic thickness, five alternative weighted recurrence rates, and randomly selected a set of rupture characteristics, as described above. Because the NGA-East GMM uses the  $r_{rup}$  distance variable, the TI Team developed a set of virtual ruptures for each of the distributed seismicity sources (ECC-AM and PEZ-N) in order to estimate the source and distance parameters needed to implement the NGA-East GMM. Figure 4-5 shows the set of **M**6 virtual ruptures for the ECC-AM source. As shown in Figure 4-5, the virtual ruptures extend out to a distance of approximately 320 km from the site and the strike angle of each rupture is randomly oriented in accordance with the weights provided in the CEUS-SSC HID. Figure 4-5 shows the updip side of each surface virtual rupture but does not show that the virtual ruptures are vertically stacked

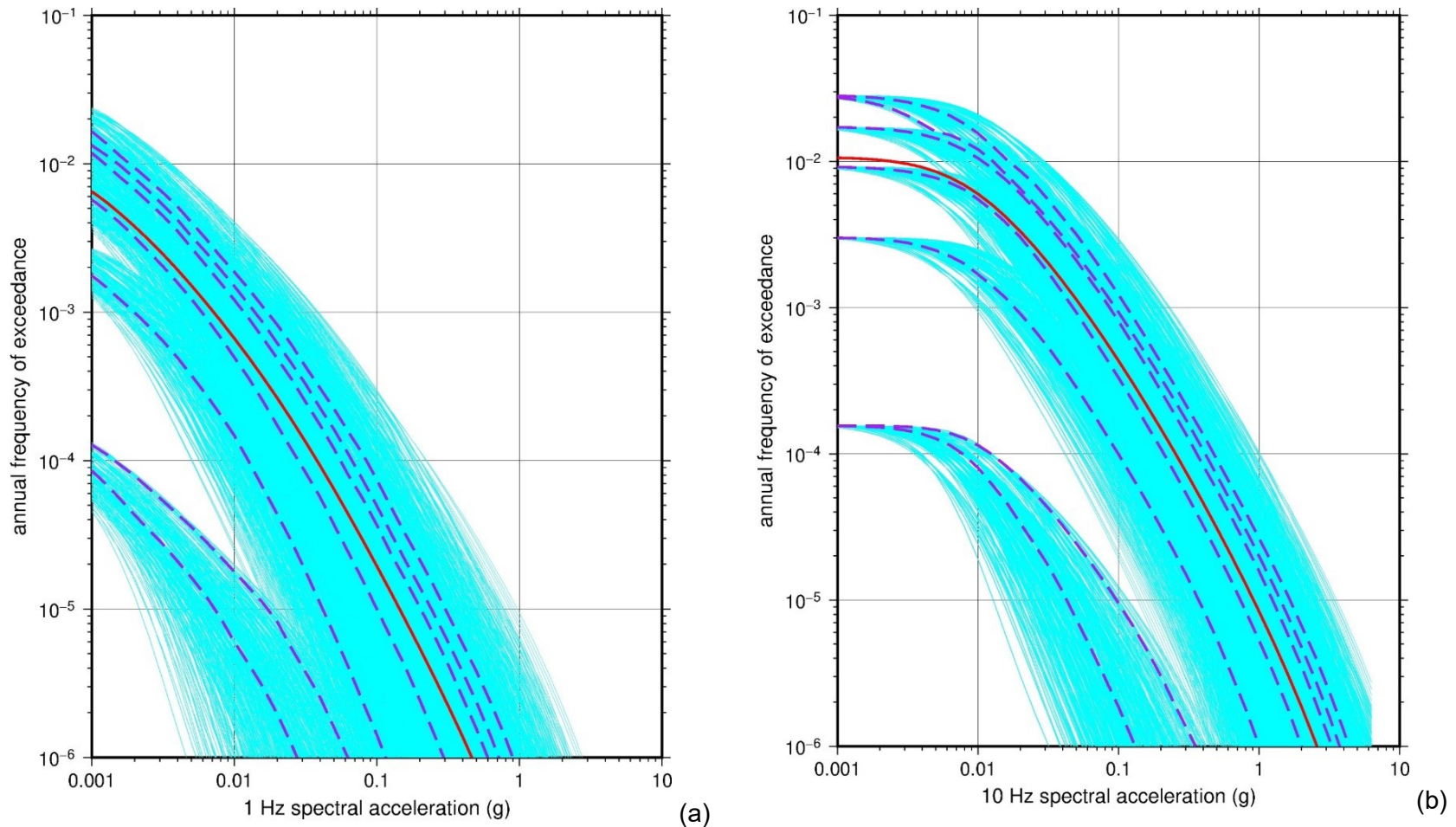
beneath the uppermost rupture. In addition, Figure 4-5 shows that the distribution of virtual ruptures is denser around the site and decreases with greater source-to-site distances. The TI Team implemented this distribution of virtual ruptures about the site and vertically within the allotted seismotectonic thickness in order to capture a fairly even distribution of source-to-site distance parameters. In contrast, for the Charleston RLME, the CEUS-SSC HID specifies a fixed set of rupture characteristics for each of the alternative source boundary configurations. For each of the distributed seismicity sources, the TI Team developed a set of virtual ruptures for each of the magnitudes ranging from the minimum magnitude of **M5** to the specified  $M_{max}$  value using a magnitude increment of 0.10. To determine the length for each virtual rupture, the TI Team used the fault area relationship specified in the NGA-East report and a length-to-width ratio of one for the lower magnitudes, which do not saturate the entire seismotectonic thickness.

Figure 4-6 shows the distribution of reference condition hazard curves as well as several fractile and mean curves for the spectral frequencies of 1 and 10 Hz for the ECC-AM source. The total number of hazard curves for each spectral frequency is 1275, which results from the implementation of five alternative  $M_{max}$  values, five alternative magnitude recurrence rates, 17 median GMMs, and three alternative  $\sigma_{ss}$  values. Figure 4-6b clearly shows the differences in hazard arising from the five alternative magnitude recurrence rates by the grouping of the hazard curves for lower spectral acceleration values. The tornado diagram plot shown in Figure 4-7 for the annual frequency of exceedance (AFE) of  $10^{-4}/\text{yr}$  and for the spectral frequency of 10 Hz demonstrates that the alternative magnitude recurrence rates and GMM medians have the largest impact on the spread of the distribution of the reference condition hazard curves. The tornado plot shown in Figure 4-7 was developed with the three alternative seismotectonic thicknesses used for the TI Team's initial hazard run. As shown in Figure 4-7, the three alternative thicknesses do not contribute significantly to the variability in the overall hazard curve distribution and, as such, the TI Team used only the average thickness for each of the CEUS-SSC sources.

Mean hazard curves for the three CEUS-SSC sources as well as the total mean are shown in Figure 4-8 for 1 and 10 Hz spectral frequencies. As shown in Figure 4-8, the Charleston RLME is the predominant contributor to the hazard at an AFE of  $10^{-4}/\text{yr}$  for both the lower and higher spectral frequencies. Figure 4-9 shows deaggregation plots for 1 and 10 Hz spectral frequencies for an AFE of  $10^{-4}/\text{yr}$ . The controlling earthquake for 1 Hz at an AFE of  $10^{-4}/\text{yr}$  has a mean magnitude of 7.3 at a mean distance of 123 km, which reflects the predominant contribution from the Charleston RLME. For the spectral frequency of 10 Hz, the controlling earthquake mean magnitude is 7.0 at a mean distance of 94 km, which shows the predominant contribution from the Charleston RLME as well as a smaller contribution from the host zone ECC-AM. Table 4-1 shows the controlling earthquake mean magnitude and distance pairs for the spectral frequencies of 1 and 10 Hz and for the AFEs of  $10^{-3}/\text{yr}$ ,  $10^{-4}/\text{yr}$  and  $10^{-5}/\text{yr}$ . Finally, Figure 4-10 shows the response spectrum for each of these controlling earthquakes (developed using the highest weighted NGA-East median model for either 1 or 10 Hz) scaled to the uniform hazard response spectrum (UHRS) value at either 1 or 10 Hz, as appropriate. These scaled response spectra were used by the TI Team to inform the range of input response spectra used for the site response evaluation for the SRS-FA.



**Figure 4-5** M6 rupture sources for CEUS-SSC ECC-AM source zone. SRS location is shown as a green triangle. The large Gulf Coast zone used for NGA-East GMM, which is below the ECC-AM source, is shown in green.



**Figure 4-6 (a) 1 Hz mean (red) and fractile (dashed, 0.05, 0.10, 0.16, 0.50, 0.84, 0.90, and 0.95) reference condition hazard curves for ECC-AM source and (b) 10 Hz mean (red) and fractile (dashed, 0.05, 0.10, 0.16, 0.50, 0.84, 0.90, and 0.95) reference condition hazard curves for ECC-AM source.**

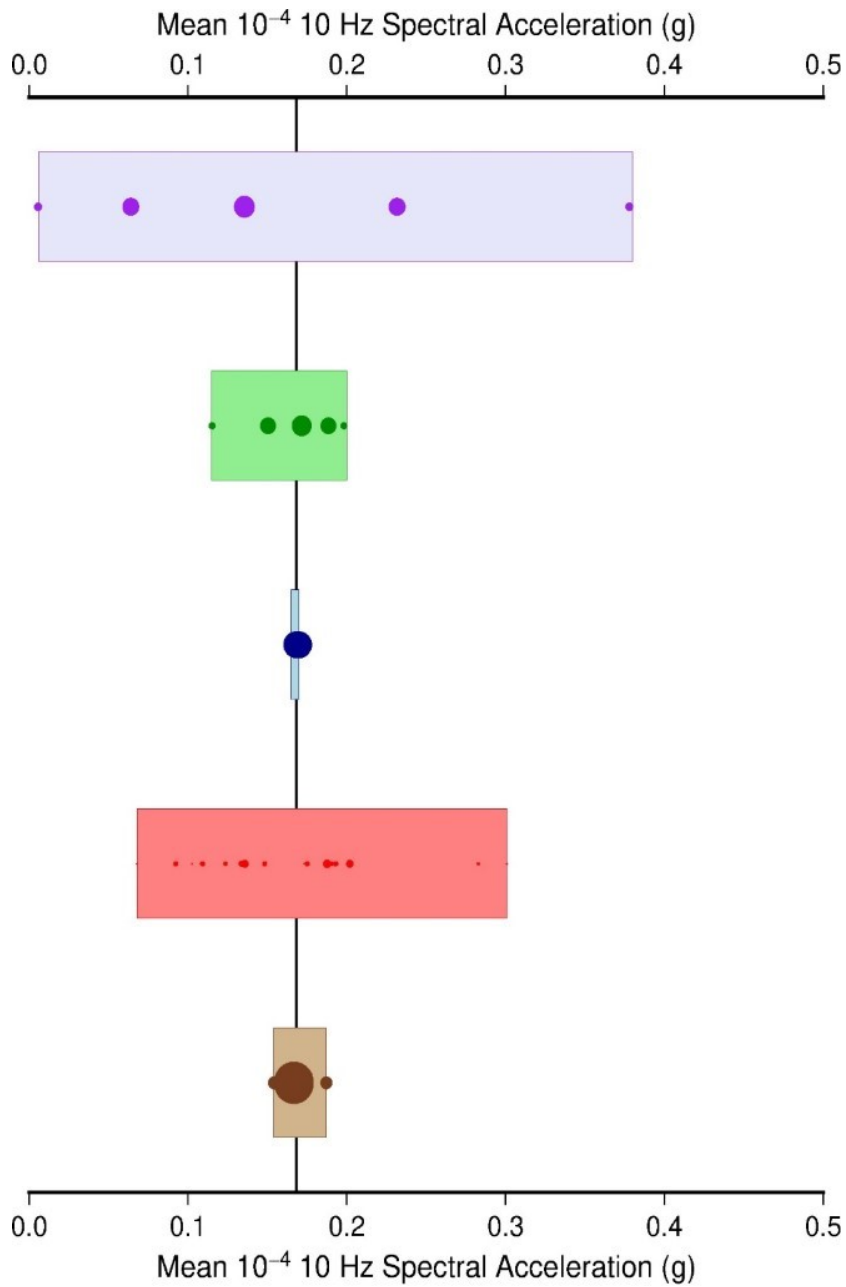


**Figure 4-7 Mean  $10^{-4}$  AFE tornado plot for ECC-AM source and NGA-East GMM.** Parameters from top to bottom are ECC-AM magnitude recurrence rate (purple), ECC-AM maximum magnitudes (green), ECC-AM seismotectonic thickness (blue), NGA-East median GMMs (red), and NGA-East aleatory variability (logarithmic standard deviations; brown). Circle size for each of the parameter values scales with the logic tree weight.

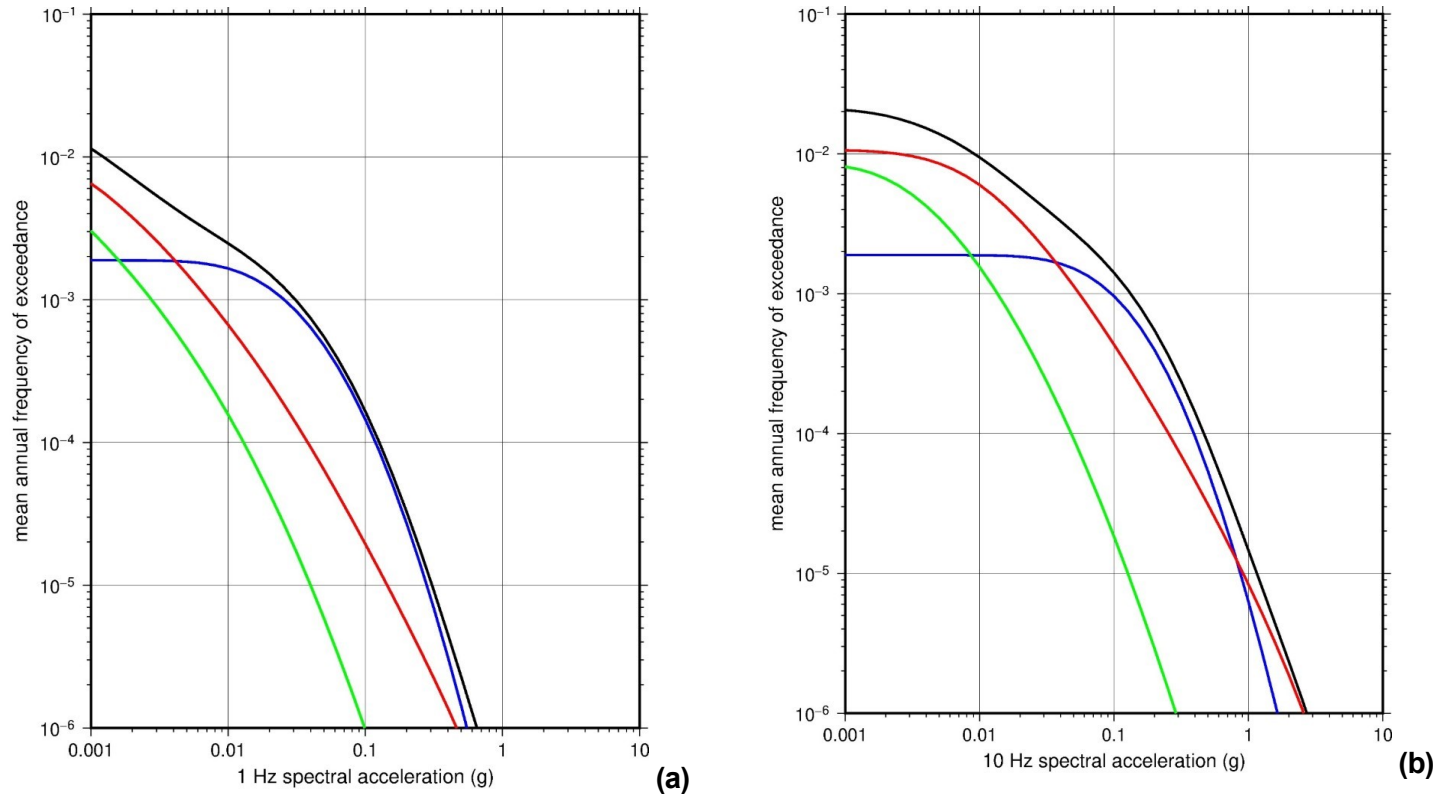
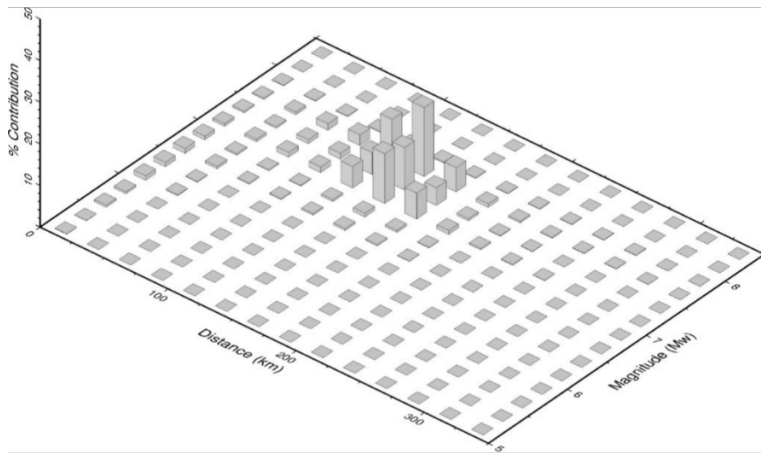
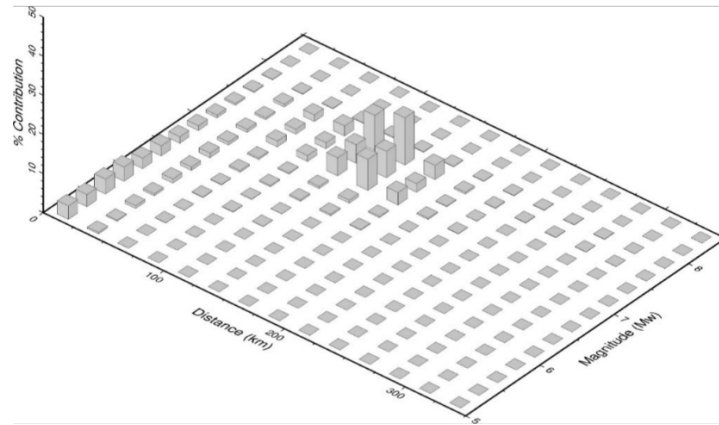


**Figure 4-8** (a) 1 Hz mean hazard curves for SRS. Total hazard (black), Charleston RLME (blue), ECC-AM (red), and PEZ-N (green) hazard curves are shown and (b) 10 Hz mean hazard curves for SRS. Total hazard (black), Charleston RLME (blue), ECC-AM (red), and PEZ-N (green) hazard curves are shown.



(a)



(b)

Figure 4-9 (a) 1 Hz  $10^{-4}$  AFE deaggregation plot for SRS. Charleston RLME source dominates the hazard and (b) 10 Hz  $10^{-4}$  AFE deaggregation plot for SRS. The host zone ECC-AM controls the local hazard and the Charleston RLME source dominates the distant hazard.

4-14

Table 4-1 Controlling earthquake mean magnitude and distance pairs for spectral frequencies		
AFE	Freq=1 Hz $\bar{M}$ and $\bar{R}$ (km)	Freq=10 Hz $\bar{M}$ and $\bar{R}$ (km)
$10^{-3}$	7.1 & 133 km	6.9 & 114 km
$10^{-4}$	7.3 & 123 km	7.0 & 94 km
$10^{-5}$	7.5 & 115 km	6.9 & 68 km

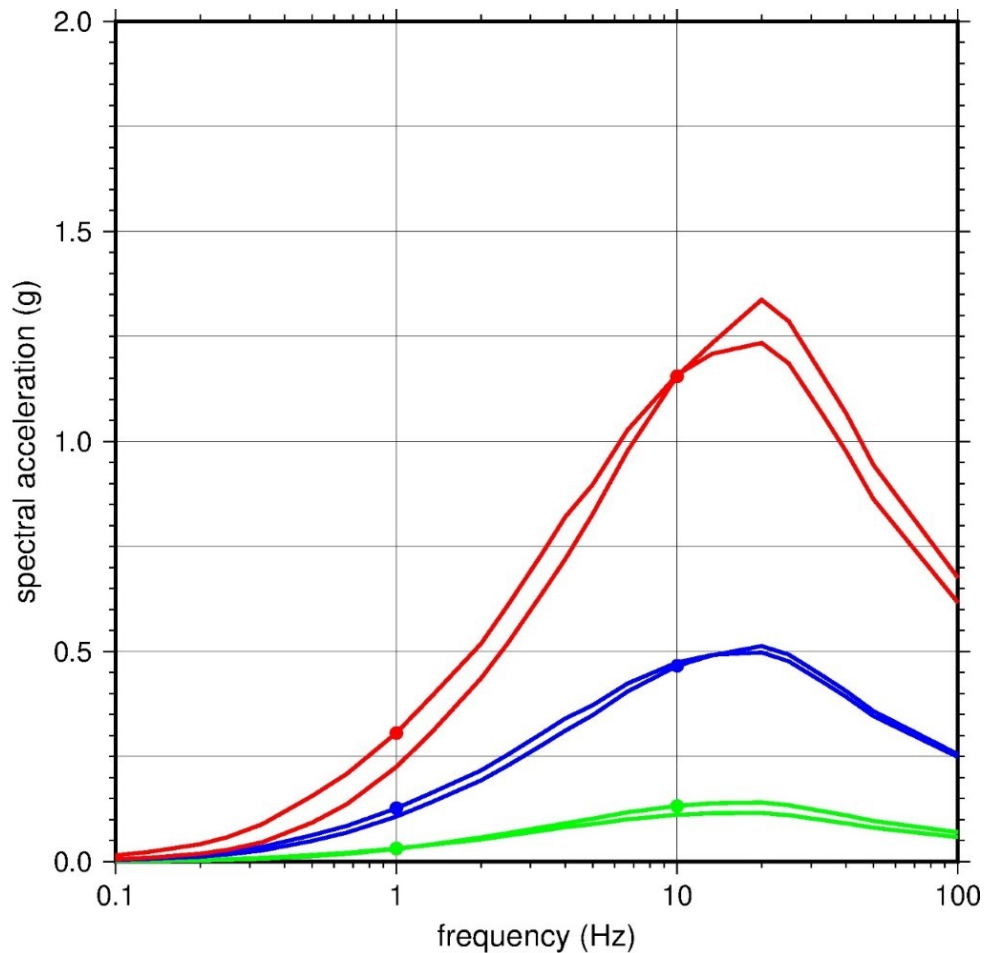


**Figure 4-10** Response spectra for  $10^{-3}$  (green),  $10^{-4}$  (blue), and  $10^{-5}$  (red) AFE, for 1 and 10 Hz deaggregation mean controlling earthquake magnitude and distance pairs. Each response spectrum is scaled (small circles) to either the 1 or 10 Hz UHRS value, as appropriate.

### 4.3 Garner Valley Site

#### 4.3.1 Geologic Setting

The Garner Valley Downhole Array (GVDA) site is located in southern California in a narrow valley within the Peninsular Ranges Batholith. The Peninsular Ranges Batholith of southern and Baja California is the largest segment of a Cretaceous magmatic arc that was once continuous from northern California to southern Baja California (Silver and Chappell, 2011). In this batholith, the emplacement of igneous rocks took place in a single sequence that consist of undersaturated gabbros through to felsic granites, with tonalite being the predominant rock type (Silver and Chappell, 2011). As shown in Figure 4-11, the GVDA is located in a seismically active area of southern California that is within about 7 km from the San Jacinto Fault and within 35 km of the San Andreas Fault (Youd, et al., 2004). The San Jacinto Fault is one of the most active strike-slip fault systems in southern California with an average slip rate of about 10 mm/yr.

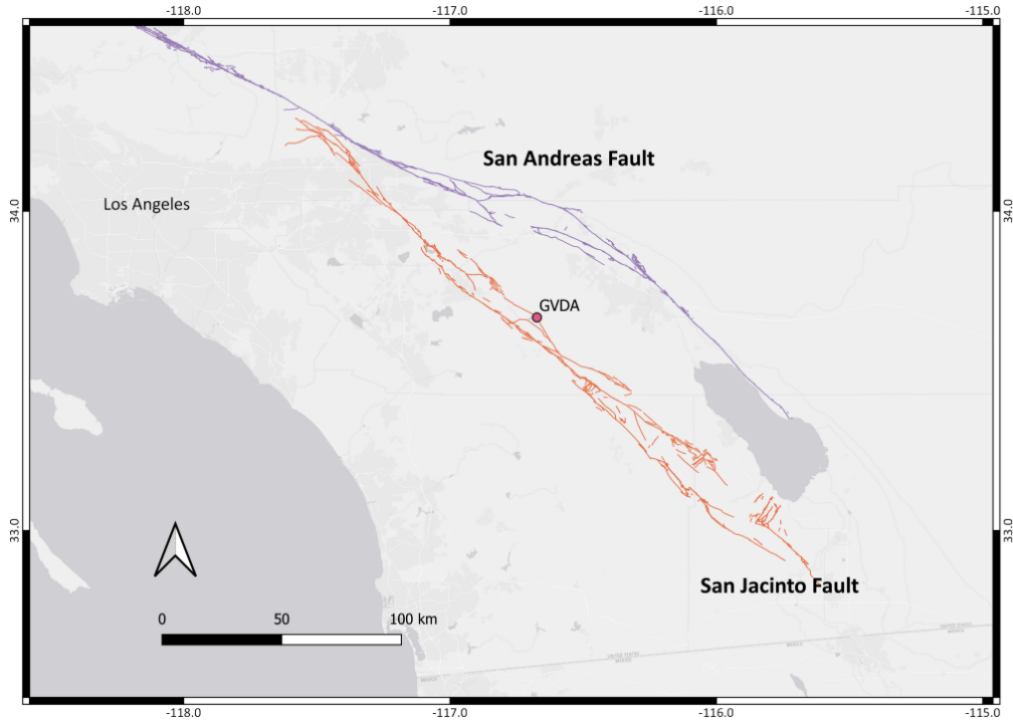


**Figure 4-11 Location of GVDA with respect to the San Andreas Fault and San Jacinto Fault**

The GVDA site is underlain by 18-25 m of lake-bed alluvium, which consists of alternating layers of sand, silty sand, clayey sand, and silty gravel. Beneath the lake-bed alluvium is a 70-m layer of weathered granite (primarily gravelly sand), which then transitions into granitic bedrock (Youd, et al., 2004). Figure 4-12 shows the stratigraphic profile beneath the GVDA site.

#### **4.3.2 Geotechnical and Geophysical Data**

The GVDA site has been thoroughly characterized by multiple geotechnical and geophysical field investigations performed from 1989 through 2018 (e.g., Stellar, 1996; Stokoe and Darendeli, 1998; Liu et al., 2000; Stokoe et al., 2004; Youd et al., 2004; Teague et al., 2018). Geotechnical field investigations at the site consist of drilling and sampling, borehole logging, cone penetration tests (including seismic cone penetration), and permeability tests. Cone penetration tests performed by Youd et al. (2004) extend to depths of approximately 18 m into the alluvium and borings to depths of 88 meters reached into the granitic bedrock (Stellar, 1996).

Laboratory tests performed on soil samples include moisture content, wet and dry density, specific gravity, particle size analysis, plasticity, consolidation, and shear strength (Youd et al., 2004). In addition, resonant column and torsional shear tests were conducted on four specimens retrieved at depths of 3.5, 6.5, 27 and 41.3 meters for which site-specific shear modulus degradation and material damping curves were developed (Stokoe and Darendeli, 1998).

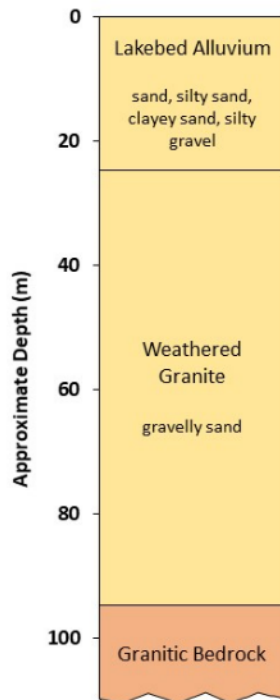


**Figure 4-12 Stratigraphic column beneath the GVDA site**

Geophysical explorations of the GVDA site consist of downhole testing (Gibbs 1989), suspension logging (Stellar, 1996), spectral analysis of surface wave (SASW) (Stokoe et al., 2004), multi-channel analysis of surface waves (MASW) (Teague et al., 2018), and microtremor array measurement (MAM) (Liu et al., 2000; Teague et al., 2018).

Instrumentation of the GVDA consists of six downhole accelerometers (depths of 6 m, 15 m, 22 m, 50 m, 220 m, and 500 m) and five surface accelerometers placed in a linear array 250 m long, which is bisected by the downhole array (Youd et al., 2004). In addition, three accelerometers were placed remotely at a nearby rock outcrop (one at the surface, at a depth of 30 m, and a depth of 150 m).

### **4.3.3 Source Characterization and Ground Motion Models**

Because this SSHAC Level 2 project is focused on site response analysis, the TI Team decided to develop a simplified SSC model and implement the Southwest United States (SWUS) GMM (GeoPentech, 2015) for the GVDA site. These two models along with the reference condition hazard for the GVDA site are described below.

#### ***Seismic Source Characterization Model***

For the SSC model for the GVDA site, the TI Team decided to limit the model to the most proximate fault source. As such, the TI Team developed a simplified model for the San Jacinto Fault Zone (SJFZ), which is shown in Figure 4-13. Along with the various strands of the San Andreas Fault and the Eastern California Shear Zone, the SJFZ takes up most of the plate

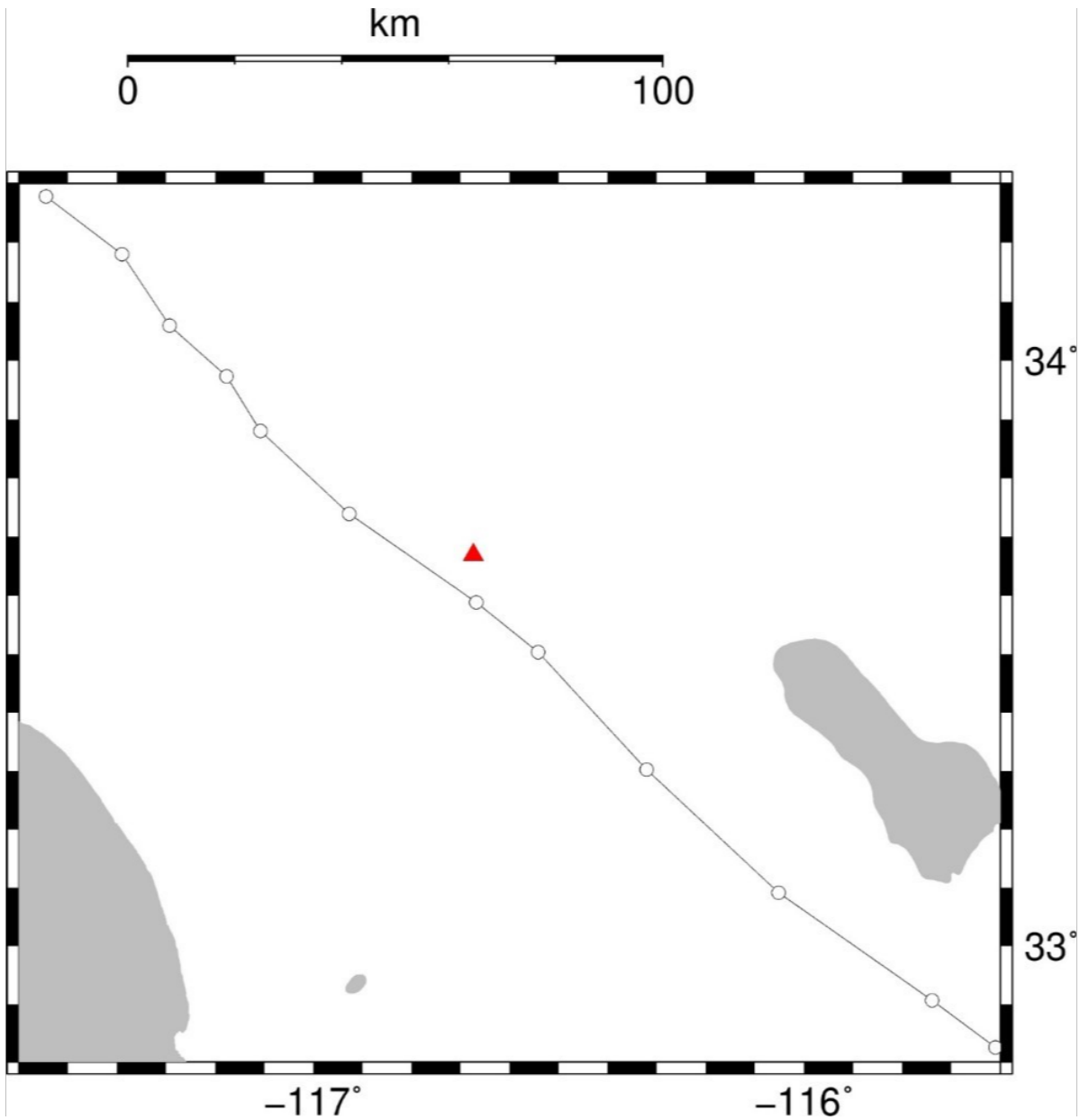


**Figure 4-13** Simplified San Jacinto Fault Zone source model (thin black line). GVDA site is shown as red triangle and is about 7 km from the San Jacinto Fault at the closest approach.

motion between the North America and Pacific plates. The SJFZ is about 210 km in length with predominantly right-lateral strike-slip faulting and slip rates that vary between 7 and 17 mm/yr (SCEDC, 2013). The SJFZ has numerous overlapping and discontinuous sub-vertical segments that influence the distribution of strike-slip rates along the fault. The GVDA site is located adjacent to the Anza segment of the SJFZ, which has not ruptured since at least 1890 (Sykes and Nishenko, 1984). As summarized in Herbert and Cooke (2012), strike-slip rates along the SJFZ range from 6 to 13 mm/yr along the northernmost segments, 7 to 15 mm/yr along the central segments, and about 1-3 mm/yr along the southernmost segments.

Based on the above information, the TI Team decided to develop a simplified source logic tree for the SJFZ that captures the epistemic uncertainty in maximum magnitude ( $M_{max}$ ) and fault slip rate. For  $M_{max}$ , the TI Team considered three alternative values of **M7.1**, **M7.4**, and **M7.7** with weights of 0.4, 0.5, and 0.1, respectively. Similarly, for the slip rate, the TI Team modeled three alternative values of 5, 9, and 13 mm/yr with weights of 0.3, 0.4, and 0.3, respectively. However, after considering the extremely high ground motions for hazard levels corresponding to AFEs of  $10^{-4}/\text{yr}$  and  $10^{-5}/\text{yr}$ , the TI Team decided to divide these three slip rates by 30 in order to produce hazard levels that are generally consistent with moderate to higher hazard sites across the U.S. For each rupture along the SJFZ, the TI Team modeled only strike-slip ruptures with a dip angle of 90 degrees. For the magnitude frequency distribution, the TI Team implemented the characteristic earthquake model (Youngs and Coppersmith, 1985). Finally, the TI Team used a single seismotectonic thickness of 13 km and a minimum magnitude of **M5** for the PSHA.

### **Ground Motion Model**

The SWUS GMM was developed using the SSHAC Level 3 process for the three nuclear power plants in the southwestern U.S.: Diablo Canyon, San Onofre, and Palo Verde in order to respond to the U.S. NRC's March 2012 50.54(f) letter (NRC, 2012c). For the GVDA site, the TI Team implemented the SWUS GMM model as developed for the Diablo Canyon nuclear power plant, which was derived for shallow crustal earthquakes in a predominantly active transpressional tectonic setting (GeoPentech, 2015).

The SWUS GMM is a set of GMMs for the median and standard deviation of predicted ground motions and their associated weights to be used in PSHAs for seismic hazard characterizations of nuclear facilities located in active tectonic settings. In particular, the SWUS GMM includes a set of multiple median GMMs (up to 31 for each spectral frequency) for the horizontal component of ground motion (5%-damped pseudo-acceleration response spectra) for 17 oscillator frequencies between 0.1 and 100 Hz. The median GMMs predict spectral acceleration values as a function of **M** and  $r_{rup}$  and were developed for the reference conditions of  $V_{S30}$  of 760 m/s and a  $\kappa_0$  of 0.04 sec. Standard deviation models for each of the spectral frequencies, which depend on **M**, are provided for site-specific analysis ( $\sigma_{SS}$ ). In addition, median adjustment factors are provided for hanging-wall effects.

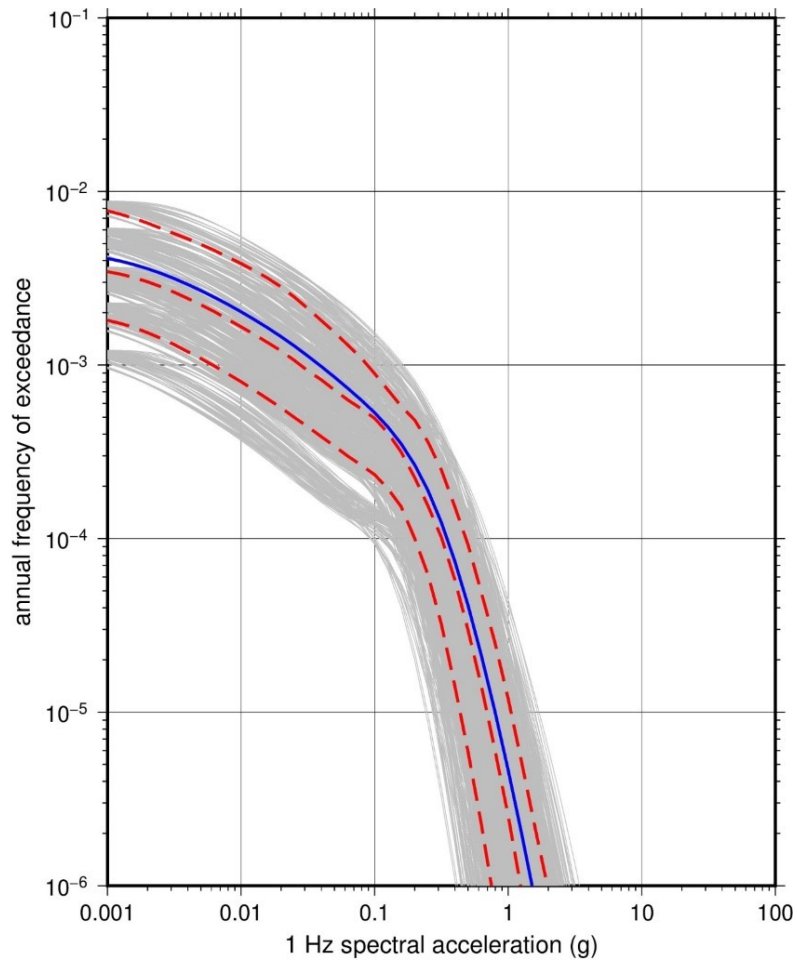
The full logic tree for the SWUS GMM, as described in the HID, consists of multiple branches for the median predictions with each branch having a single assigned hanging wall median adjustment factor. For the aleatory variability models, the logic tree consists of three branches for the standard deviation (low, medium, and high) and two branches for the aleatory variability distribution (mixture and lognormal). For this project, the TI Team decided to implement the full logic tree for the median ground motion predictions as well as the hanging-wall adjustment. For the aleatory variability logic tree, the TI Team implemented the three-alternative  $\sigma_{SS}$  estimates (low, medium, and high), but used only the mixture model for the aleatory variability distribution. The TI Team concluded that because the mixture model is more heavily weighted than the lognormal distribution (0.8 versus 0.2), the reference condition hazard curve distribution would not be impacted by implementing just the mixture model.

### **Reference Condition Hazard**

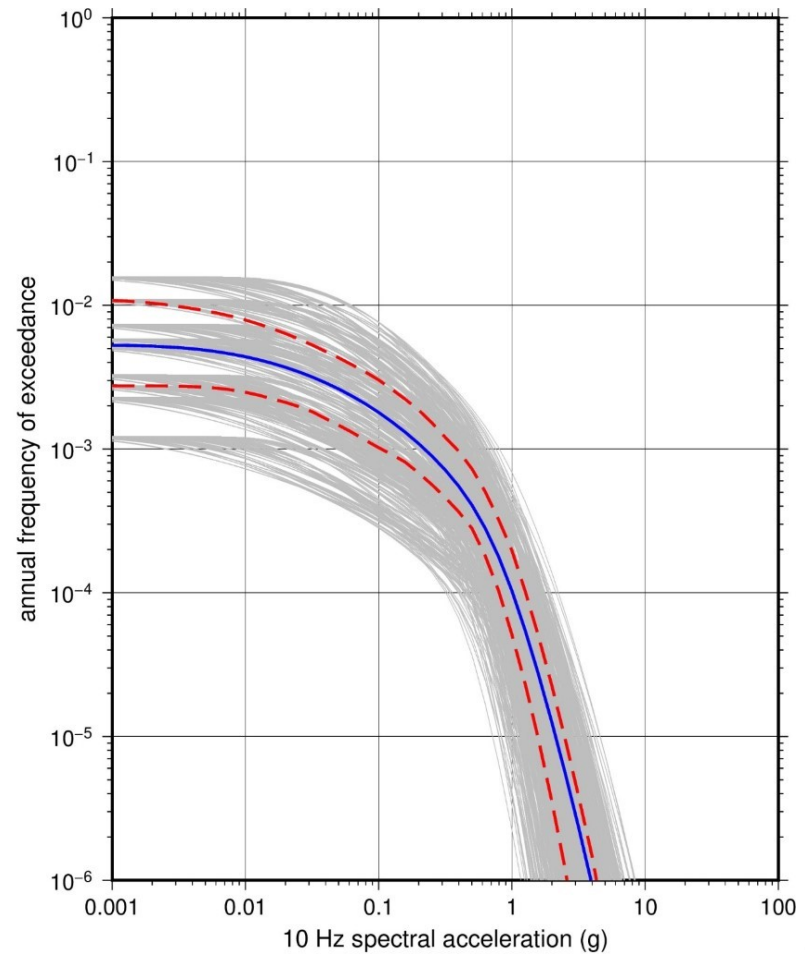
The TI Team developed the reference condition hazard model for the GVDA site by implementing the simplified SSC model for the SJFZ and the SWUS GMM. For the SJFZ, the TI Team included the three-alternative weighted  $M_{max}$  values, a single average seismotectonic

thickness, and three alternative weighted fault slip rates. For each of the  $M_{max}$  values, the TI Team developed a set of virtual ruptures along the length of the SJFZ for each of the magnitudes ranging from the minimum magnitude of **M5** to the specified  $M_{max}$  value using a magnitude increment of 0.10. To determine the length for each virtual rupture, the TI Team used the Hanks and Bakun (2014) fault-area relationship and a length-to-width ratio of one for the lower magnitudes that do not saturate the entire seismotectonic thickness.

Figure 4-14a shows the distribution of reference condition hazard curves as well as several fractile and mean curves for the spectral frequencies of 1 and 10 Hz for the SJFZ. Figure 4-14b clearly shows distinct groups of hazard curves, particularly for lower spectral accelerations, that are due to the three  $M_{max}$  and three fault slip rates. The total number of hazard curves for each spectral frequency varies depending on the number of median GMMs, as described above. Figure 4-15 shows the mean UHRS for the ground motion return periods of 1,000, 10,000 and 100,000 years, and Figure 4-16 shows deaggregation plots for 1 and 10 Hz spectral frequencies for an AFE of  $10^{-4}/\text{yr}$ . The controlling earthquake for 1 Hz at an AFE of  $10^{-4}/\text{yr}$  has a mean magnitude of 7.2 at a mean distance of 8 km and for the spectral frequency of 10 Hz, the controlling earthquake mean magnitude is 7.0 at a mean distance of 8 km. Table 4-2 shows the controlling earthquake mean magnitude and distance pairs for the spectral frequencies of 1 and 10 Hz and for the AFEs of  $10^{-3}/\text{yr}$ ,  $10^{-4}/\text{yr}$  and  $10^{-5}/\text{yr}$ . Finally, Figure 4-17 shows the response spectrum for each of these controlling earthquakes scaled to the appropriate UHRS value at either 1 or 10 Hz. These scaled response spectra were used by the TI Team to inform the range of input response spectra used for the site response evaluation for the GVDA site.



(a)



(b)

**Figure 4-14 (a) 1 Hz mean and fractile (0.16, 0.50, and 0.84) hazard curves for the GVDA site and (b) 10 Hz mean and fractile (0.16, 0.50, and 0.84) hazard curves for the GVDA site**

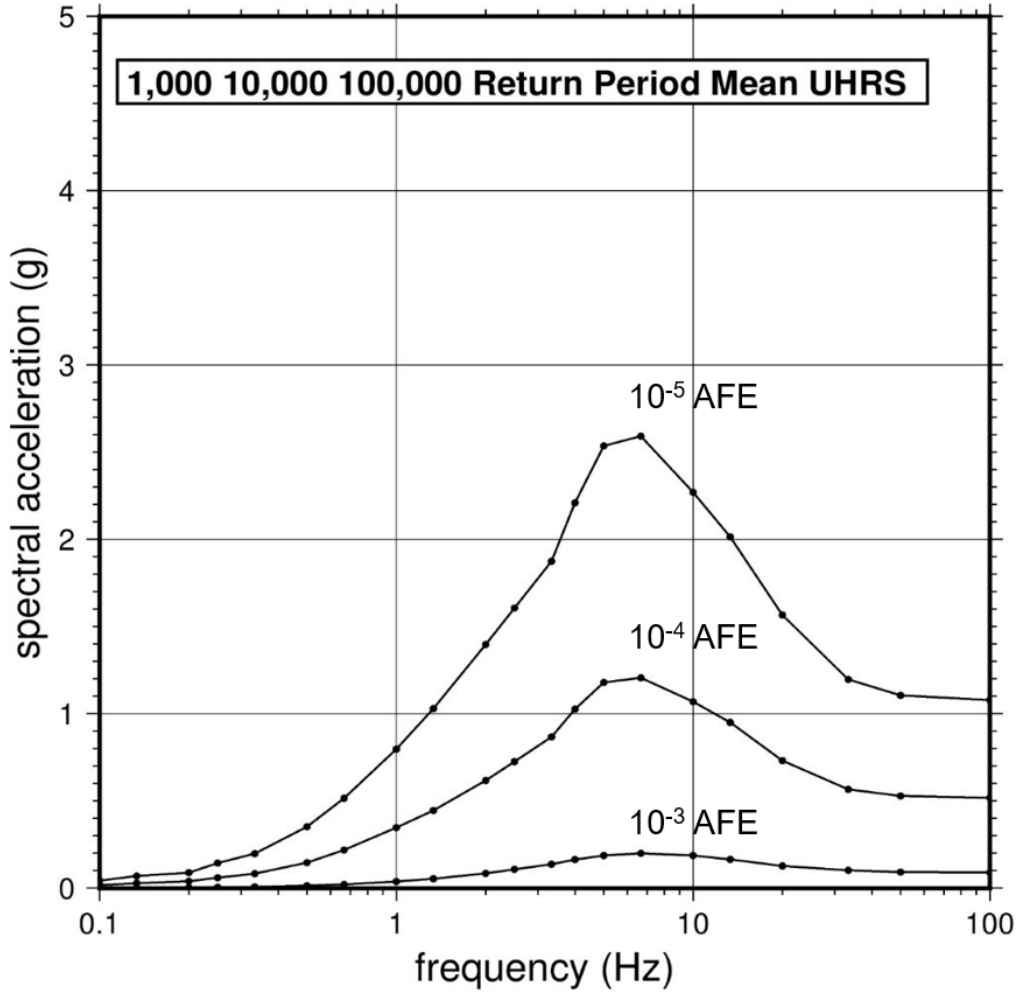
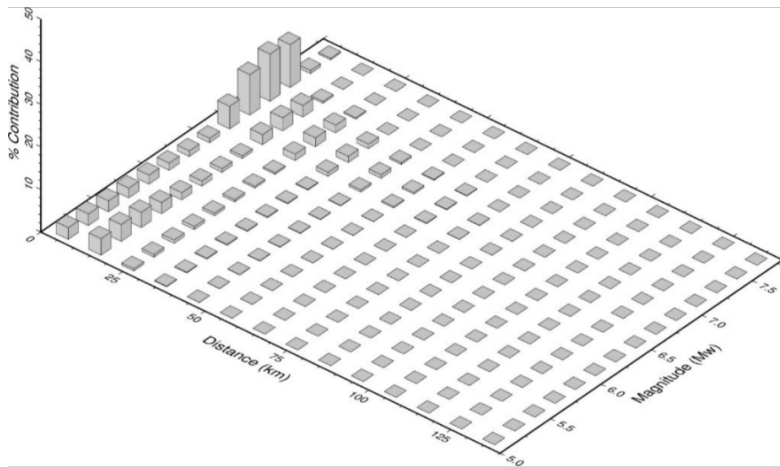
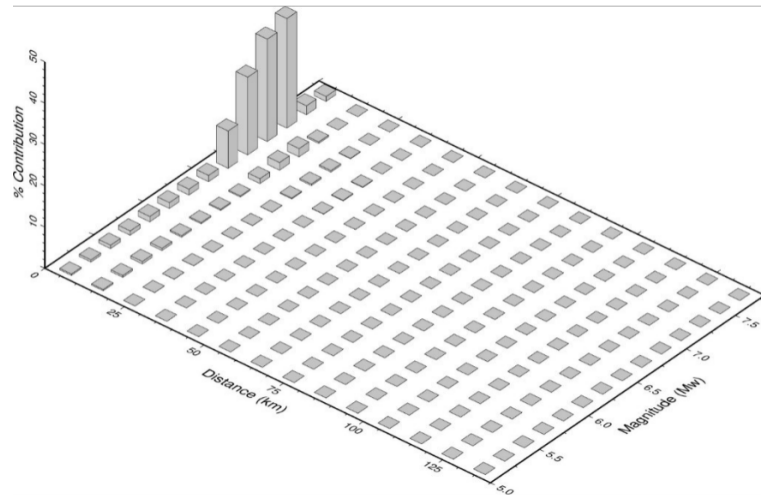


Figure 4-15 Mean UHRS for the GVDA site. Shown are UHRS for  $10^{-3}$ ,  $10^{-4}$ , and  $10^{-5}$  AFE levels.



(a)



(b)

Figure 4-16 (a) 1 Hz deaggregation results for  $10^{-3}$  AFE and (b) 10 Hz deaggregation results for  $10^{-3}$  AFE.

4-23

1

Table 4-2 Controlling earthquake mean magnitude and distance pairs		
AFE	Freq=1 Hz $\bar{M}$ and $\bar{R}$ (km)	Freq=10 Hz $\bar{M}$ and $\bar{R}$ (km)
$10^{-3}$	6.6, 18	6.4, 14
$10^{-4}$	7.2, 8	7.0, 8
$10^{-5}$	7.2, 7	7.0, 8

2

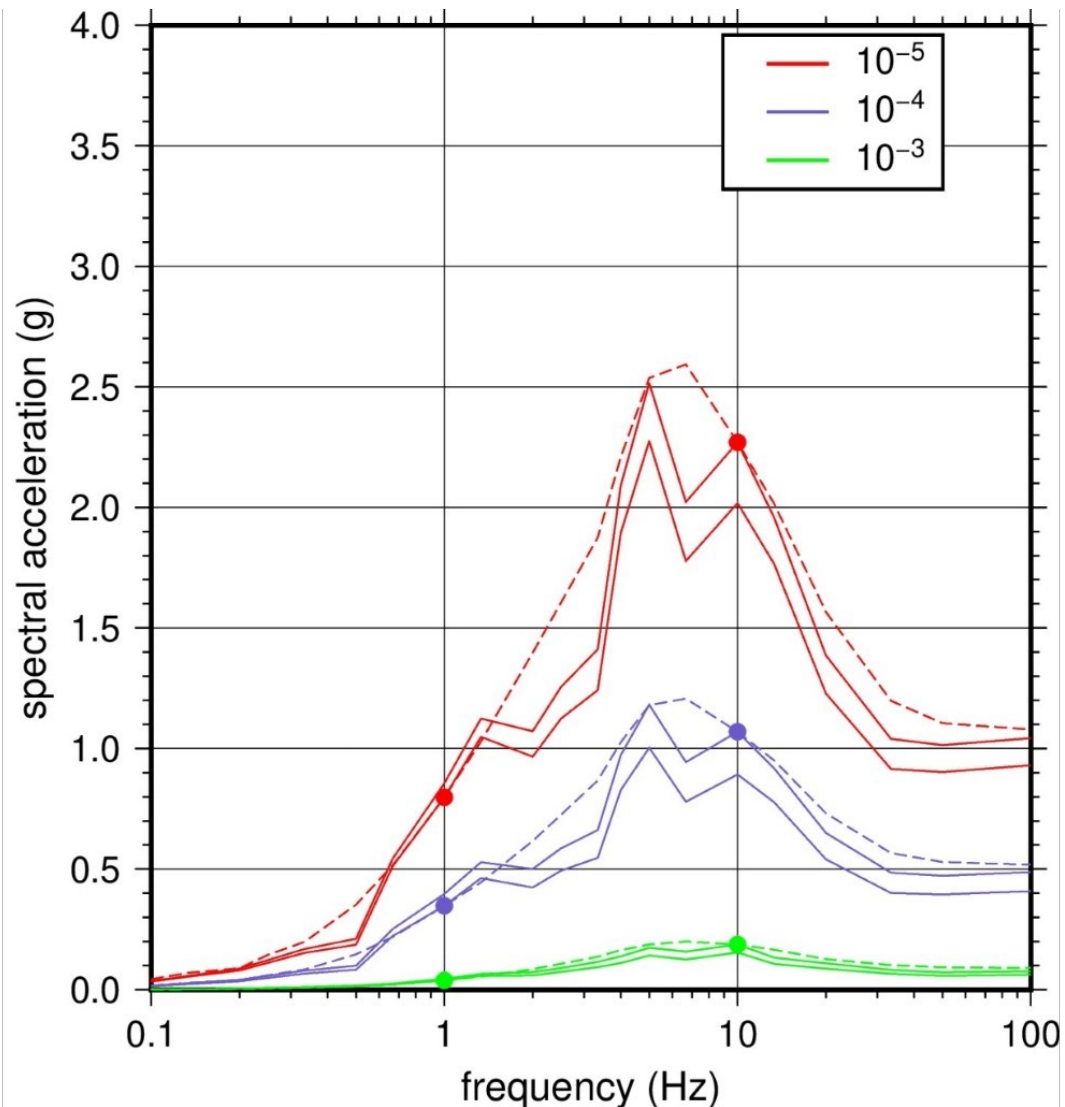


**Figure 4-17** Response spectra (solid line) from deaggregation controlling earthquake mean magnitude and distance pairs. Each response spectrum is scaled to the appropriate UHRS (dashed line) at either 1 or 10 Hz.

#### 4.4 References

Denham, M.E. *SRS Geology/Hydrogeology Environmental Information Document*. WSRC-TR-95-0046, 10526. 1999.

DOE. *MOX Fuel Fabrication Facility Site Geotechnical Report*. Washington, DC: U.S. Department of Energy. 2003.

GeoPentech. *Southwestern United States ground motion characterization SSHAC level 3, Technical Report*, Revision 2. March 2015.

Gibbs, J. F. (1989). Near-surface P- and S-wave velocities from borehole measurements near Lake Hemet, California, U.S. Geological Survey. Open-File Rep. 89-630. DOI: 10.3133/ofr89630

Goulet, C., Y. Bozorgnia, N. Abrahamson, N. Kuehn, L. Al Atik, R. Youngs, and R. Graves. "Central and Eastern North America Ground-Motion Characterization." PEER report No. 2018/08, Pacific Earthquake Engineering Research Center at the University of California, Berkeley. 2018a.

Goulet, C., Y. Bozorgnia, N. Abrahamson, N. Kuehn, L. Al Atik, R. Youngs, R. Graves, and G. Atkinson. *Next Generation Attenuation Relations for the Central and Eastern United States (NGA-East)*. United States: N. p., 2018b. Web. doi:10.2172/1593158.

Hanks T.C., Bakun W.H. (2014). M-logA Models and other Curiosities. *Bulletin of the Seismological Society of America*, 104(5):2604-2610

Herbert, J.W. and M.L. Cooke. "Sensitivity of the southern San Andreas fault system to tectonic boundary conditions and fault configurations." *Bulletin of the Seismological Society of America*. Vol. 102, No. 5. pp. 2,046–2,062. 2012.

Liu, Hsi-Ping, D.M. Boore, W.B. Joyner, D.H. Oppenheimer, R.E. Warrick, W. Zhang, J.C. Hamilton, and L.E. Brown. "Comparison of phase velocities from array measurements of Rayleigh waves associated with microtremor and results calculated from borehole shear-wave velocity profiles." *Bulletin of the Seismological Society of America*. Vol. 90, Issue 3. pp. 666–678. 2000.

Miller III, A.C. and T.R. Rice. "Discrete approximations of probability distributions." *Management Science* 29.3. pp. 352-362. 1983.

Moayerian, S. "Effect of Loading Frequency on Dynamic Properties of Soils Using Resonant Column." Thesis, University of Waterloo. 2012.

NRC. NUREG–2115, Central and Eastern United States Seismic Source Characterization for Nuclear Facilities. U.S. Nuclear Regulatory Commission Report, 6 Volumes. Washington, DC: U.S. Nuclear Regulatory Commission. 2012b

NRC. 50.54(f) letter, Title 10 of the *Code of Federal Regulations* 50.54(f) Regarding Recommendations 2.1, 2.3, and 9.3 of the Near-Term Task Force Review of Insights from the Fukushima Dai-ichi Accident. Washington, DC: U.S. Nuclear Regulatory Commission. March 2012c

SCEDC. Southern California Earthquake Center. Caltech Dataset. 2013. doi: 10.7909/c3WD3xH1.

Silver, L.T. and B.W. Chappell. "The Peninsular Ranges Batholith: an insight into the evolution of the Cordilleran batholiths of southwestern North America." *Earth and Environmental Science Transactions of the Royal Society of Edinburgh*. Vol. 79, Issue 2-3. pp. 105-121. 2011.

Steller, R. "New borehole geophysical results at GVDA." UC Santa Barbara Internal report. 1996.

Stokoe, K.H. and M.B. Darendeli. Laboratory evaluation of the dynamic properties of intact soil specimens: Garner Valley, California. Geotechnical Engineering Report GR98-3, Civil Engineering Department, Austin, Texas: The University of Texas at Austin. March 1998.

Stokoe, K.H., A. Kurtulus, and F.Y. Menq. "Data Report." *SASW Measurements at the NEES Garner Valley Test Site, California.* 2004.

Stokoe, K.H., M. Darendeli, and N.-K.J. Lee. *Correlation Study of Nonlinear Dynamic Soil Properties.* The University of Texas at Austin. 1995.

Sykes, L.R. and S.P. Nishenko. "Probabilities of Occurrence of Large Plate Rupturing Earthquakes for the San Andreas, San Jacinto, and Imperial Faults, California, 1983–2003." *Journal of Geophysical Research. Solid Earth.* 89.B7. pp. 5,905–5,927. 1984.

Teague, D.P., B.R. Cox, and E.M. Rathje. "Measured vs. predicted site response at the Garner Valley Downhole Array considering shear wave velocity uncertainty from borehole and surface wave methods." *Soil Dynamics and Earthquake Engineering.* Vol. 113. pp. 339-355. 2018.

Youd, T.L., A.J. Bartholomew, and J.S. Proctor. Geotechnical logs and data from permanently instrumented field sites: Garner Valley Downhole Array (GVDA) and Wildlife Liquefaction Array (WLA). Report to The Network for Earthquake Engineering Simulation (NEES) Colaboratories, December 17. 2004.

Youngs, R.R. and K.J. Coppersmith. "Implications of fault slip rates and earthquake recurrence models to probabilistic seismic hazard estimates." *Bulletin of the Seismological Society of America.* Vol. 75, No. 4. pp. 939–964. 1985.

## 5 Description of Site Response Logic Trees

### 5.1 Introduction

The epistemic uncertainty in the site adjustment factors (*SAF*) is captured via a site response logic tree. The site response logic tree must capture the center, body and range of technically defensible interpretations (CBR or TDI) for the properties of the site that control the site response [i.e., the shear-wave velocity, the site kappa ( $\kappa_0$ ), and modulus reduction and damping curves], as well as the epistemic uncertainties associated with the analysis methods. Sections 5.2 to 5.5 present the development of logic tree branches to account for each of these sources of uncertainty; each section starts with a discussion of the issues to be considered in the construction of the logic tree and is followed by a description of the logic tree for each of the two sites. These sections also include the technical justification for the modeling choices and for the logic tree weights. The logic trees for the two sites are then summarized and compared in Section 5.6. Also important for capturing the full range of epistemic uncertainty in site response are considerations of model error. These considerations are discussed in Section 3.2 and are not repeated here.

### 5.2 Shear-Wave Velocity

#### 5.2.1 Issues Related to Developing $V_S$ Logic Tree

The separation of epistemic uncertainty and aleatory variability regarding the shear-wave velocity ( $V_S$ ) profile is an important issue that must be considered when developing the  $V_S$  logic tree. The epistemic uncertainty in  $V_S$  is related to the uncertainties with the velocity profile that can, in principle, be reduced with additional testing. The interpretation of aleatory variability in  $V_S$  is less clear. On one hand, aleatory variability is related to spatial variability on the scale of the footprint of the facility under study. This variability would, in principle, lead to motion-to-motion variability in site response. However, aleatory variability in  $V_S$  has also been used in past practice to compensate for deviations from the one-dimensional (1D) idealization used in the site response analyses. More specifically, 1D site response predicts strong narrow-band amplifications due to resonances, and the strength of the peaks associated with these resonances often are larger in 1D site response analyses than observed in downhole arrays. Aleatory variability is incorporated via randomization of the  $V_S$  profiles. The next sections separately discuss the treatment of epistemic uncertainty and aleatory variability in  $V_S$ .

#### ***Epistemic Uncertainty***

The epistemic uncertainties related to the  $V_S$  profile at the site must be fully represented in the site response logic tree. In past studies, these uncertainties were often captured by using alternative median base case  $V_S$  profiles, with a common approach being the use of three  $V_S$  profiles that are scaled to represent a best-estimate, an upper-bound, and a lower-bound profile. The criteria of the analyst should be to ensure that the three  $V_S$  profiles appropriately represent the CBR or TDI of the site information. In this regard, it is important to consider that the absence of data should not lead to artificially low epistemic uncertainty. For this reason, the Screening, Prioritization and Implementation Details (SPID) guidelines (EPRI, 2013) recommend that the three base case profiles should be consistent with an epistemic uncertainty that is a function of the degree of site characterization at a site.

An alternative approach to the use of scaled median  $V_S$  profiles is to consider base case profiles that are obtained from different measurement methods and/or alternative interpretations of site measurements. An example of this approach would be to consider alternative inversions of surface-wave based measurements of the dispersion curve to represent alternative base-case profiles (Griffiths et al., 2016).

An additional source of epistemic uncertainty that cannot be readily represented by using scaled  $V_S$  profiles is related to the uncertainties particular to some features of a profile, such as the presence (or absence) of a certain geological unit or the characterization of a geological feature. For example, the site response logic tree could include a node that would represent the presence or absence of a low-velocity layer in the profile, provided there is epistemic uncertainty on whether this layer is present at the site under analysis, or the degree to which it is present across the site. Alternatively, a logic tree node can capture the thickness of a transition layer from soil to rock or the  $V_S$  of a particular geological unit. In addition, a source of epistemic uncertainty that should be captured by the site response logic tree is the depth to the reference condition  $V_S$  established by the ground-motion model (GMM) used for the probabilistic seismic hazard analysis (PSHA). If applicable, the site response logic tree should also incorporate the epistemic uncertainty in the host  $V_S$  profile.

### ***Aleatory Variability***

A common element of the epistemic uncertainty in  $V_S$  profiles that is described above is that, in principle, it can be reduced with additional site characterization. On the other hand, aleatory variability cannot be reduced with additional data. However, additional data or information can help quantify aleatory variability, or can help decide on an appropriate model for the aleatory variability. The uncertainty of the level of aleatory variability and the approach to capture aleatory variability is also a source of epistemic uncertainty and should be captured in the site response logic tree.

Aleatory variability in the site properties results from the spatial variability of materials across a site. Aleatory variability models are used to generate randomized  $V_S$  profiles around a median base case profile; the effect of the randomization is to smooth the resulting surface-to-bedrock outcrop amplification factors across frequencies. This smoothing is considered appropriate because 1D site response analyses [and, in particular, equivalent linear (EQL) analyses] tend to overestimate amplification at resonant frequencies of the site. While there is no agreement as to whether this smoothing process represents actual physical processes or it is simply a tool to compensate for the overprediction of resonances in 1D site response analyses, there is general agreement that the aleatory variability model should correlate to the degree of spatial variability of site properties across a site. The paragraphs below address the quantification and modeling of aleatory variability.

The most commonly used model for randomization of  $V_S$  profiles is the model by Toro (1995). The Toro (1995) model quantifies the aleatory variability through a depth-dependent standard deviation of the natural log of the velocities ( $\sigma_{\ln V_S}$  or, similarly, a depth-dependent model for the coefficient of variation (COV), a model for the correlation of  $V_S$  across depths (or across layers), and a model for randomizing the thickness of soil layers within a profile. Toro (1995) also provides values for the parameters of his randomization model. These parameters, however, represent average values for generic site classes. The parameter values of the Toro (1995) model for site-specific applications may vary significantly from the generic parameter values, and for that reason it is recommended to use, whenever possible, site-specific analyses to quantify the parameters of the spatial variability model using site-specific data. Most

critically,  $\sigma_{lnV_S}$  should be informed from site-specific data. It is more difficult to develop a site-specific correlation model or a site-specific layer randomization model, but these models should be considered if the site-specific data allows. When there is an absence of data, the value of the depth-dependent standard deviation should reflect the inferred degree of spatial variability in the  $V_S$  across a site.

An alternative approach to parametric randomization models for capturing aleatory variability is to obtain multiple profiles from the inversion of dispersion curves (Griffiths et al., 2016). The advantage of this approach is that the various profiles that are obtained in this manner are consistent with the measured dispersion curve, which can be considered a “site signature” for a site. Conversely, the use of the Toro (1995) model can result in  $V_S$  profiles that are inconsistent with any field measurements, including the dispersion data. An intermediate approach is to obtain models using a randomization approach [such as the Toro (1995) model] but apply constraints to the profiles such that only those that are consistent with measured site signatures [i.e., the dispersion curve and/or the fundamental site frequency as inferred from horizontal-to-vertical (H/V) spectral ratios (Teague et al., 2018)] are accepted.

Another approach that has been proposed to overcome the limitation of randomization models is to randomize the cumulative travel time rather than the  $V_S$  (Passeri et al. 2020). This randomization approach also requires a complementary model for the randomization of site layering. The advantage of travel-time randomization is that, compared to  $V_S$  versus depth models, the resulting models are automatically consistent with site signatures. A preliminary evaluation of the Passeri et al. (2020) model was conducted by the Technical Integration (TI) Team. Site response was computed for a suite of shear wave velocity profiles generated by this method; the resulting uncertainty in the *SAF* was very small. Additional analyses indicated that the generic inter-layer correlation parameters from Passeri et al. (2020) may not be applicable to the Savannah River Site (SRS) study site. As a result, the TI Team’s judgment is that the Passeri et al. (2020) model needs additional validation and evaluation before it can be implemented in practice.

The TI Team was able to develop a site-specific correlation model for implementation with the Toro (1995) randomization approach. Therefore, for the SRS study site, the TI Team implemented the Toro (1995) randomization approach with different alternatives for layer thickness randomization. For the Garner Valley Downhole Array (GVDA) study site, the TI Team implemented two approaches: obtaining profiles directly from the different  $V_S$  profiles obtained from the inversion of dispersion curves, and the Toro (1995) randomization approach with constraints dictated by measured dispersion curves.

### **5.2.2 $V_S$ Components of the Logic Tree for SRS**

Seismic cone penetration test (CPT) measurements are available for characterizing the near surface shear-wave velocity to a depth of approximately 43 meters (m) at the SRS F-area (SRS-FA) site. Shear-wave velocities at greater depths are determined using downhole, crosshole, and *P*-and *S*-wave (*P-S*) suspension logging measurements at locations across the SRS. The locations of the downhole, crosshole, and suspension logging measurements in relation to the SRS-FA site are shown in Figure 5-1.

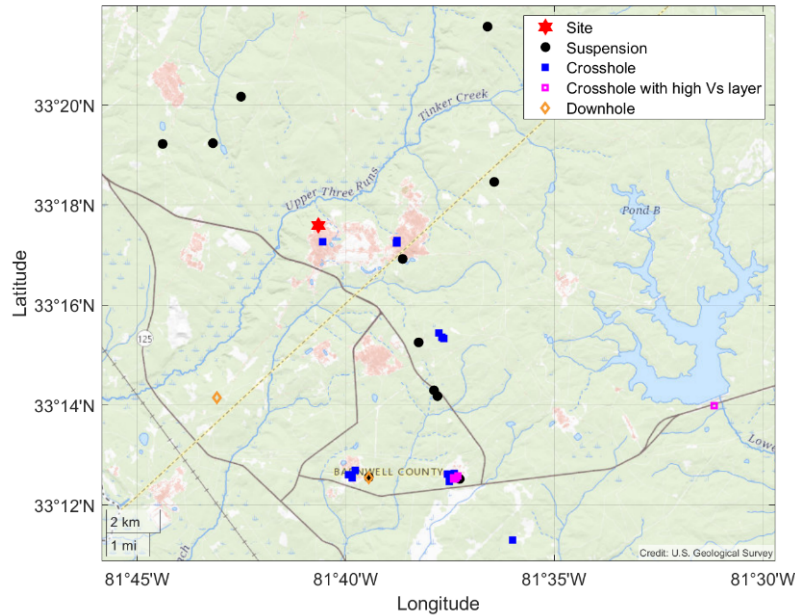


**Figure 5-1 SRS shear-wave velocity test locations**

A limited number of crosshole  $V_S$  tests located to the southeast of the site show a high velocity layer. The high velocity layer is likely associated with the Santee Formation. The Santee Formation includes calcareous deposits, which have high velocities; however, the calcareous deposits in the Santee Formation are sporadic in the middle of the SRS and missing to the northwest (Denham, 1999). Based on the SRS geology described by Denham (1999) and a review of the boring logs and CPT data from the site, a significant volume of calcareous deposits in the Santee Formation is likely not present at the SRS-FA study site; consequently, the high velocities observed in the  $V_S$  tests southeast of the site, which correspond to this calcareous layer, were not used when developing the site  $V_S$  profile.

### Epistemic Uncertainty in Velocity Profiles

The TI Team developed three alternative  $V_S$  profiles denoted as the lower-, base-, and upper-case profiles. Two factors contributed to using multiple base case  $V_S$  profiles for SRS. First, there are no site signatures available from surface wave testing or H/V ratios. Second, velocity data for depths greater than 43 m are from locations multiple kilometers (km) from the site of interest (Figure 5-1). Therefore, the TI Team concluded that uncertainty in  $V_S$  below 43 m should be captured using multiple base case profiles. The TI Team developed these three  $V_S$  profiles by evaluating the  $V_S$  cumulative distributions for multiple depths using measured  $V_S$ . There were insufficient  $V_S$  measurements in the first subsurface layer to develop a  $V_S$  cumulative distribution; therefore, the lower/upper  $V_S$  in this layer are selected to be consistent with the ratio of base- to lower-case and base- to upper-case velocities from the second layer. The base-, upper-, and lower-case  $V_S$  profiles correspond to approximate probabilities of non-exceedance of 0.08, 0.5, and 0.92 from the cumulative distributions. These probabilities, together with appropriate weights, correspond to a three-point discrete distribution that mimics the continuous  $V_S$  distribution at every depth (Miller and Rice 1983). In other words, using these fractiles and weights results in a good approximation of the distribution moments. Shear-wave velocity

measurements and the base-, upper-, and lower-case  $V_S$  profiles are shown in Figure 5-2. The weights associated with the three velocity profiles are obtained from Miller and Rice (1983) and are rounded to 0.25, 0.50, and 0.25.

The depth to reference rock for these  $V_S$  profiles is based on recorded and interpolated depths to the pre-Cretaceous surface below SRS (Denham, 1999). Based on these data, the elevation of the reference rock was taken as -176 m (a corresponding depth from the surface of 258.6 m). The TI Team determined that including multiple branches in the logic tree for the depth to reference rock was not needed based on an independent interpolation of available data and the limited effect that this range in depths would have on calculated site response. A sufficient number of measured  $V_S$  profiles reached the pre-Cretaceous bedrock; thus, the base-, upper- and lower-case  $V_S$  profiles developed from the measured  $V_S$  values are extended all the way to the bedrock.

The *SAFs* at the SRS are developed with respect to a GMM developed for the reference rock condition at the study site. For this reason, there is no need to include the host  $V_S$  profile in the site response logic tree.

### **Velocity Randomization**

The TI Team developed random  $V_S$  profiles using a lognormal distribution and a first-order autoregressive model described by Silva et al. (1996, see Appendix C of that document) to account for correlation of velocity between successive layers. The approach used by the TI Team to determine lognormal standard deviation values and the interlayer correlation coefficients are described in this section.

The TI Team used the distribution of measured  $V_S$  in each layer of the profile to inform its selection of the lognormal standard deviations used to generate the random  $V_S$  profiles. Based on this selection, the TI Team found a favorable comparison between the cumulative distribution from the measured  $V_S$  compared to the cumulative distribution from the randomly generated profiles. This process results in randomly generated  $V_S$  profiles that are consistent with the range of measured velocities.

The cumulative distribution for the  $V_S$  data is obtained by first assigning a weight to each measured velocity. Measured  $V_S$  are assumed to be equally valid; therefore, the weight is equal to one divided by the number of velocity measurements. The  $V_S$  are then ordered from lowest to highest. A cumulative weight is then calculated for each  $V_S$  as the sum of weights for all velocities less than and equal to each  $V_S$  in the data set. A similar process is used to compute the cumulative distribution for the random  $V_S$ . A total of 180 random  $V_S$  profiles are generated, with 60 random profiles being generated for each velocity base case (lower, base, and upper profiles). The weight assigned to each random velocity profile is equal to  $1/60$  times the velocity branch weight. An example of the  $V_S$  distributions at a depth of approximately 34 m is shown in Figure 5-3. This figure shows the distribution of random  $V_S$  using a layer lognormal standard deviation of 0.05. Although the distribution of  $V_S$  obtained with a lognormal standard deviation of 0.05 appears to be consistent with the  $V_S$  data distribution, a minimum lognormal standard deviation of 0.1 is used for each layer. This minimum value is chosen for the purpose of adequately spreading out the resonant peaks of the 1D analyses. Overall, the combined effects of epistemic uncertainty and aleatory variability in the  $V_S$  profiles should be generally consistent with the available data. In addition to surface measurements that provide a site signature, the TI Team believes that the quantity and quality of data can be used as a basis for constraining

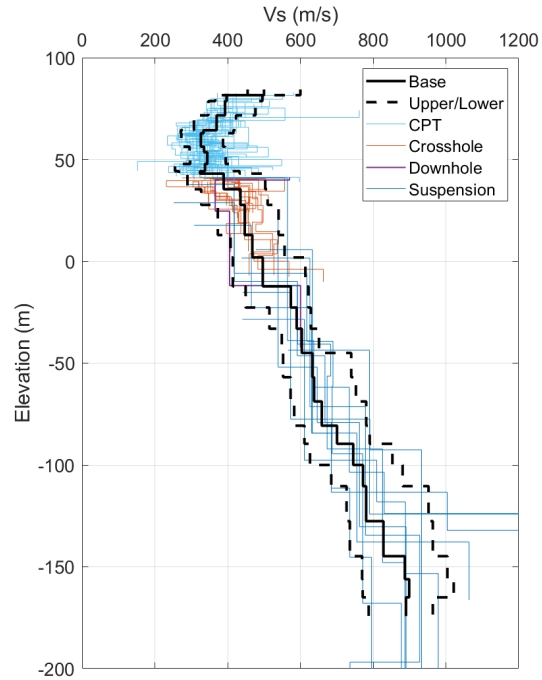


**Figure 5-2 SRS shear-wave velocity profiles from tests and the base-, upper-, and lower-case profiles**

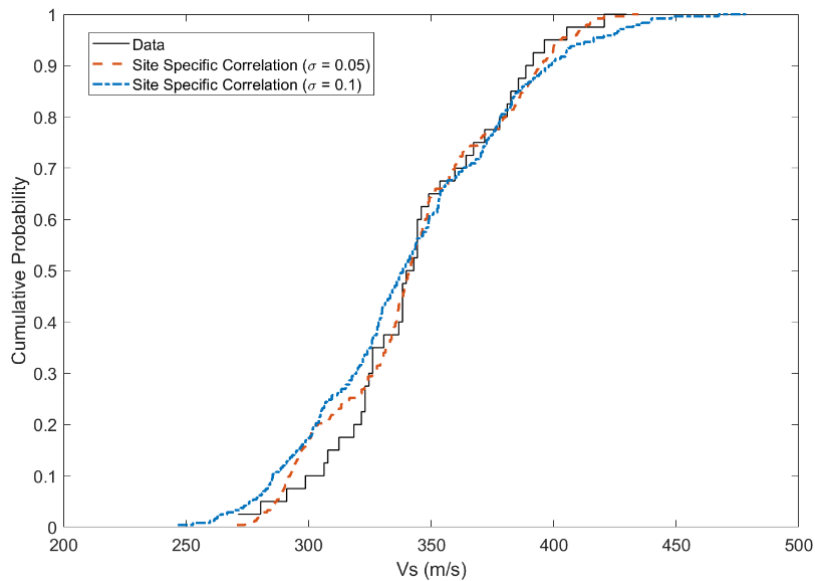


**Figure 5-3 Shear-wave velocity distribution at ~34 m depth from shear-wave velocity measurements (data), and from random velocity profiles developed using the site-specific correlation model for the SRS study site.**

uncertainty and variability. For the case of SRS, implementing a minimum aleatory standard deviation of 0.1 results in some random velocities being less than or greater than the measured  $V_S$  at the site or the site vicinity. One should not expect that the limited number of measurements captures the complete range of velocities; therefore, some  $V_S$  that are moderately outside the limits of the measurements are acceptable. Judgement should be used to verify that these random  $V_S$  are consistent with the site geology. Ultimately, the computed aleatory variability of the measured  $V_S$  (in natural log units) for each layer was used in the randomization process (Figure 5-4), with an imposed minimum value of 0.1. The logarithmic standard deviation values used for each layer are provided in Rodriguez-Marek et al. (2021).

A consensus view of the resource experts at the project workshop is that the development of site-specific correlation models, when possible, is preferable to generic models. The  $V_S$  data at the SRS study site is sufficient to constrain a site-specific correlation model. Therefore, a model for the correlation of the  $V_S$  between two contiguous layers was developed by the TI Team. The model is developed for the correlation of normalized  $V_S$  residuals, where the residuals are obtained using:

$$\varepsilon_{\ln V_S}(z) = \frac{\ln V_S - \mu_{\ln V_S}(z)}{\sigma_{\ln V_S}(z)} \quad (\text{Eq. 5-1})$$

where  $V_S$  is the shear-wave velocity at a given layer with midpoint depth  $z$ ,  $\mu_{\ln V_S}(z)$  is the mean of the velocity at the center of the layer, and  $\sigma_{\ln V_S}(z)$  is the standard deviation of the shear-wave velocity at the center of the layer (both the mean and standard deviation are computed in natural log space). Preliminary observations of the data indicated that the correlation of layers near the surface is different from that at depth. For that reason, separate models were developed for  $z < 22.9$  m and for  $z > 22.9$  m, where the depth of 22.9 m was obtained by trial and error to minimize the misfit between the data and the model, as seen in Figure 5-5. The layer-to-layer correlations are shown in Figure 5-5. The correlation model used is:

$$\rho = \rho_t(\rho_o - \rho_d) + \rho_d \quad (\text{Eq. 5-2})$$

$$\rho_t = \max\left\{1, \exp\left[-\frac{\Delta z - \Delta z_o}{a}\right]\right\} \quad (\text{Eq. 5-3})$$

where  $\rho$  is the correlation of normalized  $V_S$  residuals ( $\varepsilon_{\ln V_S}$ ) of consecutive layers,  $\Delta z$  is the separation distance between the midpoint of the two consecutive layers,  $\rho_o$  is the correlation for two layers at a separation distance less than  $\Delta z_o$ ,  $\rho_d$  is the residual correlation at large separation distances, and  $a$  is a model parameter that indicates the rate at which the correlation decays with increasing separation distance. The model parameters are given in Table 5-1 and the model fit to the data is shown in Figure 5-5.

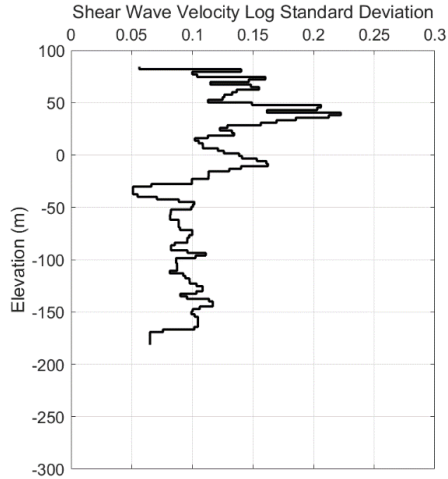


**Figure 5-4** Standard deviation of  $V_S$  (in natural log units) for the SRS study site

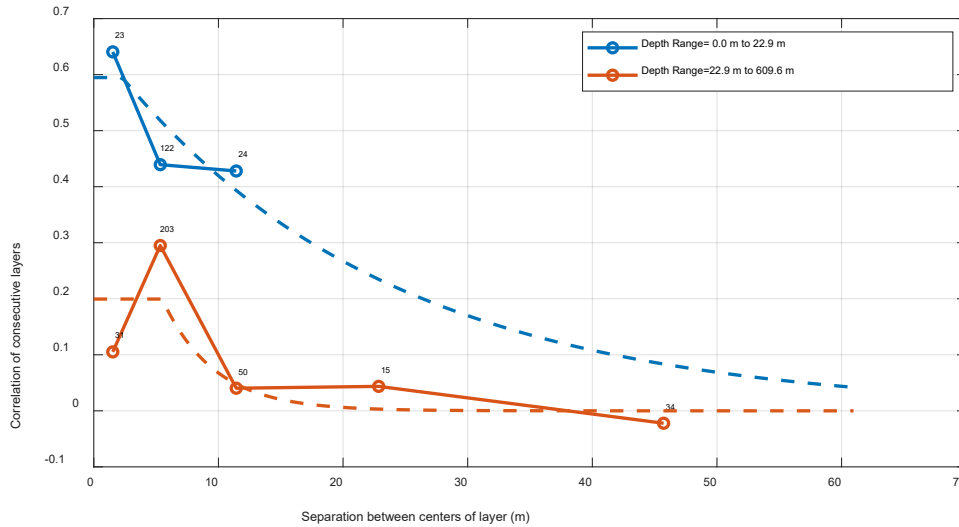


**Figure 5-5** SRS correlation model for normalized  $V_S$  residuals of two consecutive layers. The dots correspond to the sample correlation values from the  $V_S$  data and the dotted lines are the fitted model. Numbers above each dot represent the number of depth pairs that were used to obtain the sample correlation values.

Table 5-1 Parameters for the correlation model for normalized $V_S$ residuals of two consecutive layers				
Depth range for midpoint of top layer	$\rho_o$	$\rho_d$	$a$ (m)	$\Delta z_o$ (m)
0 to 22.9 m	0.59	0	22.2	2.3
> 22.9 m	0.29	0	3.0	5.5

## Thickness Randomization

The TI Team considered two approaches to characterize geologic strata thickness. The first approach consists of using the best estimate strata thickness for each layer (no thickness randomization). These estimates are obtained from the geotechnical information at the study site. The other option is to include some randomization in layer thickness. This option consisted of assuming layer thickness is lognormally distributed. The approach used to obtain the parameters for the lognormal distribution is described below.

The process for randomizing the geologic strata thickness consisted of first recording the strata thickness from each boring log. The TI Team identified ten distinct strata in the upper 41 m of the profile. The TI Team then computed statistics (mean and covariance matrix) of the natural log strata thickness values. Because the boring logs only extend to a depth of approximately 41 m, it is necessary to assume the interlayer correlation for deeper layers as well as the lognormal standard deviation of strata thickness. The TI Team assumed that there was no interlayer correlation between strata below 41 m, and that the lognormal standard deviation was approximately equal to the lognormal standard deviation at a depth of 41 m. Using a multivariate normal distribution with the covariance matrix and log mean thickness values, the TI Team developed correlated random thicknesses. When developing profiles with randomized thickness, the TI Team only accepted random profiles with a depth to reference rock within an acceptable range. The TI Team defined the acceptable range for depth to reference rock as  $258.6 \pm \sim 13$  m based on the spatial interpolation of reference rock elevation at SRS. The randomized  $V_S$  profiles around the lower-, base- and upper-case profiles are shown in Figure 5-6. Although not shown in Figure 5-6, median velocity profiles computed from the 60 random velocity profiles are equivalent to the base case  $V_S$  profiles.

### 5.2.3 $V_S$ Components of Logic Tree for GVDA

Because the one-step approach (Section 3.1) to developing *SAF* is used for the GVDA site, both a host profile consistent with the GMM and site-specific  $V_S$  profiles are needed to appropriately capture the epistemic uncertainty in site amplification. For the GVDA study site, the South-Western United States (SWUS) GMM (Geopantech, 2015) is used for the PSHA calculations. Therefore, the host  $V_S$  profile from the SWUS GMM was selected by the TI Team (Figure 5-7).

For the GVDA site  $V_S$  profiles, the TI Team reviewed the multiple geophysical techniques used over the past three decades to measure the *in situ* shear-wave velocities at GVDA. These techniques include downhole (Gibbs, 1989), *P-S* suspension logging (Steller, 1996), spectral analysis of surface waves (SASW) (Stokoe et al., 2004), multi-channel spectral analysis of surface wave (MASW) (Teague et al., 2018), and micro-tremor array measurements (MAM) (Teague et al., 2018). A unique feature of the GVDA site is the availability of surface and borehole recordings. These recordings were used to evaluate the compatibility of the measured  $V_S$  profiles with the recordings at the site. The TI Team performed this check by comparing the predicted fundamental mode resonant frequency of the measured  $V_S$  profiles with the

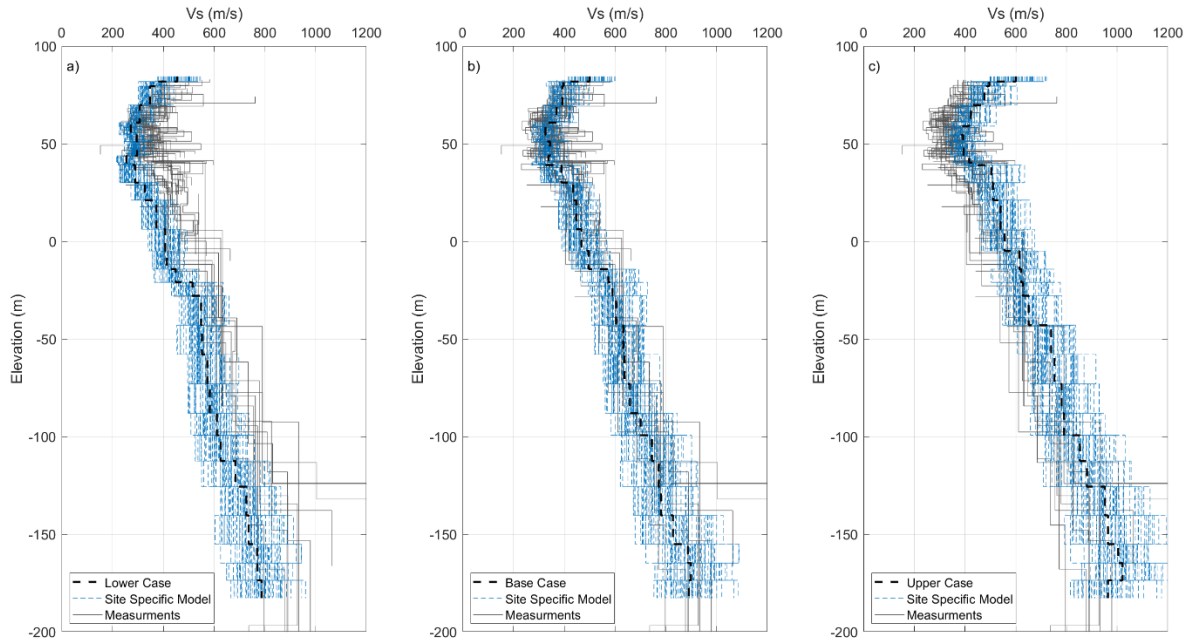


**Figure 5-6 SRS random shear-wave velocity profiles using the site-specific correlation model for the (a) lower case, (b) base case, and (c) upper case epistemic profiles.**

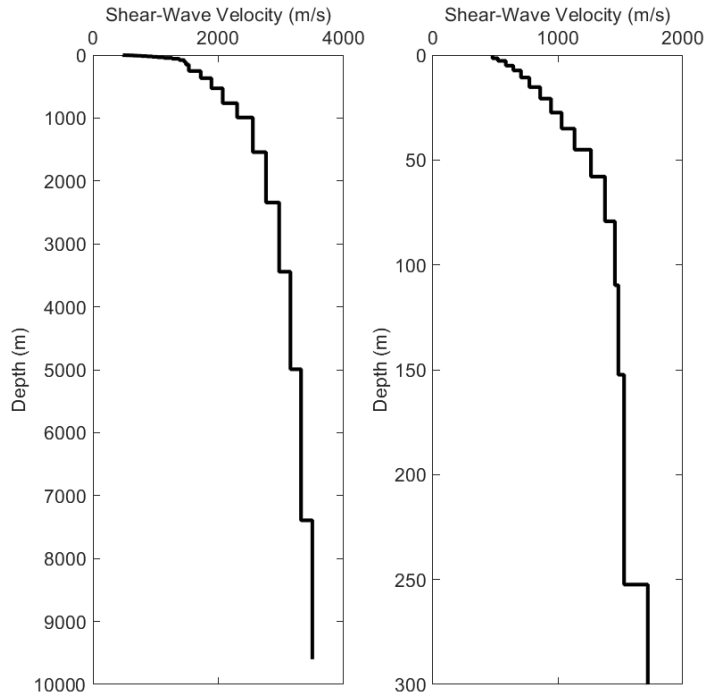


**Figure 5-7 Host profile for the SWUS ground motion model (left). Upper 300 m of the SWUS profile (right).**

fundamental mode of the empirical transfer function. The site's empirical transfer function is computed as the mean of the ratios between the Fourier amplitude at the surface and downhole (150 m depth) for multiple low amplitude motions. Any individual  $V_S$  profile with a predominant frequency inferred from the linear transfer function (computed over a depth of 150 m) that fell outside 2 standard deviations of the predominant site frequency inferred from the site's linear transfer function was considered by the TI Team to be unreliable and excluded from informing the epistemic uncertainty in site amplification. The TI Team considered this an important factor in appropriately constraining the epistemic uncertainty in the site amplification.

Figure 5-8(a) shows the  $V_S$  profiles for the downhole measurements from Gibbs (1989), the *P-S* suspension logging from Steller (1996) and SASW lines 1 and 2 from Stokoe et al. (2004). As seen in the figure, these profiles appear very similar. However, as Figure 5-8(b) shows, the linear transfer function for the *P-S* suspension logging profile has a predominant frequency that falls well outside two standard deviations (black dashed-dot lines) of the predominant frequency inferred from the site's empirical transfer function. Thus, the TI Team chose to exclude the *P-S* suspension logging profile. The TI Team also chose to exclude the SASW velocity profiles because they terminate at depths too shallow to predict the low frequency resonances in the site's linear transfer function. Moreover, the  $V_S$  profiles from SASW lines 1 and 2 are consistent with the downhole profiles; thus, the SASW lines do not add to the epistemic uncertainty at the site.

### **Epistemic Velocity Profiles**

The TI Team chose to build  $V_S$  profiles that capture the epistemic uncertainty in  $V_S$  using the downhole and MASW/MAM measurements. The downhole profile of Gibbs (1989) was developed using a surface air-powered horizontal traction device that generated shear-wave pulses that were recorded at interval depths within the downhole by a three-component geophone. Recordings were logged at interval depths of 2.5 m between the surface and 40 m depth. After a depth of 40 m, recordings were logged every 5 m until the bottom of the borehole was reached at 100 m depth. Travel time plots were generated that exhibited a shear-wave velocity profile consisting of three distinct layers (Figure 5-8(a)). The fundamental mode of the linear transfer function of the downhole  $V_S$  profile falls within two standard deviations of the site's empirical transfer function (Figure 5-8(b)).

The MASW/MAM velocity profiles from Teague et al. (2018) were inverted from dispersion data collected at three locations (North, Central and South) spanning the GVDA site (Figure 5-9). At each location, inversions of the combined MASW and MAM dispersion data were performed using seven alternative layering ratios, allowing for alternative layering models to be evaluated. The layering ratio (Cox and Teague, 2016) is a parameter that controls the potential change in thickness from adjacent layers in the inversion process: the lower the value of the parameter, the larger the number of layers that generally result from the inversion process. For each layering ratio, 33 inverted  $V_S$  profiles were generated whose forward modeled dispersion on average fit the experimental dispersion data. Figure 5-10 shows the inverted profile for the Central location. Profiles for the other locations are shown in Teague et al. (2018). In total, 594  $V_S$  profiles were inverted. For each of the inverted profiles, the fundamental mode of the linear transfer function was shown to agree well within the site's empirical transfer function (Teague et al., 2018); therefore, the TI Team chose to include all of the layering ratios within the site response logic tree.

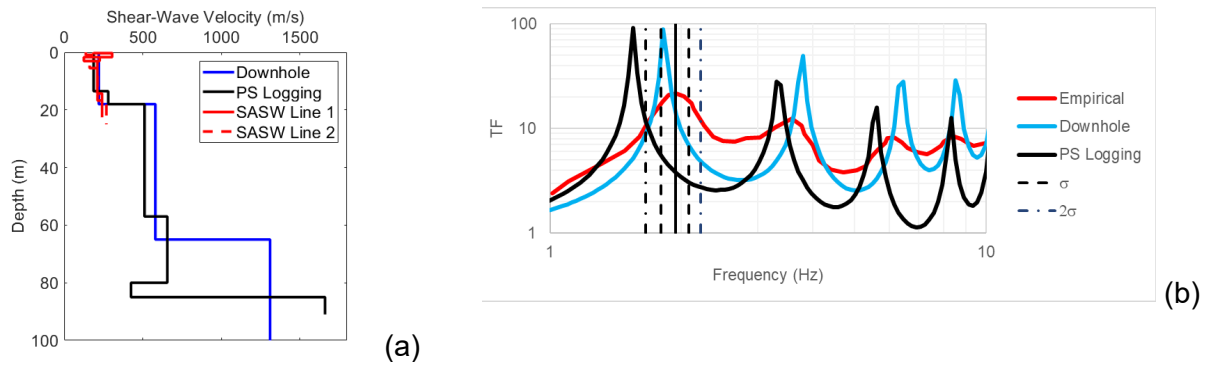


Figure 5-8 (a) Downhole, *P-S* suspension logging and SASW profiles for GVDA, (b) Comparison of linear transfer functions for the downhole and *P-S* suspension logging with the mean empirical transfer function.

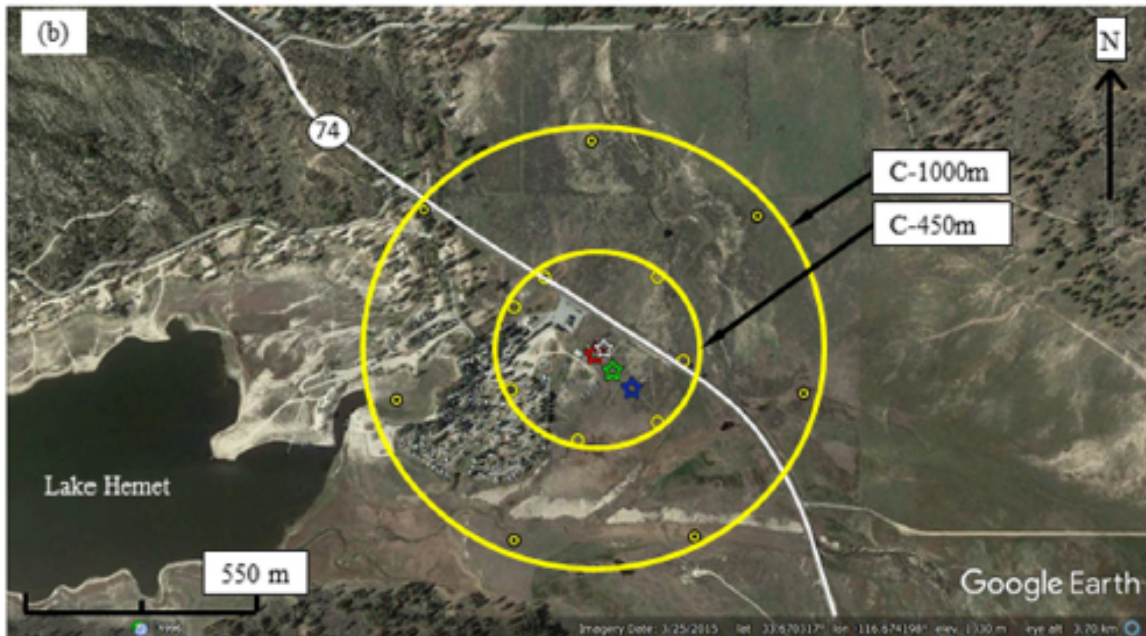
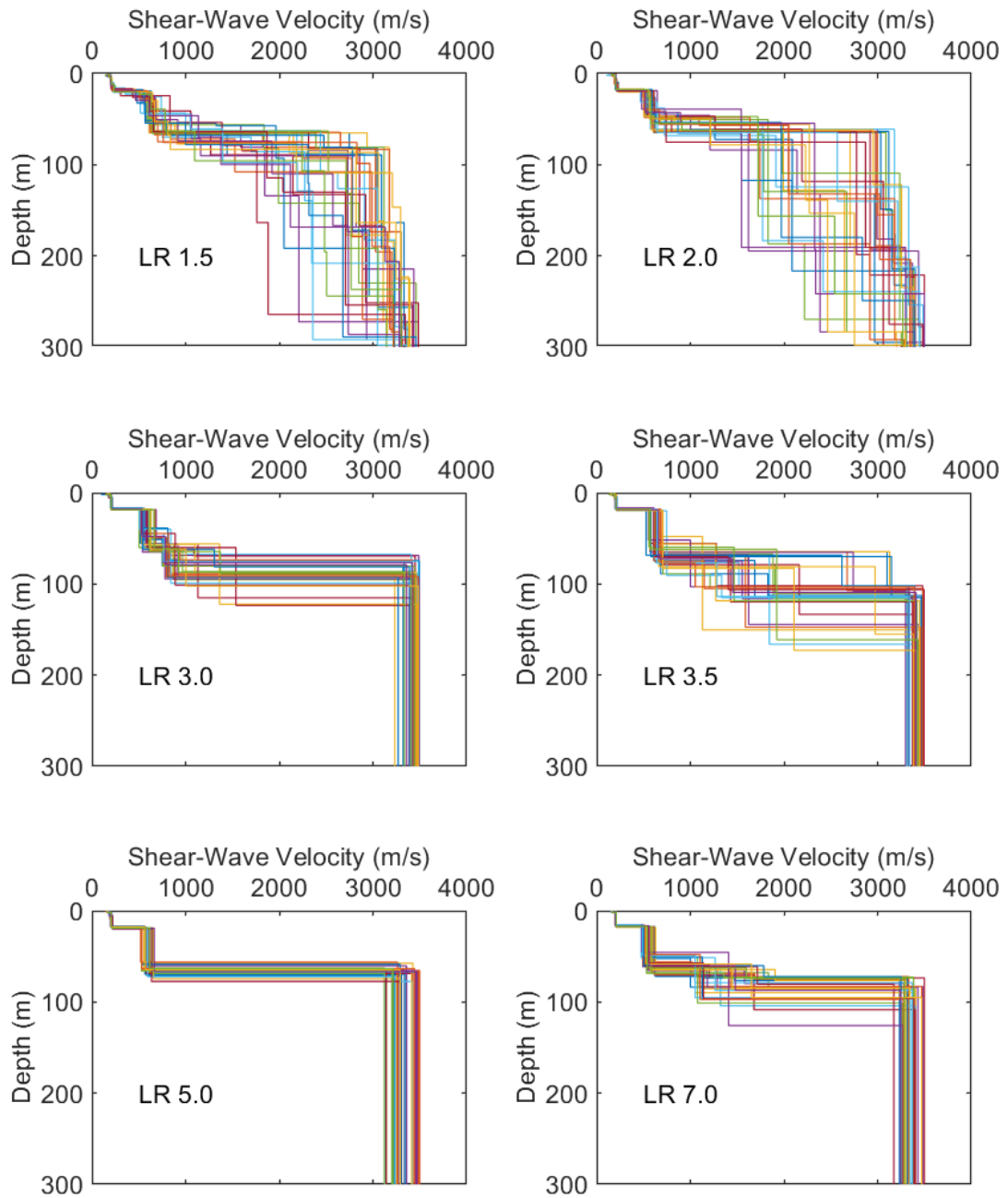


Figure 5-9 Location of MAM arrays used by Teague et al. (2018) to characterize the GVDA site



**Figure 5-10** Inverted MASW/MAM profiles from dispersion data collected at GVDA's central location for each layering ratio

For the assignment of weights to the downhole and the MASW/MAM branches of the logic tree, the TI Team took into consideration the fact that the MASW profile represents an average profile over the entire site, while the downhole profile is only a representation of the  $V_S$  profile at a point. Therefore, the TI Team considered that the MASW/MAM profiles are a better representation of the site  $V_S$  profile and assigned a weight of 0.75 for this profile, and 0.25 for the downhole profile. The alternative layering ratios used in the inversion of MASW/MAM profiles each received equal weight, since each layering ratio resulted in similar dispersion misfit values between the experimental data and their resulting theoretical dispersion curves (Teague et al., 2018).

## Velocity Randomization

For the profiles generated from MASW/MAM, the TI Team decided that the suite of 594 inverted profiles collectively captured both the spatial variability across the site and epistemic uncertainty in  $V_S$ . The spatial variability was captured in measuring dispersion across the GVDA site (North, Central and South locations) while the epistemic uncertainty was captured through the alternative layering ratios used for inversion of the dispersion data.

For the downhole profile, the statistical distribution and correlation between layering and  $V_S$  proposed by Toro (1995) was used for the generation of 60 random profiles to capture the aleatory variability. However, since only a single borehole and limited geotechnical data for the site are available, it was not clear to the TI Team the appropriate standard deviation ( $\sigma_{\ln V_S}$ ) from the Toro (1995) procedure that would accurately represent the aleatory variability of the site. Therefore, the TI Team decided to generate random velocity profiles using alternative  $\sigma_{\ln V_S}$  values whose forward modeled dispersions were constrained by the standard deviation of the experimental dispersion data across all three locations. For an individual  $\sigma_{\ln V_S}$  value, a set of 60 random profiles were generated. If all the resulting forward modeled dispersion curves fit on average within two standard deviations of the experimental dispersion data, then the TI Team considered the set of randomized profiles representative of the site. This process was repeated over multiple  $\sigma_{\ln V_S}$  values to determine the  $\sigma_{\ln V_S}$  value that would afford the largest variability in shear-wave velocities while still constrained by the experimental dispersion data. The TI Team believed that this was the best approach to assigning a reasonable level of aleatory variability while ensuring the generation of realistic velocity profiles used in the determination of site amplification. Figure 5-11 displays the forward modeled dispersions of 60 randomized profiles derived using a  $\sigma_{\ln V_S}$  of 0.15. Also plotted are error bars depicting two standard deviations of the bounded experimental dispersion data. This value was found to be the largest value that produced randomized shear-wave velocities whose forward modeled dispersions fell within two standard deviations of the experimental dispersion data.

Because the one-step approach to *SAF* is used for GVDA, each of the MASW/MAM and randomized downhole profiles must be extended to the bedrock location (9.6 km depth) of the SWUS host profile. The TI Team accomplished this by extending the depth of the last layer in each MASW/MAM and randomized downhole profile to the depth in the SWUS host profile where the  $V_S$  of the host profile equals that of the last layer in each profile. Past this depth, each profile would then inherit the velocity profile of the SWUS host profile until the bedrock is reached. Figure 5-12 shows an example of this procedure using the MASW/MAM inverted profiles for the North location with a layering ratio of 3.5.

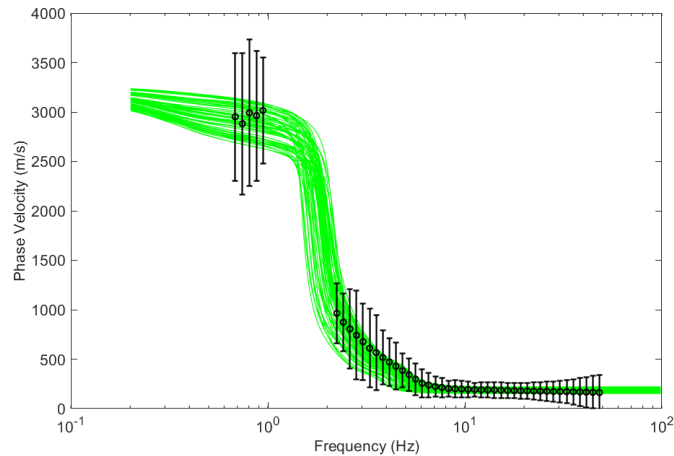


**Figure 5-11 Forward-modeled dispersions of 60 randomized shear-wave velocity profiles (green) generated using a  $\sigma_{\ln V_s}$  of 0.15. Black error bars represent two standard deviations of the bounded experimental dispersion data across the north, south and central locations.**

### 5.3 Kappa

#### 5.3.1 Issues Related to Developing Kappa Logic Tree

The spectral decay factor kappa ( $\kappa$ ) was introduced by Anderson and Hough (1984) to describe the high frequency decay of ground motions. At short distances from the source, the high-frequency decay is considered by the TI Team to be influenced exclusively by site effects; in these cases,  $\kappa$  is commonly referred to as the “site kappa” and is denoted by  $\kappa_0$ . Estimated values of  $\kappa_0$  are used to constrain the small-strain damping profiles used in site response analyses.

Alternative approaches to evaluate  $\kappa_0$  at a site are reviewed by Ktenidou et al. (2014). For this project, at GVDA, the value of  $\kappa_0$  was obtained from the measured surface ground-motion Fourier amplitude spectra (FAS) recorded at the study site. In contrast, no records are available at SRS, and therefore  $\kappa_0$  was obtained from empirical models. For both study sites, the true value of  $\kappa_0$  is not necessarily known and its uncertainty is captured by the TI Team as part of the site response logic tree. Because  $\kappa_0$  is considered a site effect, the TI Team only considered the epistemic uncertainty in  $\kappa_0$ . The aleatory component of  $\kappa_0$ , which is highly influenced by the variability in ground motions, is assumed to be captured by the aleatory component of the GMM. The following subsections provide more detail on the models and methods used to estimate the distribution of  $\kappa_0$  for both project sites, and the approach adopted to use the estimated value of  $\kappa_0$  to distribute small strain damping in the site profiles.

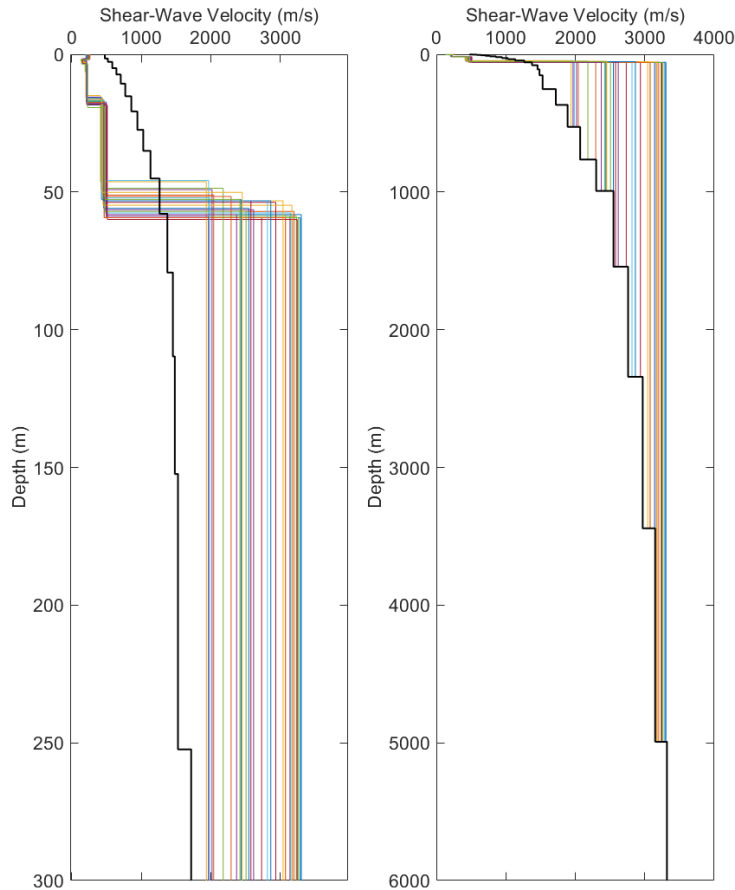


**Figure 5-12 Example combining MASW/MAM profiles (colored lines) with SWUS host profile (black line). Left shows the upper 300 m. Right shows how each inverted profile is connected into the SWUS host profile at a depth where the shear-wave velocity of the host profile equals that of the last layer in an individual inverted profile.**

### 5.3.2 Kappa Components of the Logic Tree for SRS

For the SRS study site, no on-site ground-motion data is available for the estimation of  $\kappa_0$ . Therefore, the TI Team chose to investigate alternative empirical relationships for the estimation of  $\kappa_0$  and its epistemic uncertainty. The TI Team chose four relationships for the alternative approaches in correlating site properties to estimate  $\kappa_0$  because they span the range of observations reported in the literature. The four models selected by the TI Team are (i) the  $V_{S30} - \kappa_0$  correlation model of Van Houtte et al. (2011), where  $V_{S30}$  is the average shear-wave velocity over the top 30 m of a profile; (ii) the  $V_{S30} - Z_{2.5} - \kappa_0$  correlation model of Xu et al. (2020), where  $Z_{2.5}$  is the depth to the  $V_S = 2.5$  km/s horizon; (iii) direct calculation of  $\kappa_0$  from  $V_S$  and small-strain damping ( $D_{min}$ ) profiles with the damping taken from the  $Q_{ef} - V_S$  relationships (Model 1) from Campbell (2009), where  $Q_{ef}$  is the effective quality factor and is related to small-strain damping by  $Q_{ef} = 1/(2D_{min})$ ; and (iv) direct calculation of  $\kappa_0$  from  $V_S$  and  $D_{min}$  profiles using Model 3 from Campbell (2009) to compute damping.

The  $\kappa_0$  values associated with the base case shear-wave velocity profile for each of the empirical models are presented in Table 5-2. Xu et al. (2020) reported a lognormal standard

deviation for their model of 0.22. Standard deviations for the other models listed in Table 5-2 are not known. The TI Team developed a kappa logic tree by dividing the models listed in Table 5-2 into two groups:  $Q_{ef}$  models and  $V_S$  models with each model subsequently considered as a separate branch in the logic tree (Figure 5-13). The TI Team assigned weights to the two groups of models and to each empirical model within these groups. These weights are informed by the data used to develop the empirical models. Van Houtte et al. (2011) and Xu et al. (2020) primarily used the Japanese Kik-net database to develop models for estimating  $\kappa_0$ . The data used by Van Houtte et al. (2011) considered profiles with  $V_{S30}$  ranging between approximately 500 and 2000 m/s; whereas, Xu et al. (2020) considered profiles with  $V_{S30}$  ranging between 111 and 559 m/s. Although Van Houtte et al. (2011) did not consider sites with  $V_{S30}$  less than 500 m/s, their  $\kappa_0$ - $V_{S30}$  model at lower  $V_{S30}$  values is consistent with data from Chandler et al. (2006) and Silva and Darragh (1995) which do include  $V_{S30}$  values as low as approximately 325 m/s. Site kappa values reported by Xu et al. (2020) range between 0.047 and 0.095 s for profiles with  $V_{S30}$  between 364 to 412 m/s, a narrow velocity range that includes the SRS  $V_{S30}$  of 375 m/s. The  $Q_{ef}$  models reported by Campbell (2009) are associated with central and eastern North America (CENA) velocity profiles (e.g., Boore and Joyner 1991; Cramer et al. 2004), and thus are considered by the TI Team to be more consistent with the SRS study site. Therefore, the TI Team assigned more weight to the  $Q_{ef}$  model group. However, the TI team was not able to preclude the higher  $\kappa_0$  values from the models that rely on  $V_{S30}$ . As such, the  $V_S$  models were assigned an overall weight of 0.35 by the TI Team, while the two  $Q_{ef}$  models were given a weight of 0.65. Because the  $V_S$  model developed by Xu et al. (2020) incorporates more site information into the  $\kappa_0$  estimate compared to the Van Houtte et al. (2011) model, the TI Team assigned greater weight to the Xu et al. (2020) model. The two  $Q_{ef}$  models were weighted equally.

An additional five branches were then associated with each model to incorporate uncertainty in the empirical relationship. The five branches extending from each model are assumed to represent a discrete lognormal distribution with a standard deviation of 0.22. This standard deviation is obtained from the Xu et al. (2021) model. This logic tree is illustrated in Figure 5-13. The  $\kappa_0$  logic tree illustrated in Figure 5-13 results in 20  $\kappa_0$  values and associated weights. The TI Team used these 20  $\kappa_0$  values and weights to develop a discrete  $\kappa_0$  distribution, which the TI Team then resampled using the approach from Miller and Rice (1983) to reduce the distribution to five representative values and associated weights. These  $\kappa_0$  values and weights are listed in Table 5-3.

<b>Model</b>	<b>Site Kappa (<math>\kappa_0</math>) (sec)</b>
Campbell (2009) Model 1	0.027
Campbell (2009) Model 3	0.036
Xu et al. (2020) $V_{S30}$ and $Z_{2.5}$	0.053
Van Houtte et al. (2011) $V_{S30}$	0.061

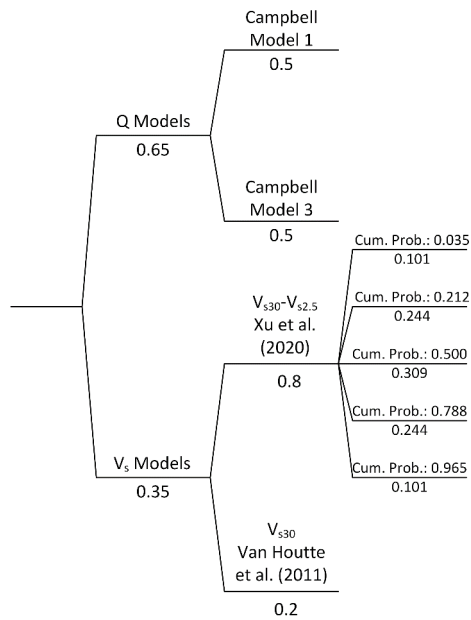


**Figure 5-13 Logic tree used to develop cumulative kappa distribution and representative five-point distribution for use in site response logic tree for SRS. Values below branches are the branch weights.**

<b>Site Kappa, <math>\kappa_0</math> (sec)</b>	<b>Weight</b>
0.021	0.10108
0.026	0.24429
0.036	0.30926
0.052	0.24429
0.076	0.10108

### 5.3.3 Kappa Components of Logic Tree for GVDA

For GVDA, multiple on-site low-amplitude ground motion recordings were used in the estimation of  $\kappa_0$ . The TI Team selected ground motions from events with moment magnitudes of 3.5 or greater with source-to-site distances less than 100 km. All ground-motion data used were extracted from the Network for Earthquake Engineering Simulations (NEES) data portal (<http://nees.ucsb.edu/data-portal>). A multi-step process was applied by the TI Team to each candidate ground motion retrieved from the data portal. First, a baseline correction was applied using a 1<sup>st</sup> order polynomial. Then, the motion was filtered using a 10<sup>th</sup> order Butterworth bandpass (1 to 50 Hz) to avoid aliasing effects. To avoid inclusion of possible surface waves into the analyses, a 5-second data window was selected by the TI Team from the ground-motion record beginning 1 second before the S-wave arrival. The TI Team selected a similar 5-second window from the end of the ground-motion record and the signal to noise ratio (SNR) between the two windows was computed. The TI Team required both horizontal components of individual ground motions to have an SNR of at least 3 dB. For those records satisfying the SNR criteria, the TI Team applied a fast Fourier transform (FFT) to the window containing the S-wave for the development of a FAS. Meeting the above criterion resulted in 110 ground motions available for the estimation of  $\kappa_0$ .

The TI Team used the Anderson and Hough (1984) approach for the estimation of  $\kappa_0$ . In this approach, individual estimates of  $\kappa$  are made for each record by measuring the slope of the logarithm of the FAS versus frequency [ $\ln A(f)$ ] over a selected frequency band. Anderson and Hough (1984) observed that if the estimates of  $\kappa$  for various records at a given station are plotted versus epicentral distance (R), the resulting plot is a linear relationship that can be written as:

$$\kappa = \kappa_0 + \kappa_r R \quad (\text{Eq. 5-4})$$

where  $\kappa_r$  results from regional attenuation effects and the intercept ( $\kappa_0$ ) represents the impact of site effects on  $\kappa$ . Figure 5-14 shows two examples of a linear regression on  $\kappa$  for the determination of  $\kappa_0$  and  $\kappa_r$  at GVDA for both the downhole (150 m depth) and surface locations.

There are several factors that contribute to the uncertainty in estimated  $\kappa_0$  values at a site. These factors include:

- Choice of frequency band to represent the linear portion of the  $\ln A(f)$  for the determination of the value of  $\kappa$  for each ground motion recording.
- Uncertainties in the regressions used to estimate the value of  $\kappa$  for each ground motion record for a given choice of frequency band [i.e., regression of  $\ln A(f)$ ]. Note that this uncertainty is also a function of the selected frequency range, since the frequency range controls the number of points involved in the regression.
- Uncertainties in the regression of  $\kappa$  versus distance (Eq. 5-4).

The GVDA site has both surface and borehole instruments. In principle, regional attenuation effects should be the same whether they are obtained from surface or borehole instruments. Therefore, values of  $\kappa_r$  estimated with surface or borehole records should be similar. Differences in the surface and borehole  $\kappa_r$  are the result of the uncertainties described above, or possibly due to additional unidentified uncertainties.

The TI Team derived an approach to systematically account for the uncertainties listed above. The approach is described in detail in Appendix D. A summary of the approach is presented in Table 5-4 and in the following paragraphs.

The lower end of the frequency bandwidth (15 Hz) in Step 2 of Table 5-4 was chosen to ensure the slope of the  $\ln A(f)$  vs.  $f$  was evaluated above the corner frequency of the selected ground motions and to avoid any influence from site resonances. The 45 Hz ceiling prevented the slope of the  $\ln A(f)$  versus  $f$  from being computed at frequencies affected by the bandpass Butterworth filter. The fitness function is described in detail in Appendix D.

With weights assigned to each  $\kappa_0$  distribution (Step 4 in Table 5-4), the approach defined by Miller and Rice (1983) was used by the TI Team to reduce the set of 34 weighted  $\kappa_0$  distributions to a representative five-point distribution to be used in the site response logic tree. Figure 5-15 shows the cumulative distribution function for the weighted median  $\kappa_0$  values from each  $\kappa_0$  distribution (red line) and the resulting Miller and Rice (1983) five-point distribution values (black dots). The five-point distribution values are also listed in Table 5-5. The values for  $\kappa_0$  in Table 5-5 show reduced uncertainty in  $\kappa_0$  compared to SRS, which uses a range of empirical relationships to define the uncertainty in  $\kappa_0$ .

### 5.3.4 Depth Partitioning of Kappa and Damping

The  $\kappa_0$  is a phenomenological parameter that captures the impact of attenuation on the high-frequency component of the FAS for low-intensity ground motions. In linear 1D site response (i.e., for low-intensity input motions), energy attenuation occurs only as a result of the equivalent viscous damping assigned to the soil column. For that reason, the cumulative impact of small-strain damping ( $D_{min}$ ) must be compatible with the assigned values of  $\kappa_0$  for each site.

The additional kappa,  $\Delta\kappa$ , that results from small-strain damping over a soil profile with  $n$  discrete layers can be computed as (Cabas et al., 2017)

$$\Delta\kappa = \sum_{i=1}^n \frac{2D_{min,i} \cdot z_i}{V_{Si}} \quad (\text{Eq. 5-5})$$

where  $z_i$ ,  $V_{S,i}$ , and  $D_{min,i}$  are the thickness, shear-wave velocity, and small-strain damping, respectively, of layer  $i$ .

A common approach is to assign the small-strain damping to shallow layers according to the low-strain damping implicit in the damping vs. shear strain curves for the modulus reduction and damping (MRD) models adopted for each soil layer. For deeper layers, the assigned value of  $D_{min}$  must be selected such that the  $\Delta\kappa$  over the full profile is consistent with the  $\kappa_0$ . This can be written as

$$\kappa_0 = \Delta\kappa_{shallow} + \Delta\kappa_{deep} + \kappa_{input} \quad (\text{Eq. 5-6})$$

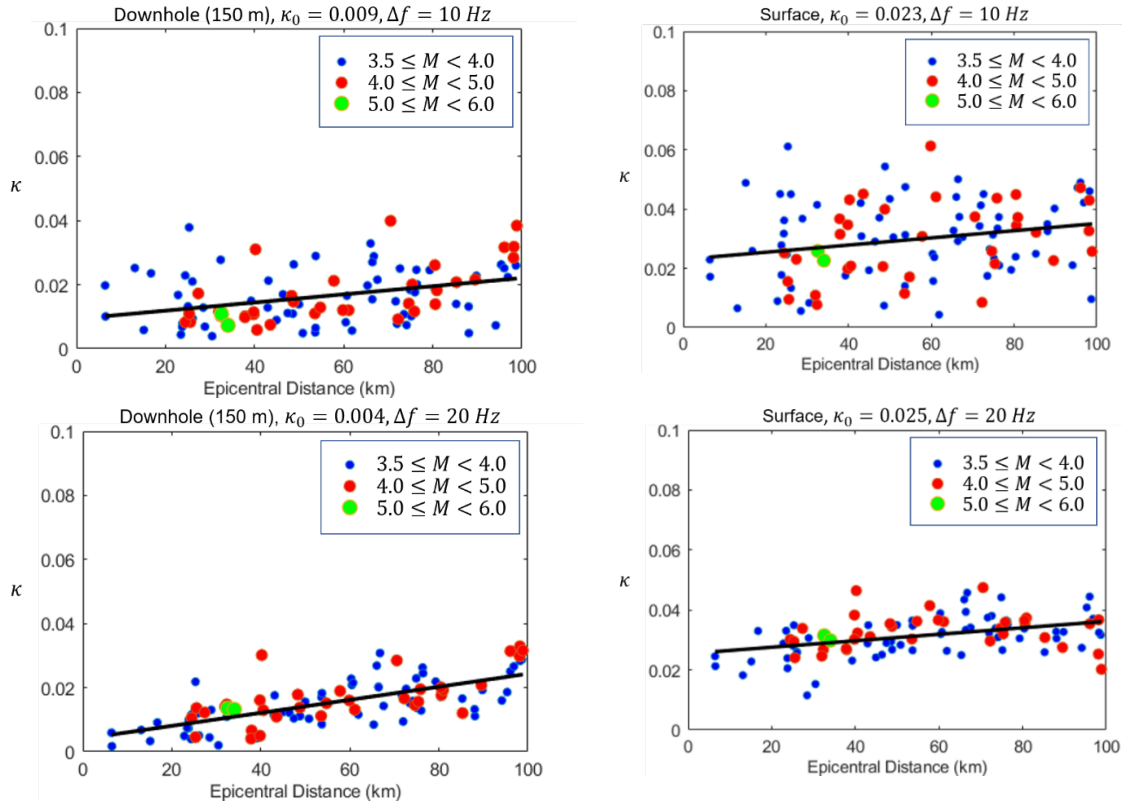


**Figure 5-14 Comparison of surface versus downhole (150 m depth)  $\kappa_r$  slopes computed from frequency bands of 25 Hz to 35 Hz (top) and 25 Hz to 45 Hz (bottom)**

<b>Table 5-4 Summary of approach used to quantify epistemic uncertainty in <math>\kappa_0</math></b>		
<b>Step</b>	<b>Uncertainty Source</b>	<b>Approach</b>
1	Frequency range to represent the linear portion of $\ln A(f)$	Sample different frequency bandwidths that cover frequencies between 15 Hz and 45 Hz. Four different frequency bandwidths were used ( $\Delta f = 15\text{Hz}$ , $\Delta f = 20\text{Hz}$ , $\Delta f = 25\text{Hz}$ , and $\Delta f = 30\text{Hz}$ ). When possible, these bands were shifted in 1 Hz increments to cover the full range from 15Hz to 45 Hz. The total number of frequency bands sampled was 34.
2	Uncertainty in the regression of $\ln A(f)$	Use a Bayesian regression over each frequency band sample from Step 1 to obtain a distribution of $\kappa$ for each selected ground motion.
3	Uncertainty in the regression of Eq. 5-4 ( $\kappa = \kappa_0 + \kappa_r R$ )	For each frequency band sample (Step 1), draw a random sample of $\kappa$ from the distributions obtained in Step 2 using a Markov chain Monte Carlo (MCMC) approach, then perform a linear regression on Eq. 5-4. The results are 34 sample distributions of $\kappa_0$ and $\kappa_r$ values.
4	Differences in $\kappa_r$ using surface and borehole records	Develop a fitness function $F_i$ to define weights for each of the 34 $\kappa_0$ distributions in Step 3. The fitness function rewards the estimates of $\kappa_0$ for which the surface and bedrock $\kappa_r$ have similar values. Branch weights are defined as $W_i = \frac{F_i}{\sum F_i}$ , where the subscript $i$ denotes the sample frequency band (Step 1).

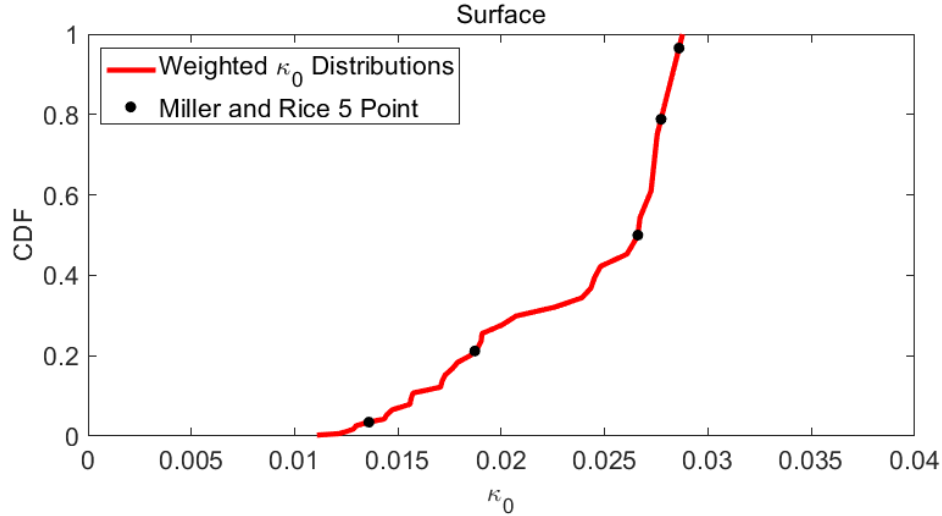


**Figure 5-15 Cumulative distribution of weighted  $\kappa_0$  values and representative five-point distribution values from Miller and Rice (1983).**

$\kappa_0$	Weight
0.0136	0.1011
0.0187	0.2433
0.0266	0.3093
0.0277	0.2443
0.0286	0.1011

where  $\Delta\kappa_{shallow}$  is obtained from Eq. 5-5 using the  $D_{min}$  values assigned to the shallow layers though the MRD curves,  $\Delta\kappa_{deep}$  is the additional kappa that results from the small-strain damping of the deeper portion of the profile, and  $\kappa_{input}$  (0.006 s) is the zero-distance kappa implicit in the input ground motion at the base of the profile. To be consistent with  $\Delta\kappa_{deep}$ , the damping profile in the deeper portion of the site is constrained such that  $Q_{ef} = \gamma \cdot V_s$ , where  $\gamma$  is a proportionality constant. The small-strain damping for the deeper portion of the profile can then be obtained by solving for  $\gamma$  using

$$\Delta\kappa_{deep} = \sum_{j=1}^N \frac{z_j}{\gamma \cdot (V_{s,j})^2} \quad (\text{Eq. 5-7})$$

where the index  $j$  indicates the layers of the deep portion of the profile. Note that the small-strain damping of each layer can then be obtained as

$$D_{min,j} = \frac{1}{2Q_j} = \frac{1}{2\gamma \cdot (V_{s,j})} \quad (\text{Eq. 5-8})$$

An alternative approach is used to assign small-strain damping to the deep layers for the SRS study site. Given the  $\kappa_0$ , shallow kappa ( $\Delta\kappa_{shallow}$ ) associated with the small-strain damping

from the laboratory damping curve, and the kappa associated with the reference rock ( $\kappa_{input}$ ), Eq. 5-6 is rearranged to solve for  $\Delta\kappa_{deep}$ . A constant small-strain damping value is then assigned to the deeper layers that will produce  $\Delta\kappa_{deep}$ . This small-strain damping value is computed using Eq. 5-9.

$$D_{min} = \frac{\Delta\kappa_{deep}}{\sum_{j=1} 2 \cdot z_j / V_{s,j}} \quad (\text{Eq. 5-9})$$

As demonstrated in Section 6, the distribution of small-strain damping is not expected to produce significant differences in site response as long as small-strain damping from all layers in the profile plus the input kappa add up to equal  $\kappa_0$ .

For the GVDA study site, the above procedure is applied to both the host and target profile to distribute  $\kappa_0$  as  $D_{min}$  over the entire profile. In the computation of the *SAF*, care must be taken that the implicit zero-distance kappa of the input motions ( $\kappa_{input}$ ) is the same for the input motions used for the host and target profiles. A relevant question is how to separate the shallow and deep part of the profiles in the above procedure. A sensitivity study to this effect was conducted for the SRS study site and is presented in Section 6. The sensitivity study showed that the resulting *SAFs* are not sensitive to this choice.

## 5.4 Modulus Reduction and Damping

### 5.4.1 Issues Related to Developing a Logic Tree for Modulus Reduction and Damping Curves

MRD curves are used in EQL analyses to capture the effects of non-linear soil behavior. MRD curves are used in non-linear analyses to determine constitutive model parameters that will reproduce equivalent modulus reduction and damping. In this project, the TI Team used multiple sets of MRD curves to capture epistemic uncertainty. When necessary, the MRD curves are modified at large strains so shear stresses are consistent with the soil shear strength. The TI Team captured the aleatory variability that results from spatial variability in MRD curves via a randomization approach of the MRD curves. A general discussion of issues relating to the implementation of MRD curves is provided below.

#### ***Epistemic Uncertainty***

Analysts commonly use more than one set of MRD curves [such as those from EPRI (1993), Darendeli (2001), and curves from site-specific laboratory testing] to capture epistemic uncertainty in the soil nonlinear behavior. The quantity and quality of laboratory cyclic shear tests informs the selection of MRD curves and the associated epistemic uncertainty. In cases where there is little or no laboratory testing, MRD curves are chosen to provide reasonable bounds for nonlinear behavior. This can result in significantly different MRD curves and large differences in site response. In cases with many high quality cyclic shear tests, the differences in alternative MRD curves reduces significantly.

The TI Team used two branches in the site response logic tree to incorporate epistemic uncertainty in the MRD curves for both the SRS and GVDA study sites. Laboratory cyclic shear testing data is available and used to define site-specific MRD curves for both sites. In addition, both sites implement generic MRD curves as alternatives to the site-specific curves.

### ***Shear Strength Correction***

Laboratory tests used to define modulus reduction curves are typically limited to shear strains near 0.3%. These strains are not sufficient to fully mobilize the soil shear strength (Gingery and Elgamal, 2013). As a result, modulus reduction curves may produce biased shear stress estimates at large strain (e.g., Yee et al., 2013). Yee et al. (2013) developed a procedure to modify the modulus reduction curve so that associated stresses are consistent with the soil shear strength at large strains. The TI Team implemented the Yee et al. (2013) procedure to adjust modulus reduction curves in the site response analyses.

The Yee et al. (2013) procedure uses a hyperbolic function to calculate the modulus reduction curve at strains greater than a transitional shear strain. The MRD curve is only modified in the Yee et al. (2013) procedure beyond this transition strain. When implementing the Yee et al. (2013) procedure, the TI Team found that the procedure produced modulus reduction curves that indicated brittle soil behavior when the estimated shear strength of the soil was significantly less than the strength implied by the laboratory modulus reduction curve. Brittle behavior is inconsistent with curves developed from laboratory tests on similar soils at similar confining stresses. In limited cases, the TI Team increased the estimated shear strengths in some layers to obtain modulus reduction curves consistent with laboratory tests at strains up to 0.3%. Figure 5-16 shows two examples where the TI Team implemented the Yee et al. (2013) procedure to modify the modulus reduction curve. Example 1 is a case where the soil shear strength is considerably less than the large-strain stress obtained from the modulus reduction curve. Example 1 illustrates the issue described above where the strength-corrected modulus reduction curve is not consistent with laboratory test observations. In this case, there is a significant kink in the modulus reduction curve, which may be indicative of brittle behavior [strength corrected (a)]. Increasing the shear strength removes the kink [strength corrected (b)]. Example 2 is a case where the soil shear strength is greater than the large-strain stress associated with the modulus reduction curve. For this case, the modulus reduction curve has a more realistic shape, with the strength-corrected curve simply flattening out at large strains.

### ***Aleatory Variability***

When randomizing MRD curves, the TI Team adopted the logit function approach used in the Seismic Evaluation Guidance SPID for the Resolution of Fukushima Near-Term Task Force Recommendation 2.1: Seismic (EPRI, 2013) and the Hanford Sitewide Probabilistic Seismic Hazard Analyses Report (Coppersmith et al., 2014). The TI Team assumed the modulus reduction curves are negatively correlated with the damping curves and used a correlation coefficient of -0.5. When generating randomized curves, the TI Team used a multivariate normal distribution with this negative correlation coefficient to generate correlated random epsilon values, where epsilon has a mean of zero and a standard deviation of one. These correlated random variables ( $\varepsilon_1, \varepsilon_2$ ) are used to define sets of MRD curves. The TI Team multiplied the random epsilon values by the MRD curve standard deviation and added this value to a transformed median MRD curve to obtain the randomized curve, as described below.

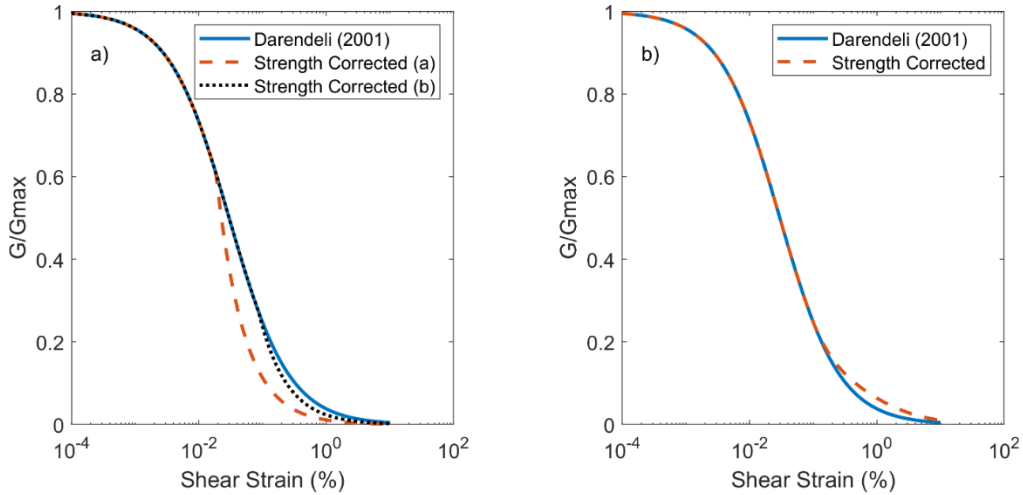


**Figure 5-16 Illustration of the effects of strength correction on the modulus reduction curve, (a) Example 1 where shear strength is less than the curve large strain stress and (b) Example 2 where the strength is greater than the large-strain stress.**

This SPID (EPRI, 2013) procedure for randomizing the modulus reduction curve uses a logit function (James et al. 2017) to transform the modulus reduction curve into a linear function using Eq. 5-10. This linear function is then randomized using Eq. 5-11. In Eq. 5-11,  $\varepsilon_1$  is a random value from the multivariate normal distribution and  $\sigma_{\ln_G}$  is the modulus reduction curve lognormal standard deviation. When randomizing the linear function, the random perturbation ( $\varepsilon_1 \times \sigma_{\ln_G}$ ) is multiplied by a factor to ensure that the randomized curves standard deviation is equal to  $\sigma_{\ln_G}$  at a reference strain where  $G/G_{max}$  is equal to 0.5. The randomized function is transformed back into the original hyperbolic form for the site response analyses using Eq. 5-12. The damping curve is transformed by taking the natural log of the damping values as shown in Eq. 5-13. In Eq. 5-13,  $\varepsilon_2$  is a random value from the correlated, multivariate normal distribution, and  $\sigma_{\ln_D}$  is the damping lognormal standard deviation. Natural log standard deviation values of 0.15 and 0.3 are used for randomizing the modulus reduction and damping curves, respectively.

$$\text{logit}\left(\frac{G}{G_{max}}(\gamma)\right) = \ln\left(\frac{\frac{G}{G_{max}}(\gamma)}{1 - \frac{G}{G_{max}}(\gamma)}\right) = \ln[f(\gamma)] \quad (\text{Eq. 5-10})$$

$$f(\gamma)_{rand} = \exp\left[\ln[f(\gamma)] + \varepsilon_1 \times \sigma_{\ln_G} \times \frac{1}{1 - \frac{G}{G_{max}}(\gamma_{ref})}\right] \quad (\text{Eq. 5-11})$$

$$\left[\frac{G}{G_{max}}(\gamma)\right]_{rand} = \frac{f(\gamma)_{rand}}{1 + f(\gamma)_{rand}} \quad (\text{Eq. 5-12})$$

$$D(\%)_{rand} = \exp[\ln[D(\%)] + \varepsilon_2 \times \sigma_{\ln_D}] \quad (\text{Eq. 5-13})$$

#### 5.4.2 Modulus Reduction and Damping Curve Components of the Logic Tree for the SRS Study Site

Darendeli (2001) notes that there will always be discrepancies between the behavior assumed in models based on engineering properties from laboratory tests and field performance.

Possible explanations for these differences are that only small volumes of soil can be sampled for laboratory testing, and that sampling introduces sample disturbance. Geotechnical engineers need to consider these effects when using laboratory samples to determine soil engineering properties. The TI Team considered two sets of MRD curves to capture the CBR of TDI for the SRS site. These MRD curves are those obtained from site-specific laboratory testing and those obtained from the Darendeli (2001) model. The TI Team expects that the site-specific curves will capture site-specific behavior, and that the Darendeli (2001) model, which is derived from a large number of tests, will better capture the effects of confining stress, plasticity index, and overconsolidation on the cyclic behavior of soils.

Stokoe et al. (1995) performed resonant column and torsional shear testing on soils from across the SRS. The Stokoe et al. (1995) report is found as an enclosure to a summary report on dynamic testing at SRS by Lee (1996). The MRD curves recommended by Stokoe et al. (1995) are depth-dependent. Some of the curves are applicable for specified geologic formations, whereas other curves are assigned based on soil type and depth. Lee (1996) provides mean and mean  $\pm$  sigma reference strains that can be used to compute modulus reduction curves using a hyperbolic function. Lee (1996) also provides a table of recommended damping curve values. These tables provide damping values for shear strains of 0.1% to 0.5%. At the maximum shear strain for the shallow sand and deep clay curves, the damping values are 14.8% and 13%, respectively. These damping curves are extrapolated to strains where 15% damping is reached. The TI Team limited all damping curves to a maximum damping of 15%. The SRS site-specific MRD curves are shown in Figure 5-17. Additional site-specific testing was performed as part of the geotechnical investigation for the SRS-FA site (DOE, 2003). The MRD curves are generally consistent with the MRD curves reported by Stokoe et al. (1995) and Lee (1996) with the exception that laboratory small strain damping curves for the SRS-FA site are significantly higher. As discussed in Section 4, the TI Team believes the high damping values are an overestimation due to the effects of excitation frequency in the resonant column tests at small strains. Therefore, the TI Team used the damping curve values reported by Lee (1996) in the site response analyses.

The TI Team used the SRS geotechnical report to obtain the soil parameters needed for computing MRD curves from the Darendeli (2001) model. The TI Team assumed overconsolidation ratio (OCR) and plasticity index values for depths where laboratory testing was not available. The SRS depositional environment is within the Atlantic Coastal Plain and consists of fluvial, deltaic, and shallow marine deposits. Overconsolidation values from the shallow profile show a trend of decreasing overconsolidation with depth, indicating that desiccation and partial saturation are a contributing cause of overconsolidation. Therefore, at depths where preconsolidation stresses are not available, the TI Team assumed the OCR is equal to 1. The Team assumed that deep sands are non-plastic and that the deep clays have a plasticity index of 30, which is consistent with the plasticity index of the shallow clays.

Table 5-6 lists the site-specific MRD curves that were used for the SRS. Figure 5-18 compares the Darendeli (2001) MRD curves with SRS site-specific curves for one of the soil types in the profile (Dry Branch). The difference between site-specific and Darendeli (2001) MRD curves is small to moderate across all depths.

Because a significant number of laboratory tests have been conducted to develop MRD curves for the SRS, the TI Team concluded that the site-specific curves should have a greater weight than the generic curves. Weights assigned to the SRS site-specific and generic Darendeli (2001) MRD curve branches are 0.7 and 0.3, respectively.

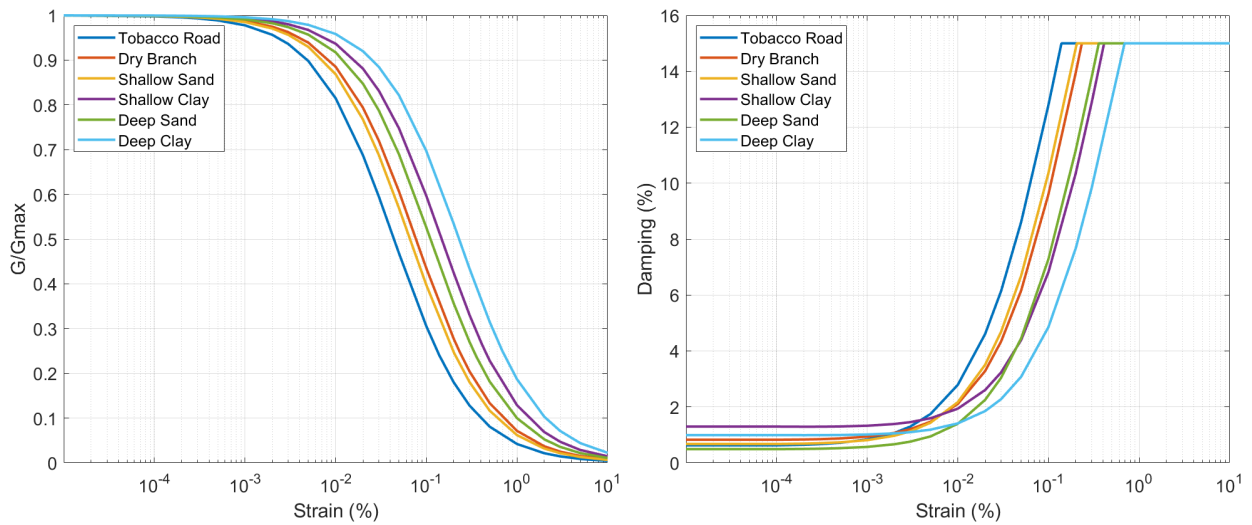


**Figure 5-17 SRS-specific MRD curves**

As noted earlier, the TI Team used the procedure developed by Yee et al. (2013) to modify the modulus reduction curves at large strains so that stresses implied by the modulus reduction curve are consistent with the soil shear strength. The TI Team used empirical correlations with CPT tip resistance to obtain friction angle and undrained strength for sand and clay layers, respectively. The TI Team then evaluated the epistemic uncertainty for these strength parameters by developing estimates of measurement error and transformation (empirical model) uncertainty to quantify the standard deviation using an approach proposed by Phoon and Kullhawy (1999). The TI Team obtained upper- and lower-case strength parameters that represent approximately the 5<sup>th</sup> and 95<sup>th</sup> percentile values. Weights assigned by the TI Team to lower-, base-, and upper-case strengths are 0.25, 0.5, and 0.25, respectively. This results in a discrete representation of the shear strength distribution with moments consistent with the continuous distribution (Miller and Rice 1983).

Near the ground surface and in the deep clay layers, the shape of the strength-corrected modulus reduction curves was not consistent with laboratory curves at moderate strain levels unless the TI Team artificially increased the estimated soil shear strength. At shallow depths, increasing the shear strength is reasonable to account for increased effective stresses in unsaturated soils. In the deep layers, the strains remain within the range observed in laboratory tests (less than 0.3%). Therefore, artificially increasing the strength in these layers to maintain consistency between laboratory and strength-corrected curves is justified.

The TI Team randomized the MRD curves using the logit function approach discussed earlier. The lognormal standard deviation of 0.15 used for the modulus reduction curves produces random curves that are consistent with calculated curves obtained using a hyperbolic function with reported mean plus sigma and mean minus sigma reference strains for SRS soils (Lee, 1996). The damping lognormal standard deviation of 0.3 is used to randomize the damping curves and is based on recommendations in the SPID (EPRI, 2013).

Table 5-6 SRS site-specific MRD curves	
Depth Range (m)	Site-Specific MRD Curves
0 – 20	Tobacco Rd

20 – 21.5	Shallow Clay
21.5 – 40.1	Dry Branch
40.1 – 41.3	Shallow Clay
41.3 – 56.7	Dry Branch
56.7 – 82.5	Shallow Sand
82.5 – 117.5	Deep Sand
117.5 – 165.1	Deep Clay
165.1 – 240.5	Deep Sand
240.5 – 249.4	Deep Clay
249.4 – 258.6	Deep Sand

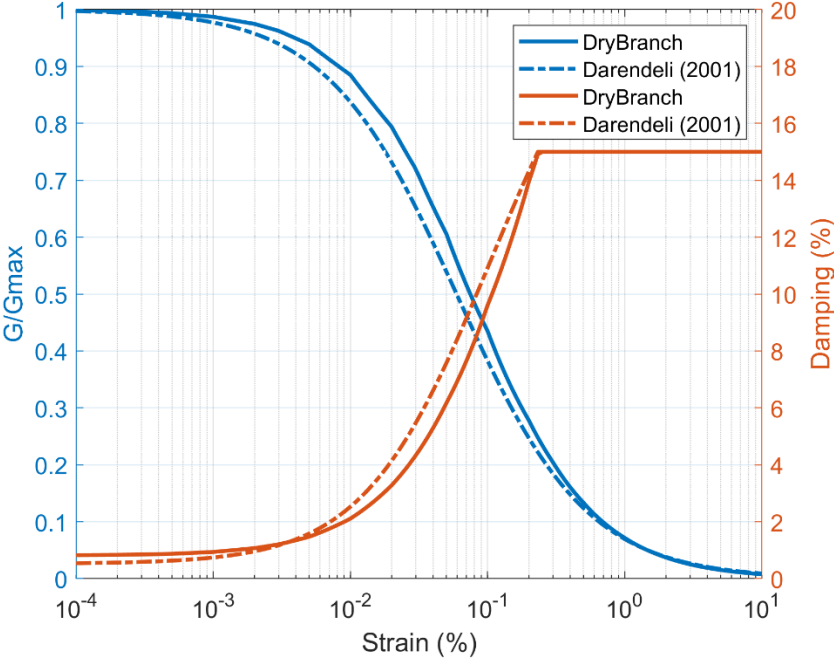


**Figure 5-18 Comparison of site-specific and generic MRD curves used to capture epistemic uncertainty in dynamic material properties for SRS**

**5.4.3 Modulus Reduction and Damping Curve Components of Logic Tree for GVDA**

Stokoe and Darendeli (1998) performed resonant column (RC) and torsional shear (TS) tests at GVDA on four silty sand (SM) soil samples retrieved at depths of 3.5, 6.5, 27 and 41.3 m where the *in situ* mean effective stresses were estimated to be 44, 64, 233, and 273 Kilopascals (kPa), respectively. Modulus reduction curves were constructed from best fits of RC and TS results with the hyperbolic equation recommended by Hardin and Drnevich (1972). Stokoe and Darendeli (1998) constructed damping curves from RC and TS results with extrapolation for values at strain levels not achieved during sample testing. While the TI Team had confidence that the resulting site-specific MRD curves represent the nonlinear properties at specific depths, significant gaps in the modeled MRD exist between depths of 27 m to 41.3 m and between 41.3 m to 88 m before reaching competent rock material.

These gaps require that the TI Team estimate the dynamic material properties over large depth ranges using only a single site-specific MRD curve set. The TI Team was concerned that this could result in the nonlinear properties of soil being poorly modeled over these depth ranges. Therefore, the TI Team decided to include the stress-dependent MRD curves of Darendeli

(2001) to capture epistemic uncertainty in nonlinear material properties. Because the sampled material from Stokoe and Darendeli (1998) was classified as SM and non-plastic, a plasticity index of 0 was used in the model. Also, because no preconsolidation stresses are available, an OCR of 1 was assumed.

A comparison between the two sets of modulus reduction curves is shown in Figure 5-19. The differences in shear modulus reduction between the two sets of curves is minimal at shallow depth (< 4 m) and increases slightly to a maximum difference at 6.5 m where the site-specific model suggests a slightly weaker material. As depth increases, the two sets of modulus reduction curves begin to collapse back on one another. The most significant difference between the two sets of MRD curves is in damping (Figure 5-20). The site-specific curves suggest much higher damping in the material than predicted by the generic model of Darendeli (2001) over the full range of depths. For weighting of the MRD logic tree branches, the TI Team concluded that although the site-specific curves should have greater weight than the generic curves, the difference in weight should be small due to the significant gaps in modeled MRD over large depth ranges. Therefore, to appropriately capture the epistemic uncertainty in dynamic material properties, the TI Team decided on weights of 0.6 and 0.4 for the GVDA site-specific and Darendeli (2001) MRD curve branches, respectively.

As noted in Section 5.4.1, the TI Team used the procedure developed by Yee et al. (2013) to modify the modulus reduction curves at large strains so that stresses implied by the modulus reduction curve are consistent with the soil shear strength. The TI Team used empirical correlations with CPT tip resistance to obtain friction angle and undrained strength for sands in the upper 17 m from Youd et al (2004). The TI Team then evaluated the epistemic uncertainty for these strength parameters by developing estimates of measurement error and transformation (empirical model) uncertainty to quantify the standard deviation using an approach proposed by Phoon and Kulhawy (1999). The TI Team obtained upper- and lower-case strength parameters that represent approximately the 5th and 95th percentile values. Weights assigned by the TI Team to lower-, base-, and upper-case strengths are 0.25, 0.5, and 0.25, respectively. This results in a discrete representation of the shear strength distribution with moments consistent with the continuous distribution (Miller and Rice 1983).

The TI Team randomized the MRD curves using the approach presented in Section 5.4.1. A lognormal standard deviation of 0.15 used by the TI Team for the modulus reduction curves produces random curves that are consistent with calculated curves obtained using a hyperbolic function with reported mean plus sigma. The damping lognormal standard deviation of 0.3 selected by the TI Team to randomize the damping curves is based on recommendations in the SPID (EPRI, 2013).

## **5.5 Site Response Analysis Method**

Different methods are available for the computation of site response, and three different approaches are considered in this study: (1) equivalent linear (EQL) analysis, (2) kappa-corrected EQL analysis, and (3) NL analysis. These different methods are considered alternative sources of epistemic uncertainty because at this time none of these

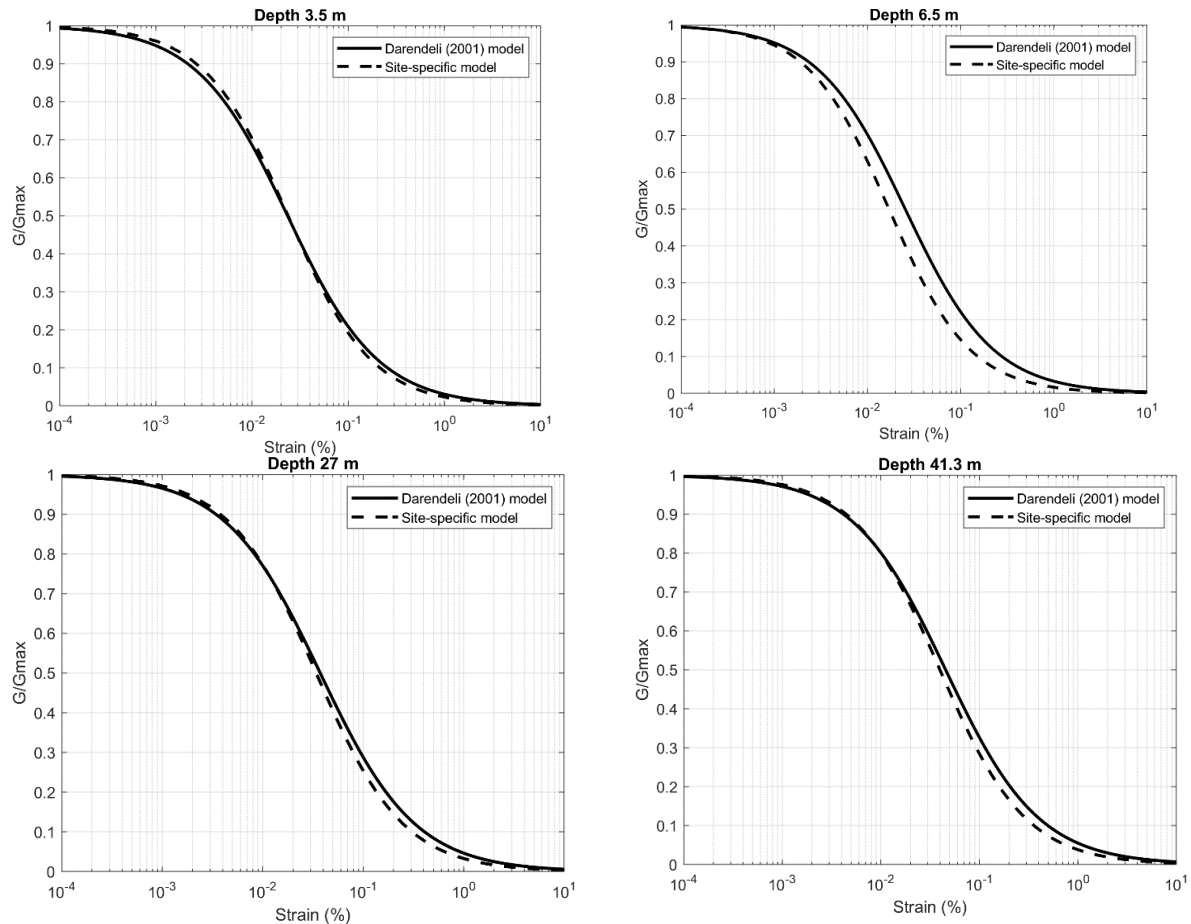


**Figure 5-19 Comparison of stress-dependent modulus reduction curves (Darendeli 2001) and GVDA site-specific modulus reduction curves developed by Stokoe and Darendeli (1998).**

methods has been definitively demonstrated to produce superior results over a wide range of input intensities. The three methods of site response used in this study were introduced in Section 3.1, but specific implementation details are described here along with the common attributes to the different analyses.

### **Commonalities Among Approaches**

As noted in Section 3, the TI Team used the one-step approach to site adjustment. This approach includes two site response analyses: one for the site-specific reference + near-surface profile and one for the GMM reference profile. The site profiles extend to the depth at which the site-specific profile coincides with the GMM profile. The TI Team assigned nonlinear modulus reduction and damping curves to each of the soil and rock layers based on laboratory testing and/or material type, with shear strength considerations used to constrain the large-strain segment of the modulus reduction curve. The  $D_{min}$  in the profile is constrained to provide an appropriate, site-specific  $\kappa_0$  at the surface.

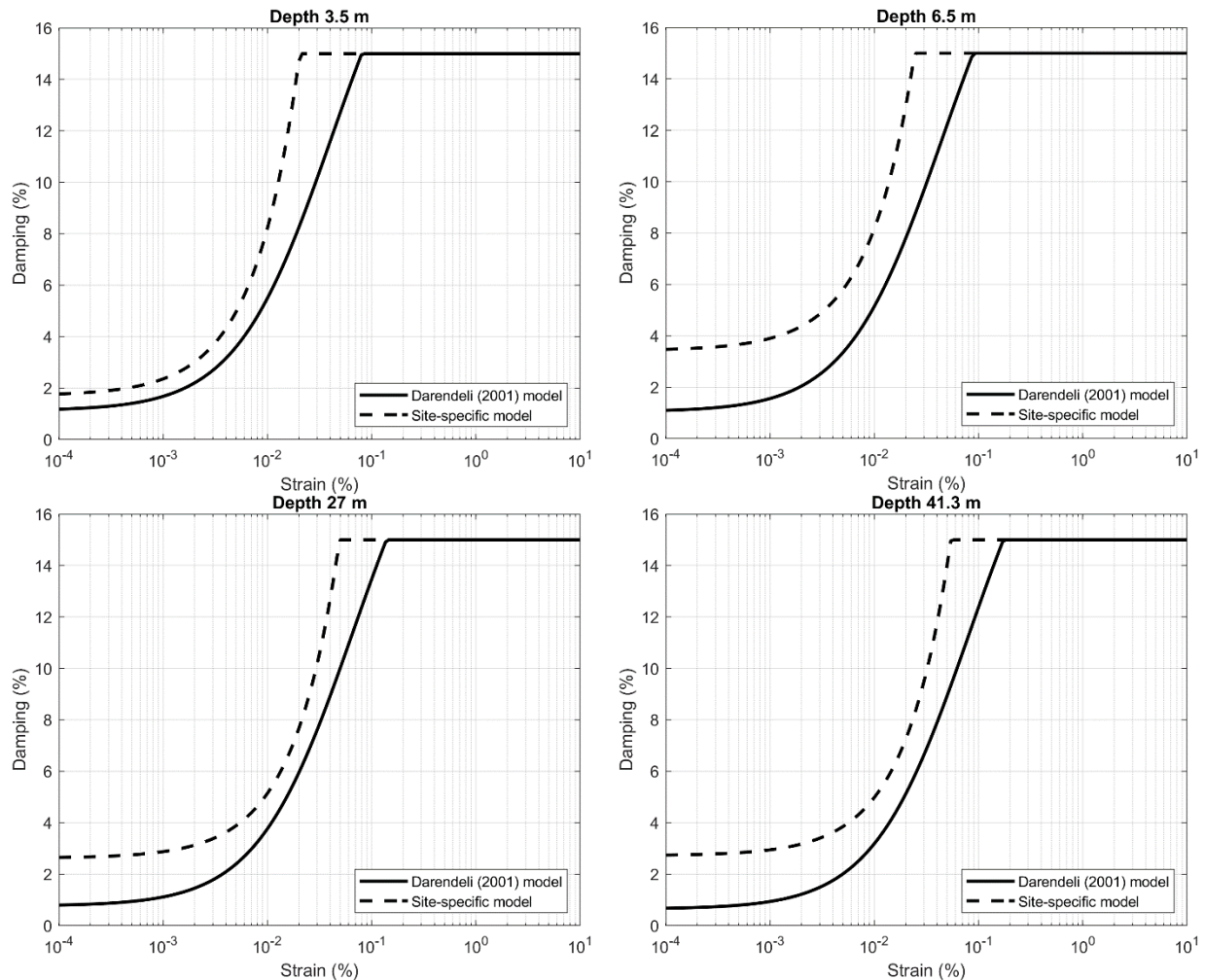


**Figure 5-20 Comparison of stress-dependent damping curves (Darendeli, 2001) and GVDA site-specific damping curves developed by Stokoe and Darendeli, (1998).**

### ***Equivalent Linear Analysis***

The EQL analysis utilized in this study is performed using the RVT approach, and thus the input motions are specified using only a FAS and duration. The EQL analysis solves the 1D wave equation in the frequency domain and uses strain-compatible, linear viscoelastic material properties that are iteratively adjusted to be consistent with an effective level of shear strain induced in each layer. Research studies have shown EQL analysis to be accurate for strains up to about 0.5% (e.g., Kaklamanos et al., 2015; Zalachoris and Rathje, 2015), but EQL analysis underpredicts the high-frequency components of motion for strains larger than 0.5%. For high intensity reference rock ground motions in this study, shear strains in the site response analyses may exceed 0.5%.

### ***Kappa-Corrected EQL Analysis***

To address the underprediction of the high-frequency components of motion at large strains, Xu and Rathje (2021) proposed a kappa correction to the FAS computed from an EQL analysis. This approach adjusts the high-frequency FAS from an EQL site response analysis to be

consistent with a target kappa,  $\kappa_{target}$ . The adjustment incorporates  $\Delta\kappa$ , defined as the difference between  $\kappa_{target}$  and the kappa of the surface FAS computed from EQL analysis ( $\kappa_{EQL}$ ). The resulting frequency-dependent adjustment factors are defined from

$$F(f) = \exp(-\pi \cdot [\kappa_{target} - \kappa_{EQL}] \cdot f) = \exp(-\pi \cdot \Delta\kappa \cdot f) \quad (\text{Eq. 5-14})$$

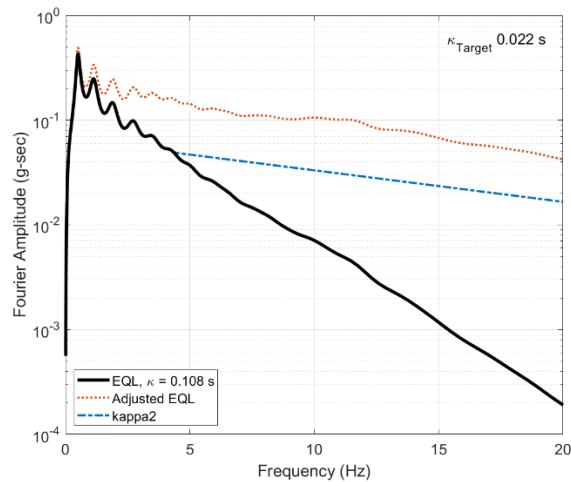
Using more than 2,500 motions from 32 sites, Xu and Rathje (2021) observed that  $\kappa$  did not vary systematically with the induced shear strain but instead remained at its small-strain value. The study also demonstrated that using the small-strain  $\kappa$  as  $\kappa_{target}$  in a kappa-corrected EQL analysis for large-intensity motions at four downhole array sites produces surface motions that are more consistent with the recorded motions. Thus, for this study, the TI Team used the small-strain  $\kappa_0$  for each study site as the target kappa.

Figure 5-21 shows a surface FAS computed by EQL analysis for a large strain input motion. The high-frequency shape of the FAS represents a  $\kappa_{EQL} = 0.108$  s. This large value indicates significant strains and damping have been induced in the soil. Using the  $\Delta\kappa$  approach in Eq. 5-14 and  $\kappa_{target} = 0.022$  s (i.e., small strain  $\kappa_0$ ), the adjusted EQL FAS is shifted up. The difference between the EQL FAS and the kappa-corrected FAS increases with an increase in frequency (Figure 5-21).

If  $\Delta\kappa$  is large, the  $\Delta\kappa$  approach may apply significant adjustments at lower frequencies, where a kappa correction is not needed. An alternative to the  $\Delta\kappa$  approach is the kappa2 approach (NCREE, 2021) in which the EQL FAS remains unmodified below a specified transition frequency ( $f_{tr}$ ) and then a slope equal to  $\kappa_{target}$  is imposed at frequencies above  $f_{tr}$ . The kappa2 correction is applied to the same EQL FAS in Figure 5-21, and the FAS clearly show that the kappa2 approach results in smaller adjustments to the FAS across a broad range of frequencies. However, the kappa2 approach requires specification of not only  $\kappa_{target}$ , but also  $f_{tr}$ . Based on a limited number of surface ground motions recorded at sites that experienced significant nonlinearity, as well as a limited number of nonlinear site response analyses, NCREE (2021) recommends specifying  $f_{tr}$  based on the frequency at which the EQL FAS decreases below some fraction of its peak. Values of this fraction range from about 0.05 to 0.20 of the peak. The TI Team used fractions of 0.05, 0.11, and 0.17 with weights of 0.2, 0.6, and 0.2, respectively.

### **Nonlinear (NL) Analysis**

Nonlinear analysis solves the 1D wave equation in the time domain using either a finite element or finite difference approximation. The nonlinear stress-strain response of the materials is modeled directly, with the soil stiffness modified at each time step and the hysteretic stress-strain response generating energy dissipation and damping. Modeling the full nonlinear stress-strain response should provide a more accurate prediction of site response, particularly at large strains, but some studies have not found a meaningful benefit (e.g., Kaklamanos et al., 2015; Zalachoris and Rathje, 2015). Important issues that must be addressed when considering NL analysis are the need for a suite of input time series for each intensity level (i.e., RVT cannot be utilized) and the associated computational cost. Additionally, there are many computational details associated with NL analysis that can affect the results. Because of the computational costs of performing nonlinear analysis for all intensity levels, particularly considering that the NL



**Figure 5-21 Illustration of the different approaches to the kappa correction applied to a FAS from EQL analysis.**

and EQL analysis results should be similar at strains less than about 0.5%, as well as the issues related to computational details, NL analyses in this study are performed for only a subset of input intensities: low intensity where site response is nearly linear and large intensity where some shear strains in the profile will exceed 0.5%. The TI Team used these site response results to inform the logic tree weights assigned to EQL and kappa-corrected EQL branches of the logic tree.

### **Logic Tree Weights**

A comparison of the results of EQL, the modified kappa-corrected EQL (i.e., the kappa2 approach), and NL analyses is presented in Section 6. A general observation is that the EQL analyses introduce a large degree of damping at high frequencies for strong input motions. Also, the results of the kappa2 and NL analyses are similar. The TI Team expressed a strong preference for the kappa2 approach because it is supported by the NL analyses and avoids the pitfalls of the EQL at large strains (i.e., excessive damping levels). The standard of practice in the nuclear industry implies that the EQL approach has been deemed technically adequate in the past, thus it survives as a null hypothesis unless proven wrong. Therefore, the EQL approach could not be precluded by the TI Team and was given a non-zero weight in the logic tree.

## **5.6 Summary of Final Logic Trees**

The final site response logic trees are shown in Figure 5-22 for the SRS study site and Figure 5-23 for the GVDA study site. The TI Team believes that the logic trees represent the CBR of TDI of the data (i.e.,  $V_S$  profile,  $\kappa_0$ , and nonlinear properties) as well as models (i.e., site response approach) and methods (i.e., different valid randomization approaches). The CBR of TDI for  $V_S$  profiles were captured via a careful consideration of all the available measurements at the study sites. For the site kappa, the approach used by the TI Team differed for each site. At the SRS study site, the TI Team captured the CBR of TDI via the considerations of different existing correlations between site proxies and  $\kappa_0$ . At the GVDA study site, the TI Team developed an approach to capture all possible sources of uncertainty in obtaining  $\kappa_0$  from recordings at the site. For the MRD curves, the TI Team captured the CBR of TDI via consideration of site-specific laboratory measurements and generic models. The generic

models were included by the TI Team to compensate for the limited number of available measurements. The task of capturing the CBR of TDI of models for site response analyses is more difficult. However, the TI Team believes that the selected models provide an uncertainty characterization that represents defensible approaches for computing site response. Considerations of model error (Section 3.2) provide an additional uncertainty on the model.

It is interesting to compare the epistemic uncertainty implicit in both logic trees. The epistemic standard deviation  $\sigma_{ep}$  for a parameter  $x$  with  $i$  logic tree branches ( $x_i$ ), each with weight  $w_i$ , is obtained using:

$$E[x] = \sum_i w_i x_i \quad (\text{Eq. 5-15})$$

$$\sigma_{ep} = \sqrt{\sum_i w_i x_i^2 - E[x]^2} \quad (\text{Eq. 5-16})$$

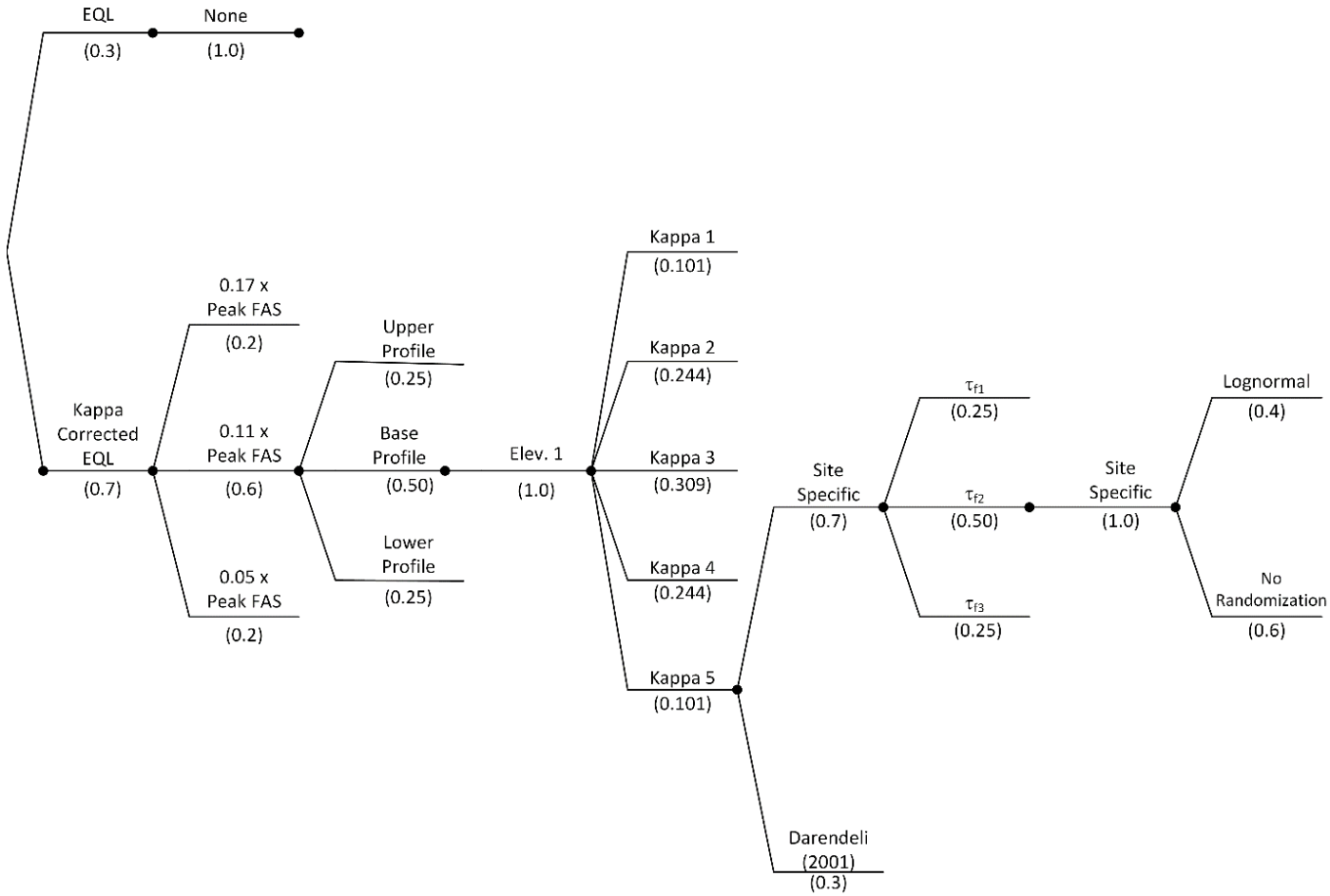
Figure 5-24 plots the  $V_S$  profiles resulting from the site response logic trees for the two study sites. The epistemic uncertainty in  $V_S$  oscillates around 0.1 natural log units for the SRS study site. For the GVDA study site, the values of  $\sigma_{ep, \ln V_S}$  reach higher values over depth intervals where there is a transition between low velocity near-surface layers and stiffer layers at depth (depths from 50 m to 100 m). The smaller epistemic uncertainties for the SRS are consistent with the fact that the site stratigraphy is well characterized across the site with no uncertainty associated with the transition depth to reference rock conditions.

The epistemic uncertainty in  $\kappa_0$  in natural logarithm units is 0.379 for the SRS study site and 0.266 for the GVDA study site. The larger uncertainty at the SRS is because at this site,  $\kappa_0$  is inferred from correlations, while the values are obtained from recordings at the GVDA site.

The epistemic uncertainty in MRD curves for both sites is shown in Figure 5-25. The uncertainty in MRD curves is at a strain level corresponding to  $G/G_{\max} = 0.5$  for the site-specific curves. The uncertainty in damping is the component associated solely with strain-dependent damping, and not to the  $D_{min}$ , which is controlled by  $\kappa_0$ . For the SRS, the variations in the level of epistemic uncertainty with depth correspond to stratigraphic changes (Table 5-6). The small uncertainty in damping at the SRS at depths below about 165 m is due to the fact that  $D_{min}$  for this soil is increased significantly to produce the appropriate  $\kappa_0$ , and as a result, the damping at the reference strain (including its uncertainty) is controlled by  $\kappa_0$ . Overall, the uncertainty in MRD curves is larger for the GVDA than for the SRS. This is consistent with the fact that a larger number of soils from the SRS were used to develop the site-specific curves, whereas the tests for the GVDA were only conducted for a limited number of samples.

Another contributor to the uncertainty in MRD curves is the uncertainty in the shear strength. The epistemic uncertainty branches of the undrained strength are obtained using consideration of measurement error and transformation uncertainty (Section 5.4). This uncertainty is different for sands and clays. As a result, the resulting epistemic uncertainty in shear strength is a function of the soil types, being lower for sands than for clays. The profiles of shear strength and its epistemic uncertainty are shown in Figure 5-26. The GVDA profile is composed exclusively of sands, while the SRS profiles has both sands and clays. The jumps in shear strength and epistemic uncertainty are associated with changes in soil type.

Analysis Method	Kappa Correction Factor	Vs Profile	Reference Rock Elevation	Site Kappa	MRD Curves	Shear Strength	Vs Randomization	Layer Thickness Randomization
-----------------	-------------------------	------------	--------------------------	------------	------------	----------------	------------------	-------------------------------



5-35

Figure 5-22 SRS site response logic tree. Values under branches represent branch weights. Kappa values are provided in Table 5-3.



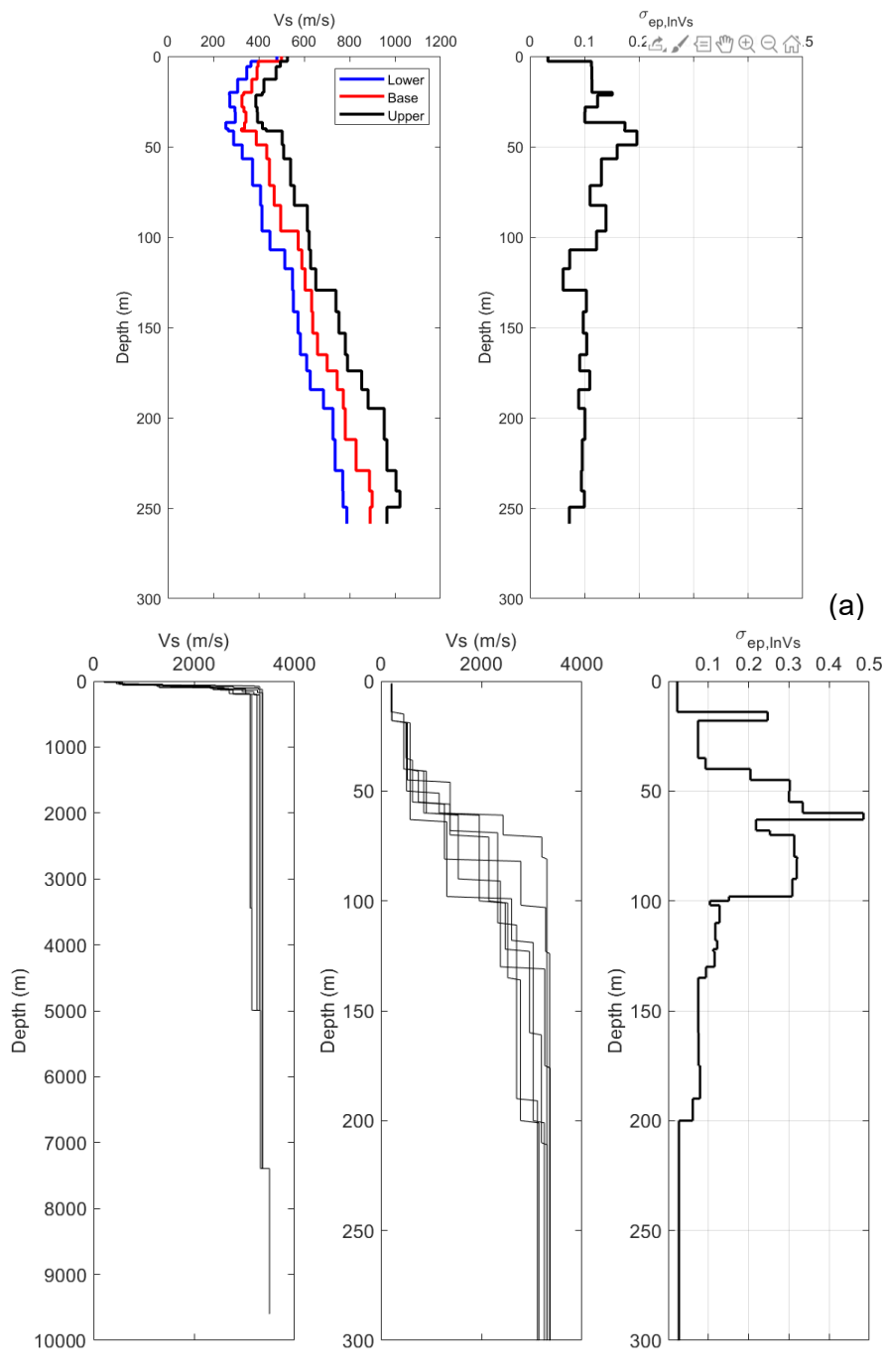


**Figure 5-24 Epistemic uncertainty in shear-wave velocity versus depth for (a) the SRS study site and (b) the GVDA study site. For the SRS, the left plot shows the alternative base case profiles. For the GVDA, the black lines in the left two plots are alternative median velocity profiles.**

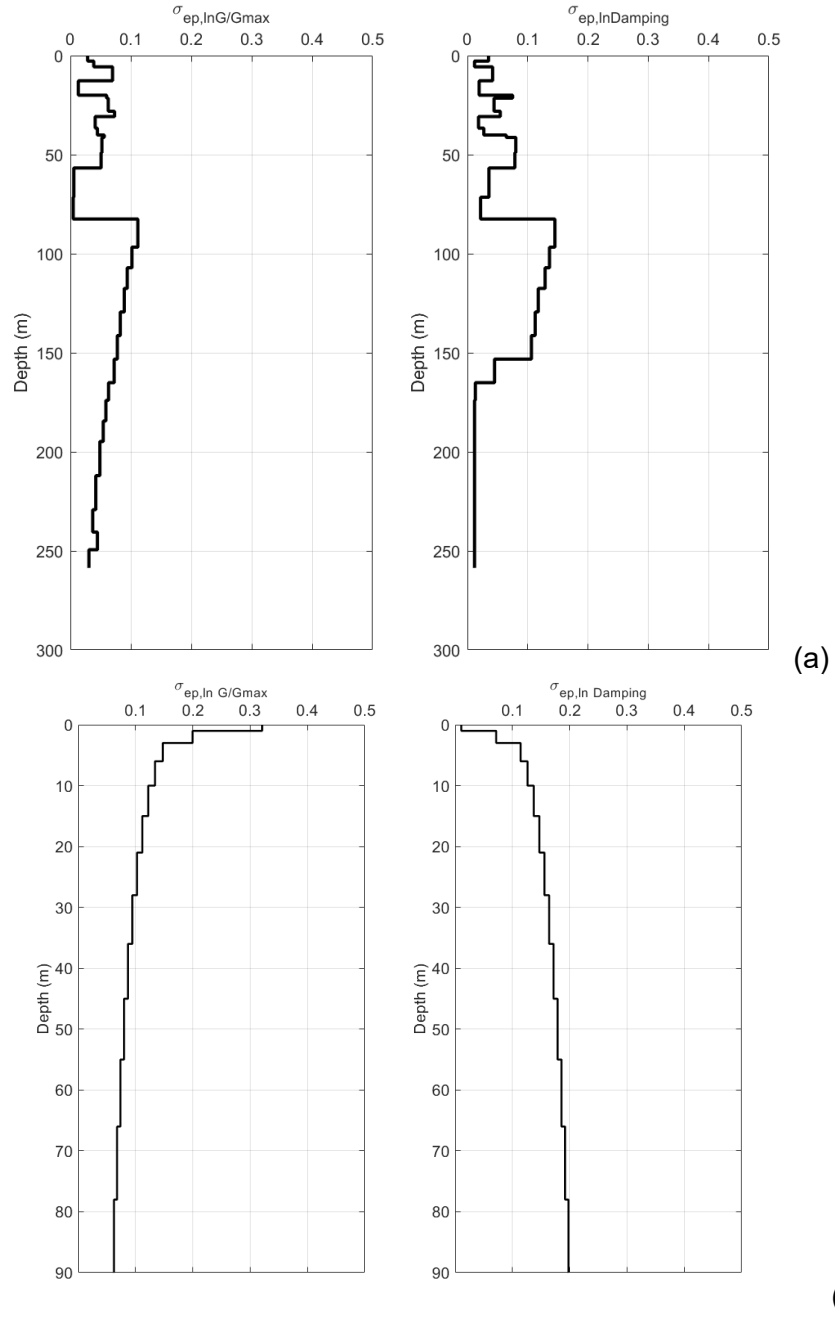
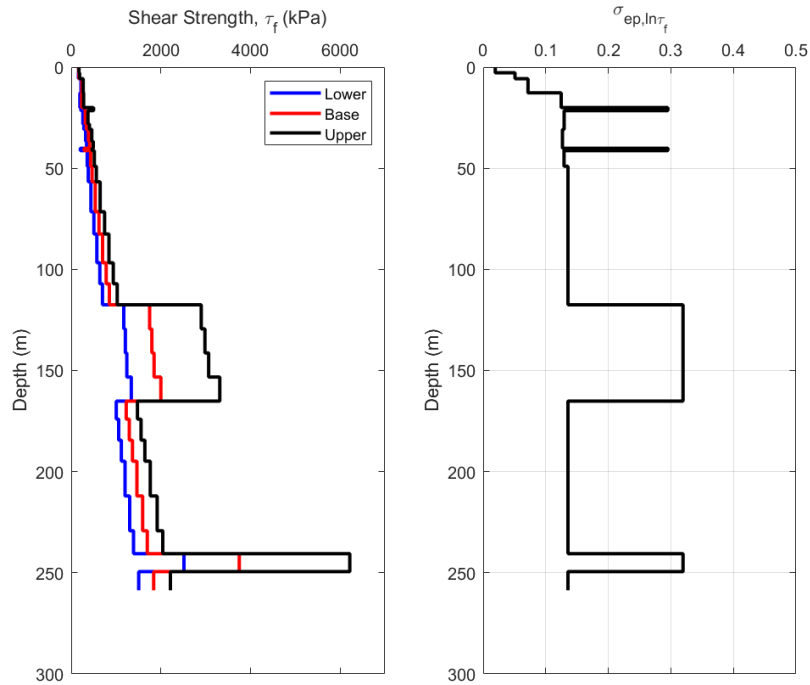
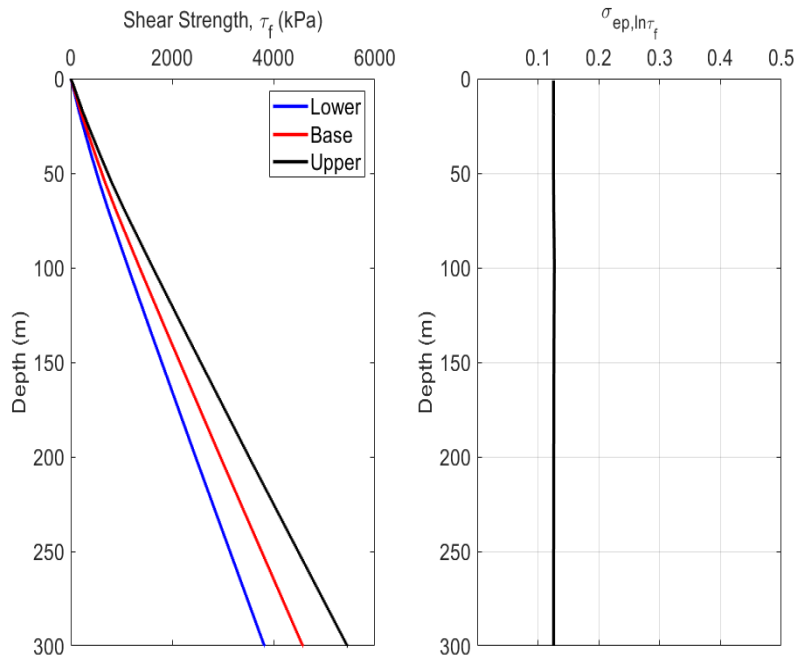


Figure 5-25 Epistemic uncertainty in MRD for (a) the SRS and (b) the GVDA site



(a)



(b)

**Figure 5-26 Base case shear strength profiles and associated epistemic uncertainty for (a) SRS and (b) GVDA**

## 5.7 References

Anderson, J.G. and S.E. Hough. "A Model for the Shape of the Fourier Amplitude Spectrum of Acceleration at High Frequencies." *Bulletin of the Seismological Society of America*. Vol. 74, No. 5. pp. 1969–1993. 1984. doi: <https://doi.org/10.1785/BSSA0740051969>

Boore, D.M. and W.B. Joyner. "Estimation of Ground Motion at Deep-Soil Sites in Eastern North America." *Bulletin of the Seismological Society of America*. Vol. 81, No. 6. pp. 2167–2185. 1991.

Cabas, A., A. Rodriguez-Marek, and L.F. Bonilla. "Estimation of Site-Specific Kappa ( $\kappa_0$ )-Consistent Damping Values at KiK-Net Sites to Assess the Discrepancy Between Laboratory-Based Damping Models and Observed Attenuation (of Seismic Waves) in the Field." *Bulletin of the Seismological Society of America*. Vol. 107, No. 5. pp. 2258–2271. 2017.

Campbell, K.W. "Estimates of Shear-Wave Q and  $\kappa_0$  for Unconsolidated and Semiconsolidated Sediments in Eastern North America." *Bulletin of the Seismological Society of America*. Vol. 99, No. 4. pp. 2365–2392. 2009.

Chandler, A.M., N.T.K. Lam, and H.H. Tsang. "Near-Surface Attenuation Modelling Based on Rock Shear-Wave Velocity Profile." *Soil Dynamics and Earthquake Engineering*. Vol. 26, No. 11. pp. 1004–1014. 2006.

Coppersmith, K., J. Bommer, K. Hanson, J. Unruh, R. Coppersmith, L. Wolf, B. Youngs, L. Al Atik, A. Rodriguez-Marek, G. Toro, and V. Montaldo-Falero. "*Hanford Sitewide Probabilistic Seismic Hazard Analysis*." Richland, Washington: Pacific Northwest National Laboratory. 2014.

Cox, B.R. and D.P. Teague. "Layering Ratios: A Systematic Approach to the Inversion of Surface Wave Data in the Absence of *A Priori* Information." *Geophysical Journal International*. Vol. 207, No. 1. pp. 422–438. 2016.

Cramer, C.H., J.S. Gombert, E.S. Schweig, B.A. Waldron, and K. Tucker. "*The Memphis, Shelby County, Tennessee, Seismic Hazard Maps*." Open-File Report. 2004.

Darendeli, M.B. "*Development of a New Family of Normalized Modulus Reduction and Material Damping Curves*." Dissertation. University of Texas, Austin, Texas. 2001.

Denham, M.E. "*SRS Geology/Hydrogeology Environmental Information Document*." WSRC-TR-95-0046, 10526. 1999.

DOE. "MOX Fuel Fabrication Facility Site Geotechnical Report." DCS01-WRS-DS-NTE-G-00005-E. Washington, DC: U.S. Department of Energy. 2003.

EPRI. "Seismic Evaluation Guidance Screening, Prioritization and Implementation Details (SPID) for the Resolution of Fukushima Near-Term Task Force Recommendation 2.1: Seismic." Palo Alto, California: Electric Power Research Institute. 2013.

EPRI. "Guidelines for Determining Design Basis Ground Motions." Palo Alto, California: Electric Power Research Institute, Vol. 1-5, EPRI TR-102293. 1993.

GeoPentech. "Southwestern United States Ground Motion Characterization SSHAC Level 3. *Technical Report*, Revision 2." March 2015.

Gibbs, J.F. "Near-Surface P- and S-Wave Velocities From Borehole Measurements Near Lake Hemet, California." *U.S. Geol. Surv. Open-File Rept.* pp. 89–630. 1989.

Gingery, J.R. and A. Elgamal, A. "Shear Stress-Strain Curves Based on the  $G/G_{max}$  Logic: A Procedure for Strength Compatibility." *IACGE 2013*, American Society of Civil Engineers, Chengdu, China. pp. 721–729. 2013.

Griffiths, S.C., B.R. Cox, E.M. Rathje, and D.P. Teague. "Mapping Dispersion Misfit and Uncertainty in  $V_s$  Profiles to Variability in Site Response Estimates." *Journal of Geotechnical and Geoenvironmental Engineering*. Vol. 142, No. 11. p. 04016062. 2016.

Hardin, B.O. and V.P. Drnevich. "Shear Modulus and Damping in Soils: Design Equations and Curves." *Journal of the Soil Mechanics and Foundations Division*. Vol. 98, No. 7. pp. 667–692. 1972.

James, G., D. Witten, T. Hastie, and R. Tibshirani. *An Introduction to Statistical Learning: With Applications in R*. Springer Texts in Statistics, Springer, New York Heidelberg Dordrecht London. 2017.

Kaklamanos, J., L.G. Baise, E.M. Thompson, and L. Dorfmann. "Comparison of 1D Linear, Equivalent-Linear, and Nonlinear Site Response Models at Six KiK-Net Validation Sites." *Soil Dynamics and Earthquake Engineering*. Vol. 69. pp. 207–219. 2015.

Ktenidou, O.J., F. Cotton, N.A. Abrahamson, and J.G. Anderson. "Taxonomy of  $\kappa$ : A Review of Definitions and Estimation Approaches Targeted to Applications." *Seismological Research Letters*. Vol. 85, No. 1. pp. 135–146. 2014.

Lee, R.C. "*Investigations of Nonlinear Dynamic Soil Properties at the Savannah River Site (U)*." Aiken, South Carolina: Westinghouse Savannah River Company. 1996.

Miller, A.C. and T.R. Rice. "Discrete Approximations of Probability Distributions." *Management Science*. Vol. 29, No. 3. pp. 352–362. 1983.

NCREE. "Development of GMRS and FIRS for Nuclear Power Plants in Taiwan." National Center for Research on Earthquake Engineering. 2021.

Passeri, F., S. Foti, and A. Rodriguez-Marek. "A New Geostatistical Model for Shear Wave Velocity Profiles." *Soil Dynamics and Earthquake Engineering*. Vol. 136. p. 106247. 2020.

Phoon, K.-K. and F.H. Kullhawy. "Evaluation of Geotechnical Property Variability." *Canadian Geotechnical Journal*. Vol. 36, No. 4. pp. 625–639. 1999.

Rodriguez-Marek, A., J. Ake, C. Munson, E. Rathje, S. Stovall, T. Weaver, K. Ulmer, and M. Juckett. "Site Amplification Factors Developed Using SSHAC Guidance." DesignSafe-CI. 2021. <https://doi.org/10.17603/ds2-9t3a-kz92>.

Silva, W.J., N.A. Abrahamson, G. Toro, and C. Costantino. "*Description and Validation of the Stochastic Ground Motion Model*." Pacific Engineering and Analysis. 1996.

Silva, W.J., and R.B. Darragh. "Engineering Characterization of Strong-Ground Motions at Rock Sites." Palo Alto, California: Electric Power Research Institute, EPRI-TR-102262. 1995.

Steller, R. "New Borehole Geophysical Results at GVDA." UCSB Internal report. 1996.

Stokoe, K.H. and M.B. Darendeli. "Laboratory Evaluation of the Dynamic Properties of Intact Soil Specimens: Garner Valley, California." Geotechnical Engineering Report GR98-3, Civil Engineering Department, The University of Texas at Austin, Austin, Texas. 1998.

Stokoe, K.H., A. Kurtulus, and F.Y. Menq. "Data Report." *SASW Measurements at the NEES Garner Valley Test Site, California.* 2004.

Stokoe, K.H., M. Darendeli, and N.-K.J. Lee. "*Correlation Study of Nonlinear Dynamic Soil Properties.*" The University of Texas at Austin, Austin, Texas. 1995.

Teague, D.P., R.C. Brady, and E.M. Rathje. "Measured vs. Predicted Site Response at the Garner Valley Downhole Array Considering Shear Wave Velocity Uncertainty From Borehole and Surface Wave Methods." *Soil Dynamics and Earthquake Engineering.* Vol. 113. pp. 339–355. 2018.

Toro, G. "Probabilistic Models of the Site Velocity Profiles for Generic and Site-Specific Ground-Motion Amplification Studies." Technical Rep. No. 779574. Upton, New York: Brookhaven National Laboratory. 1995.

Van Houtte, C., S. Drouet, and F. Cotton. "Analysis of the Origins of  $\kappa$  (kappa) to Compute Hard Rock to Rock Adjustment Factors for GMPEs." *Bulletin of the Seismological Society of America.* Vol. 101, No. 6. pp. 2926–2941. 2011.

Xu, B. and E.M. Rathje. "The Effect of Soil Nonlinearity on High-Frequency Spectral Decay and Implications for Site Response Analysis." *Earthquake Spectra.* p.8755293020981991. 2021.

Xu, B., E.M. Rathje, Y. Hashash, J. Stewart, K. Campbell, and W.J. Silva. " $\kappa_0$  for Soil Sites: Observations From KiK-Net Sites and Their Use in Constraining Small-Strain Damping Profiles for Site Response Analysis." *Earthquake Spectra.* Vol. 36, No. 1. pp. 111–137. 2020.

Yee, E., J.P. Stewart, and K. Tokimatsu. "Elastic and Large-Strain Nonlinear Seismic Site Response From Analysis of Vertical Array Recordings." *Journal of Geotechnical and Geoenvironmental Engineering.* Vol. 139, No. 10. pp. 1789–1801. 2013.

Youd, T.L., A.J. Bartholomew, and J.S. Proctor. "Geotechnical Logs and Data From Permanently Instrumented Field Sites: Garner Valley Downhole Array (GVDA) and Wildlife Liquefaction Array (WLA)." Report to The Network for Earthquake Engineering Simulation (NEES) Colaboratories. 2004

Zalachoris, G. and E.M. Rathje. "Evaluation of One-Dimensional Site Response Techniques Using Borehole Arrays." *Journal of Geotechnical and Geoenvironmental Engineering.* Vol. 141, No. 12. p. 04015053. 2015.

## 6 Site Adjustment Factor Results

The Technical Integration (TI) Team performed equivalent linear (EQL) site response analyses to develop frequency-dependent site adjustment factors (*SAF*) for response spectral acceleration for the Savannah River Site (SRS) and Garner Valley Downhole Array (GVDA) study sites. The TI Team developed sixty random shear-wave velocity ( $V_S$ ) profiles for each terminal branch of the logic tree associated with the EQL analysis branch. For the kappa-corrected EQL analysis, the TI Team corrected the surface Fourier amplitude spectra (FAS) from the EQL analyses using the kappa2 approach described in Section 5.5. The TI Team obtained the site adjustment factor by dividing the computed surface response spectrum by the outcrop response spectrum for the reference condition ( $S_{a_{ref}}$ ). For SRS, the reference response spectrum is the input response spectrum used in the site response analysis. For GVDA, the reference response spectrum is the surface response spectrum computed at the top of the Southwest United States (SWUS) profile (see Section 5.2.3). The TI Team computed the mean log *SAF* (i.e., median *SAF*) and standard deviation of the log *SAF* using the 60 *SAF* functions for each terminal branch of the logic tree. Results from these analyses and the sensitivity of *SAF* to various inputs are presented in the sections below.

To facilitate implementing the *SAF* within the seismic hazard integral, at each frequency, the TI Team reduced the median *SAF* from the logic tree terminal branches to seven branches using the re-sampling procedure outlined by Miller and Rice (1983) for developing discrete approximations to probability distributions. These seven branches capture epistemic uncertainty in *SAF* and can be used in the probabilistic seismic hazard analyses (PSHA) to develop the mean seismic hazard and hazard fractiles.

In addition to reducing the number of *SAF* function branches for hazard calculations, the aleatory standard deviation from the terminal branches must also be simplified to make the hazard calculations tractable. The TI Team considered using multiple epistemic aleatory standard deviation branches or only the weighted mean aleatory standard deviation. Preliminary hazard calculations demonstrated that differences between using multiple aleatory standard deviation branches and the mean aleatory standard deviation are negligible. Therefore, the TI Team used the mean aleatory standard deviation for each of the seven *SAF* functions within the hazard integral. Additional details on how the TI Team implemented aleatory standard deviation in the hazard integral is provided in Section 7.

*SAF* results from each branch of the logic tree were used to determine the epistemic uncertainty in *SAF* resulting from the different analysis methods, base case  $V_S$  profiles, site kappa ( $\kappa_0$ ) values, and the other alternative models and methods used in the site response analyses. Rodriguez-Marek et al. (2021) recommended implementing a minimum epistemic uncertainty to ensure estimates of site response incorporate model uncertainty. The TI Team implemented a minimum epistemic uncertainty of 0.15 for this project based on the recent outcomes of the Senior Seismic Hazard Analysis Committee (SSHAC) work conducted in Taiwan<sup>4</sup>. The TI Team of that study considered the modeling uncertainty reported by Silva (2015) for seven downhole array sites in which the  $V_S$  profiles were optimized to minimize measurement error, and by Stewart and Afshari (2021) for California downhole array sites for which measured  $V_S$

---

<sup>4</sup> Several members of the TI Team and PRRP for this project also participated in the SSHAC studies conducted in Spain and Taiwan. Results from these studies are not currently published or publicly available; thus, no specific citation is provided.

profiles were used. The Silva (2015) analyses indicated low values of model uncertainty (generally lower than 0.1), while Stewart and Afshari (2021) reported larger values of 0.2 to 0.35. While these values are similar to those found by Kaklamanos et al. (2013) for Kik-net downhole array stations, they include the uncertainty in the  $V_S$  profile because the  $V_S$  profile was not optimized to fit the downhole array response. Because the uncertainty in the  $V_S$  profile is incorporated in the logic tree branches, the Taiwan SSHAC TI Team judged the values from Silva (2015) to represent modeling uncertainty alone, and to be the appropriate value of minimum epistemic uncertainty. The values computed by Silva (2015) were increased to account for sampling uncertainty that results from using only seven profiles, and the estimates of modeling uncertainty were smoothed across periods, resulting in a period-independent value of 0.15. Additional research can strengthen the basis for selecting a specific minimum epistemic uncertainty value, but this additional research is outside the scope of the current project.

## **6.1 SRS Study Site**

### **6.1.1 Site Adjustment Factor Branches**

Figure 6-1 shows the *SAF* as a function of reference rock spectral acceleration for the re-sampled seven branches for four response spectral frequencies of 0.5 Hertz (Hz), 5 Hz, 10 Hz, and 100 Hz. The mean log standard deviation is also shown below the *SAF*. The *SAF* for the 0.5 Hz oscillator frequency is relatively flat from 0.003 g to 0.02 g and ranges between 2 and 4. Due to the nonlinear response, the  $V_S$  begin to reduce, and the site natural frequency reduces from the small-strain value of  $\sim 0.7$  Hz and approaches 0.5 Hz. This results in an increase in site amplification for many of the *SAF* branches from  $Sa_{ref} = 0.02$  g to almost 0.2 g. With increasing reference rock spectral acceleration, there is more nonlinearity, which results in a further decrease in  $V_S$  and increased damping. This produces a gradual decrease in *SAF* with increasing  $Sa_{ref}$ . A review of the mean natural log standard deviation for the 0.5 Hz oscillator frequency shows almost no change with increasing spectral acceleration until  $Sa_{ref}$  exceeds 0.07 g.

The amplification functions for 5 and 10 Hz oscillator frequencies are very similar, showing a small decrease in *SAF* with increasing  $Sa_{ref}$  between 0.05 g to 0.1 g, followed by a more significant decrease in amplification at larger  $Sa_{ref}$ . The *SAF* for 100 Hz shows different behavior with a nearly log-log linear decrease in *SAF* at  $Sa_{ref}$  greater than 0.03 g. A review of the *SAF* for the 5 Hz, 10 Hz, and 100 Hz oscillator frequencies shows that at large reference rock spectral accelerations, the *SAF* continues to decrease. The TI Team considers this to be a representation of true physical response and does not consider it necessary to impose a lower limit on *SAF*.

For the SRS study site, the aleatory variability is relatively small when the site is behaving essentially linearly. This is primarily due to the small  $V_S$  aleatory variability, which is constrained based on a review of the site-specific  $V_S$  data. The aleatory variability at each frequency increases with increasing  $Sa_{ref}$ , with the most substantial increases occurring at frequencies close to the site's natural frequency.

### **Minimum Epistemic Uncertainty**

Epistemic uncertainty in  $SAF$  as a function of frequency for reference rock motions with peak ground accelerations (PGAs) of 0.01 g, 0.43 g, and 1.2 g are presented in Figure 6-2. Epistemic uncertainty in  $SAF$  is shown by the thick black line and the horizontal red line

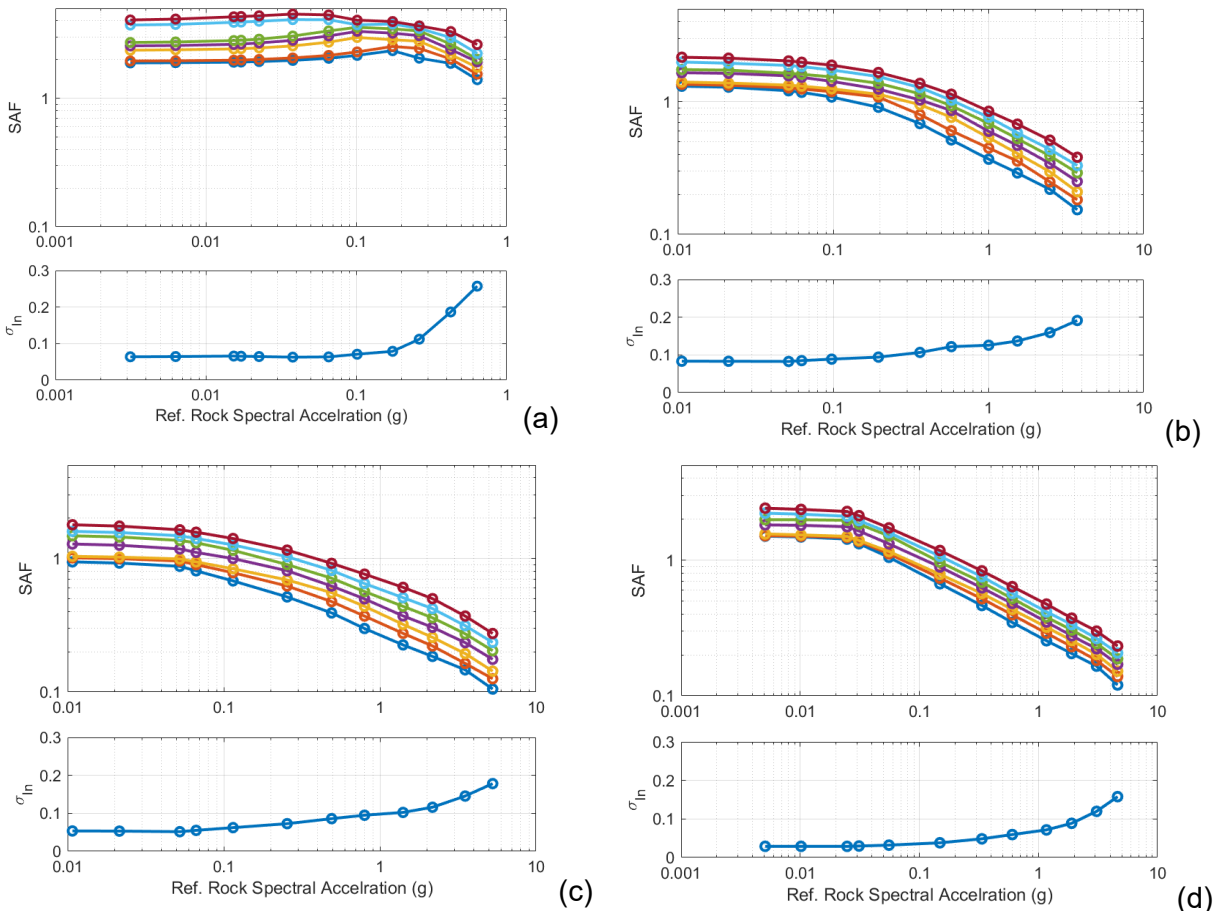


**Figure 6-1 Site adjustment factors ( $SAF$ ) for seven re-sampled epistemic branches for the SRS and mean of the log standard deviations (aleatory variability) for (a) 0.5 Hz, (b) 5 Hz, (c) 10 Hz, and (d) 100 Hz**

highlights the minimum epistemic uncertainty of 0.15. The TI Team observed that the epistemic uncertainty from the logic tree typically varies between 0.1 and approximately 0.15. The TI Team recognized that the epistemic uncertainty associated with results from the SRS-specific logic tree is smaller than results from recent studies (e.g., Coppersmith et al., 2014). This is likely a result of constraints on the range of  $V_S$  and modulus reduction and damping (MRD) curves implemented in the logic tree, which are based on data used to characterize the site. In the vicinity of 1 Hz and at small input loading levels, the epistemic uncertainty is much smaller compared to other frequencies. This is the result of the  $SAF$  from the three base-case  $V_S$  profiles crossing each other (see a). This behavior was also noted by Rodriguez-Marek et al. (2021) and Ulmer et al. (2021).

Figure 6-3 shows the  $SAF$  for the 1 Hz oscillator frequency as a function of  $Sa_{ref}$  with and without imposing the minimum epistemic uncertainty. Prior to imposing a minimum epistemic uncertainty of 0.15, the epistemic uncertainty is approximately 0.055. Imposing the minimum epistemic uncertainty moderately spreads out the branches of the  $SAF$ . At large input loading levels where the epistemic uncertainty is greater than or equal to 0.15, the  $SAF$  with an imposed

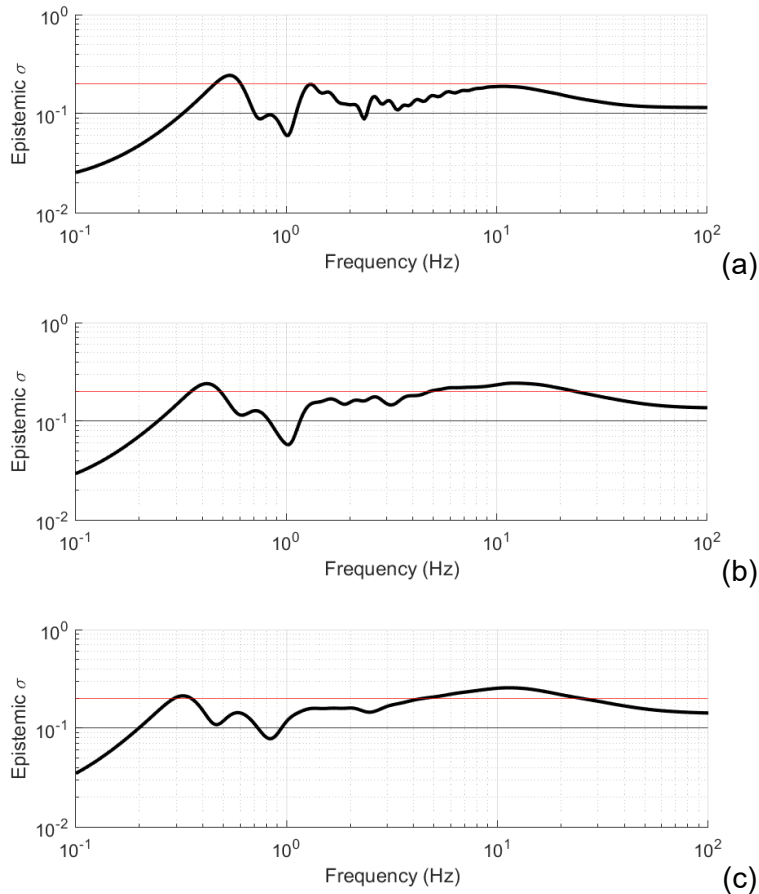


**Figure 6-2 Epistemic standard deviation of natural  $SAF$  for the SRS study site as a function of frequency for reference rock PGA of (a) 0.01 g, (b) 0.43 g, and (c) 1.2 g.**

minimum epistemic uncertainty merges with the  $SAF$  where no minimum was imposed. To implement the minimum epistemic uncertainty, Eq. 6-1 is used to compute the mean of the natural log  $SAF$  branch values. The modified branch  $SAF$  is then obtained using Eq. 6-2. In Eq. 6-2, the difference between the unmodified branch log  $SAF$  and the log mean  $SAF$  is multiplied by the ratio of the minimum epistemic standard deviation to the branch standard deviation and added to the log mean  $SAF$ .

$$\overline{\ln SAF} = \sum_i w_i (\ln SAF_i) \quad (\text{Eq. 6-1})$$

$$SAF_{i\text{ Mod}} = \exp\left(\overline{\ln SAF} + (\ln SAF_i - \overline{\ln SAF}) \frac{\sigma_{min}}{\sigma_i}\right) \quad (\text{Eq. 6-2})$$

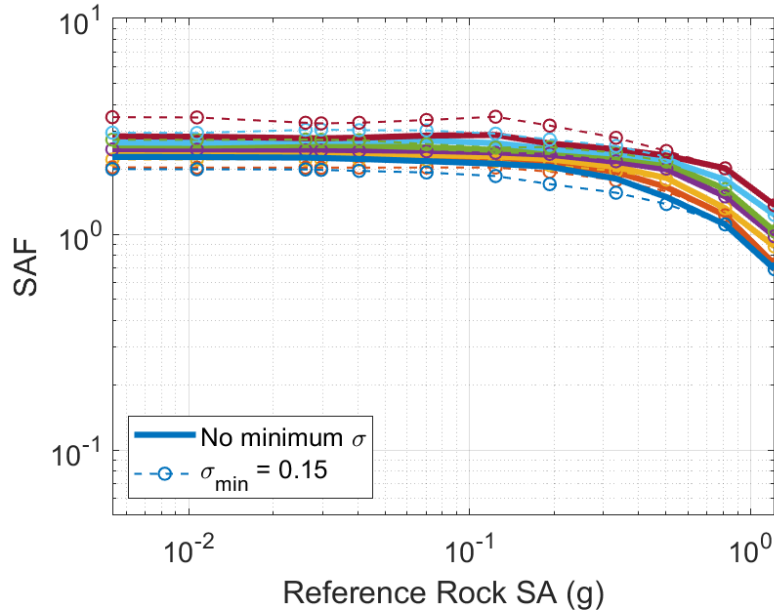


**Figure 6-3** *SAF* for 1 Hz as a function of  $Sa_{ref}$  at the SRS site with and without imposing minimum epistemic uncertainty.

### 6.1.2 Sensitivity Studies

Some simplifying assumptions were made for the site response analyses. Sensitivity studies were performed to assess the impact of these simplifying assumptions on *SAF* or seismic hazard. Sensitivity studies for SRS include the following: evaluating the impact of input response spectral shape on *SAF*, comparing the nonlinear (NL) analysis method to EQL and kappa-corrected EQL site response analyses, and assessing how the distribution of small strain damping through the profile impacted *SAF* results. Results from these studies and a discussion of these results are provided below. In addition, the sensitivity of *SAF* to the various inputs associated with nodes of the logic tree are also presented and discussed in this section.

#### Input Motion Specification

Point source models (PSMs) are commonly used to develop input motions for random vibration theory (RVT) EQL analyses. When using a PSM, a single magnitude earthquake is typically chosen, with a range of source-to-site distances to develop input motions that span the desired range of reference spectral acceleration amplitudes. Using a single magnitude is not consistent with seismic hazard deaggregations where the mean magnitude changes with oscillator frequency and annual frequency of exceedance. Using a range of magnitudes in addition to a range of source to site distances will result in changes to the reference spectral acceleration shape. According to Bazzurro and Cornell (2004), changes in spectral shape associated with earthquake magnitude do not appear to significantly impact resulting amplification functions.

An alternative approach for developing input motions is to use conditional mean spectra (CMS). Baker (2011) developed an approach to develop CMS. When developing CMS for an oscillator frequency at a given target spectral acceleration with the mean magnitude and source-to-site distance from a deaggregation, a ground motion model (GMM) and the model standard deviation are used to determine the epsilon value for the conditioning oscillator frequency. Then, using the correlation model developed by Baker (2011), epsilon values for other response spectral frequencies are determined. These epsilon values are used with the GMM and model

standard deviation to compute the spectral acceleration for all other oscillator frequencies. After the CMS is obtained, an inverse RVT method is used to develop a FAS that is used as the input motion for the site response analysis.

In this study on the effect of input motion specification on *SAF*, the TI Team used the two approaches described above (PSM and CMS) to define the input motion (i.e., define the FAS and response spectra) at five input loading levels. The resulting *SAF* functions were compared by the TI Team to determine if different specifications of the input motions impacted the results.

In this study, the TI Team deaggregated the reference rock seismic hazard to obtain the mean magnitude and distance for five input loading levels with annual rates of exceedance of  $10^{-2}$ ,  $10^{-3}$ ,  $10^{-4}$ ,  $10^{-5}$ , and  $10^{-6}$ . The TI Team used these magnitudes and distances along with typical PSM parameters for the eastern United States to develop input Fourier response spectra. If the response spectral acceleration for the oscillator frequency at which hazard is being computed did not match the spectral acceleration for the specified annual rate of exceedance, the FAS from the PSM was multiplied by a scale factor that resulted in obtaining a matching response spectrum at that oscillator frequency.

To develop the CMS for the input motions, the TI Team used the approach developed by Baker (2011). When developing CMS for a given target spectral acceleration with the mean magnitude and source to site distance, the TI Team used the mean of the 17 median GMMs from the Next-Generation Attenuation (NGA) relationships for regions in Central and Eastern North America (NGA-East) (Goulet et al. 2018) with the mean single station standard deviation to determine the epsilon value for the conditioning frequency. Then, using the correlation model developed by Baker (2011), epsilon values for other response spectral frequencies were determined. After the CMS was obtained, an inverse RVT method was used to develop a FAS that was used as the input motion for the site response analysis. The conditioning frequency ( $f^*$ ) was set to the oscillator frequency under consideration, such that different CMS were derived for each *SAF* frequency.

The PSM and CMS input response spectra for five different hazard levels are shown in Figure 6-4, conditioned on  $f^* = 25$  Hz. For this conditioning frequency, the PSM and CMS are similar at frequencies greater than  $f^*$ , but the CMS is significantly smaller at lower frequencies due to the reduction in correlation as frequencies diverge from  $f^*$ . For smaller values of  $f^*$ , the CMS would be smaller than the PSM at frequencies both larger and smaller than  $f^*$ .

The *SAF* obtained when using the PSM and CMS input motions are shown in Figure 6-5. At oscillator frequencies of 1 and 10 Hz, the *SAF* at smaller values of  $Sa_{ref}$  are similar for the PSM input and CMS input motions. At larger values of  $Sa_{ref}$ , the *SAF* from the CMS input is larger than for the PSM input, and this difference is greater for the 10 Hz oscillator than the 1 Hz oscillator (i.e., approximately 63 percent larger at the largest input loading level for the 10 Hz oscillator). The larger strains induced in the profile by the PSM lead to a stronger nonlinear response that causes the smaller PSM amplification at these frequencies. At oscillator frequencies of 25 Hz and 100 Hz, the *SAF* obtained from the PSM input spectra are generally larger than the *SAF* obtained using the CMS.

The larger *SAF* for the 25 Hz oscillator frequency may not seem intuitive. When looking at the 25 Hz input response spectra (Figure 6-4), the PSM input spectra are significantly larger than the CMS at lower frequencies, and these frequencies coincide with the site natural frequency of  $\sim 0.7$  Hz. The larger spectral accelerations near the site frequency results in larger shear strains being induced by the PSM, which generates more modulus reduction and increased

damping. The resulting surface FAS and response spectra for the different input motions are shown in Figure 6-6. The surface FAS from the PSM are significantly higher than the FAS from the CMS at low frequencies. The large FAS at these low frequencies affect the high frequency oscillator response. As a result, the *SAF* from the PSM are larger at 25 Hz.

These results illustrate that spectral shape does affect the spectral amplification function. This study on input motions is preliminary, and the TI Team believes a more detailed study is needed to justify using CMS to define input motions for site response analyses. Because the use of PSMs are generally accepted as a reasonable approach to developing input response spectra for site response analyses and since other research has indicated that spectral shape does not affect amplification functions (such as Bazzurro and Cornell, 2004), the TI Team decided to continue using PSMs to define the input motions for the site response analyses. Additional research is recommended to further evaluate the impact of these different input motion specifications on the calculated hazard.

### **Nonlinear Analysis**

The TI Team considered a NL analysis approach in addition to the EQL approach for capturing epistemic uncertainty in site response from analysis methods. There is a computational challenge associated with implementing NL analysis methods within the full site response logic tree because multiple time histories must be used for each loading level. Therefore, the TI Team performed analyses to compare EQL, kappa-corrected EQL, and NL analyses to determine if NL analyses are required to adequately capture the analysis method epistemic uncertainty. The TI Team performed the NL analyses using the program DeepSoil (Hashash et al., 2020).

When performing analyses for this comparison, the base case  $V_S$  was used with a  $\kappa_0$  of 0.036 s. Darendeli and Stokoe MRD curves (Darendeli, 2001) were used with the shear strength modification from the highest weighted shear strength from the logic tree. Layer thickness was not randomized for these analyses. The input loading was large, having a PGA of 1.9g, to produce a significant nonlinear response where one expects to see larger differences between EQL and NL analyses. Surface FAS from these analyses are shown in Figure 6-7. Overdamping of site response at high frequencies in the EQL analyses results in a much steeper decline in Fourier amplitude for the EQL RVT analysis compared to the NL analysis. Applying a kappa correction (i.e., the kappa2 approach, see Section 5.5) to the EQL RVT produces a high frequency decline similar to the nonlinear analysis. There are also some differences between the FAS from EQL and NL analyses at lower frequencies; specifically, the EQL FAS are higher than the NL FAS. When computing the high frequency oscillator response, the larger EQL response at low frequencies is compensated by the smaller EQL response at higher frequencies such that the *SAF* from NL analysis is similar to the *SAF* from EQL analysis at high oscillator frequencies (Figure 6-8).

These results suggest that the kappa correction branches for the analysis method node are sufficient to capture epistemic uncertainty associated with different analysis methods at frequencies above 3 Hz. There are some moderate differences between the EQL and NL *SAF* at frequencies less than about 3 Hz (Figure 6-8). These differences were not sufficient in the TI Team's view to warrant adding this analysis method to the logic tree.

Rock,  $f^* = 25$  Hz,  $M = 6.8$ ,  $R = 83.88$ km,  $T_{gm} = 10.847$ s

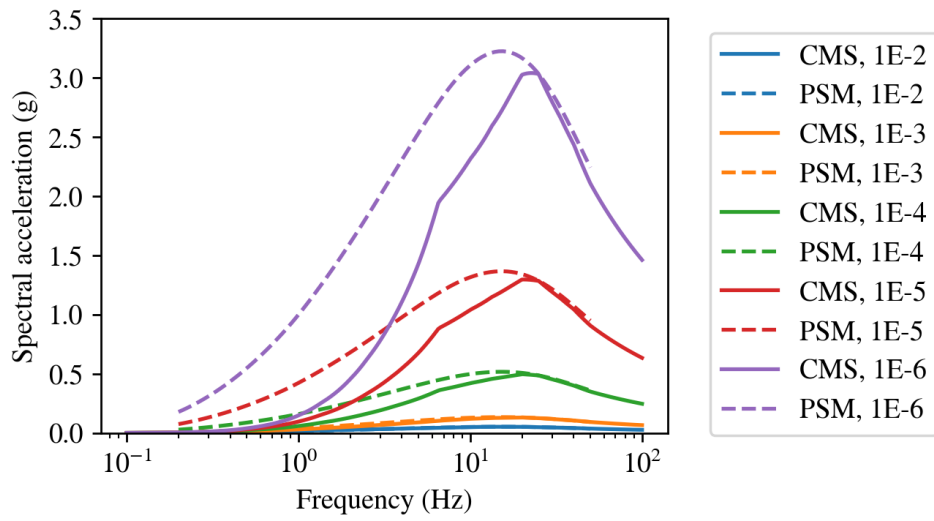


**Figure 6-4** Input reference rock spectral acceleration for five hazard levels using PSM and CMS conditioned at a frequency ( $f^*$ ) of 25 Hz.

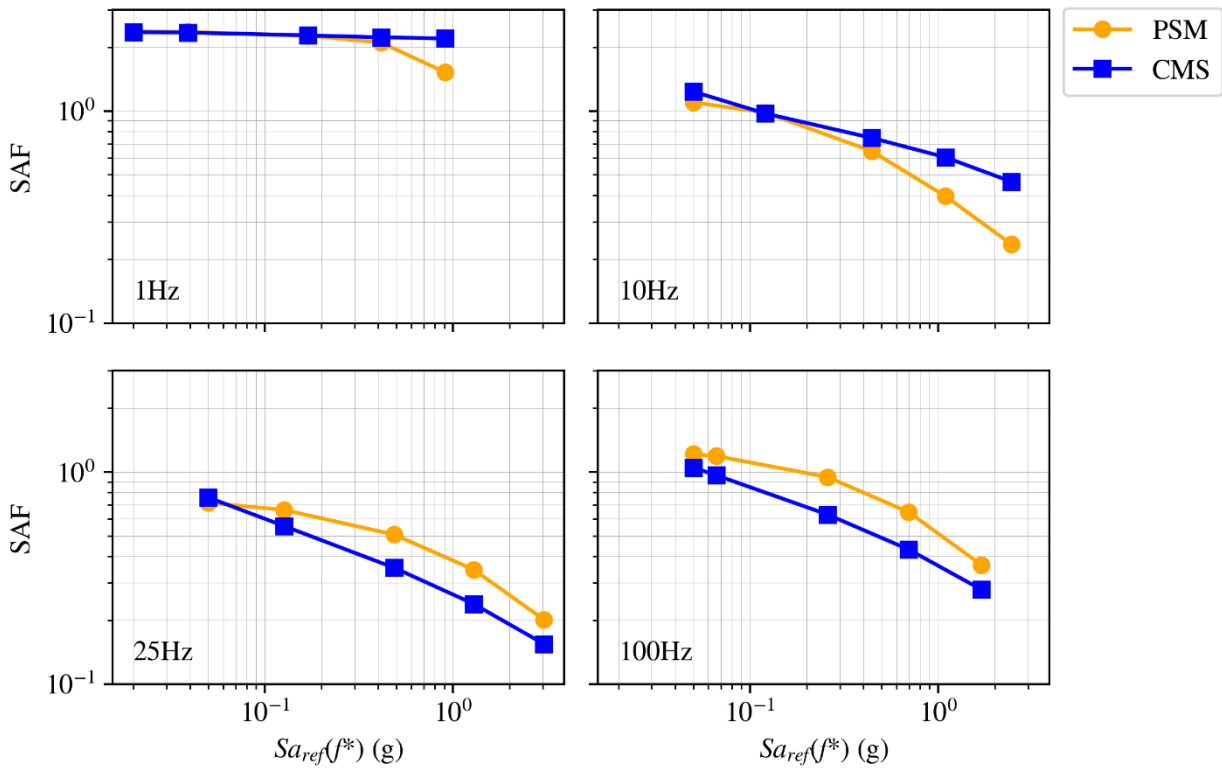
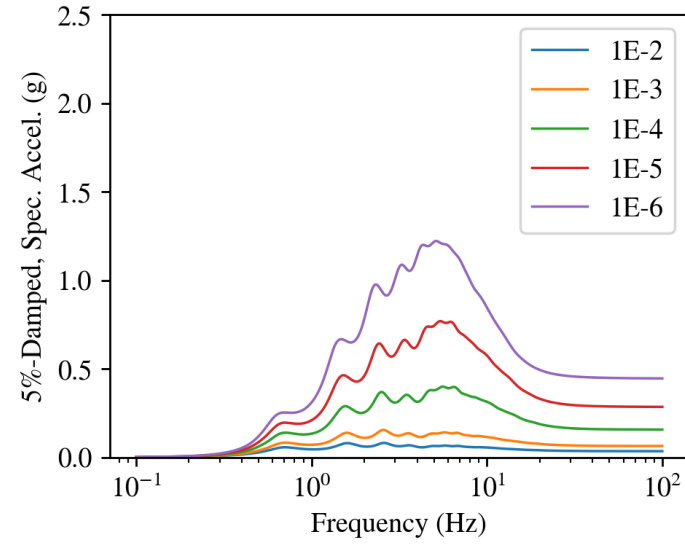
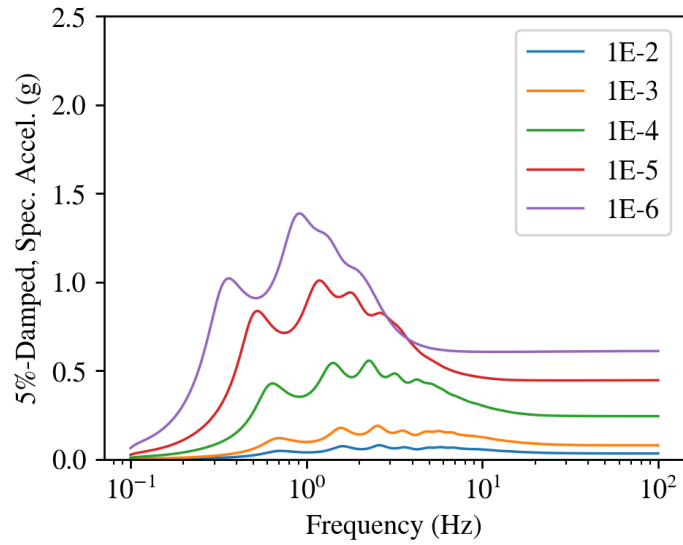
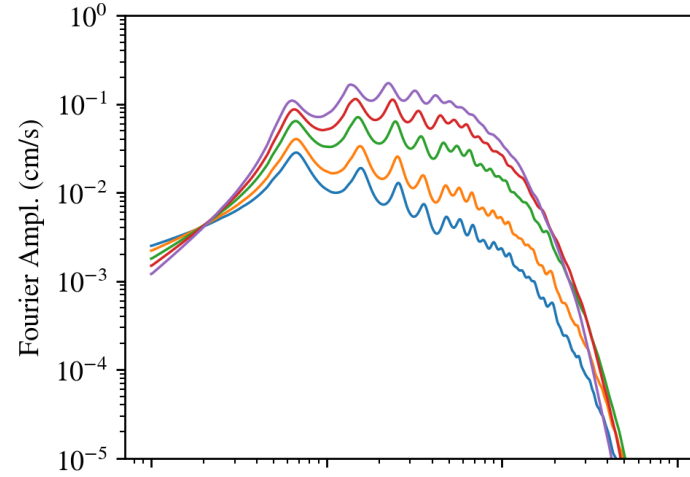
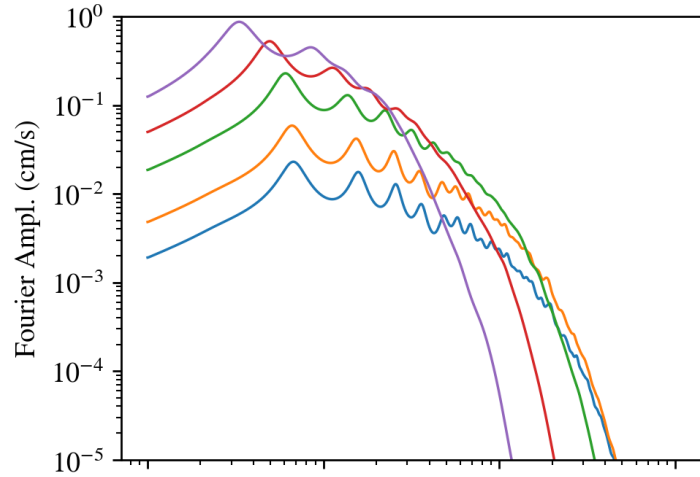


**Figure 6-5** SAF developed from PSM and CMS input motions.



(a)

(b)

**Figure 6-6** Surface FAS and response spectra for input motions derived from (a) point source model and (b) conditional mean spectra conditioned at an oscillator frequency ( $f^*$ ) of 25 Hz.

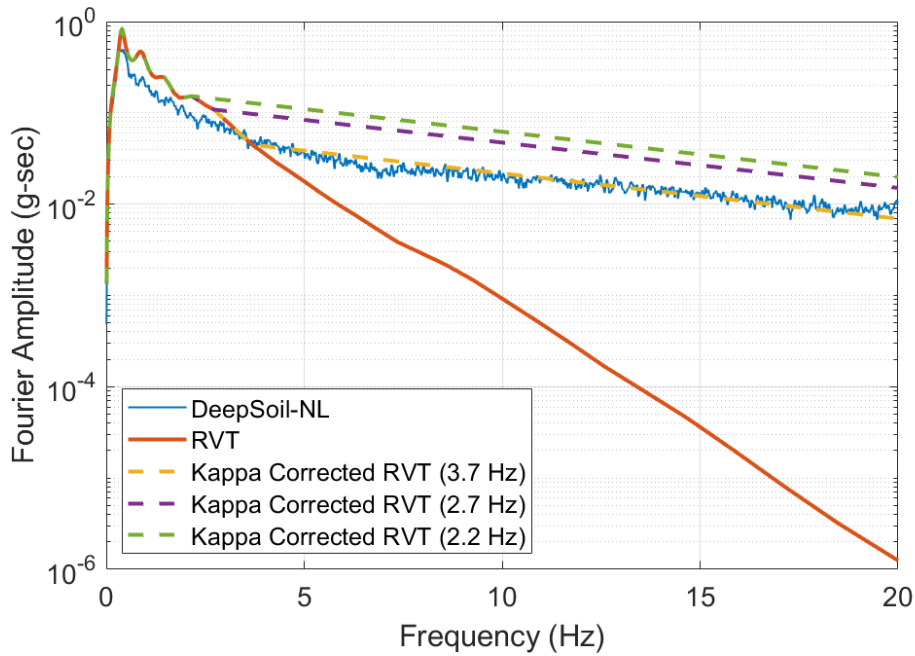


**Figure 6-7** Numbers in parentheses indicate the value of the transition frequency (ftr) for the kappa2 approach.

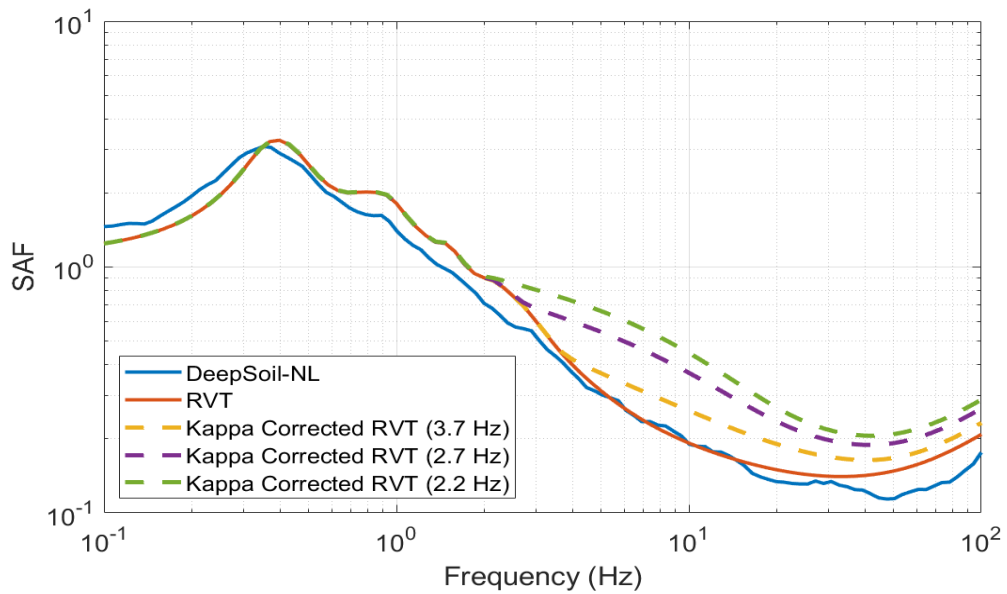


**Figure 6-8** Spectral amplification for NL DeepSoil analysis and EQL RVT and EQL analyses using RVT and kappa-corrected RVT.

## Low Strain Damping to Produce Kappa Consistent Surface Response

Low-strain damping associated with laboratory-based damping curves is not sufficient to produce a  $\kappa_0$  consistent with the empirical-based  $\kappa_0$  values at SRS. To obtain a surface response with an appropriate  $\kappa_0$ , low strain damping was increased over a specified depth range in the profile. The TI Team performed analyses to evaluate how the depth range over which low strain damping is modified affects the surface response and strain profile. Three depth ranges are considered in our analyses: depths deeper than 3 m, deeper than 50 m, or deeper than 153 m. Over these depths, the small strain damping value is increased and remains constant with increasing strain until the damping curve exceeds this new increased small strain damping value. When the damping modification starts at a shallower depth, the small strain damping value does not change as much at each depth to achieve the same  $\kappa_0$ .

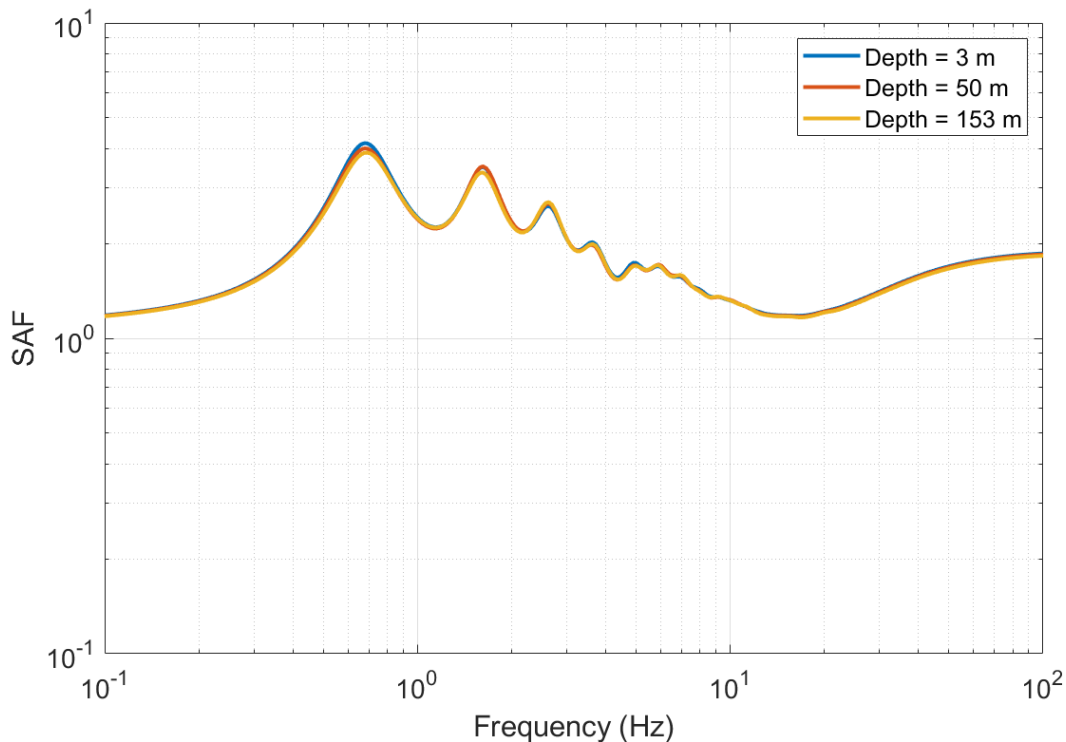
The *SAF*s associated with these analyses where low strain damping was modified at all depths deeper than 3 m, 50 m, or 153 m is shown in Figure 6-9. The *SAF* for these analyses are nearly identical. Similarly, the effective strain profiles shown in Figure 6-10 are nearly identical. Based on these results and similar results from analyses with larger amplitude input spectra, the TI Team determined that the depth range over which the damping profile is modified does not affect the site response results significantly. The SRS analyses performed to produce *SAF* for the PSHA modified the small strain damping at depths below 153 m.

## Sensitivity to Logic Tree Nodes

The SRS site response logic tree has six nodes with multiple branches. This section evaluates the sensitivity of the *SAF* associated with different branches at a logic tree node. Plots of mean *SAF*, bar charts of variance contribution, and tornado plots are three visual approaches that illustrate the sensitivity of the *SAF* to differences associated with specific branches of the logic tree at these nodes.

Figures 6-11 through Figure 6-16 show the mean *SAF* as a function of frequency for two loading levels (PGA = 0.43 g and PGA = 1.2 g or 3.0 g) for the six different nodes. The sensitivity of the *SAF* to the analysis method (i.e., EQL and kappa-corrected EQL) is illustrated in Figure 6-11. The *SAF* is not sensitive to the analysis method at low frequencies. There is sensitivity to the analysis method at relatively high frequencies with increasing sensitivity to analysis method as the input load increases and the nonlinear soil behavior increases. The increased sensitivity to analysis method with greater soil nonlinearity is expected because one expects the EQL method to overdamp site response, whereas the kappa-corrected analysis enforces a specific Fourier amplitude decay that is substantially smaller compared to the non kappa-corrected analyses.

Figure 6-12 illustrates the sensitivity of *SAF* to the base case  $V_S$ . Each velocity base case produces a different resonant frequency, which contributes significantly to epistemic uncertainty at low frequencies. At low input loading levels, the conditional mean *SAF* functions cross near 1 Hz. This is the primary reason for the low epistemic uncertainty observed in Figure 6-12-. At higher input loading levels and at high frequencies, *SAF* becomes less sensitive to the base case velocity profiles.



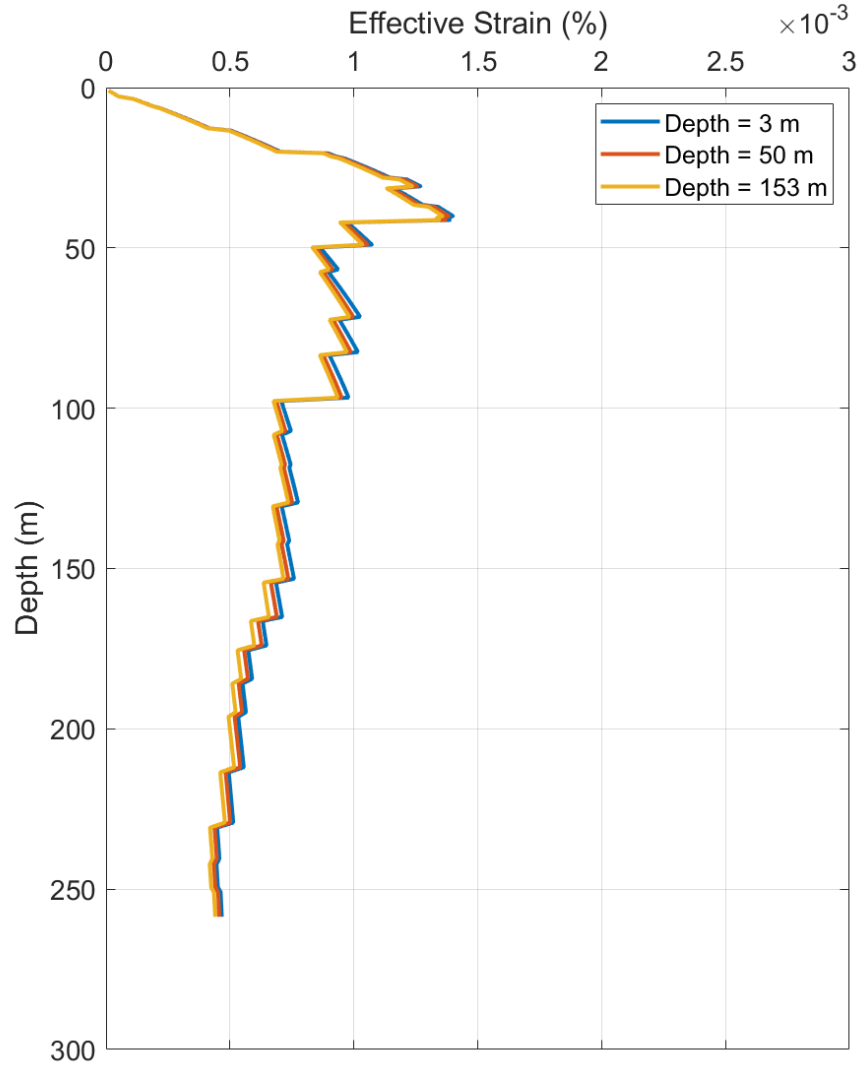
**Figure 6-9** *SAF* for a target site kappa of 0.036 s where the small strain damping curves are modified at depths deeper than 3 m, deeper than 50 m, and deeper than 153 m to achieve the target site kappa.

Figure 6-13 shows the sensitivity of *SAF* to the  $\kappa_0$ , which ranges from 0.021 to 0.076 s. The *SAF* is most sensitive to kappa at higher frequencies and low loading levels. As the soil becomes more nonlinear, the sensitivity of *SAF* to the input site kappa decreases slightly.

Figure 6-14 presents conditional mean *SAF* for the two sets of MRD curves used in the site response analyses. The results from the site-specific curves and the Darendeli and Stokoe MRD curves (Darendeli 2001) are generally similar. As a result, the *SAF* function is not very sensitive to the MRD curves used in the analyses.

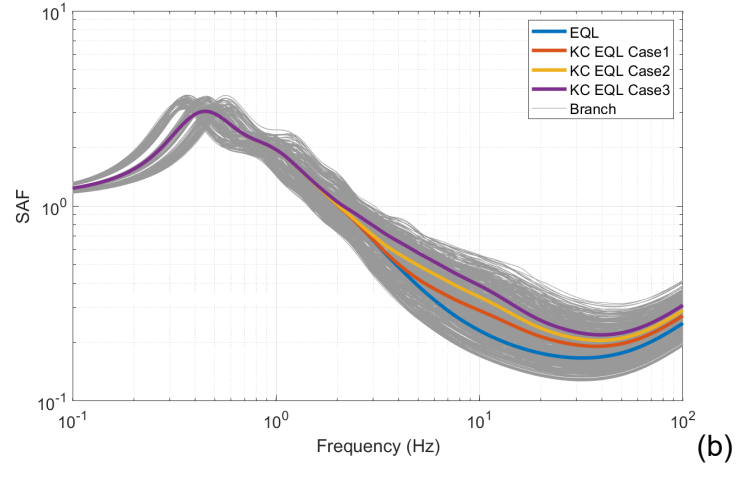
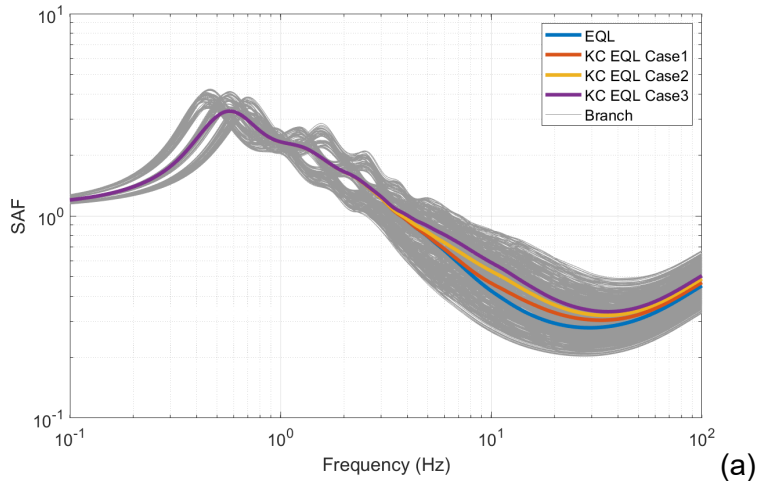
Figure 6-15 shows the sensitivity of *SAF* to the soil shear strength, which is used to constrain the shear modulus reduction at large strains. The *SAF* values do not demonstrate sensitivity to shear strength at low input loading levels because the shear strength does not affect the MRD curves at low strains. When shear strains are sufficiently large, the site response becomes sensitive to the specified soil shear strength. At SRS, this sensitivity did not become significant until the input PGA was 3 g. This high PGA at the reference rock is not expected to contribute significantly to the hazard at SRS.

Finally, Figure 6-16 shows that the *SAF* is not sensitive to the layer thickness randomization methods used for SRS. This is in part due to the constraints placed on the depth to reference rock in the randomization process. If the depth to reference rock was less constrained due to the absence of site information, the spectral amplification would likely be more sensitive to the thickness randomization approach.



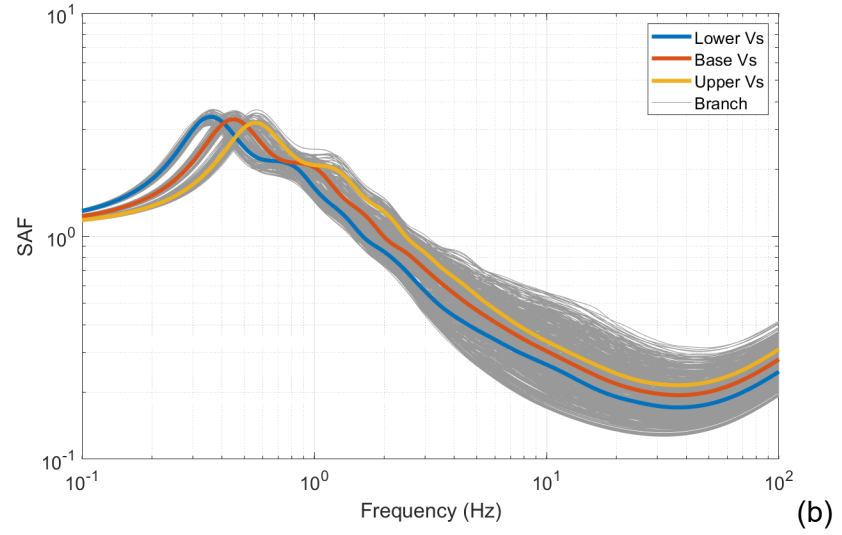
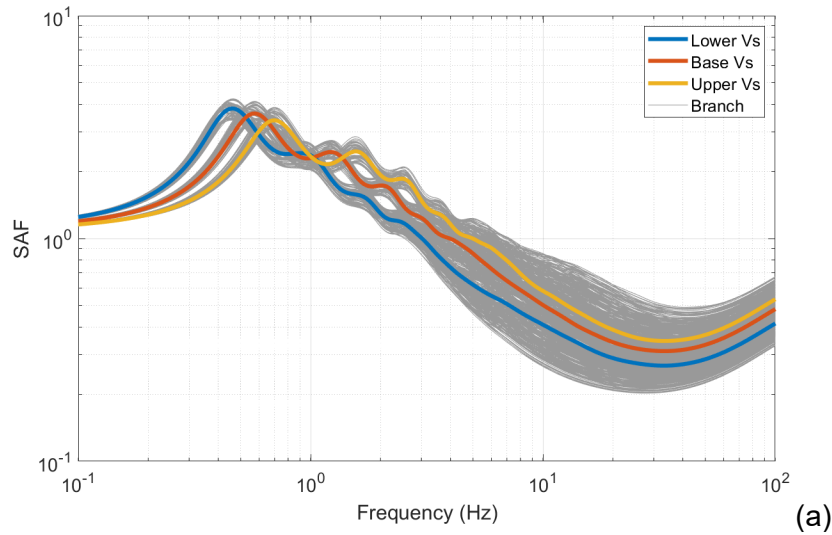
**Figure 6-10 Effective strain profiles with a target site kappa of 0.036 s where small strain damping was modified at depths below 3 m, 50 m, and 153 m to achieve the target site kappa.**

Figure 6-17 shows the variance contribution for each of the six logic tree nodes at four reference rock PGA levels. The bar charts show the percent contributions these six nodes make to the total variance for six oscillator frequencies (0.5 Hz, 1 Hz, 5 Hz, 10 Hz, 25 Hz, and 100 Hz). In Figure 6-17a, almost all the variance at low input loading levels comes from the  $V_S$  profile branches (for low frequencies) and  $\kappa_0$  branches (for higher frequencies). As the input loading level increases, the analysis method (EQL versus kappa-corrected EQL methods) begins to contribute more to the total variance, with the exception of the 0.5 Hz oscillator frequency, where the analysis method never significantly contributes to the variance. When the reference rock PGA is 0.43g, Figure 6-17c shows that the MRD curves are a stronger contributor to the variance only at the 1 Hz oscillator frequency. The *SAF* shown in Figure 6-14 do not show significant sensitivity to MRD curves, but because the total variability at 1 Hz is so low (natural log standard deviation of 0.06), the small changes in amplification due to differences in the MRD curve become a significant contributor to the variance.

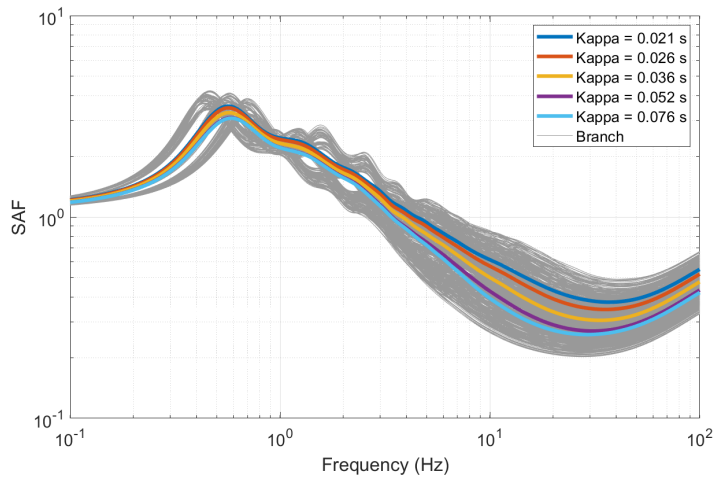


**Figure 6-11** *SAF* as a function of frequency for reference rock PGA of (a) 0.43 g, and (b) 1.2 g. The colored lines show *SAF* for the EQL and kappa-corrected analysis methods.

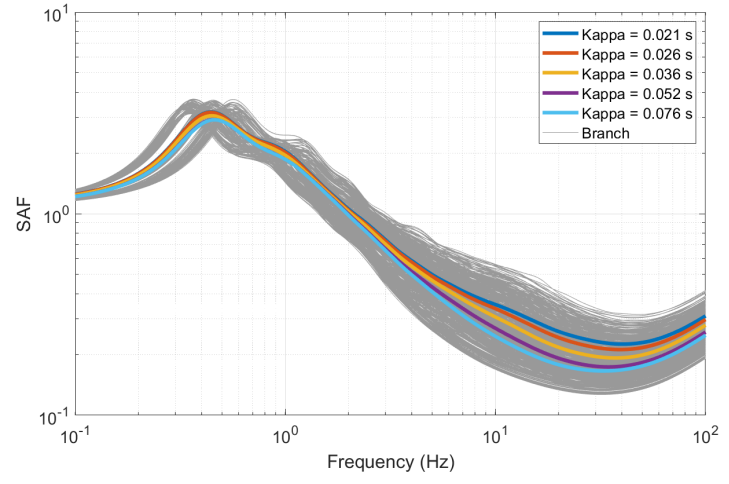
6-14



**Figure 6-12** *SAF* as a function of frequency for reference rock PGA of (a) 0.43 g, and (b) 1.2 g. The colored lines show *SAF* for the lower-, base-, and upper-case velocity profiles.

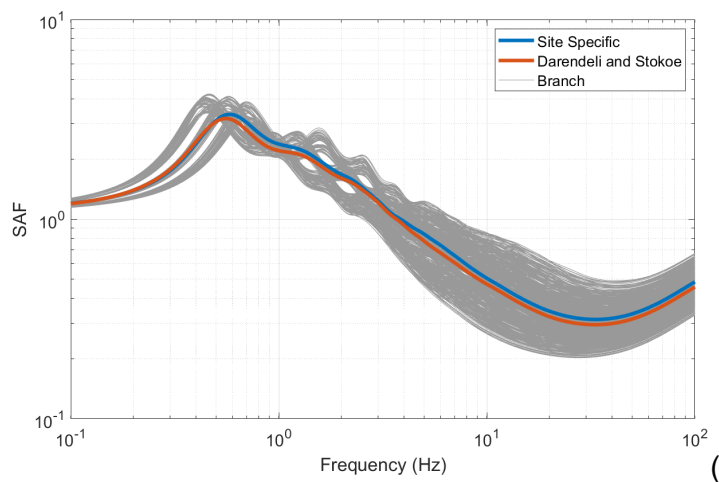


(a)

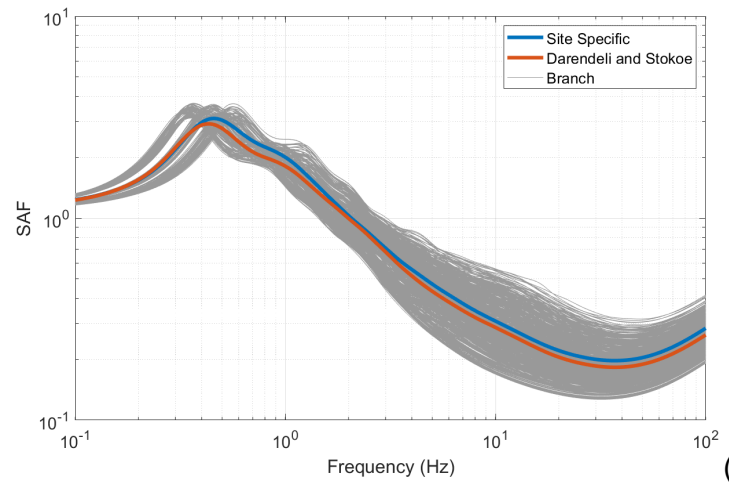


(b)

**Figure 6-13** SAF as a function of frequency for reference rock PGA of (a) 0.43 g, and (b) 1.2 g. The colored lines show SAF for the profile kappa values ranging from 0.021 to 0.076 s.

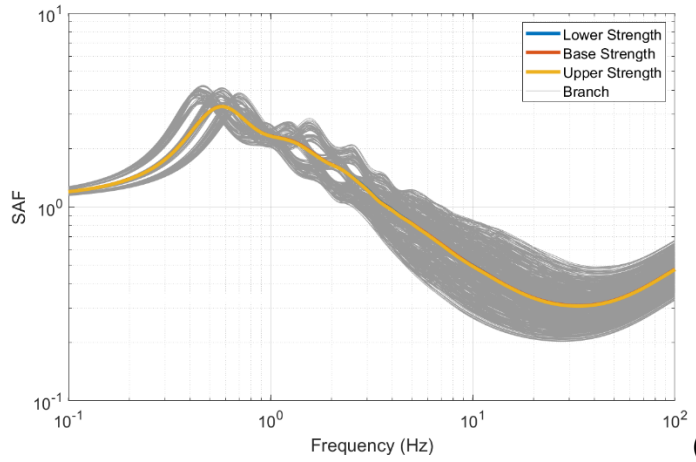


(a)

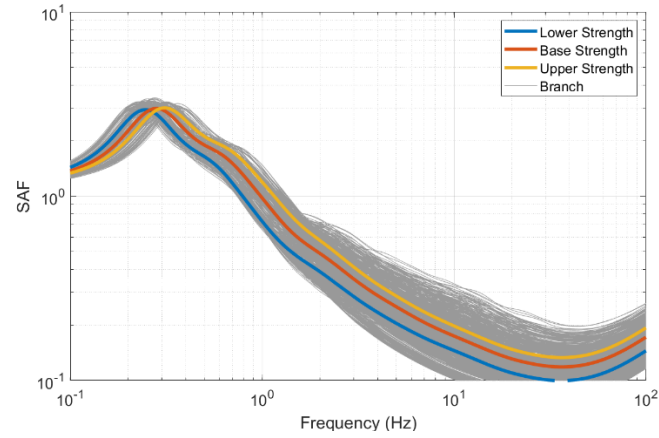


(b)

**Figure 6-14** SAF as a function of frequency for reference rock PGA of (a) 0.43 g, and (b) 1.2 g. The colored lines show SAF for the two MRD curve models.



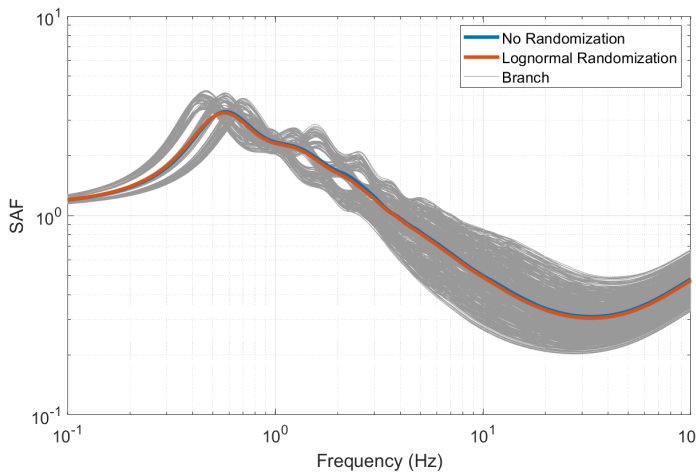
(a)



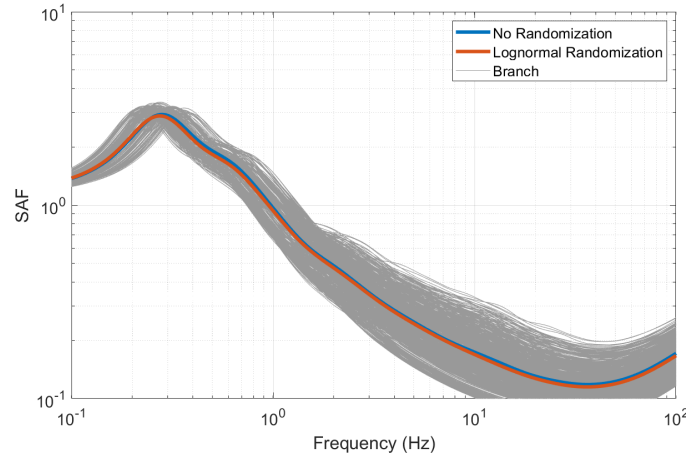
(b)

**Figure 6-15** *SAF* as a function of frequency for reference rock PGA of (a) 0.43g, and (b) 3g. The colored lines show *SAF* for the lower-, base- and upper-shear strength cases.

6-16

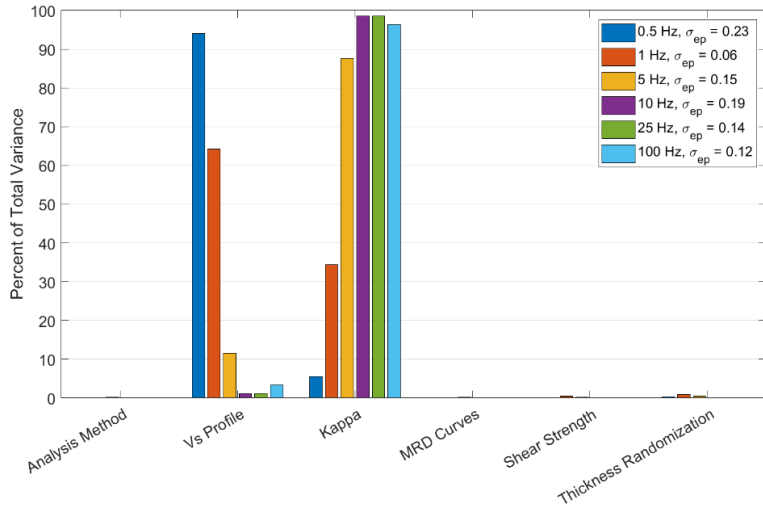


(a)

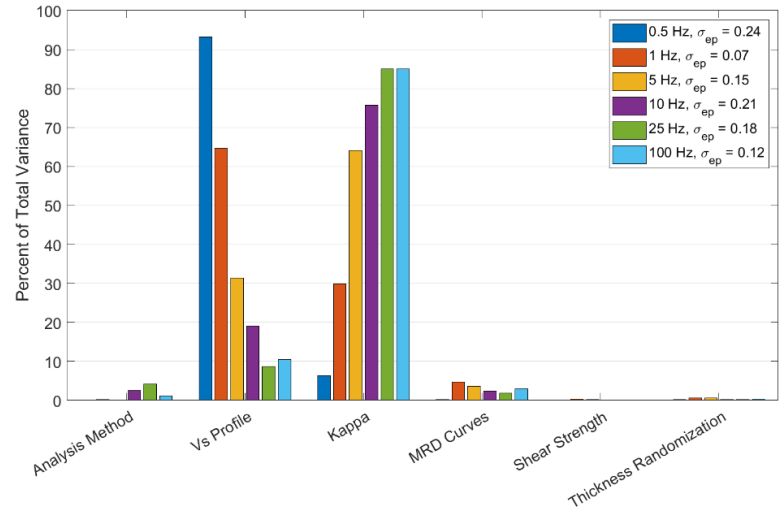


(b)

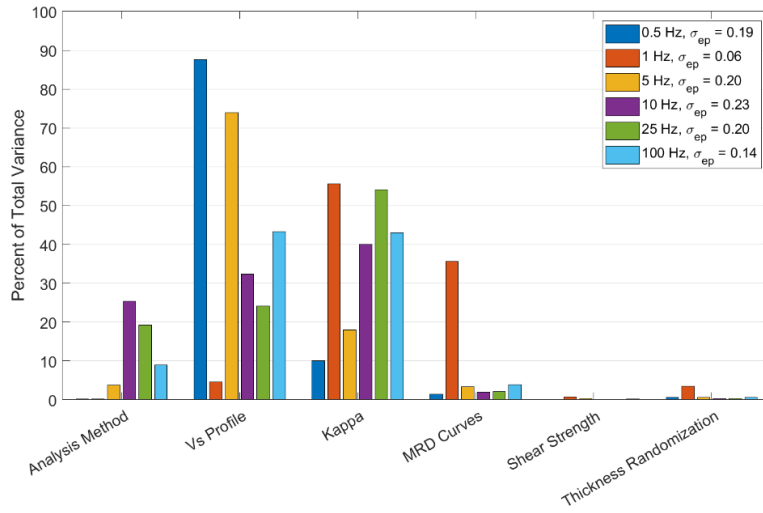
**Figure 6-16** *SAF* as a function of frequency for reference rock PGA of (a) 0.01 g, and (b) 3 g. The colored lines show amplification for when layer thickness is not randomized and when layer thickness is randomized assuming a lognormal distribution.



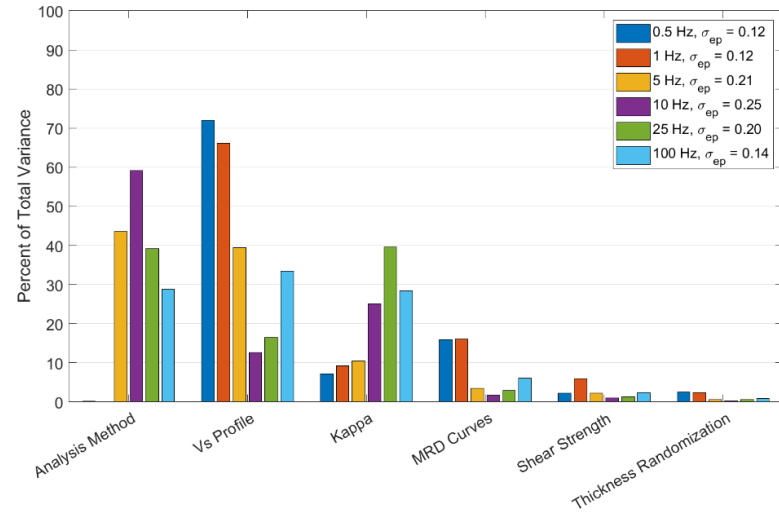
(a)



(b)



(c)



(d)

Figure 6-17 Variance contribution for a reference rock PGA of (a) 0.01 g, (b) 0.12 g (c) 0.43 g (d) 1.2 g.

The tornado plots shown in Figure 6-18 are another way to illustrate which nodes are contributing most to the variance in the *SAF*. Each tornado plot in Figure 6-18 is associated with one of the six oscillator frequencies and with an input reference rock PGA of 1.2g. The tornado plots illustrate that at the 1.2g input loading level and at low frequencies, the base case  $V_S$  profile contributes most to the variance in the *SAF*. At oscillator frequencies of 5 and 10 Hz, the analysis method is contributing most to *SAF* variance. Then, at the 25 Hz oscillator frequency  $\kappa_0$  is the most significant contributor followed closely by the analysis method. Finally, at 100 Hz, the  $V_S$  profile,  $\kappa_0$ , and analysis method all appear to have similar contributions to the *SAF* variance. These observations are consistent with the variance contribution calculations presented in Figure 6-17.

## 6.2 GVDA Study Site

### 6.2.1 Site Adjustment Factor Branches

Figure 6-19 shows the *SAF* as a function of the reference rock (760 m/s) spectral acceleration for the seven branches at four response spectral frequencies (1 Hz, 5 Hz, 10 Hz, and 100 Hz) for the GVDA study site. The mean log standard deviation is also shown below the *SAF*. The amplification function for each frequency shows a quick departure from a linear response at low amplitudes. The site's high impedance contrast between the shallow and deeper structure produces large *SAF*, which induces large strains for low input ground motion levels. For the 1 Hz oscillator frequency, the *SAF* rises from low to moderate loading levels and then begins to decrease at large loading levels. This can be explained by the nonlinear site response causing the  $V_S$  to reduce, and the site's natural frequency shifting from 2 Hz towards lower frequencies. Also, the *SAF* for the 1 Hz oscillator show two groupings of median *SAF* departing from one another for loading levels between 0.2g and 0.6g. This is a result of the significant differences in the alternative MRD curves used in the site response analyses, as will be shown later in this section. This effect can also be seen in the 5 Hz oscillator response between loading levels of about 0.3 and 1.0g. For frequencies above 5 Hz, a consistent gradual decrease in *SAF* occurs with increasing reference rock spectral acceleration. A review of the *SAF* for the 5 Hz, 10 Hz, and 100 Hz oscillator frequencies shows that at large reference rock spectral accelerations, the *SAF* continues to decrease. The TI Team considers this to be a representation of true physical response and does not consider it necessary to impose a lower limit on *SAF*. For all oscillator frequencies, the general trend of the aleatory variability is increasing with increased input loading levels.

### Minimum Epistemic Uncertainty

Epistemic uncertainty as a function of frequency for reference rock input motions with PGA of 0.01g, 0.39g, and 1.0g are presented in Figure 6-20. Epistemic uncertainty in spectral amplification is shown by the thick black line, and the horizontal red line highlights the desired minimum epistemic uncertainty of 0.15. For PGA = 0.01g, the epistemic uncertainty hovers at or below 0.15 for low input loading levels. The small epistemic uncertainty is most likely due to a combination of effects. First, the range of  $V_S$  profiles is constrained by surface wave inversions that are required to fit with the specific bounds of the experimental dispersion data. Second, the range of  $\kappa_0$  is small due to the availability of on-site recordings. For larger input loading levels, the epistemic uncertainty becomes larger than 0.15 minimum for all frequencies above 0.3 Hz.

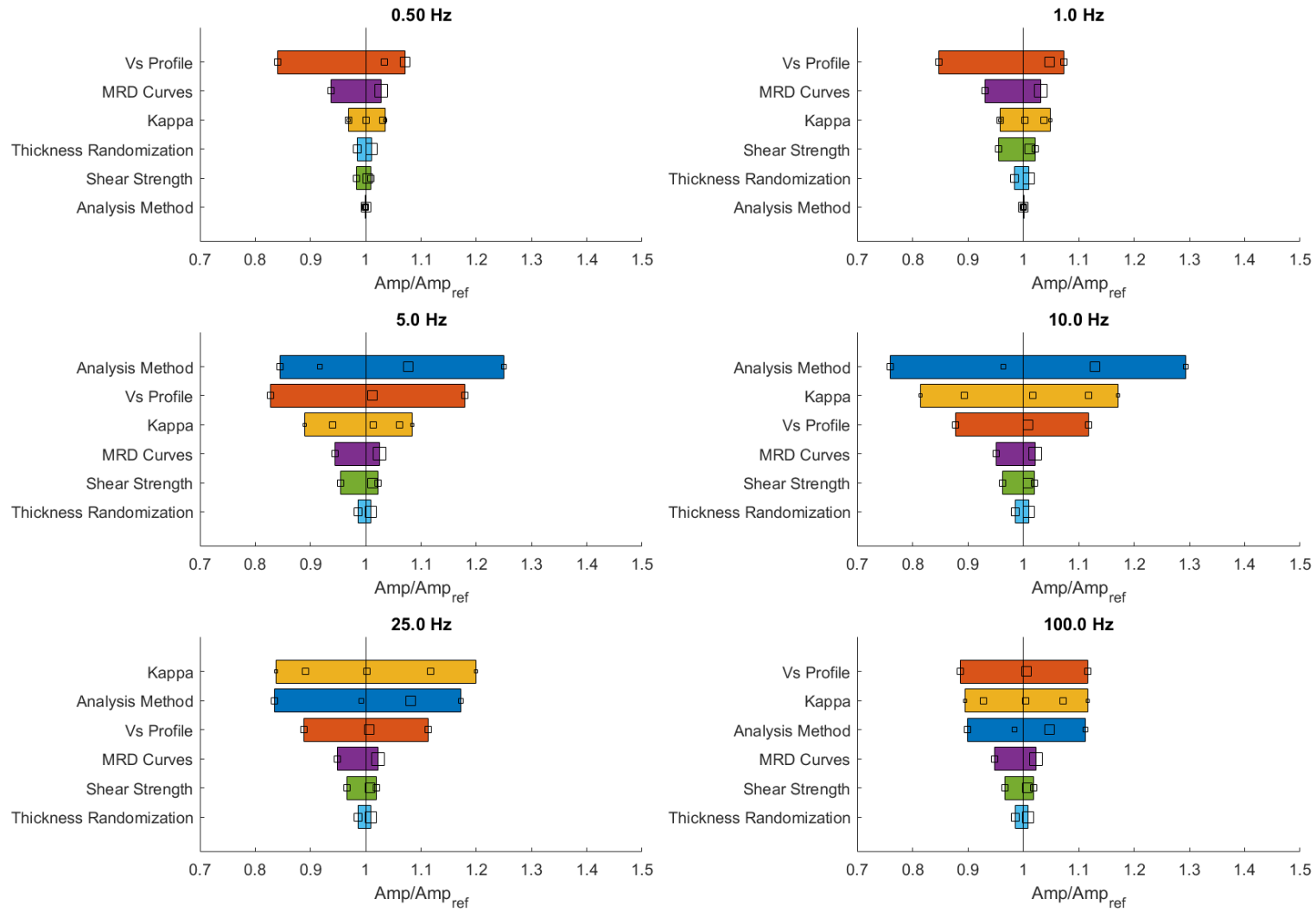


**Figure 6-18 Tornado plots for reference rock PGA of 1.2 g. The open square symbols represent mean branch amplification.**

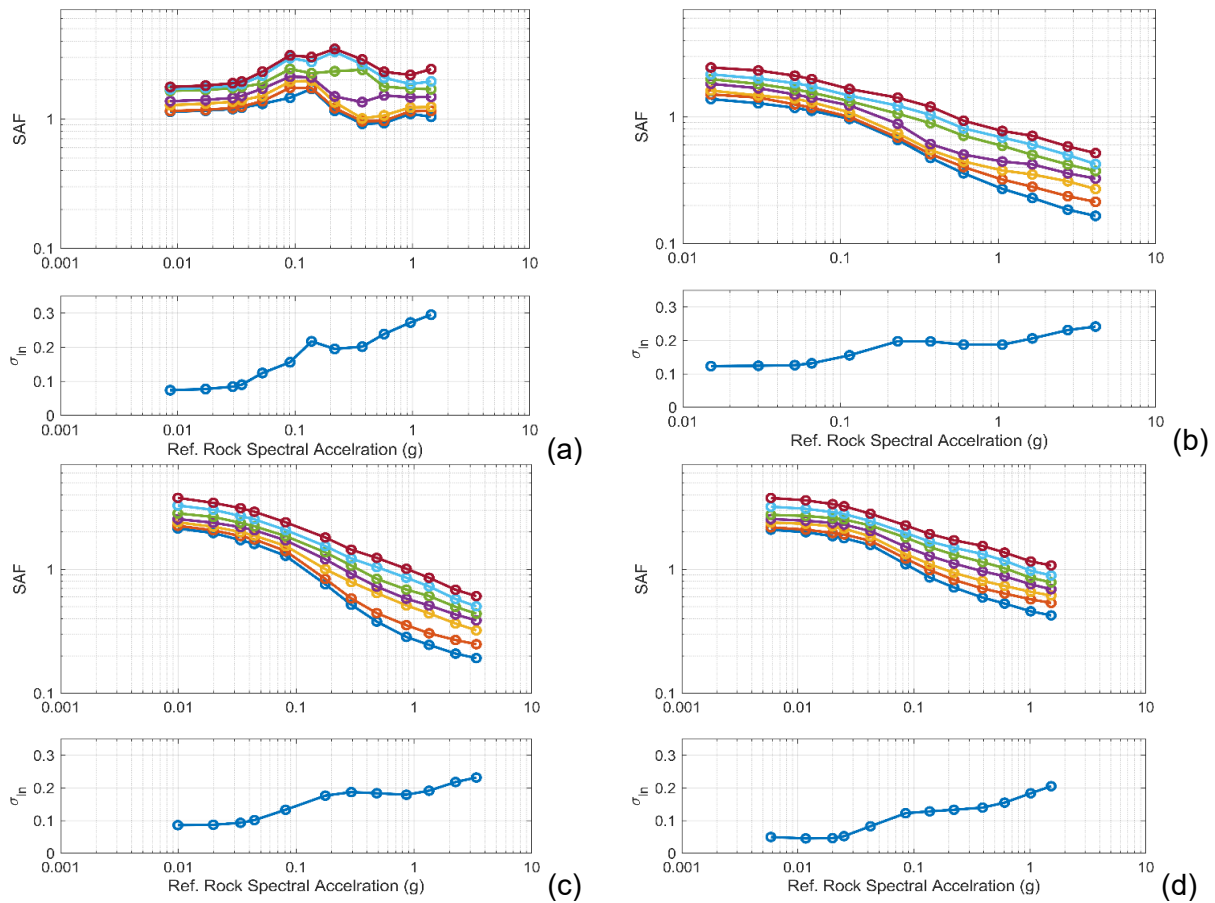


**Figure 6-19 SAF for seven epistemic branches and the log standard deviations (aleatory variability) for (a) 1 Hz, (b) 5 Hz, (c) 10 Hz, and (d) 100 Hz.**

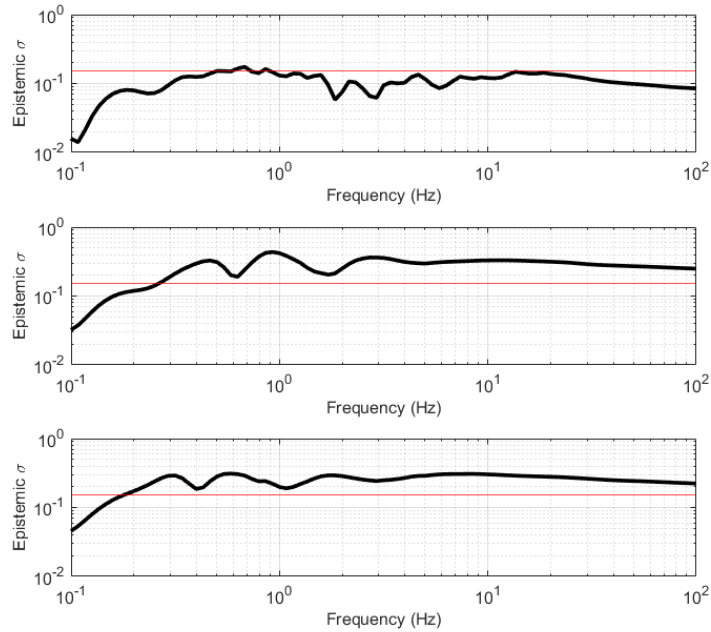


**Figure 6-20 Epistemic standard deviation of natural log spectral acceleration as a function of frequency for input reference rock PGA of (a) 0.01 g, (b) 0.39 g, and (c) 1.0 g.**

Figure 6-21 shows *SAF* for the 100 Hz oscillator with and without imposing a minimum epistemic uncertainty of 0.15. For the smaller loading levels, the epistemic uncertainty at 100 Hz (Figure 6-20) is below the threshold, so the median *SAF* are spread out to reflect the desired minimum epistemic uncertainty. For medium to large loading levels, the epistemic uncertainty at 100 Hz is above the minimum threshold and the resulting median *SAF* are unaffected.

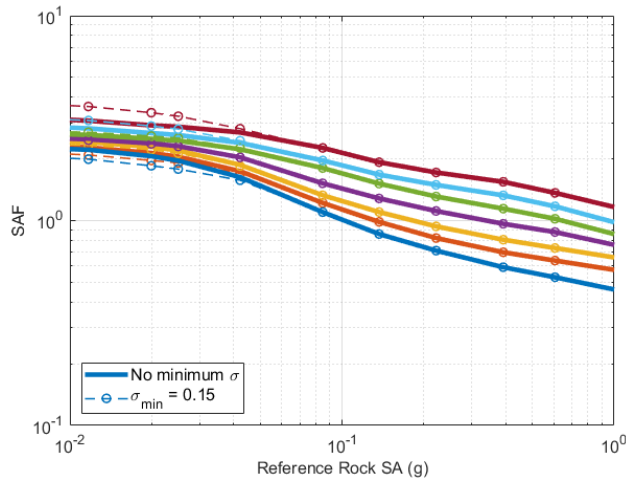


**Figure 6-21 100 Hz amplification with and without imposing minimum epistemic uncertainty.**

## Sensitivity to Logic Tree Nodes

The GVDA site response logic tree has five nodes (Figure 5-23) for which analyses were performed to determine individual branch effects on *SAF* and nodal contributions to the epistemic uncertainty on site amplification. Plots of conditional mean *SAF*, bar charts of variance contribution, and tornado plots are three visual approaches used to illustrate sensitivity on *SAF* with changes in input loading levels.

Figure 6-22 through Figure 6-26 show the conditional mean *SAF* as a function of frequency for two loading levels for each of the five nodes. The sensitivity on *SAF* from alternative analysis methods is illustrated in Figure 6-22, where one observes that *SAF* is not sensitive to alternative analysis methods at frequencies below 2 Hz. This is expected because kappa corrections will have little to no effect on the FAS at low frequencies. At higher frequencies, effects of the kappa correction method on *SAF* are more apparent with increased sensitivity as loading levels increase. The increased sensitivity to analysis method with loading level is expected due to increased soil nonlinearity that produces a steeper drop-off of the FAS resulting in the kappa correction method producing higher spectral acceleration values at high frequencies. Figure 6-23 illustrates the sensitivity of *SAF* to the base case  $V_S$  profiles. Each velocity case produces varying levels of amplitude and alternative resonant frequencies which contribute to a larger epistemic uncertainty at low frequencies compared to high frequencies, where resonant peaks are not present. Similar trends are seen for both loading levels, with the lower loading level showing somewhat more epistemic uncertainty.

Figure 6-24 shows the sensitivity of *SAF* to the  $\kappa_0$ , which ranges from 0.013 to 0.028 s. The low sensitivity to kappa can be explained by the small range of kappa values measured from on-site recordings. The amplification function is somewhat sensitive to kappa at higher frequencies and low loading levels. As the soil becomes more nonlinear, the sensitivity of spectral amplification to  $\kappa_0$  reduces.

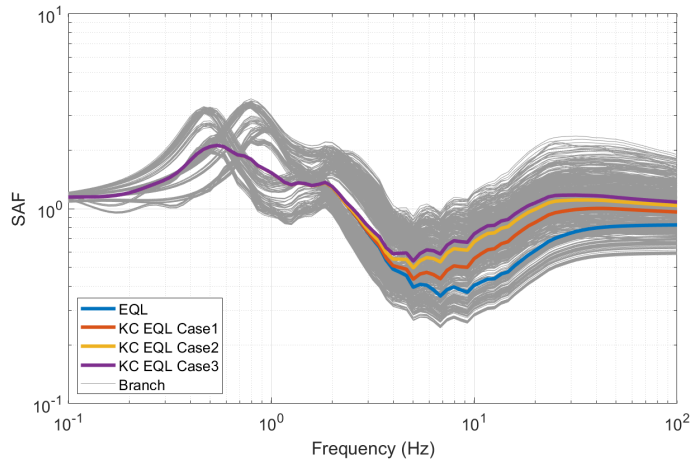
Figure 6-25 presents *SAF* for the MRD curves used in the site response analyses. The site specific curves and Darendeli and Stokoe MRD curves (Darendeli, 2001) are significantly different, resulting in *SAF* that are highly sensitive to the MRD curves used in the analyses. Figure 6-25 helps to explain the results in 1 Hz site amplification shown in Figure 6-19. For the moderate loading level of 0.39g, the modal peaks resulting from the alternative MRD curves are very different due to the different levels of nonlinearity modeled by the two sets of MRD curves. The modal peak from the Darendeli and Stokoe MRD curves (Darendeli, 2001) falls close to 1 Hz, while the modal peak for the site-specific curve falls around 0.5 Hz. The separation of the two distinct modal peaks is large enough such that, at some oscillator frequencies (e.g, 1 Hz), the spectral amplitudes from the site-specific MRD curves are significantly smaller than those of Darendeli and Stokoe (Darendeli, 2001). For higher loading levels (1.0 g), the separation of modal peaks is not as severe, and thus the contribution to epistemic uncertainty is less.

Figure 6-26 shows the sensitivity of *SAF* to the soil shear strength, which is used to constrain the shear modulus reduction at large strains. The *SAF* values do not demonstrate sensitivity to shear strength at low to moderate input loading levels because the shear strength does not affect the modulus reduction curves at low to moderate strains. When shear strains are sufficiently large, the site response is sensitive to the specified soil shear strength.

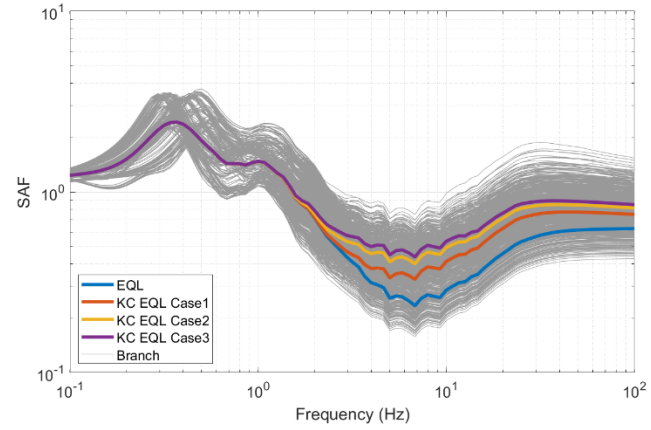
Figure 6-27 shows the variance contribution for the five logic tree nodes at four reference rock input PGAs. The bar charts show the percent contribution these five nodes make to the total variance for six oscillator frequencies (0.5 Hz, 1 Hz, 5 Hz, 10 Hz, 25 Hz, and 100 Hz). This

figure clarifies how each node in the logic tree contributes to the epistemic uncertainty in site amplification. For example, in Figure 6-27a, one can see that for 0.5 Hz, almost all variance at low input loading levels comes from the velocity profile with only a small portion contributed from  $\kappa_0$ . As input loading levels increase (Figure 6-27 b, c, and d), the contribution from the  $V_S$  profile node decreases while the contributions from the MRD node and analysis method node increase.

The tornado plots shown in Figure 6-28 are another way to illustrate which nodes are contributing most to variance in the *SAF*. Each tornado plot in Figure 6-28 is associated with one of the six oscillator frequencies and with an input reference rock PGA of 1.0 g. The tornado plots illustrate that at the 1.0g input loading level, the MRD curves contribute most to variance in *SAF* at 0.5 Hz. At 1.0 Hz, the  $V_S$  profile contributes most, and at frequencies of 5, 10, and 25 Hz, the analysis method contributes most. These observations are consistent with the variance contribution calculations presented in Figure 6-27.



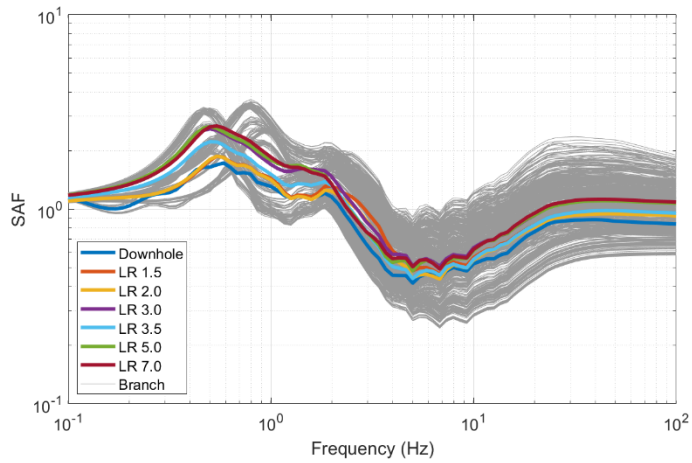
(a)



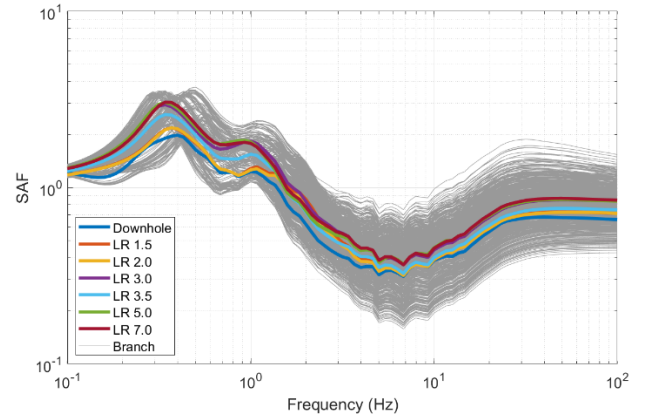
(b)

**Figure 6-22** *SAF* as a function of frequency for reference rock PGA of (a) 0.39 g and (b) 1.0 g. The colored lines show *SAF* for the EQL and kappa-corrected analysis methods.

6-24

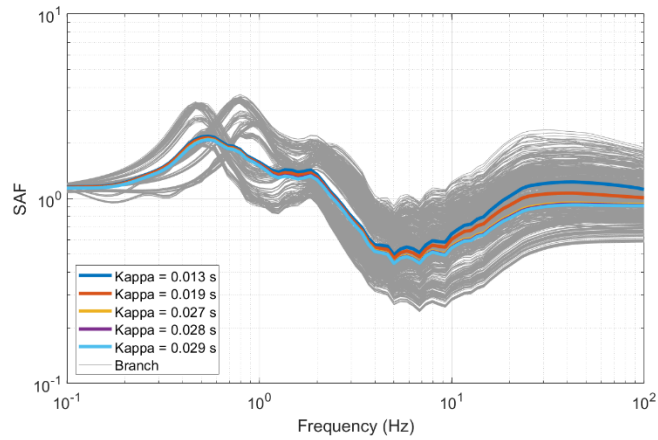


(a)

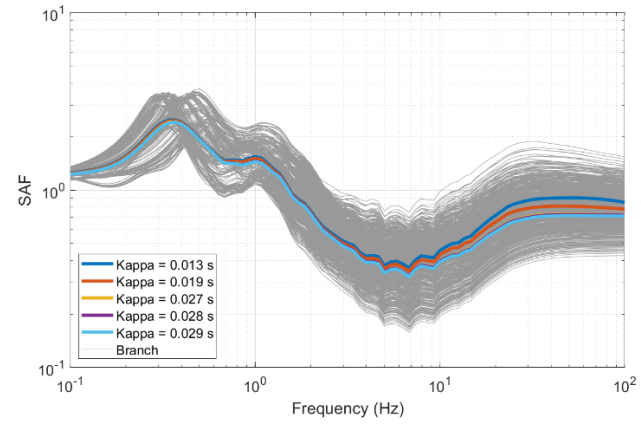


(b)

**Figure 6-23** *SAF* as a function of frequency for reference rock PGA of (a) 0.39 g and (b) 1.0 g. The colored lines show *SAF* for the alternative velocity profiles.



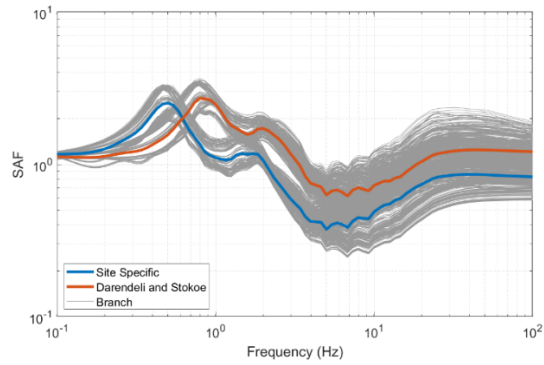
(a)



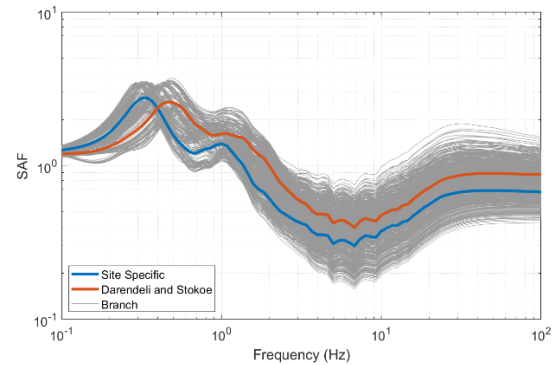
(b)

**Figure 6-24** *SAF* as a function of frequency for reference rock PGA of (a) 0.39 g and (b) 1.0 g. The colored lines show *SAF* for the profile kappa values ranging from 0.013 to 0.028 s.

6-25

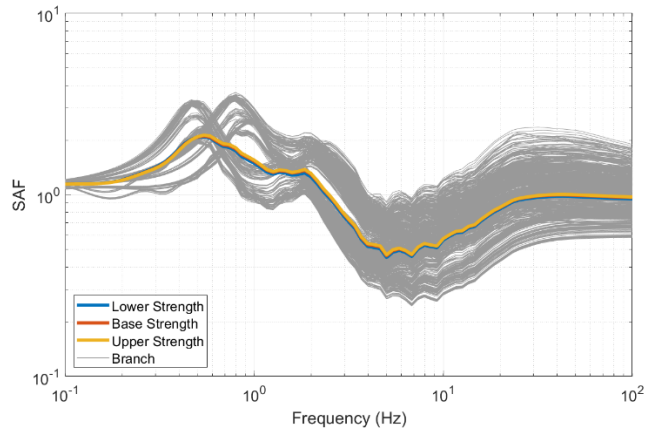


(a)

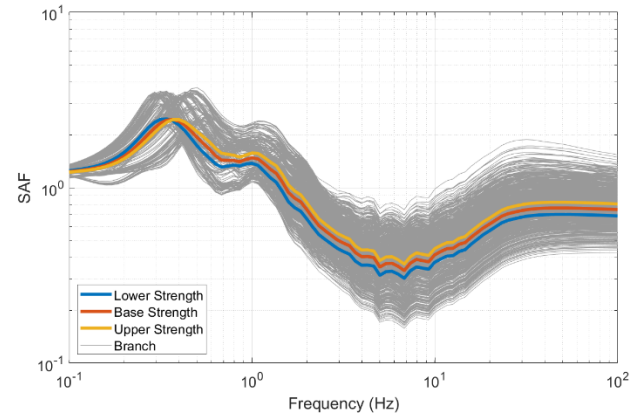


(b)

**Figure 6-25** *SAF* as a function of frequency for reference rock PGA of (a) 0.39 g, and (b) 1.0 g. The colored lines show *SAF* for the two MRD curves models.

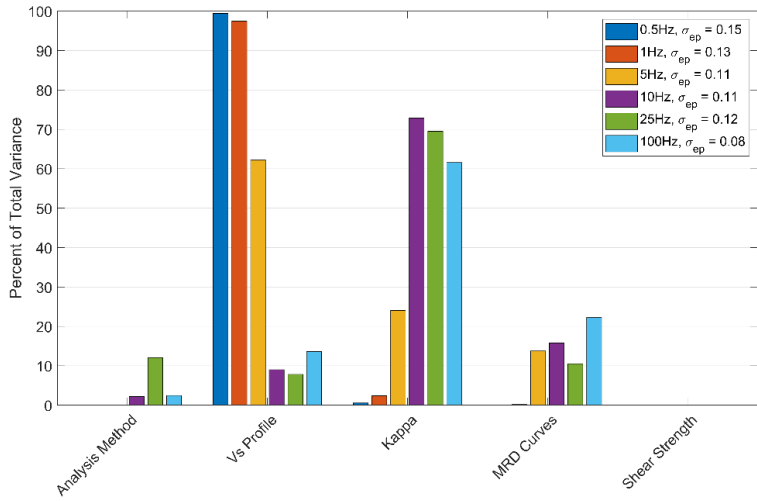


(a)

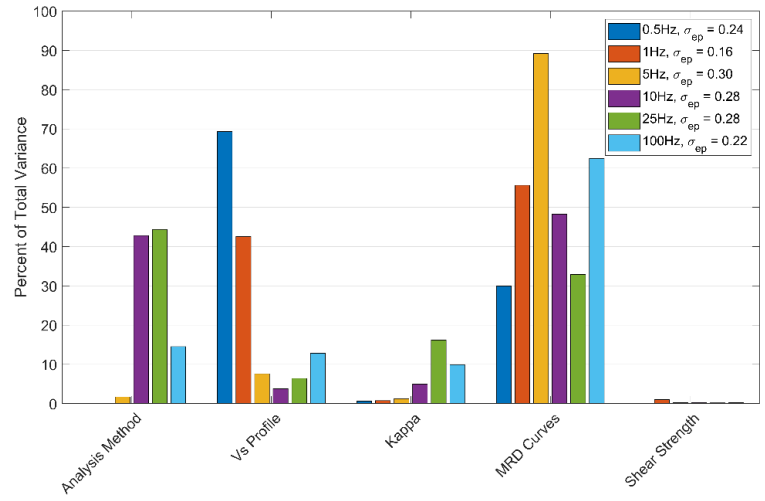


(b)

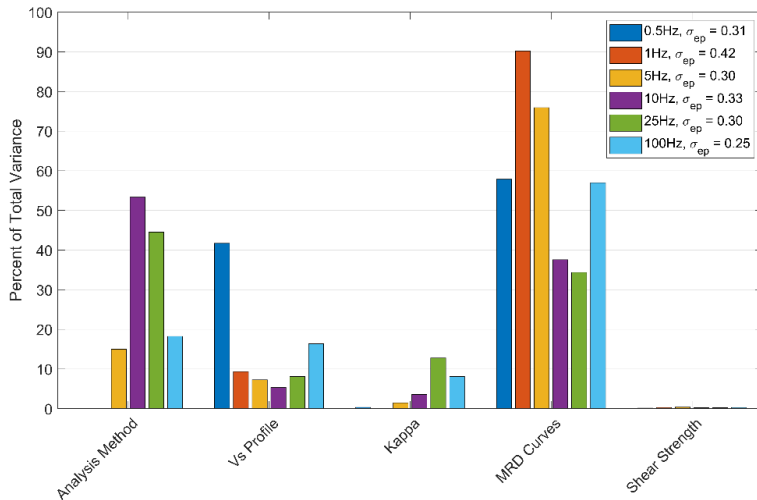
**Figure 6-26** *SAF* as a function of frequency for reference rock PGA of (a) 0.39 g and (b) 1.0 g. The colored lines show *SAF* for the lower-, base- and upper-shear strength cases.



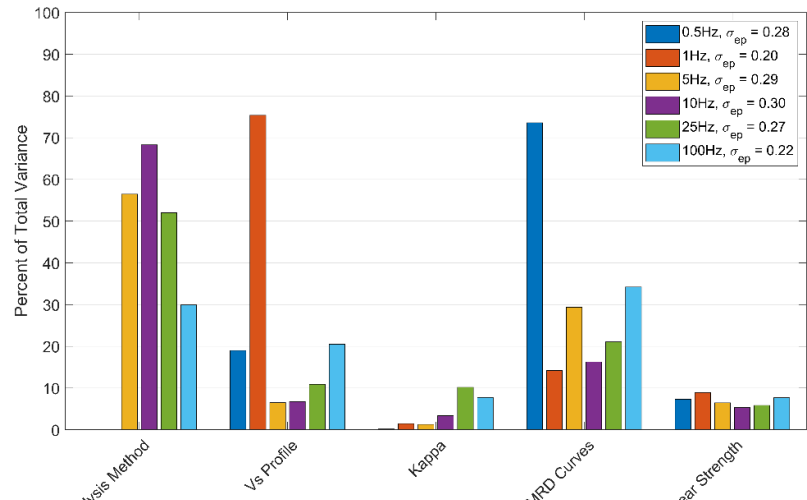
(a)



(b)



(c)



(d)

Figure 6-27 Variance contribution for a reference rock PGA of (a) 0.01 g, (b) 0.14 g, (c) 0.39 g, and (d) 1.0 g.

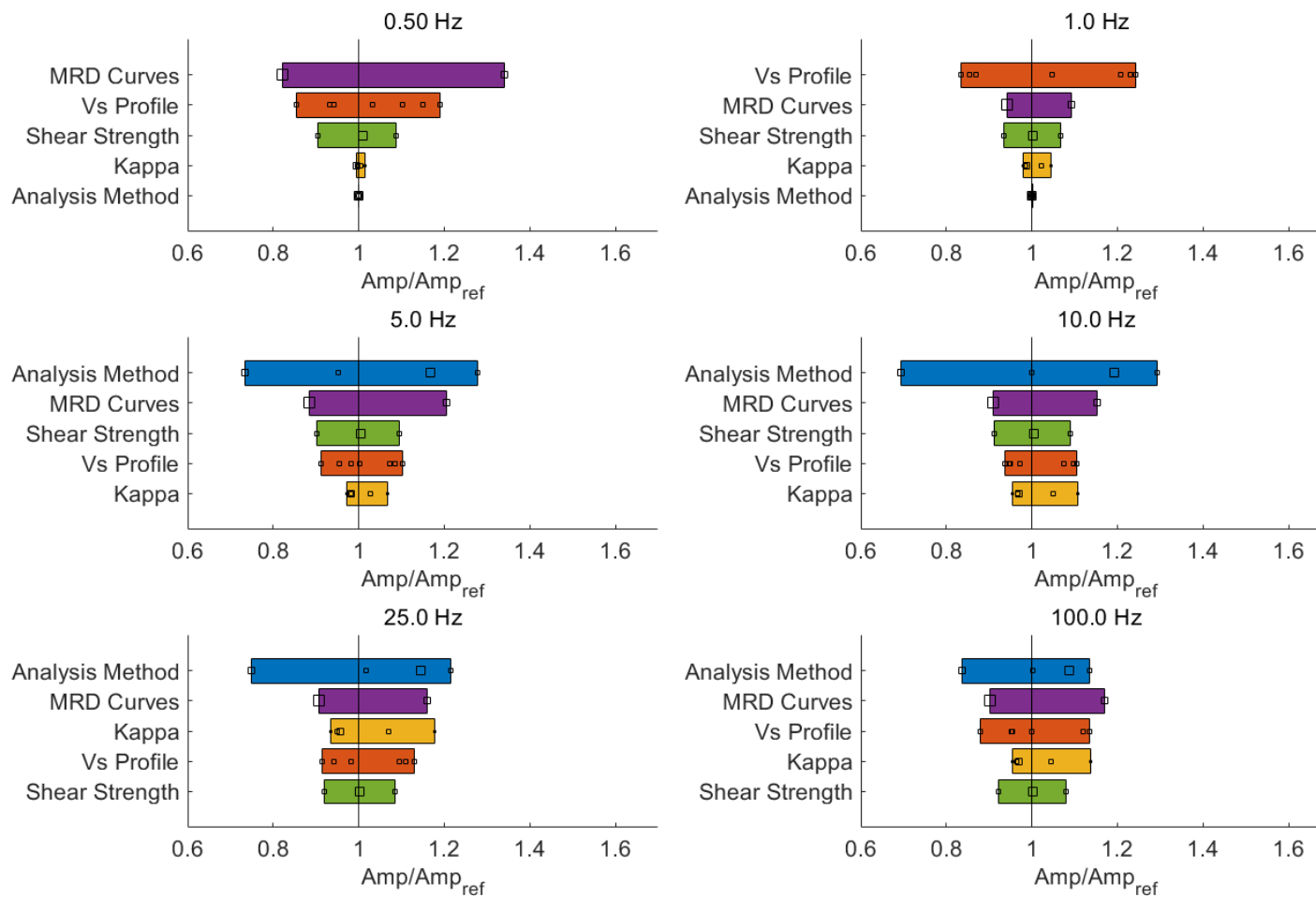


**Figure 6-28** Tornado plots for reference rock PGA of 1.0 g. The open square symbols represent mean branch *SAF*, where the size of the symbol represents the relative weight for a branch.

## 6.2.2 Empirical Site Term

Because the GVDA study site has a significant number of on-site recordings, the TI Team investigated the possibility of computing an empirical site term to be used in soil hazard calculations. However, the SWUS GMM used in the hazard calculation is missing two key components necessary for computing an empirical site term. First, the SWUS GMM does not allow for  $V_{S30}$  corrections, and thus does not afford the determination of within-event residuals that are a key component in the computation of an empirical site term. Secondly, the SWUS GMM does not have a nonlinear site amplification component to adjust predicted ground motions at higher loading levels for sites with in-situ conditions less than the SWUS reference condition of 760 m/s. In spite of these issues, the TI Team wanted to use the site-specific data in some way to inform the results of the analytical site response analyses. Thus, the TI Team chose to compute a linear empirical site term to evaluate how well the analytical approach to linear site amplification compared with the observed ground motions. However, another hurdle in computing a site term is that there are no event terms for the SWUS GMM. To work around this, the TI Team assumed that the NGA-West2 models (Abrahamson et al., 2013; Boore et al., 2013; Campbell and Bozorgnia, 2013; and Chiou and Youngs, 2013) which have event terms, apply to the SWUS GMM. Thus, the average empirical site term for GVDA can be computed by

$$\delta S2S = \frac{1}{N} \sum_{e=1}^N \frac{1}{M} \sum_{j=1}^M \delta W_{es,j} \quad (\text{Eq. 6-3})$$

Where  $\delta S2S$  is the average site term,  $N$  is the number of events,  $M$  is the number of NGA-West2 GMMs evaluated and  $\delta W_{es,j}$  is the within-event residual with respect to the site-specific condition defined as

$$\delta W_{es,j} = \ln(Sa_{obs,e}) - (Sa_{e,j}) \quad (\text{Eq. 6-4})$$

Where  $Sa_{obs,e}$  is the observed ground motion from event  $e$ , and  $Sa_{e,j}$  is the modified predicted ground motion for event  $e$ , defined as

$$\ln(Sa_{e,j}) = \ln AF_{rel} + \ln(Sa_{GMPE,j}) + \delta B_{e,j} \quad (\text{Eq. 6-5})$$

where  $\ln AF_{rel}$  is the relative linear amplification between the site and the reference site condition (derived from the analytical site response modeling),  $Sa_{GMPE,j}$  is the predicted ground motion from NGA-West2 GMM  $j$  for the reference site condition, and  $\delta B_{e,j}$  is the event term for event  $e$  associated with NGA-West2 GMM  $j$ . Modifying the predicted ground motion by  $\ln AF_{rel}$  and observing the resulting empirical site term affords the TI Team the ability to assess how well analytical site response analyses predict actual site response at the GVDA study site.

For computation of the empirical site-term, the TI Team required that events recorded on-site be selected from the NGA-West2 database that met the following three criteria. First, the event must have an on-site recorded ground motion of 0.01g or less to ensure a linear response. Second, the closest distance to the earthquake rupture plane ( $r_{rup}$ ) must be less than 100 km. Finally, event terms (GeoPentech, 2015) must be available for each of the NGA-West2 GMMs. A total of 16 events meeting the above requirements were selected from the database, and the magnitudes of those events ranged from 3.6 to 4.73 with  $r_{rup}$  distances ranging from 27 km to 90 km. The observed on-site ground motion  $Sa_{obs,e}$  was computed as the geometric mean of the two recorded horizontal components of motion for each event  $e$ .

The relative amplification  $lnAF_{rel}$  used in the determination of the site term is computed using linear site response analyses consistent with the one-step approach of Section 3.1. The  $lnAF_{rel}$  is computed as the average amplification between the 594 multi-channel analysis of surface wave (MASW)/microtremor array measurements (MAM) inverted profiles (extended to the bottom of the host profile depth as described in Section 5.2) and the SWUS host profile. The site kappa for the GVDA and SWUS profiles are 0.027 s and 0.041 s, respectively. The input motion used in the analyses is a single corner point source model with western U.S. source parameters with a magnitude and  $r_{rup}$  distance of 4.0 and 66 km, respectively. The magnitude and distance parameters were computed from the average of the 16 events selected from the NGA-West2 database.

The resulting empirical site term, with respect to the site-specific  $V_S$  profile, is shown in Figure 6-29. If the computed  $lnAF_{rel}$  for GVDA were exact, then the site term would have values of zero across all frequencies represented by the red line. While not exact, the empirical site term hovers close to zero over a wide range of frequencies and generally falls within the 95% confidence interval represented by the error bands. These results gave the TI Team confidence that the analytical amplification functions being computed are representative of the site amplification for the GVDA study site.

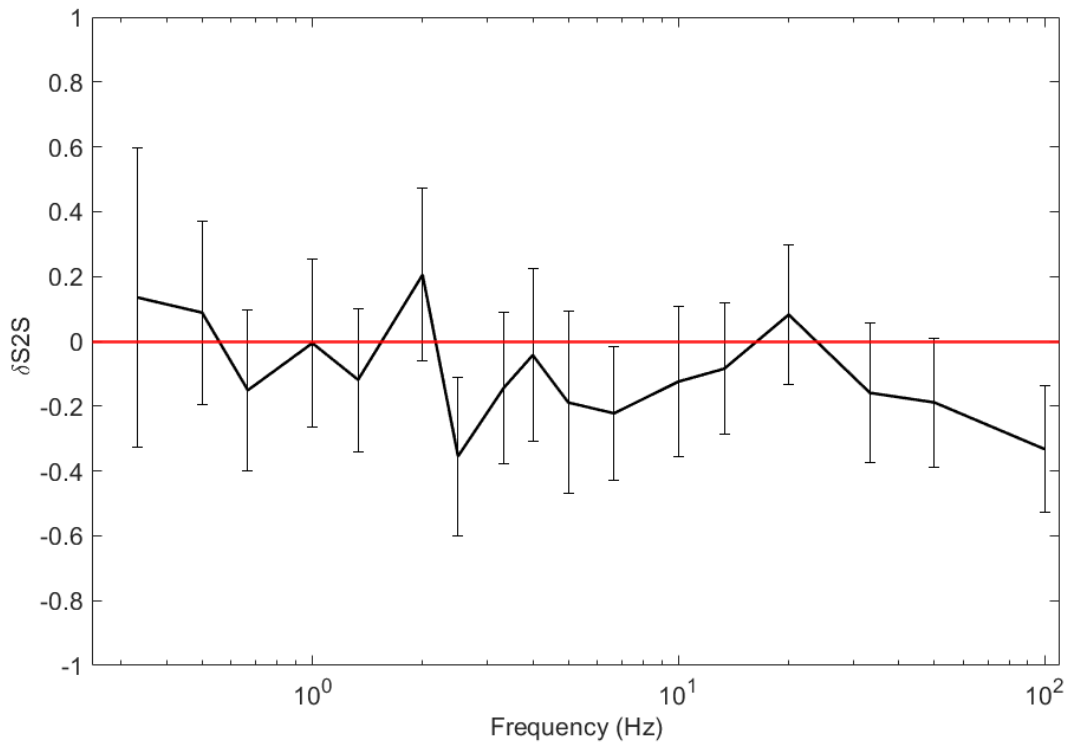


**Figure 6-29 Empirical site term with respect to the site-specific condition (solid black line) with 95% confidence intervals (black bars).**

### 6.3 References

Abrahamson, A., W. Silva, and R. Kamai. "Update of the AS08 Ground-Motion Prediction Equations Based on the NGA-West2 Data Set." PEER Report 2013/04. Pacific Earthquake Engineering Research Center, University of California, Berkeley, California. 2013.

Baker, J.W. "Conditional Mean Spectrum: Tool for Ground-Motion Selection." *Journal of Structural Engineering*. Vol. 137, No. 3. pp. 322–331. 2011.

Bazzurro, P. and C.A. Cornell. "Ground-Motion Amplification in Nonlinear Soil Sites with Uncertain Properties." *Bulletin of the Seismological Society of America*. Vol. 94, No. 6. pp. 2090–2109. 2004.

Boore, D., J. Stewart, E. Seyhan, and G. Atkinson. "NGA-West2 Equations for Predicting Response Spectral Accelerations for Shallow Crustal Earthquakes." PEER Report 2013/05. Pacific Earthquake Engineering Research Center, University of California, Berkeley, California. 2013.

Campbell, K. and Y. Bozorgnia. "NGA-West2 Campbell-Bozorgnia Ground Motion Model for the Horizontal Components of PGA, PGV, and 5%-Damped Elastic Pseudo-Acceleration Response Spectra for Periods Ranging from 0.01 to 10 sec." PEER Report 2013/06. Pacific Earthquake Engineering Research Center, University of California, Berkeley, California. 2013.

Chiou, B. and R. Youngs. "Update of the Chiou and Youngs NGA Ground Motion Model for Average Horizontal Component of Peak Ground Motion and Response Spectra." PEER Report

2013/07. Pacific Earthquake Engineering Research Center, University of California, Berkeley, California. 2013.

Coppersmith, K., J. Bommer, K. Hanson, R. Coppersmith, J. Unruh, L. Wolf, B. Youngs, L. Al Atik, A. Rodriguez-Marek, and G. Toro. "Hanford Sitewide Probabilistic Seismic Hazard Analysis." Prepared for the U.S. Department of Energy Under Contract DE-AC06076RL01830, and Energy Northwest, Pacific Northwest National Lab Report PNNL-23361. November 2014.

Darendeli, M.B. "*Development of a New Family of Normalized Modulus Reduction and Material Damping Curves.*" Dissertation. University of Texas, Austin, Texas. 2001.

GeoPentech. "Southwestern United States Ground Motion Characterization SSHAC Level 3, *Technical Report, Revision 2.*" 2015.

Goulet, C., Y. Bozorgnia, N. Abrahamson, N. Kuehn, L. Al Atik, R. Youngs, and R. Graves. "Central and Eastern North America Ground-Motion Characterization." PEER Report No. 2018/08, Pacific Earthquake Engineering Research Center at the University of California, Berkeley. 2018.

Hashash, Y.M.A., M.I. Musgrove, J.A. Harmon, O. Ilhan, G. Xing, O. Numanoglu, D.R. Groholski, C.A. Phillips, and D. Park. "DEEPSOIL 7, User Manual." Urbana, Illinois: Board of Trustees of University of Illinois at Urbana-Champaign. 2020.

Kaklamanos, J., B.A. Bradley, E.M. Thompson, and L.G. Baise. "Critical Parameters Affecting Bias and Variability in Site-Response Analyses Using KiK-net Downhole Array Data." *Bulletin of the Seismological Society of America*. Vol. 103, No. 3. pp. 1733–1749. 2013.

Miller, A C. and T.R. Rice. "Discrete Approximations of Probability Distributions." *Management Science*. Vol. 29, No. 3. pp. 352–362. 1983.

Rodriguez-Marek, A., J.J. Bommer, R.R. Youngs, M.J. Crespo, P.J. Stafford, and M. Bahrapouri. "Capturing Epistemic Uncertainty in Site Response." *Earthquake Spectra*. Vol. 37, No. 2. pp. 921–936. 2021.

Silva, W. "Modeling Uncertainty for Site Response at INL, Excerpts From Pacific Engineering and Analysis Report. personal communication. 2015.

Stewart, J.P. and K. Afshari. "Epistemic Uncertainty in Site Response as Derived From One-Dimensional Ground Response Analyses." *Journal of Geotechnical and Geoenvironmental Engineering*. Vol. 147, No. 1. p. 04020146. 2021.

Ulmer, K.J., A. Rodriguez-Marek, and R.A. Green. "Accounting for Epistemic Uncertainty in Site Effects in Probabilistic Seismic Hazard Analysis." *Bulletin of the Seismological Society of America*. Vol. 111. pp. 2005–2020. 2021. doi: 10.1785/0120200343

## 7 Control Point Hazard Results

### 7.1 Background

The Technical Integration (TI) Team calculated the control point hazard at the Savannah River Site (SRS) and Garner Valley Downhole Array (GVDA) study sites using both Approach 3 and Approach 4, as described in Section 3.4. Approach 3 was implemented using both the Hazard Integral Approach, which simultaneously determines the reference condition hazard and incorporates the site response into the full hazard integral, and the Convolution Approach, which convolves the pre-determined reference condition hazard with the site adjustment factors (*SAFs*). To determine the control point hazard at these two demonstration sites, the TI Team implemented the *SAFs* calculated from the site response analyses, which are presented in Section 6 of this report. For both sites, the control point elevation was chosen at the ground surface. The TI Team calculated control point hazard curves for the spectral frequencies specified by the Next Generation Attenuation (NGA)-East Ground Motion Model (GMM) (Goulet et al., 2018) for the SRS study site and the spectral frequencies of the southwestern United States-Diablo Canyon Power Plant (SWUS-DCPP) GMM (GeoPentech, 2015) for the GVDA study site. Seismic hazard was calculated for 39 ground motion amplitudes ranging from 0.001g to 6.31g. From the distribution of control point hazard curves for each of the spectral frequencies, the TI Team determined the mean hazard as well as the hazard for multiple fractile levels. In addition to calculating control point hazard curves for both demonstration sites, the TI Team also determined horizontal mean uniform hazard response spectra (UHRS) and ground motion response spectra (GMRS) using the equations in ASCE/SEI 43-19 (ASCE/SEI, 2021). All ground motions presented in this report are pseudo horizontal spectral accelerations at 5 percent of critical damping.

As described in Sections 6.1.1 (SRS) and 6.2.1 (GVDA) of this report, prior to implementing the *SAFs* into Approaches 3 and 4, the TI Team evaluated the epistemic uncertainty of the seven *SAF* medians for each of the GMM spectral frequencies to ensure that a minimum epistemic value of 0.15 was obtained. When this was not the case, the range of *SAFs* was extended to match the target minimum epistemic uncertainty. In addition, the TI Team evaluated the mean logarithmic standard deviation of the *SAF* to estimate the ground motion level at which the *SAF* standard deviation transitions from linear to nonlinear site response. As described in Section 3.4, the TI Team assumed that the single-station standard deviation from the GMM captures the aleatory variability of the spectral acceleration in the linear site response range. As such, the TI Team implemented into the probabilistic seismic hazard analysis (PSHA) only the additional *SAF* standard deviation that is associated with nonlinear site response. In addition, the TI Team observed that the nonlinear component of the *SAF* standard deviation is small relative to the larger single-station standard deviation from the GMM. For this reason, rather than using multiple branches to represent the epistemic uncertainty in the aleatory variability of the *SAF*, the TI Team decided that a single branch consisting of the weighted mean *SAF* standard deviation from the multiple terminal site response logic tree branches would adequately represent the aleatory variability of the *SAF*.

### 7.2 Ground Motion Hazard Results

As discussed in the next two subsections, for the two project study sites, control point hazard curves and response spectra, calculated using Approach 4, are shown for 1 and 10 Hertz (Hz). To demonstrate the impact of the local site effects, the corresponding reference condition

hazard curves and *SAF* medians and standard deviations are shown for the same two frequencies. The number of hazard curves for each of the spectral frequencies is determined by the total number of alternative logic tree nodes for each of the branches from the seismic source characterization (SSC), GMM, and site response model logic trees. The mean hazard curves for each of the sources are overlain on the complete set of alternative curves. Next, mean UHRS are shown for three return periods (RPs) (1,000, 10,000, and 100,000 years) for both the control point and reference condition hazard results. GMRS are then shown for seismic design category 3, 4, and 5 facilities.

Next, Approach 3 and 4 results for 1 and 10 Hz hazard curves, as well as mean UHRS, are compared for the two study sites. In addition, alternative Approach 3 implementations (Hazard Integral vs Convolution Approach, see Table 3-1) are compared for both sites. Finally, tornado plots are used to show how each alternative element of the SSC, GMM, and site response model logic trees scales the total mean hazard up or down, and to rank each element on the relative effect on the hazard.

### 7.2.1 SRS Hazard Results and Sensitivity

Figure 7-1 shows the 1 Hz reference condition hazard curves (Figure 7-1a), median and logarithmic standard deviation *SAF* (Figure 7-1b) and control point hazard curves (Figure 7-1c) for each of the seismic sources used for the SRS. Overlain on the hazard curves (Figures 7-1a and 7-1c) are the mean hazard curves for each of the sources (dashed red curves) and the total mean hazard (black curve). At this frequency, the site response amplifies the ground shaking at all hazard levels, which is driven by the *SAF* exceeding 1.0 over most ground motion intensity levels (Figure 7-1b). Figure 7-2(a-c) shows the same results for 10 Hz spectral acceleration for each of the seismic sources used for SRS. At this higher frequency, the site response deamplifies ground shaking at hazard levels less than about  $4 \times 10^{-4}$ . This de-amplification is caused by the *SAF* falling below 1.0 at larger intensity levels for this frequency (Figure 7-2b). Figure 7-3a, which shows the total mean reference condition and control point hazard curves for 1 Hz and 10 Hz, clearly shows the impact of the SRS *SAF* for these two spectral frequencies on the control point hazard. The mean horizontal UHRS is shown in Figure 7-3b for three RPs (i.e., 1,000, 10,000, and 100,000 years) for both the reference condition and control point. The UHRS clearly show ground motion amplification at low frequencies and de-amplification at high frequencies, although the level of amplification and de-amplification varies with RP due to the different ground motion intensity levels and *SAF* associated with the reference condition at each RP. Figure 7-4 shows the GMRS for seismic design category 3, 4, and 5 facilities. A comparison of the GMRS for seismic design category 5 facilities (GMRS-5) with the 10,000-year RP mean UHRS (Figure 7-3b) shows a fairly close match between the two response spectra.

Rather than combining all the control point hazard curves for the two distributed seismicity sources together with the four possible configurations for the Charleston repeated large magnitude earthquake (RLME), the TI Team implemented a repeated sampling approach to develop total fractile hazard curves for SRS. Because each of the six sources has 8,925 alternative hazard curves, determining the fractiles for the total hazard would necessitate combining 8,925 curves raised to the sixth power to capture all the total possible combinations. Instead, the TI Team randomly selected 1,000 annual frequency of exceedance (AFE) values and their associated weights for each of the spectral acceleration columns of the hazard curves (a “vertical slice”) for each of the sources. These randomly selected columns of AFE values for each of the sources were then added and a set of fractiles developed for each spectral acceleration column after ordering the AFE and determining a cumulative distribution. For each

of the spectral acceleration columns, the TI Team repeated this random sampling approach ten times, computing fractiles for each of the ten iterations. By repeating the random sampling of

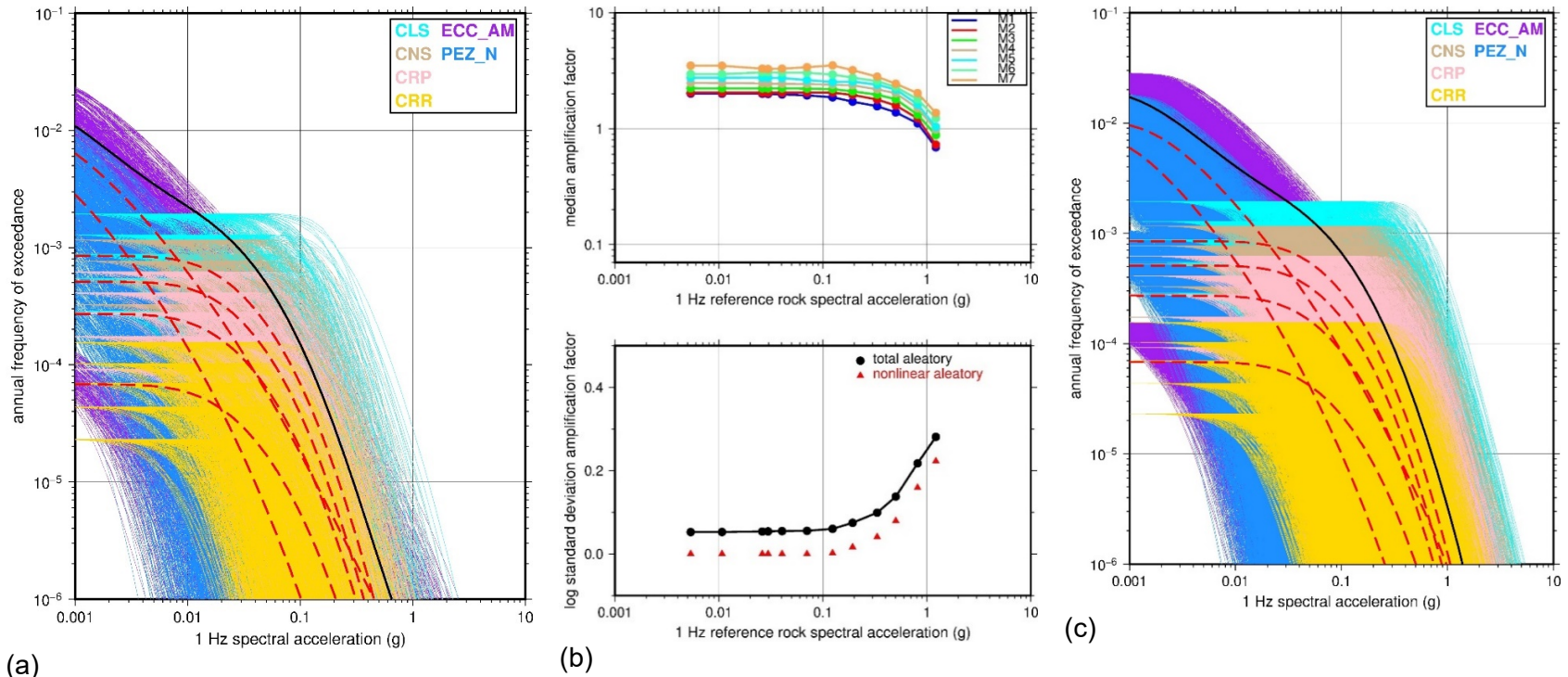
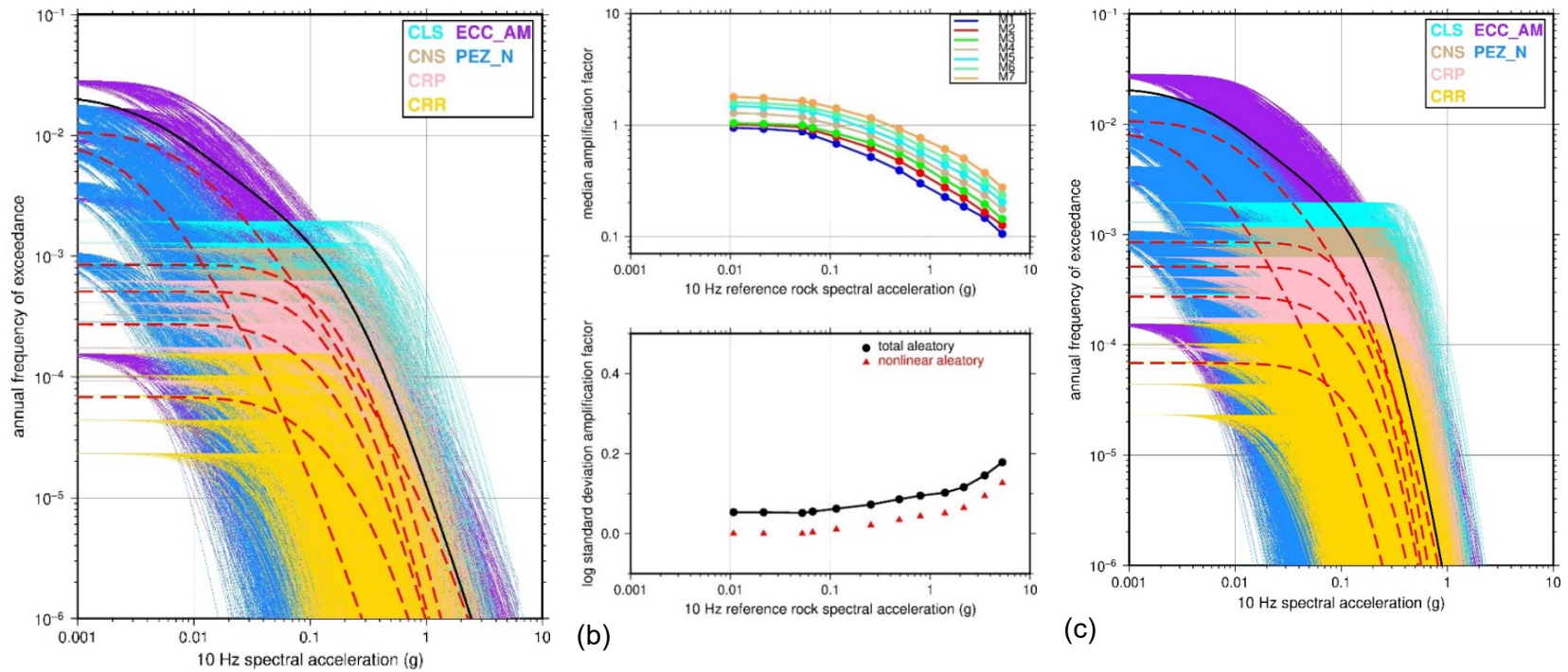


**Figure 7-1** (a) Reference condition 1 Hz hazard curves for seismic sources implemented for SRS-FA. Mean hazard curves for each source are shown (dashed red curves) as well as the total hazard (black curve). (b) SRS median site adjustment factors and logarithmic standard deviation for 1 Hz. (c) Control point 1 Hz hazard curves for seismic sources implemented for SRS-FAZ. Mean hazard curves for each source are shown (dashed red curves) as well as the total hazard (black curve).



(a) Reference condition 10 Hz hazard curves for seismic sources implemented for SRS-FA. Mean hazard curves for each source are shown (dashed red curves) as well as the total hazard (black curve). (b) SRS median site adjustment factors and logarithmic standard deviation for 10 Hz. (c) Control point 10 Hz hazard curves for seismic sources implemented for SRS-FA. Mean hazard curves for each source are shown (dashed red curves) as well as the total hazard (black curve).

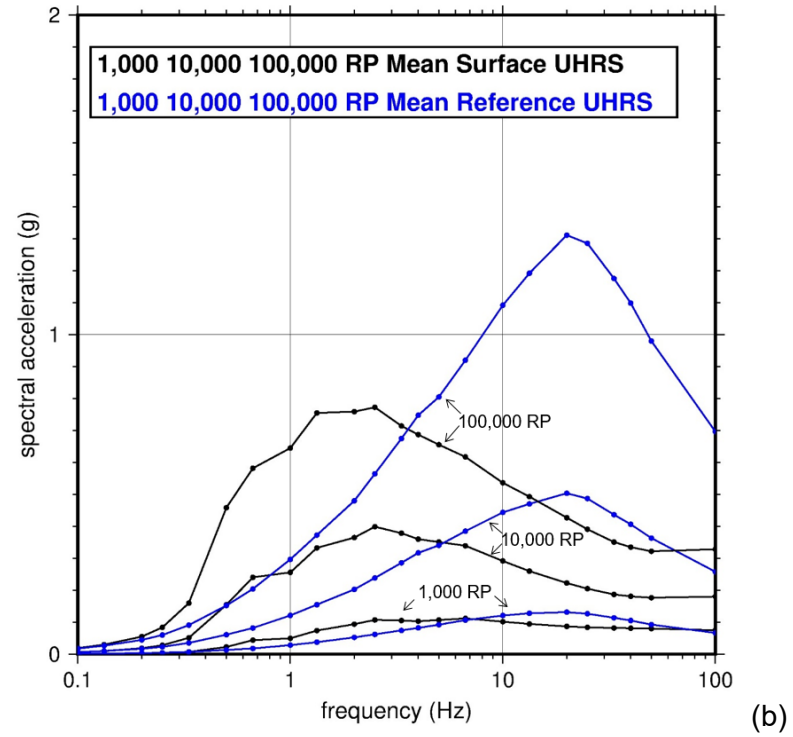
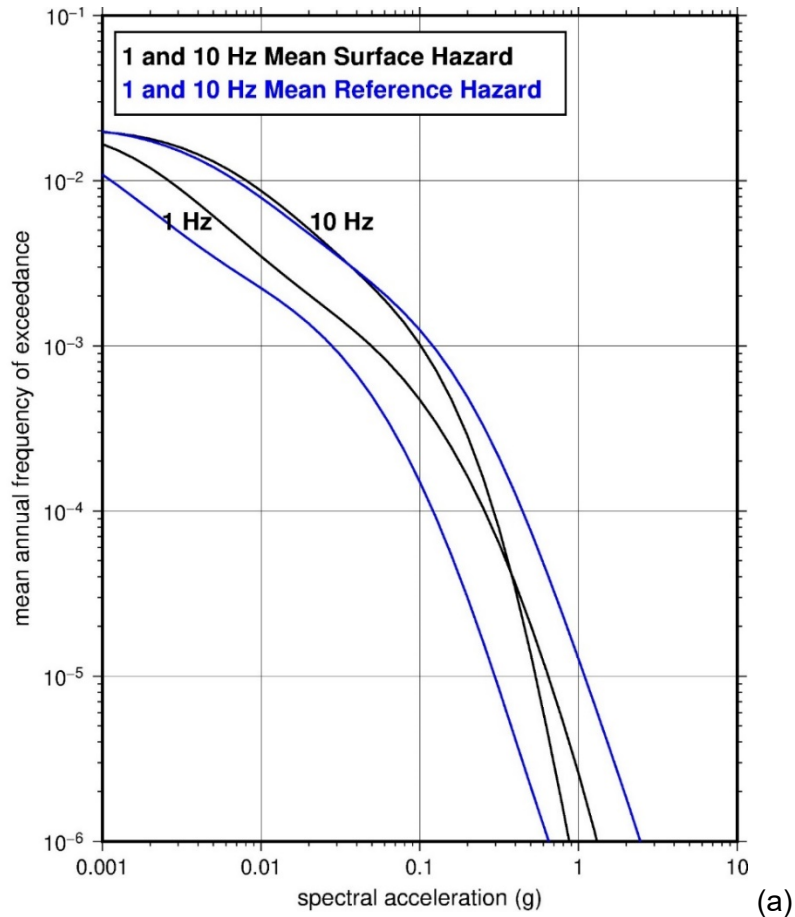


**Figure 7-3 (a) 1 and 10 Hz total mean hazard for reference condition and control point elevation and (b) Uniform hazard response spectra for reference condition and control point (surface).**

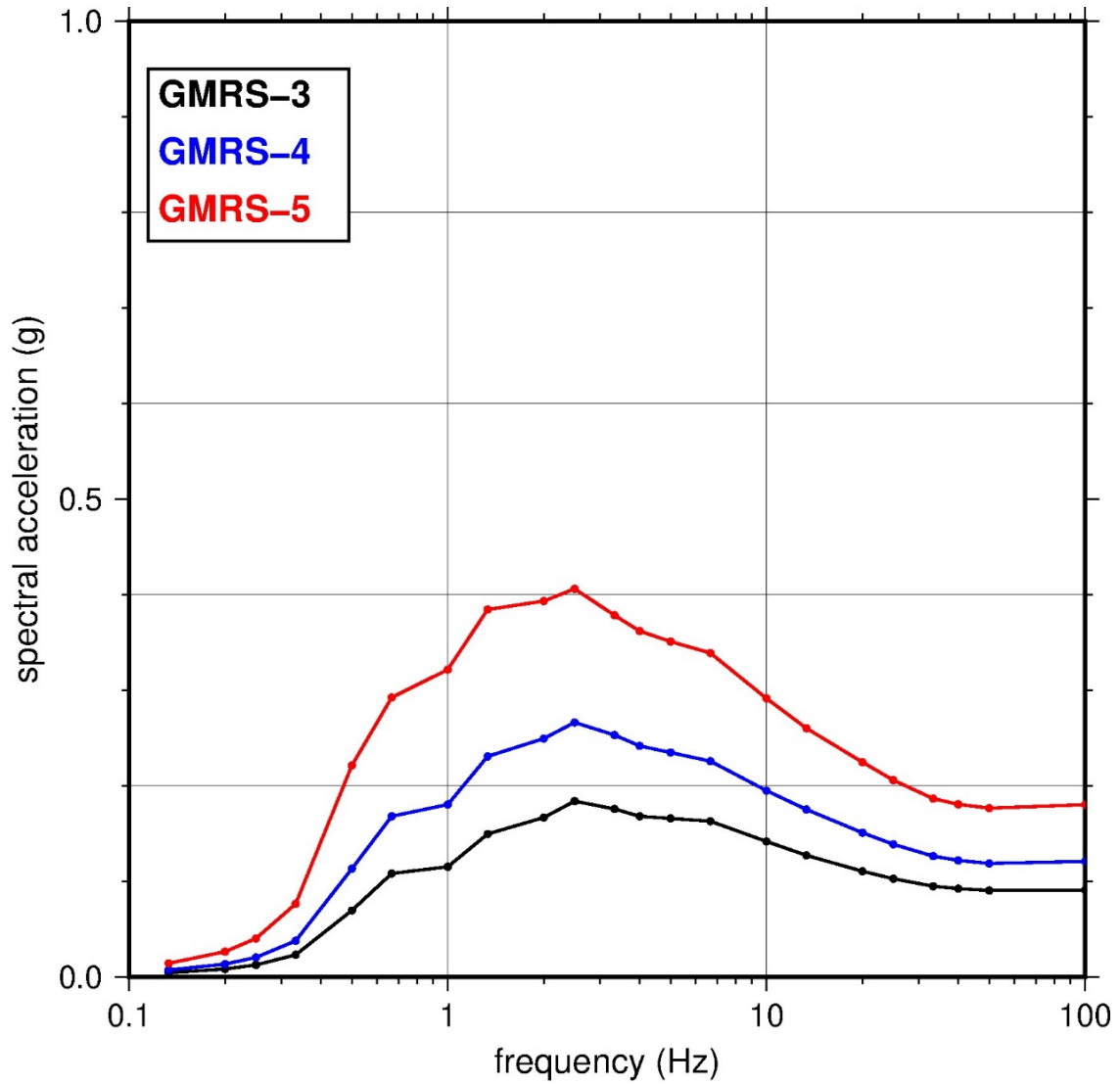


Figure 7-4 GMRS for seismic design category 3, 4, and 5 structure.

1

1,000 AFE and determining the fractiles from the summed sources ten times, the TI Team was able to achieve more stable results. The TI Team then determined the average fractile values from the ten iterations to arrive at the final set of fractile hazard curves. Figure 7-5 shows the total fractile hazard curves (0.05, 0.16, 0.50, 0.84, and 0.90) developed from each of the combined randomly sampled 1,000 AFE values for each of the spectral acceleration columns. Also shown is the mean (green curve) developed from the same repeated random sampling approach. The TI Team compared this mean with the combined means from each of the sources as a check on the accuracy of the procedure. Appendix C has a more complete description of the repeated random sampling approach implemented by the TI Team.

The comparison of the Hazard Integral Approach 3 and Approach 4 mean and fractiles is shown for both 1 and 10 Hz in Figures 7-6a and 7-6b, respectively, as well as the UHRS for multiple RPs in Figure 7-7. Figures 7-6a and 7-6b show that the mean (dashed curve) and fractiles (i.e., 0.05, 0.16, 0.50, 0.84, and 0.95) for the two approaches match reasonably well over a wide range in annual frequencies of exceedance. The exception to the close match between the two approaches is for the higher 1 Hz fractile curves (0.84 and 0.95) below the AFE of  $1 \times 10^{-4}$  per year. Below this AFE, the Hazard Integral Approach 3 hazard curve (red) falls off more rapidly than the hazard curve for Approach 4 (blue). A comparison of the two approaches for multiple spectral frequencies and RPs is provided by Figure 7-7, which shows the mean UHRS for three RPs (1,000, 10,000, and 100,000 years). The similarity of the two sets of UHRS for each RP demonstrates that both Approaches 3 and 4 produce approximately the same control point mean hazard.

In addition to comparing the Hazard Integral Approach 3 with Approach 4, the TI Team also compared two alternative implementations for Approach 3: Hazard Integral and Convolution. To develop the mean control point hazard curve using the Convolution Approach 3, the TI Team convolved the predetermined mean reference condition hazard curve with the seven *SAF* logarithmic means. The TI Team then determined the mean hazard curve by taking the weighted average of the seven hazard curves. As expected, the mean control point hazard curves using either the Hazard Integral Approach 3 or the Convolution Approach 3 match very closely. To develop fractile control point hazard curves using the Convolution Approach 3, the TI Team developed a set of ten reference condition fractile hazard curves to represent the total distribution of reference hazard from the multiple seismic sources using the percentiles and weights recommended in Table 3 of Miller and Rice (1983). The TI Team then convolved each of these 10 reference condition hazard curves with the seven *SAF* logarithmic means to develop 70 weighted control point hazard curves for each GMM spectral frequency. The TI Team then computed the standard control point fractile (i.e., 0.05, 0.10, 0.16, 0.50, 0.84, 0.90, and 0.95) hazard curves and compared these fractile curves to the same control point fractile hazard curves developed from the Hazard Integral Approach 3. Figures 7-8a and 7-8b show the comparison of the 10 Hz control point fractile hazard curves for the two different Approach 3 implementations for the 10<sup>th</sup> and 90<sup>th</sup> percentiles (Figure 7-8a) and the 16<sup>th</sup> and 84<sup>th</sup> percentiles (Figure 7-8b). For each of the control point hazard fractile curves, there is a close match between the two different implementations of Approach 3.

The tornado plots (Figures 7-9a and 7-9b) for the SRS study site demonstrate that the NGA-East GMM medians (Goulet et al., 2018) provide the largest epistemic uncertainty relative to the other parameters from the SSC model logic tree and *SAFs*. The range in *SAF* for 10 Hz at an AFE of  $1 \times 10^{-4}$  per year (Figure 7-9b) does increase relative to the range in *SAF* for 1 Hz at the same AFE level (Figure 7-9a).

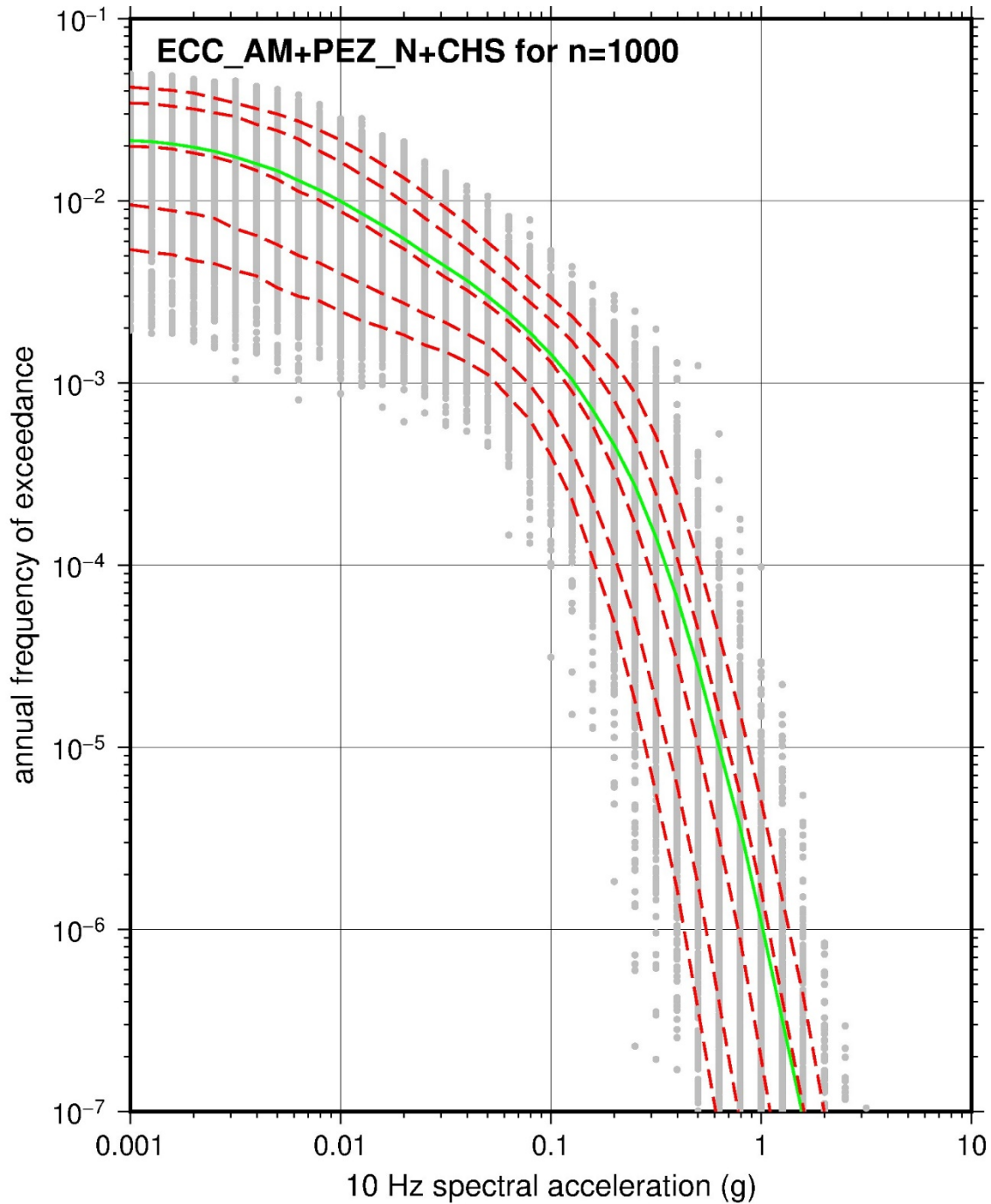
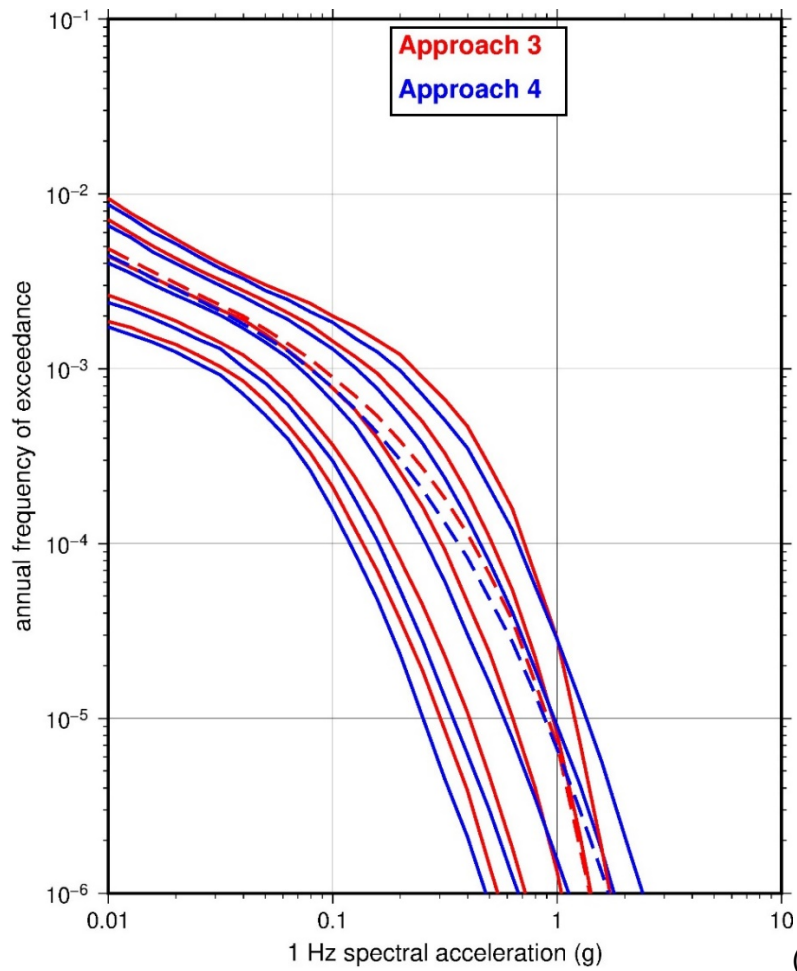
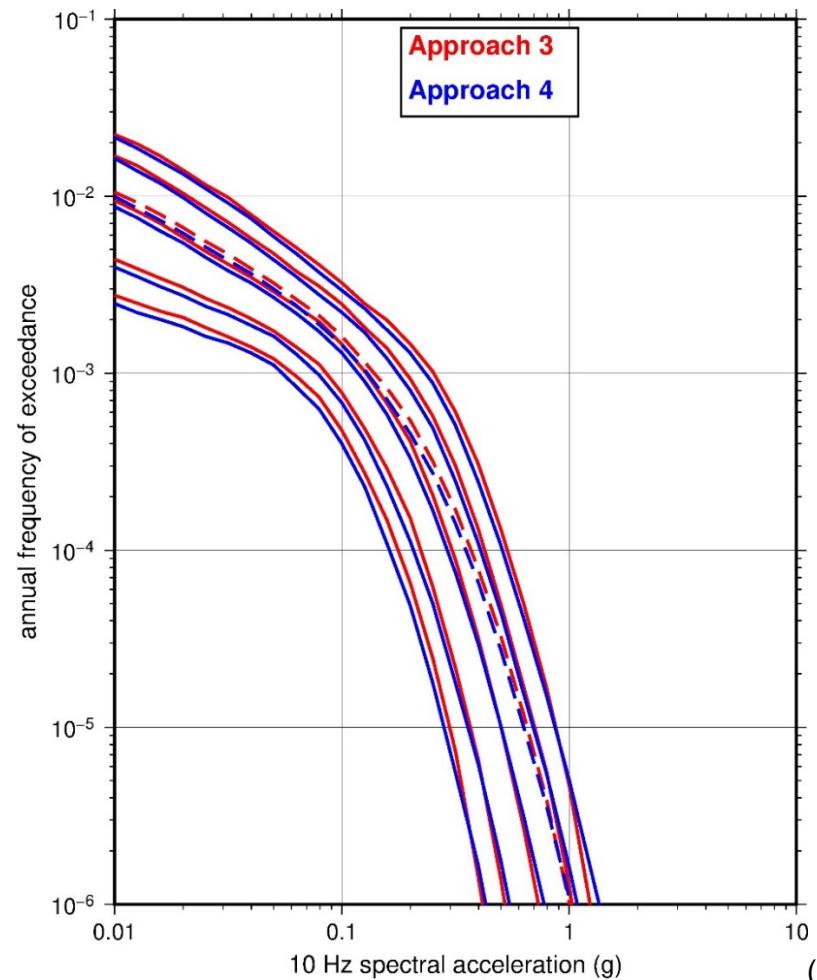


**Figure 7-5** Total control point hazard curve fractiles (dashed red curves) and mean (green curve) developed for SRS using repeated sampling approach.



(a)



(b)

**Figure 7-6 (a) 1 Hz control point total mean (dashed) and fractile (solid) hazard curves for the Hazard Integral Approach 3 compared to Approach 4 and (b) 10 Hz control point total mean (dashed) and fractile (solid) hazard curves for Hazard Integral Approach 3 compared to Approach 4.**

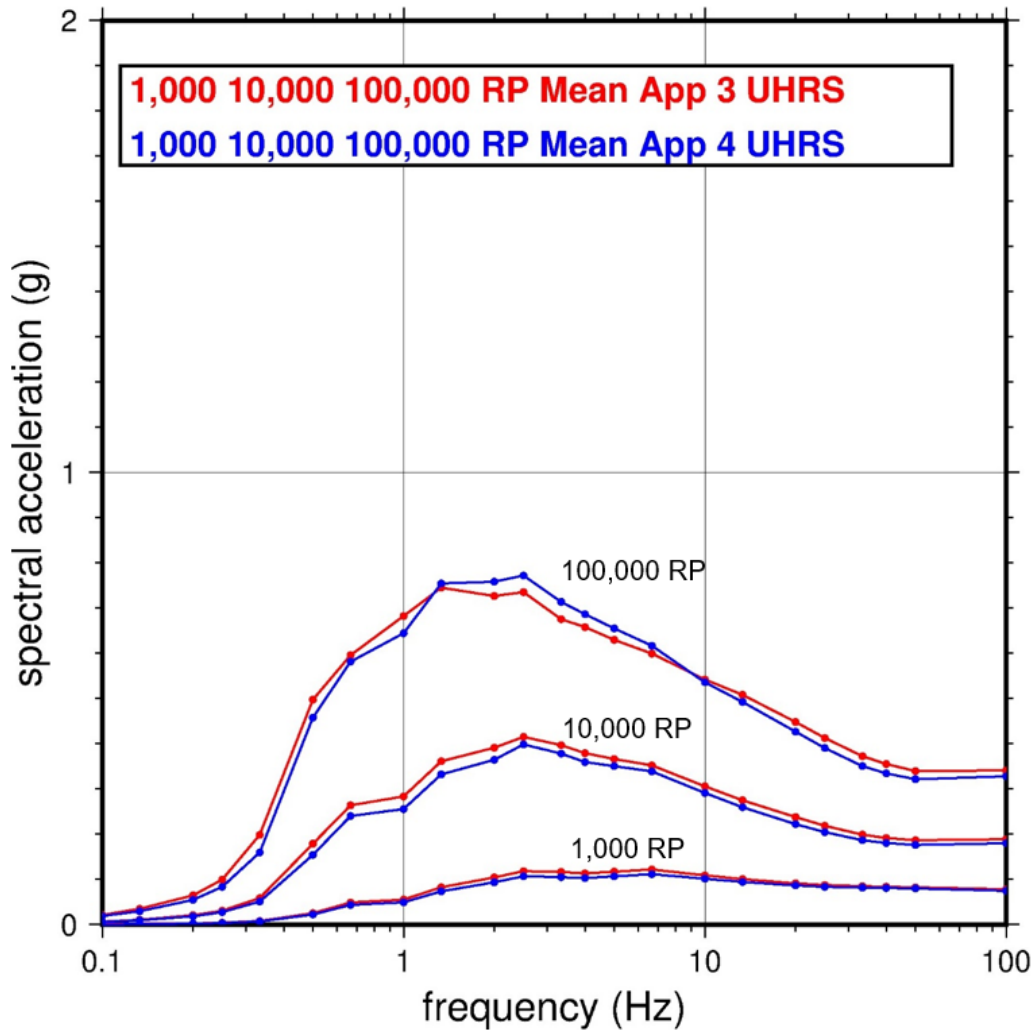
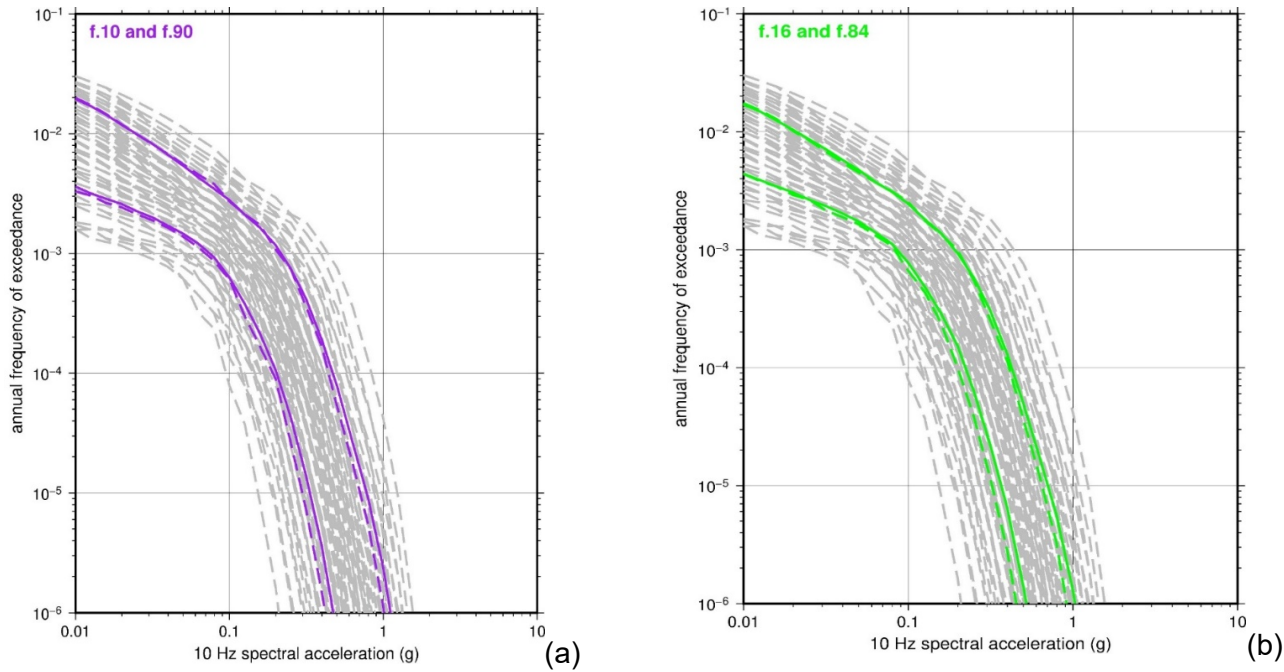
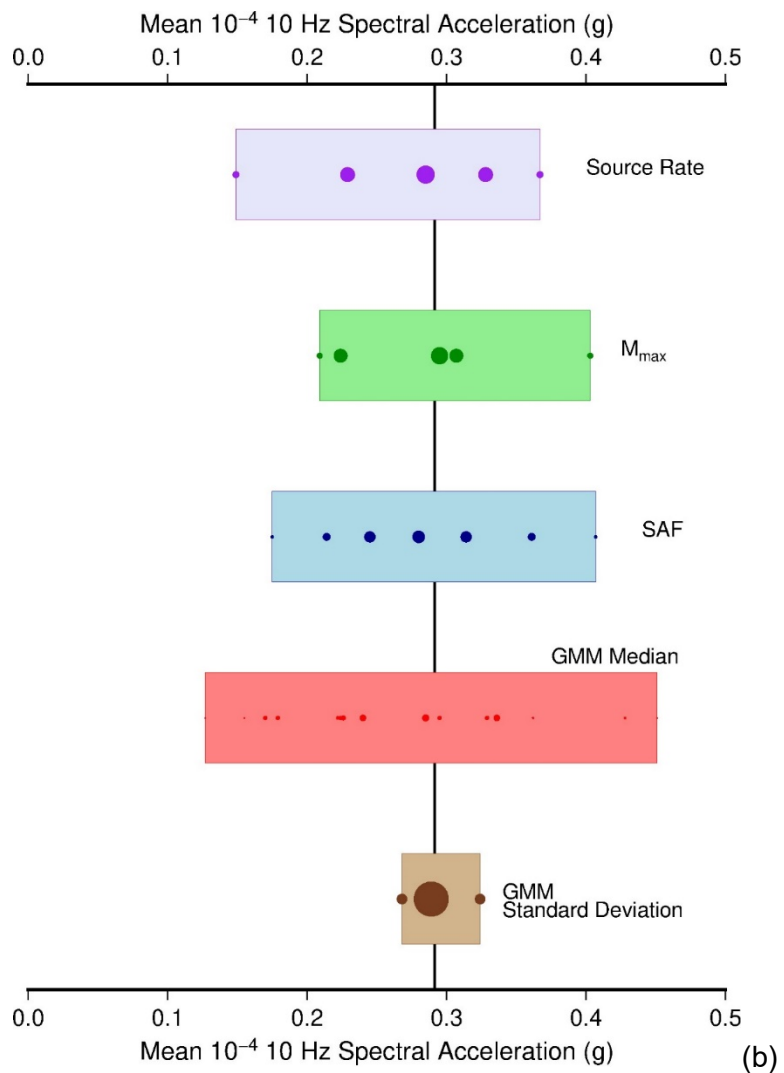
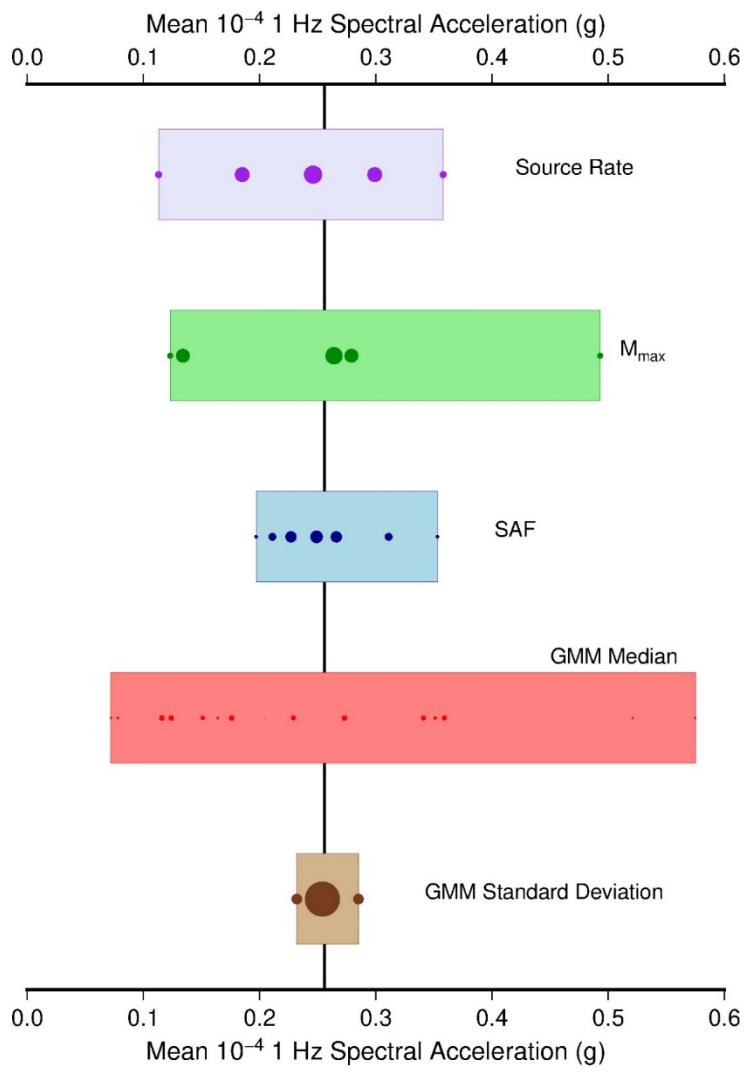


Figure 7-7 Mean control point UHS for the Hazard Integral Approach 3 versus Approach 4

1



**Figure 7-8 (a) Comparison of the 10 Hz control point fractile hazard curves for the two different Approach 3 implementations for the 10th and 90th percentiles, SRS study site and (b) Comparison of the 10 Hz control point fractile hazard curves for the two different Approach 3 implementations for the 16th and 84th percentiles, SRS study site.**

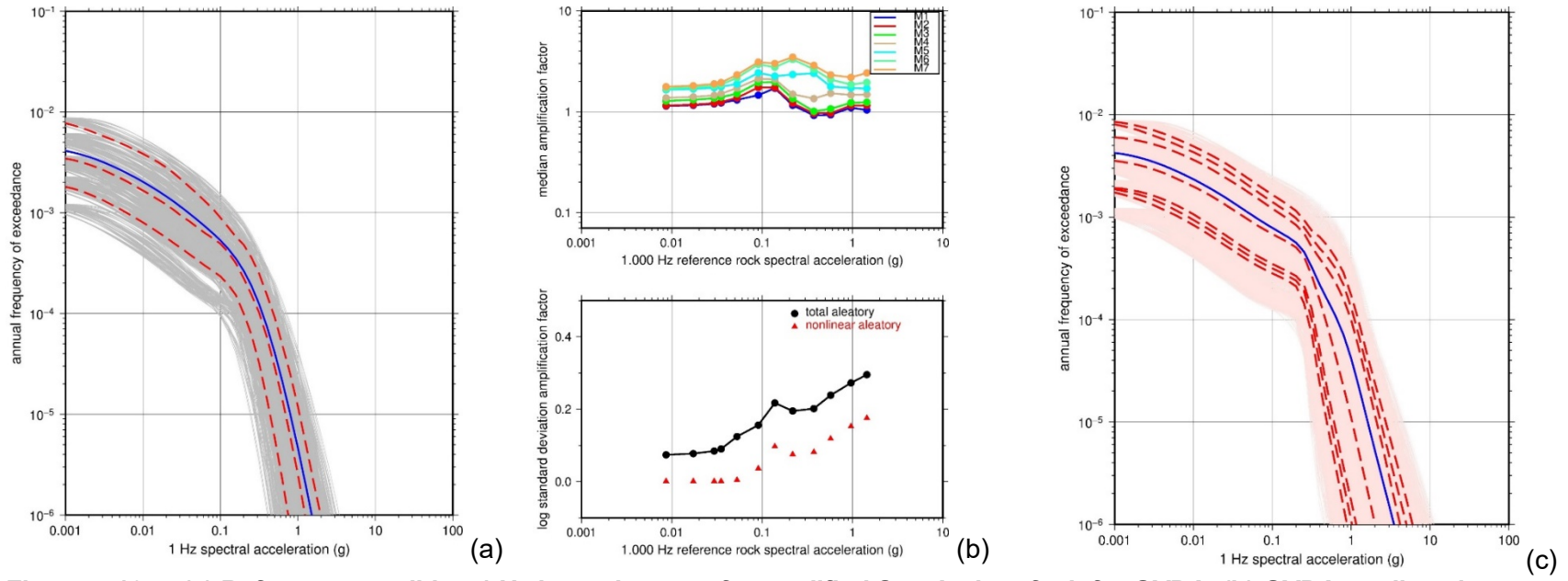


**Figure 7-9 (a) 1 Hz tornado plot for mean 10-4 AFE and (b) 10 Hz tornado plot for mean 10-4 AFE.**

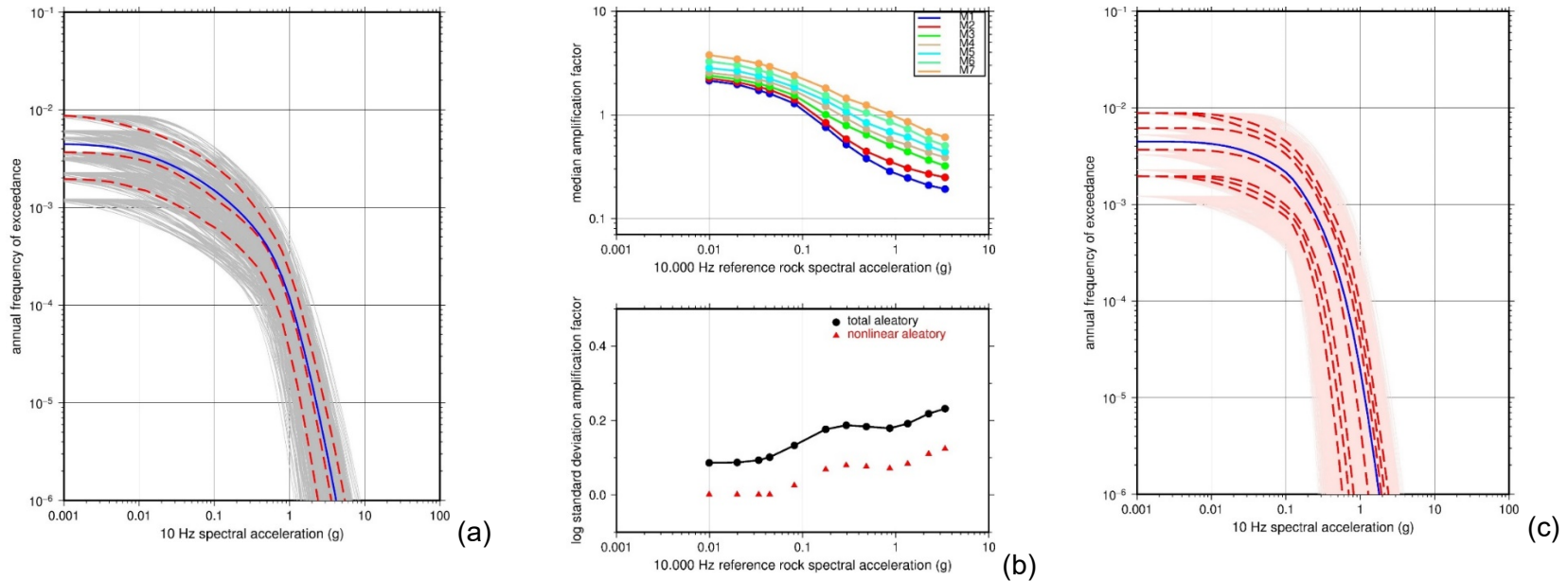
## 7.2.2 GVDA Hazard Results and Sensitivity

Figure 7-10 shows the 1 Hz reference condition hazard curves (Figure 7-10a), median and logarithmic standard deviation SAF (Figure 7-10b) and control point hazard curves (Figure 7-10c) for the San Jacinto Fault Zone (SJFZ) for the GVDA study site. Similarly, Figure 7-11 (a-c) shows the 10 Hz results for the modified SJFZ for the GVDA study site. For both the 1 Hz and 10 Hz cases, the effects of the SAF from the site response for the GVDA study site are clearly demonstrated in the resulting control point hazard curves. At 1 Hz, the site response amplifies shaking due to the SAF exceeding 1.0. Also, the larger epistemic variability in SAF at reference spectral accelerations between 0.3-0.5 g (Figure 7-11b) generates a kink in the mean hazard at the control point (Figure 7-11c). At 10 Hz, the GVDA site response (Figure 7-11b) de-amplifies the ground shaking at reference spectral accelerations above 0.2 g, which corresponds to AFE levels less than about  $1 \times 10^{-3}$ . As a result, the 10 Hz control point hazard curves (Figure 7-11c) fall off rapidly. Figure 7-12a, which shows the total mean reference condition and control point hazard curves for 1 Hz and 10 Hz, clearly shows the impact of the GVDA SAFs for these two spectral frequencies on the control point hazard. The mean horizontal UHRS is shown in Figure 7-12b for three RPs (i.e., 1,000, 10,000, and 100,000 years) for both the reference condition and control point. The UHRS clearly show ground motion amplification at low frequencies and de-amplification at high frequencies, although the level of amplification and de-amplification varies with RP due to the different ground motion intensity levels and SAF associated with the reference condition at each RP. Figure 7-13 shows the GMRS for seismic design category 3, 4, and 5 facilities. A comparison of the GMRS for seismic design category 5 facilities (GMRS-5) with the 10,000-year RP mean UHRS (Figure 7-12b) shows a fairly close match between the two response spectra. The comparison of the Hazard Integral Approach 3 and Approach 4 is shown for both 1 and 10 Hz in Figures 7-14a and 7-14b, respectively, as well as the UHRS for multiple RPs in Figure 7-15. Figures 7-14a and 7-14b show that the mean (dashed curve) and fractiles (i.e., 0.10, 0.16, 0.50, 0.84, and 0.90) for the two approaches match reasonably well. A comparison of the two approaches for multiple spectral frequencies and RPs is provided by Figure 7-15, which shows the mean UHRS for three RPs (i.e., 1,000, 10,000, and 100,000 years). The mean hazard spectra for 1,000- and 10,000-year RPs are fairly similar, although the Approach 4 spectra have slightly larger amplitudes. For the mean UHRS for the 100,000-year RP, the Approach 4 spectra have larger amplitudes and also show the impact of the kink in the GVDA SAF (see Figure 7-10b) that is smoothed out for mean UHRS produced from the Hazard Integral Approach 3 implementation. This result indicates that the Approach 4 analytical implementation developed by Bazzurro and Cornell (2004) may be more susceptible to abrupt slope changes in the SAF as a function of the reference condition spectral acceleration. However, GMRS developed for the highest seismic design category (GMRS-5) generally follow the mean UHRS for the 10,000-year RP, such that the use of analytical Approach 4 would not likely result in a GMRS that differs significantly from a GMRS developed using Hazard Integral implementation of Approach 3.

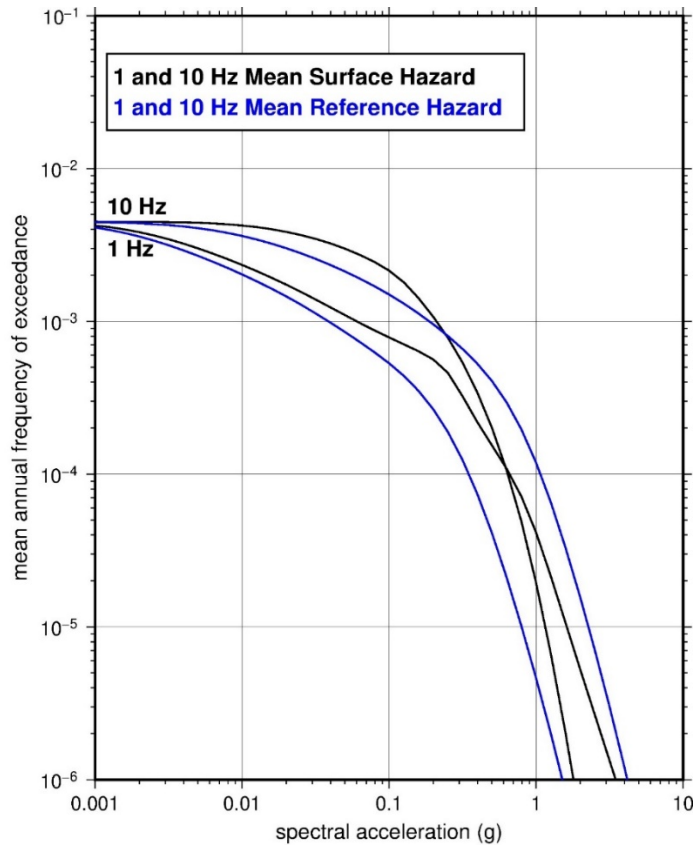
In addition to comparing the Hazard Integral Approach 3 with Approach 4, the TI Team also compared two alternative implementations for Approach 3: Hazard Integral and Convolution. The TI Team developed fracture control point hazard curves using the Convolution Approach 3 for the GVDA site using the same method described above in Section 7.2.1 for SRS. Figures 7-16a and 7-16b show the comparison of the 10 Hz control point fracture hazard curves for the two different Approach 3 implementations for the 10<sup>th</sup> and 90<sup>th</sup> percentiles (Figure 7-16a) and 16<sup>th</sup> and 84<sup>th</sup> percentiles (Figure 7-16b). For each of the control point hazard fracture curves, there is a close match between the two different implementations of Approach 3.



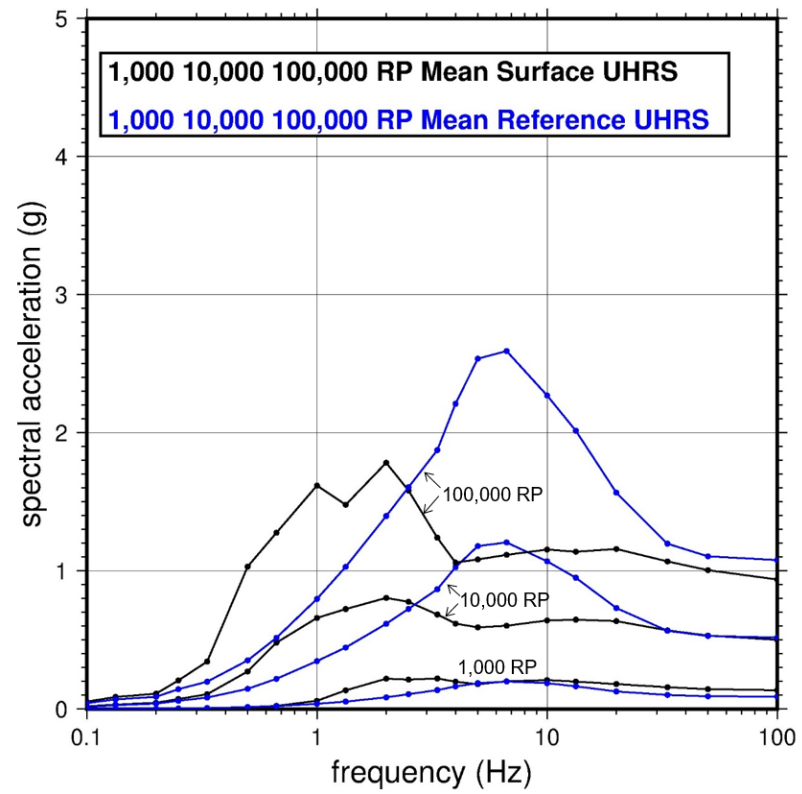
**Figure 7-10 (a) Reference condition 1 Hz hazard curves for modified San Jacinto fault for GVDA, (b) GVDA median site adjustment factors and logarithmic standard deviation for 1 Hz, and (c) control point 1 Hz hazard curves for modified San Jacinto fault for GVDA.**



**Figure 7-11 (a) Reference condition 10 Hz hazard curves for modified San Jacinto fault for GVDA, (b) GVDA median site adjustment factors and logarithmic standard deviation for 10 Hz, and (c) control point 10 Hz hazard curves for modified San Jacinto fault for GVDA.**



(a)



(b)

**Figure 7-12 (a) 1 and 10 Hz total mean hazard for reference condition and control point elevation and (b) UHRS for reference condition and control point (surface).**

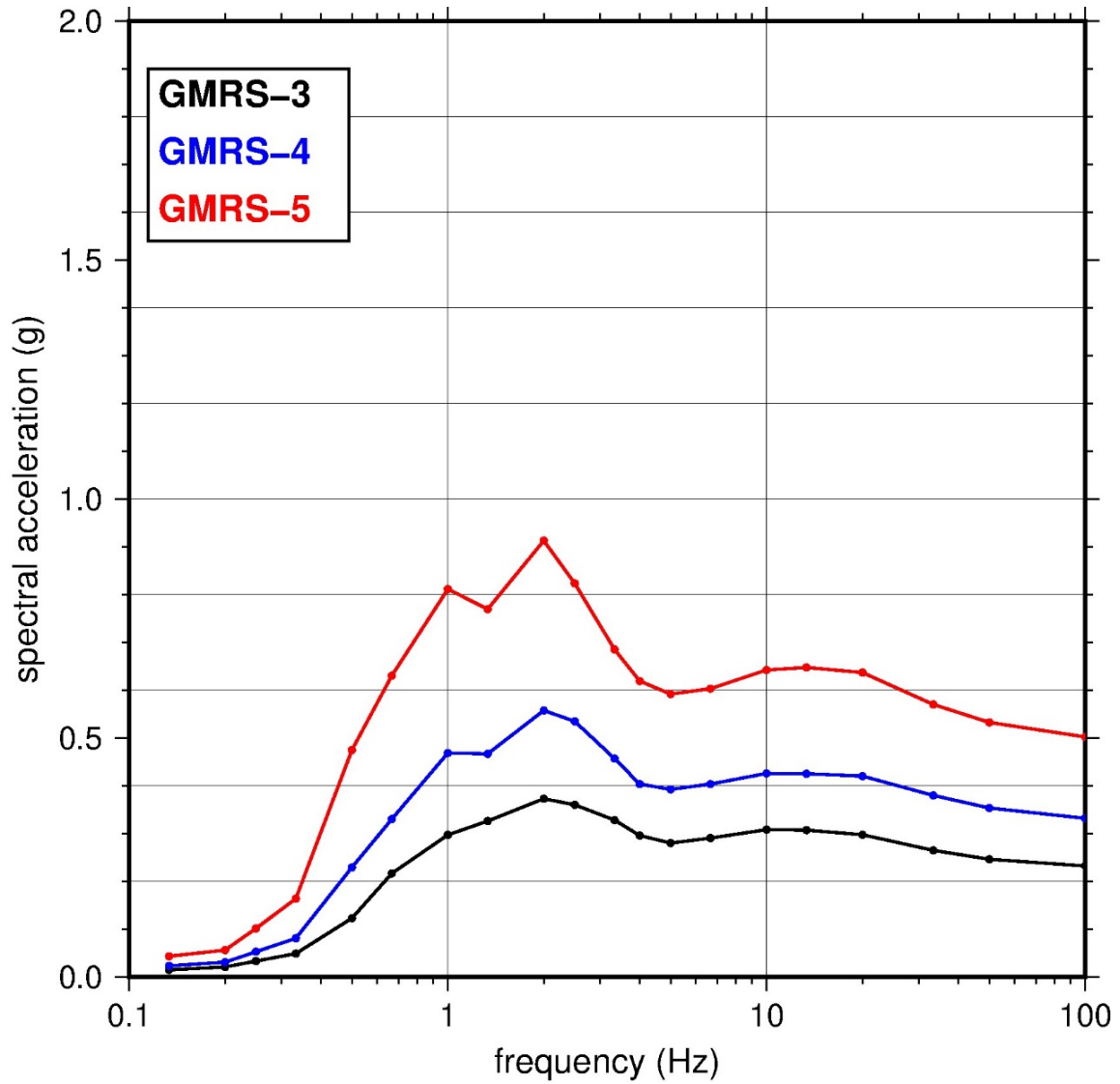
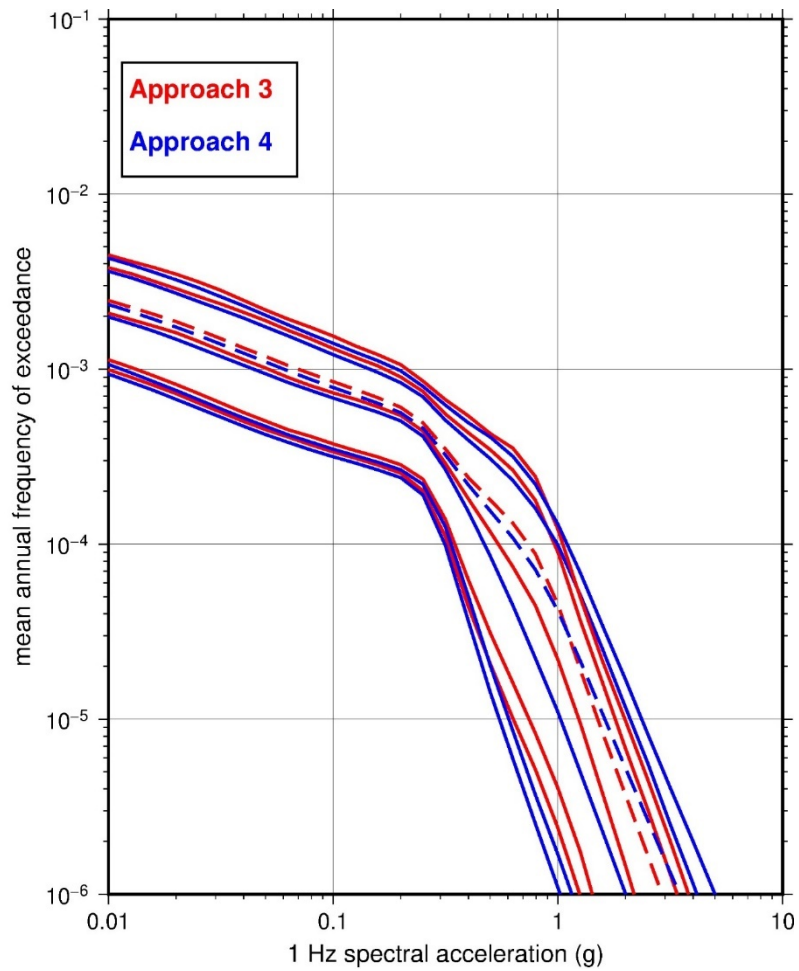
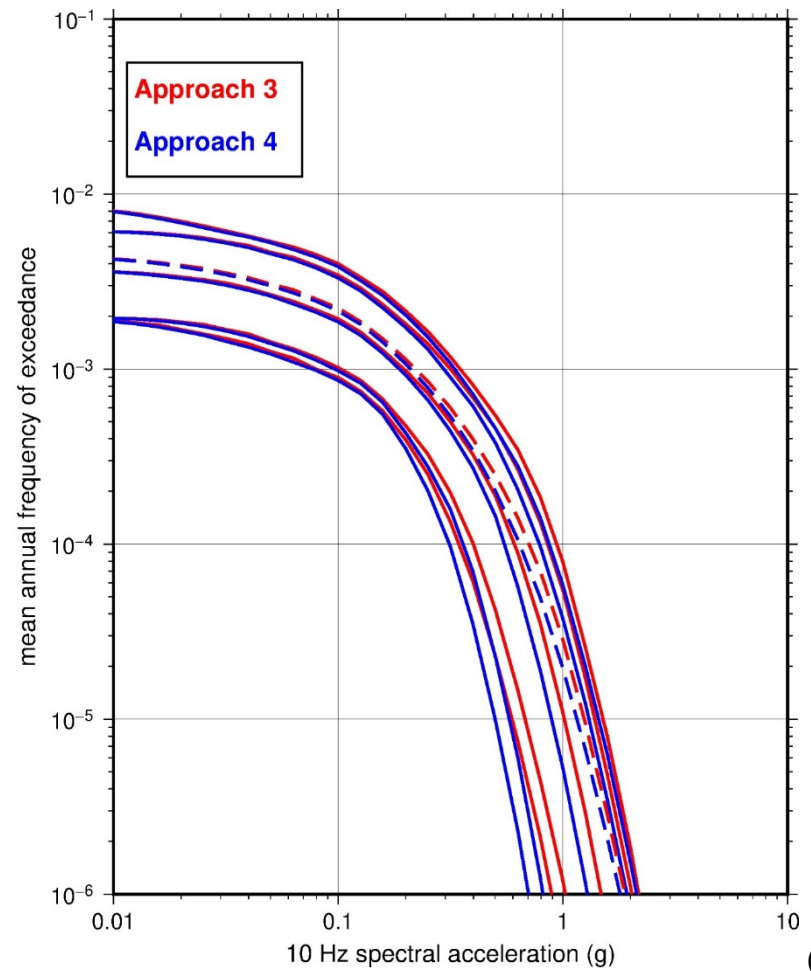


Figure 7-13 GMRS for seismic design category 3, 4, and 5 structures.

1



(a)



(b)

**Figure 7-14 (a) 1 Hz control point total mean (dashed) and fractile (solid) hazard curves for Hazard Integral Approach 3 compared to Approach 4 and (b) 10 Hz control point total mean (dashed) and fractile (solid) hazard curves for Hazard Integral Approach 3 compared to Approach 4.**

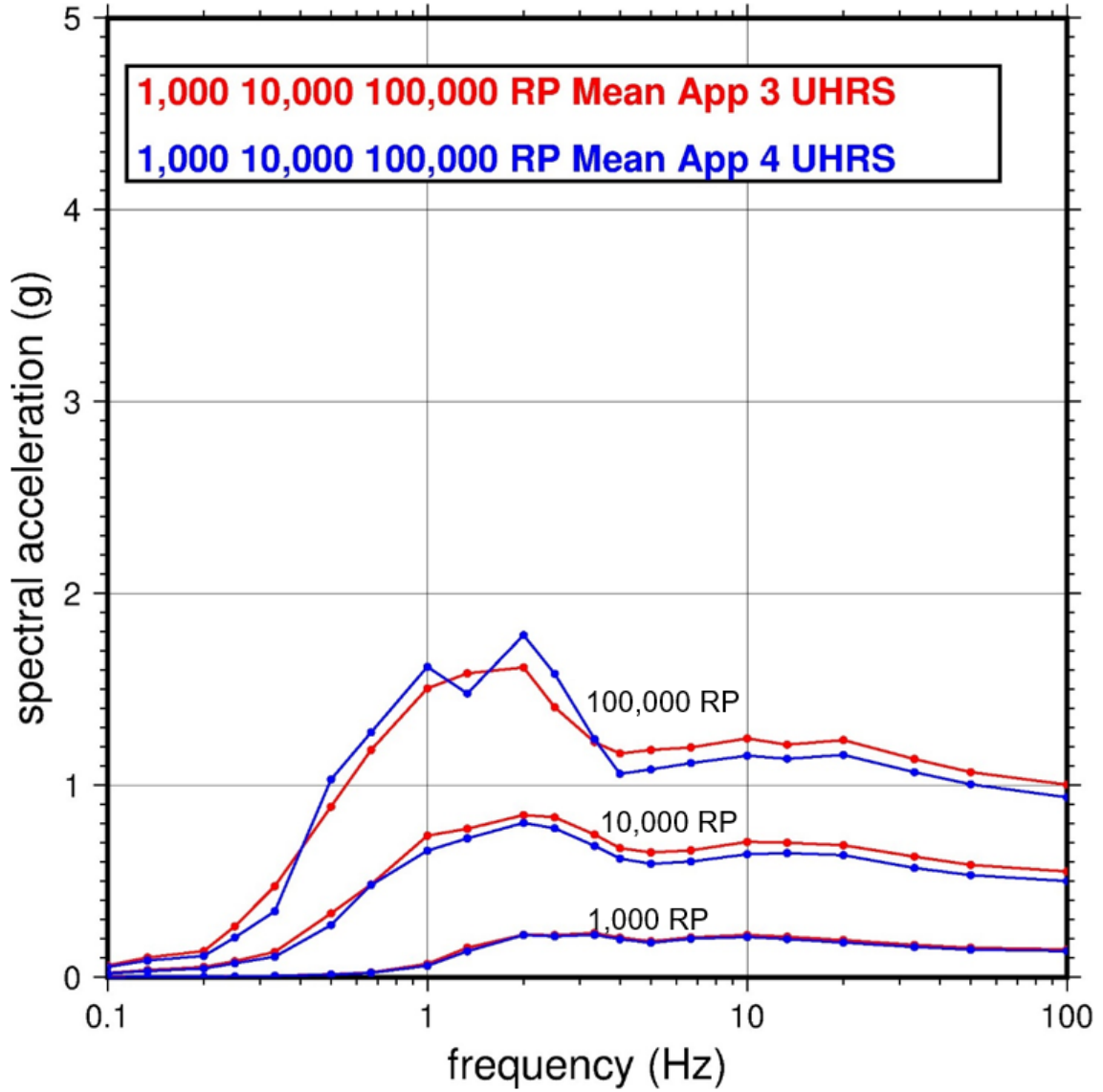
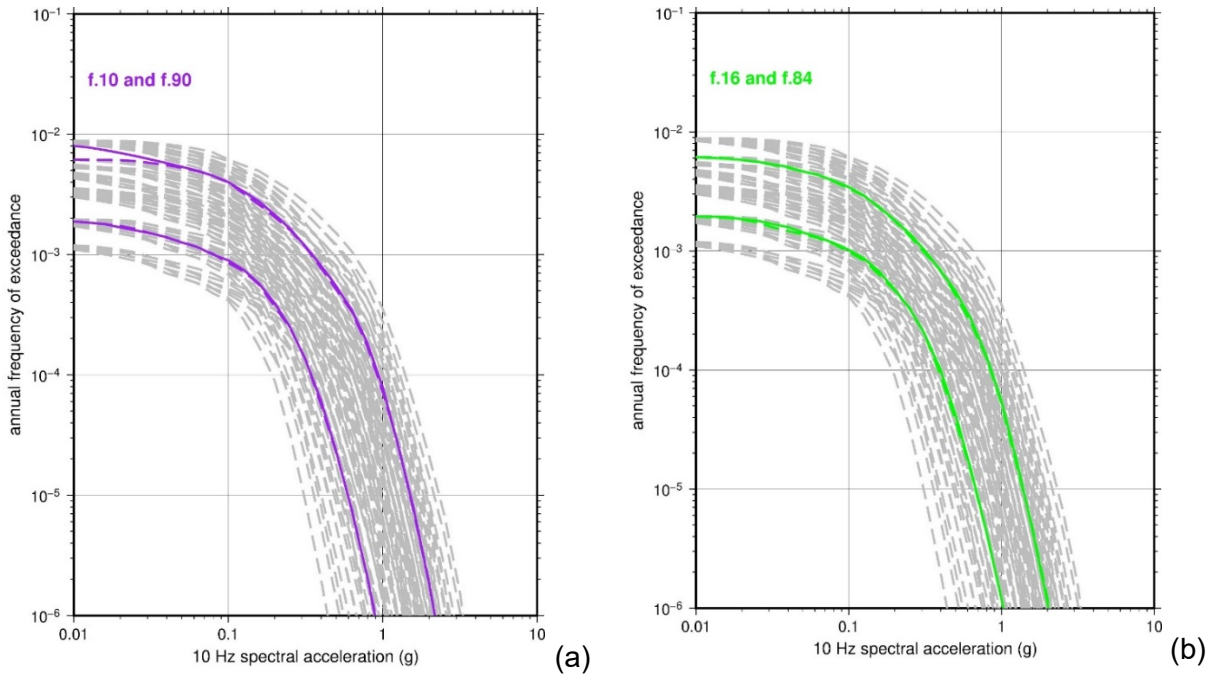


Figure 7-15 Mean control point UHS for Hazard Integral Approach 3 versus Approach 4.

1



**Figure 7-16 (a) Comparison of the 10 Hz control point fractile hazard curves for the two different Approach 3 implementations for the 10th and 90th percentiles, GVDA study site and (b) comparison of the 10 Hz control point fractile hazard curves for the two different Approach 3 implementations for the 16th and 84th percentiles, GVDA study site.**

The tornado plots (Figures 7-17a and 7-17b) for the GVDA site demonstrate that the GVDA *SAF* provide the largest epistemic uncertainty relative to the other parameters from the SSC model and GMM logic trees. The large range in *SAF* for GVDA relative to the other SSC model and GMM parameters indicates that the GVDA site response results are the most important factor in the shape and amplitude of the control point hazard curves at the  $10^{-4}$  AFE.

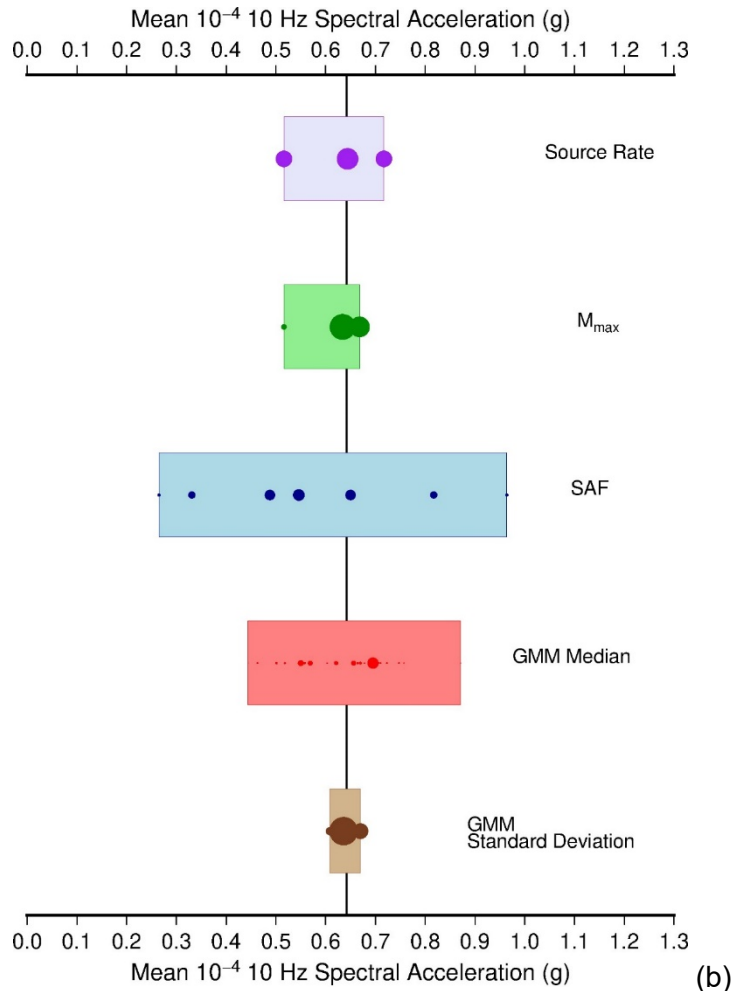
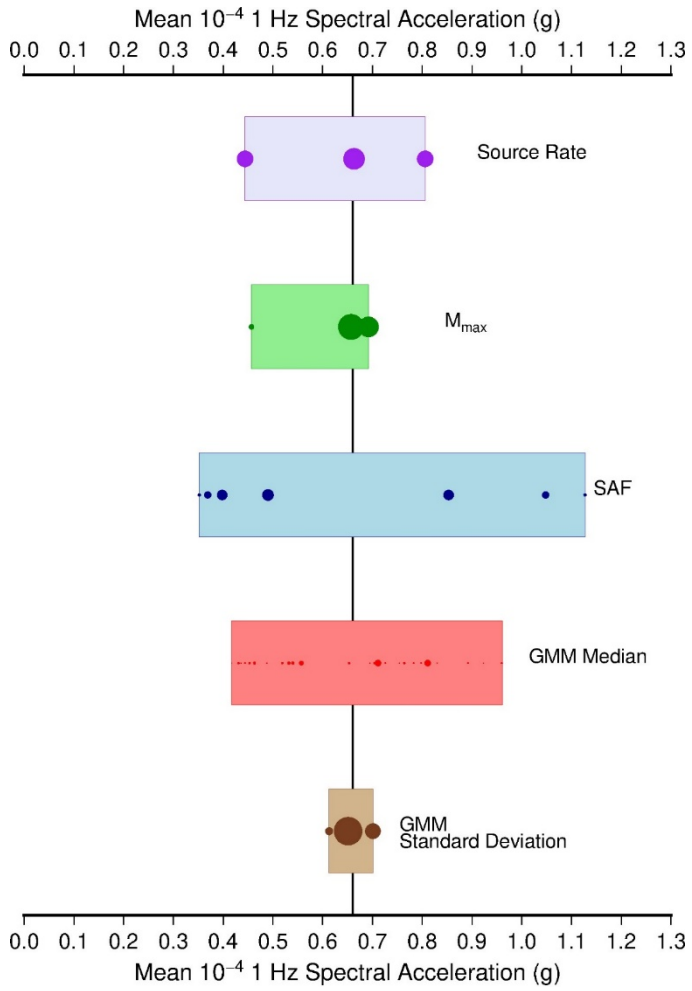


Figure 7-17 (a) 1 Hz tornado plot for mean  $10^{-4}$  AFE and (b) 10 Hz tornado plot for mean  $10^{-4}$  AFE

### 7.2.3 Conclusions from Multiple Hazard Implementations

As described in Section 7.2.1 and 7.2.2, the TI Team used multiple approaches to incorporate the *SAFs* into the PSHA to compute the control point hazard. Based on a comparison of the results, the TI Team found that each of the approaches (Hazard Integral Approach 3, Convolution Approach 3, and Analytical Approach 4) provide similar estimates of the mean and fractile hazard curves, UHRS and GMRS. The two key factors in producing similar hazard results for each of the approaches are 1) the use of multiple loading levels for the site response analysis, and 2) the piecewise interpolation of the median *SAFs* as a function of reference spectral acceleration. For the site response analysis described in Section 5, the TI Team used 12 loading levels that captured a wide range of very low, intermediate, and high spectral accelerations. As such, the TI Team was able to characterize the response of the site from the linear to nonlinear range, covering most of the range of predicted reference motions from the multiple magnitude and distance scenarios produced by the seismic sources used for the two sites. For the second key factor, the TI Team found that doing a piecewise interpolation in logarithmic space of the median *SAFs* as a function of reference spectral acceleration resulted in a much better approximation of the function than using a simple linear regression fit.

Previously, the use of Convolution Approach 3 had been restricted to developing mean control point hazard results to produce mean UHRS and GMRS. However, as described above, the TI Team was able to develop control point hazard fractiles from Convolution Approach 3 that matched the control point fractiles from the use of Hazard Integral Approach 3. This result was achieved by using a set of 10 weighted fractile reference hazard curves to represent the distribution of total reference hazard and convolving these curves with the set of seven median *SAFs* from the site response analysis. The benefit of using Convolution Approach 3 versus the Hazard Integral Approach 3 is in the reduction of computing time when the Convolution Approach is used. The Hazard Integral Approach 3 took the TI Team several days to run, while the Convolution Approach 3 took only the amount of time needed to develop the reference condition hazard for each of the sources and then a small amount of extra time for the convolution of the *SAF* with the reference hazard. The Analytical Approach 4 implemented by the TI Team also ran much faster than the Hazard Integral Approach 3 since the median *SAF* were directly implemented into the GMM to develop predicted control point spectral accelerations from the predicted reference rock spectral accelerations. This avoided the innermost summation over reference rock that is used for the Hazard Integral Approach 3.

### 7.3 References

ASCE/SEI. "ASCE/SEI 43-19 Seismic Design Criteria for Structures, Systems, and Components in Nuclear Facilities." Reston, Virginia: American Society of Civil Engineers. 2021. DOI:10.1061/9780784415405

Bazzurro, P. and C.A. Cornell. "Ground-Motion Amplification in Nonlinear Soil Sites With Uncertain Properties." *Bulletin of the Seismological Society of America*. Vol. 94, No. 6. pp. 2090–2109. 2004.

GeoPentech. "Southwestern United States Ground Motion Characterization SSHAC Level 3, *Technical Report*, Revision 2." March 2015.

Goulet, C., Y. Bozorgnia, N. Abrahamson, N. Kuehn, L. Al Atik, R. Youngs, R. Graves, and G. Atkinson. "Next Generation Attenuation Relations for the Central and Eastern United States (NGA-East) United States: N". p. 2018. Web. doi:10.2172/1593158.

Miller III, A.C. and T.R. Rice. "Discrete Approximations of Probability Distributions." *Management Science*. Vol. 29, Issue 3. pp. 352–362. 1983.

## 8 Conclusions

### 8.1 Summary

The goal of this project was to conduct a site response analysis for two study sites that follows the guidance for a Senior Seismic Hazard Analysis Committee (SSHAC) Level 2 study, as described in NUREG–2213 (NRC, 2018). The fundamental goal of the SSHAC process is to produce a probabilistic seismic hazard analysis (PSHA) that captures the center, body, and range (CBR) of technically defensible interpretations (TDI). The SSHAC process has been consistently applied to the seismic source characterization (SSC) and ground motion model (GMM) components of the PSHA for more than 15 years, but often the site response analysis has been performed outside of the SSHAC process and without the same rigor for systematically addressing the uncertainties associated with different data, models, and methods. Moreover, different approaches are available to incorporate the site response and its uncertainty into the PSHA, and a clear assessment of these approaches when utilized in the SSHAC process has not been performed. Therefore, this study also had the additional goals of providing clarity in terminology and definitions, evaluating different approaches, and demonstrating the full integration of site response analysis into the PSHA.

The project included a Workshop (summarized in Section 2 of this report) in which participants discussed various technical issues related to site response analyses, the significant sources of uncertainty in terms of data, models, and methods, and the consistent characterization of the uncertainties as either epistemic or aleatory. The Workshop discussions helped identify key issues to be addressed as part of this project and guided the decision-making throughout the SSHAC process.

Important technical background is described in Section 3, focusing on topics that have been unclear or ambiguous in the past. The need for site response adjustments associated with both the reference rock condition and the near-surface, site-specific conditions is described, as well as the two-step and one-step approaches that are available to develop these adjustments. The concepts of a site response logic tree, partitioning epistemic uncertainty and aleatory variability, and minimum epistemic uncertainty are also addressed. Finally, the implementation details for probabilistically incorporating the site adjustments into the PSHA are outlined, along with relevant equations for the different approaches that have been proposed. The two main approaches considered for incorporating the site adjustments are Approaches 3 and 4 from NUREG/CR-6728 (see Section 3.4).

The SSHAC process, as applied to the two study sites [Savannah River Site (SRS), and Garner Valley Downhole Array (GVDA)], is described in Sections 4 through 7. Section 4 describes the geologic setting for each site, as well as the SSC and reference GMM used for each site. The reference condition hazard is presented in terms of hazard curves, deaggregations, and uniform hazard spectra, along with tornado plots describing the contributions of different parts of the SSC and GMM on the reference hazard. It is important to note that simplifications to the SSC models for both sites generated hazard results that are not representative of the actual seismic hazard at these sites. Section 5 presents the site response logic trees for the two sites, as well as the detailed data and technical justifications used to develop and populate the logic trees. Section 6 summarizes the results of the site response analyses associated with the site response logic trees. These results include the median and aleatory variability of the site adjustment factors (*SAFs*) as a function of reference ground motion intensity, the epistemic

variability in the *SAFs*, and tornado and variance contribution plots that describe the contributions of different components of the site response logic tree to the variability in the *SAFs*. Data files containing the *SAFs* and shear-wave velocity ( $V_s$ ) profiles are provided in Rodriguez-Marek et al. (2021). Section 7 presents the final hazard results at the ground surface of each site in terms of mean hazard curves, hazard fractiles, uniform hazard spectra, ground motion response spectra (GMRS), and tornado plots. The results for Approach 3 (both Hazard Integral and Convolution methods) and Approach 4 are also compared.

Following the process described in NUREG–2213 (NRC, 2018), capturing the CBR of TDI is achieved through disciplined execution of the evaluation and integration phases of the SSHAC methodology. The TI Team did not encounter any difficulty in executing the necessary steps to apply the SSHAC guidance to the site response analyses at the two study sites. Applying a process that parallels the process used in the SSC and GMM components of the PSHA, which emphasizes a rigorous assessment and categorization of all sources of uncertainty, has a significant benefit when integrating the site response analysis results into the final hazard calculations. This allows for a much more transparent linkage between the GMM and site response analysis portions of the hazard study and provides a fully integrated PSHA that benefits from the enhanced assurance that is derived from the application of the SSHAC process. Several recent high-level studies have included the site response analysis as part of the overall PSHA.

Historically, performing the site response analysis outside of the SSHAC process was dictated by the belief that the uncertainties associated with the SSC and GMM models are much larger than those associated with the site response. As documented in Section 7 of this report, the epistemic uncertainty in the surface motion that is associated with the *SAFs* is as large, or larger, than the epistemic uncertainty associated with the SSC and GMM components of the logic tree. Figure 8-1 repeats from Section 7 the 10 Hertz (Hz) spectral acceleration tornado plots for  $10^{-4}$  annual frequency of exceedance (AFE) for the two study sites. For the SRS, the *SAF* epistemic uncertainty is comparable to the epistemic uncertainty in the median GMMs, and for the GVDA study site, the epistemic uncertainty is larger than the epistemic uncertainty in the median GMMs. These results support the rationale for implementing a structured process such as SSHAC to capture and document the uncertainties associated with *SAFs*.

## **8.2 Technical Lessons Learned and Research Opportunities**

The epistemic uncertainty in the *SAF* is captured via the site response logic tree. The site response logic tree must capture the CBR of TDI for the properties of the site that control the site response [i.e.,  $V_s$ , the site kappa ( $\kappa_0$ ), and modulus reduction and damping curves (MRD)], as well as the epistemic uncertainties associated with the analysis methods. Based upon previous experience and input from the workshop, the TI Team developed a draft site response logic tree for each study site and refined the tree through the course of the project. Sensitivity studies were also performed by the TI Team as part of this project to inform choices made in the development of the logic trees (Section 6.1.2). The final logic trees for each site are presented in Section 5.

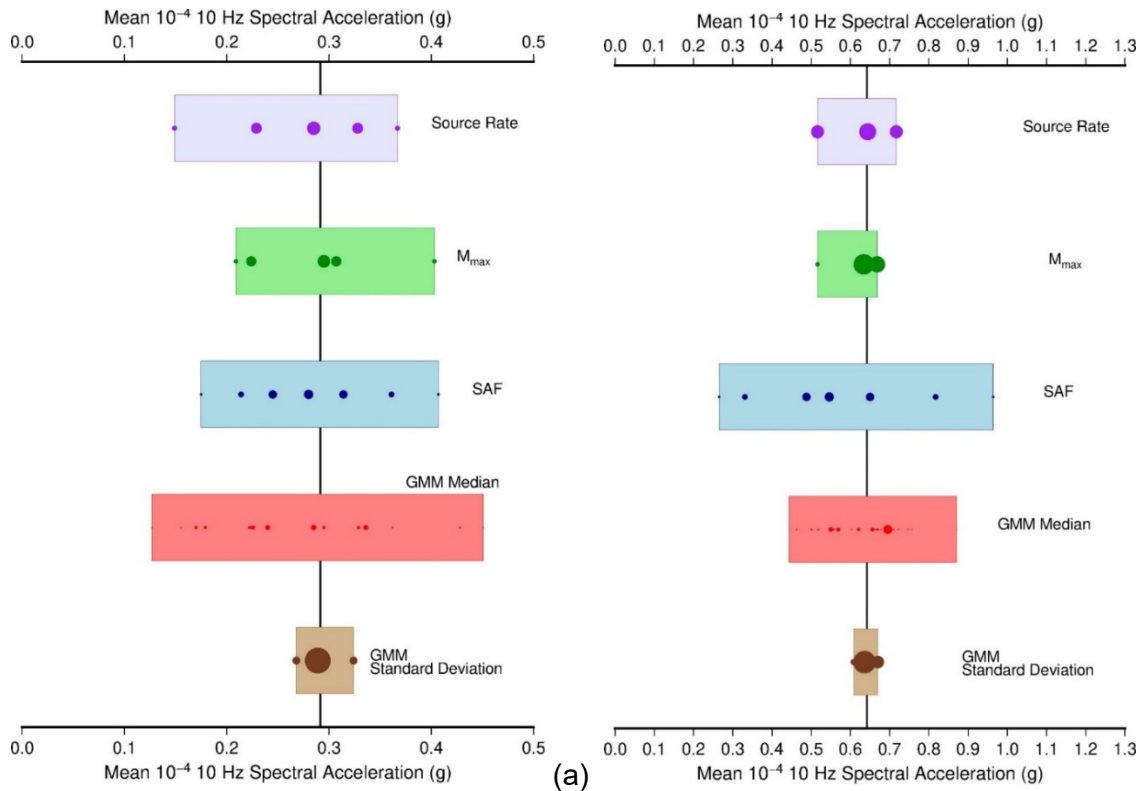


**Figure 8-1 Tornado plot for mean 10 Hz spectral acceleration at 10-4 AFE for (a) SRS and (b) GVDA sites**

The implementation of the logic tree approach in future SSHAC site response projects is strongly recommended. The logic tree approach allows for a methodical accounting of all sources of epistemic uncertainty and its use was essential to properly capturing the epistemic uncertainty in site response for the two study sites. An essential component of the approach adopted in this study is that the epistemic uncertainty in site response is defined in terms of the range of *SAFs* that resulted from considering all branches of the site response logic tree. The definition of epistemic uncertainty in *SAF* space allows for the implementation of a minimum epistemic uncertainty and ensures that the treatment of uncertainties is consistent across all oscillator frequencies.

The remainder of this section identifies additional salient lessons learned in the conduct of this study along with important research opportunities that will improve site response analyses for critical facilities.

### 8.2.1 Shear-Wave Velocity Characterization

The availability of good  $V_S$  and geotechnical data remains a key element for conducting site response analyses. Although both study sites would be considered “well-characterized” in terms of the available data regarding site properties, the two sites were distinctly different in terms of the types of data available, as well as the characteristics of the GMM models used. For the GVDA site, abundant multi-channel analysis of surface wave (MASW)/microtremor array measurements (MAM) data and single-station horizontal-to-vertical spectral ratio (HVSr) measurements are available. These data were used to inform the base-case  $V_S$  profiles and to constrain the  $V_S$  randomizations. For the SRS, there is a significant amount of  $V_S$  data but no measured surface wave dispersion data or HVSr data, and thus constraints on the  $V_S$

randomizations could not be imposed by the TI Team. On the other hand, the SRS has abundant geotechnical data that allowed for a good characterization of the site stratigraphy. This detailed site stratigraphy data resulted in less epistemic uncertainty in the  $V_S$  profiles at the SRS site compared to the GVDA site.

The ability to use surface wave and HVSR data at GVDA to constrain the  $V_S$  profiles obtained from other measurement methods and to constrain the randomization models is important. Surface wave data provides measurements that are representative of global averages of the site profiles at the site, and the information embedded in these data should be carefully considered in the development of the site response logic tree. Nonetheless, additional work is needed on how best to utilize these data to inform both the epistemic uncertainty and aleatory variability in  $V_S$ .

### 8.2.2 Kappa

The availability of ground motion recordings at a site leads to substantially smaller epistemic uncertainties in  $\kappa_0$  compared to sites that rely on empirical relationships that use global parameters. For example,  $\kappa_0$  at the GVDA site was estimated from earthquake recordings while at SRS,  $\kappa_0$  was estimated from several empirical correlations. As a result, the GVDA had significantly smaller epistemic uncertainty in  $\kappa_0$  than SRS. The availability of recordings at GVDA also allowed for the use of a rational, data-based approach to assigning logic tree weights. Installation of instrumentation at an early stage at sites that are candidates for future PSHA studies is strongly encouraged so that recordings can be obtained and used to assess  $\kappa_0$ .

Site kappa has a large impact on the uncertainty in  $SAF$  at high frequencies, but estimates of  $\kappa_0$  can be affected by site effects that are present at high frequencies. Additional research is needed to improve the estimation of  $\kappa_0$  from strong motions, to account for high-frequency resonances, and to develop empirical estimates of  $\kappa_0$  that are region-specific. The large amount of data from the Transportable Array (Ktenidou et al., 2017) may be able to empirically constrain  $\kappa_0$  over broad regions in the U.S. and thus improve existing models correlating  $\kappa_0$  to site proxies (e.g.,  $V_{S30}$ ).

### 8.2.3 Kappa Correction and Site Response Analysis Methods

Several site response approaches were considered by the TI Team during this study, including equivalent linear (EQL) analysis, fully nonlinear (NL) analysis, and EQL analysis with an a-posteriori kappa correction (the *kappa2* approach; see Section 5.5). The application of the *kappa2* approach requires parameter choices that result in epistemic uncertainty. The results for the SRS study site suggest that the logic tree branches for the *kappa2* approach are sufficient to capture the epistemic uncertainty associated with different analysis methods (i.e., NL vs. EQL) at frequencies above 3 Hz. There are some moderate differences between the  $SAFs$  from EQL and NL analyses at frequencies less than about 3 Hz. The TI Team judged these differences to be insufficient to warrant adding NL analysis as an alternative analysis method to the logic tree.

The *kappa2* approach was adopted by the TI Team after evaluating the site response results and comparing them to other approaches (i.e., NL analyses). However, additional work is still needed to fully validate this approach and to calibrate the input parameters needed in the implementation of the kappa correction for site-specific applications.

## 8.2.4 One-Step Approach for Development of Site Adjustments Factors

The TI Team utilized the one-step approach for developing *SAF* in this study, which accounts for changes in the reference condition and the site-specific, near-surface condition in one adjustment. However, the *SAFs* were developed differently for the two sites because of differences in the reference condition associated with the GMMs for the two study sites. The western U.S. GMM used at the GVDA site can be associated with a generic, reference  $V_S$  profile consistent with the site conditions implicit in the GMM. However, this generic  $V_S$  profile at depth differs from the  $V_S$  profile at the GVDA site. Therefore, the *SAFs* for the GVDA study site required running two separate site response analyses: one for the GMM reference  $V_S$  profile and one for the site-specific  $V_S$  profile, with both profiles extended to a common, hard-rock reference horizon at depth ( $\sim 5$  km). The ratio of the surface motions from these two analyses represent the *SAF*. On the other hand, the central and eastern U.S. (CEUS) GMM used at the SRS study site was developed for a reference condition consistent with the reference condition (i.e.,  $V_S = 3000$  m/s) at the base of the SRS study site. Therefore, only a single site response analysis for the site profile above the reference horizon was required. In this case, the *SAF* was computed from the ratio of the surface motion to the outcropping input motion.

## 8.2.5 Input Motion Specification

This project included a sensitivity study regarding the influence on the *SAF* from the approach used to specify the input motion. This investigation showed that input motions developed by point source models and those developed as conditional mean spectra can produce significantly different *SAF*. This result reveals that the approach used to develop input motions for site response analyses may represent another source of epistemic uncertainty, and this source of uncertainty generally has not been incorporated into site response analyses. The TI Team did not observe a consistent difference in the *SAF* when using input motions developed from these two methods and thus adopted the more commonly used method of using point source models. Additional research is needed to determine if these different approaches to input motion specification generate significant differences in *SAF* for other sites, and to develop a recommended approach.

## 8.2.6 Variance Contributions

The use of a logic tree approach facilitates the analysis of the results from the site response analysis to quantify the contributions of the different components of the logic tree to the range and variance in the *SAF*. This analysis can be done via tornado plots or variance contribution plots. This analysis is important to identify the key contributors to epistemic uncertainty in the  $V_S$ . The TI Team evaluation of tornado plots and variance contribution plots showed that for both sites, no single logic tree node dominated the total variability across all cases, indicating that all the nodes in the logic trees were necessary to fully capture the epistemic uncertainty. We strongly recommend that these sensitivity analyses be conducted to develop a clear understanding of how components of the logic tree affect the *SAF*.

The TI Team also observed that the epistemic uncertainty in the *SAF* can vary across frequencies as a result of the discrete sampling of the parametric uncertainty in the logic tree. For this reason, the TI Team recommends that future projects represent epistemic uncertainty due to site effects as epistemic uncertainty in the resulting *SAF*. The TI Team conducting the study must then make a judgment on whether the range of *SAF* properly represents the CBR of TDI. If this is not the case, the epistemic uncertainty in *SAF* should be smoothed across periods.

### **8.2.7 Model Error**

The results of this study show that model error is an important contributor to epistemic uncertainty. The TI Team opted to apply the model error as a minimum epistemic uncertainty. The value of model error selected for this study controlled the epistemic uncertainty in the *SAF* at a large number of frequencies, particularly for the SRS study site. This result highlights that care must be placed in selecting the value of the model error.

Additional research is needed to develop appropriate estimates of model error for 1D site response analyses, particularly for strong ground motions. The application of model error to capture the CBR of TDI hinges on the ability to separate model error from parametric uncertainty because the parametric uncertainty is already captured by the site response logic tree. Therefore, future research on model error should focus on understanding how much parametric uncertainty contributes to estimates of model error.

### **8.2.8 Lower Bound Adjustment Factors**

The TI Team considered that there are no technical justifications for the imposition of a lower bound on the *SAF*. This conclusion is in contrast to previous guidance (EPRI, 2012) which suggested the use of a lower bound of 0.5 for the computed amplification factors at a site as a conservative lower bound on the impact of nonlinearity on estimated ground motions. These limits were put in place to ensure that the overdamping that results when soil layers are taken to large strains in EQL analysis do not result in underestimation of the site hazard. If proper care is taken to ensure that the site response analysis results are valid at the observed strains, then there is no technical basis for a lower limit on the *SAF*. Additional research on the validity of site response analyses at large strains will shed further light on this issue.

### **8.2.9 Empirical Validation**

Empirical validation at the GVDA study site provided confidence that the analytically derived, linear elastic *SAFs* computed in this study were representative of the site. The GVDA study site has an abundance of low amplitude earthquake ground motion recordings with good signal/noise ratios. To assess the efficacy of the SSHAC process at capturing the epistemic uncertainty in *SAFs* at this site, the TI Team computed a linear empirical site term with respect to the site-specific conditions for the GVDA study site. This facilitated an evaluation of how well the analytical approach to linear site amplification used in the present study compared with the observed ground motions. The resulting empirical site-terms have median values near zero over a broad range of oscillator frequencies; and, in general, fall within a 95% confidence interval.

### **8.2.10 Implementation of Site Response into PSHA**

For both study sites, the TI Team calculated the control point (i.e., ground surface) hazard using both Approach 3 and Approach 4, as described in McGuire et. al (2001) and Section 3.4. Approach 3 was implemented using both the Hazard Integral approach, which simultaneously determines the reference hazard and incorporates the *SAF* into the full hazard integral, and the Convolution approach, which convolves the predetermined hazard for the reference condition with the *SAFs*. For the SRS study site, Approach 3 (Hazard Integral) and Approach 4 produce approximately the same mean hazard and fractiles. For the GVDA study site, both approaches produce approximately the same mean hazard for the 1,000- and 10,000-year return periods,

though with slightly higher amplitudes when Approach 4 is used. For the 100,000-year return period, the Approach 4 UHRS have larger amplitudes and appear to be more susceptible to abrupt slope changes in the relationship between *SAF* and the reference spectral acceleration. However, GMRS developed for the highest seismic design category (GMRS-5) generally follow the mean UHRS for the 10,000-year return period, such that the use of analytical Approach 4 would not likely result in a GMRS that differs significantly from a GMRS developed using the Hazard Integral Approach 3. Comparisons of the two implementations of Approach 3 (Hazard Integral and Convolution) at both study sites show that the mean and fractile hazard curves match very closely. As described in Section 7, the TI Team observed that the two key factors in producing similar hazard results for each of the approaches are 1) the use of multiple loading levels for the site response analysis, and 2) the piecewise interpolation of the median *SAFs* as a function of reference spectral acceleration.

Previously, the use of Convolution Approach 3 has been restricted to developing mean control point hazard results to produce mean UHRS and GMRS. However, as described in Section 7, the TI Team was able to develop control point hazard fractiles from Convolution Approach 3 that matched the control point fractiles from the use of Hazard Integral Approach 3. The benefit of using Convolution Approach 3 versus the Hazard Integral Approach 3 is reduced computing time. The Hazard Integral Approach 3 took the TI Team several days to run, while the Convolution Approach 3 took only the amount of time needed to develop the reference condition hazard for each of the sources and then a small amount of extra time for the convolution of the *SAF* with the reference hazard.

### **8.2.11 Downstream Applications That Utilize PSHA Results**

The results of the PSHA (including the site response analysis) are used in a number of ways after the completion of the study. One use of the hazard curves is to develop design response spectra, which are derived based on the risk significance of the facility or the structure, system, or component. This typically uses the mean hazard. Another use of the results is in seismic probabilistic risk analyses (SPRA), which utilize both the mean hazard curves as well as the fractiles. An additional use of the PSHA and site response analyses is to develop strain-compatible material properties for use in the soil-structure interaction (SSI) analyses. The results developed in this study would be applicable to each of the uses above, but some issues remain regarding how best to use the results in the SSI analyses in a manner consistent with the site response analysis. This issue stems from the modeling of the soil in the SSI analyses and how to incorporate epistemic uncertainties.

For most studies, only a relatively small number of SSI analyses are performed because of the computational resources required. Additionally, many SSI codes can only model the soil as linear elastic, a consequence of trying to reduce the computational cost of the SSI analyses. As a result, the SSI analysis cannot incorporate the full range of epistemic uncertainty that was used in the site response analyses for the PSHA. Current practice for developing the soil properties used in SSI analysis identifies three deterministic sets of strain-compatible, linear-elastic properties (i.e.,  $V_s$  and material damping). Each of the three deterministic cases are exercised with an input motion consistent with the design foundation input response spectrum. The response of the structure is often enveloped across the three sets of properties. Because the uncertainties across the full site response logic tree are not incorporated into the analyses, and because the focus is on defining a range in properties as opposed to modeling the resulting variability in *SAF*, it is likely that SSI analyses will not be consistent with the site response analyses used in the PSHA.

This project focused on developing a distribution of *SAF* that captures the CBR of TDI of the elements in the site response analysis logic trees. Each of the individual *SAFs* is associated with a discrete weighted combination of the branches in the logic tree. Currently, there is no straight-forward mapping of the *SAF* distribution to a very small sample of cases that can be used to develop the strain-compatible soil properties that maintain a probabilistic context and are consistent with the *SAF* distribution. This is clearly a necessary future research topic beyond the scope of this project.

### **8.3 Conclusions**

This study demonstrates that the SSAHC process can be applied to the conduct of site response analyses for seismic hazard assessment of nuclear facilities. Through the course of the study, the uncertainties associated with different data, models, and methods associated with site response were systematically addressed. This report documents the process used to develop the site response logic tree and provides detailed descriptions of the data and analyses used to inform the process. The results of the site response analysis and the effect of the site adjustments on the resulting hazard curves are presented in a manner such that the contribution of the site response analysis is clear. It is anticipated that this report can be used by others as a road map for site response analysis associated with PSHA for nuclear facilities. Research may continue to develop in the areas outlined above, as well as in other areas, but the use of the SSHAC process will allow these developments to be considered and incorporated into the site response analysis.

### **8.4 References**

EPRI. "Seismic Evaluation Guidance: Screening, Prioritization and Implementation Details (SPID) for the Resolution of Fukushima Near-Term Task Force Recommendation 2.1: Seismic." Report 1025287. Palo Alto, California: Electric Power Research Institute. 2012.

Ktenidou, O.J., W.J. Silva, R.B. Darragh, N.A. Abrahamson, and T. Kishida. "Squeezing kappa ( $\kappa$ ) out of the Transportable Array: A Strategy for Using Bandlimited Data in Regions of Sparse Seismicity." *Bulletin of the Seismological Society of America*. Vol. 107, No. 1. pp. 256–275. 2017.

McGuire, R.K., W.J. Silva, and C.J. Costantino. NUREG/CR-6728, "Technical Basis for Revision of Regulatory Guidance on Design Ground Motions: Hazard- and Risk-Consistent Ground Motion Spectra Guidelines." Washington, DC: U.S. Nuclear Regulatory Commission. ML013100232. 2001.

NRC. NUREG–2213, "Updated Implementation Guidelines for SSHAC Hazard Studies." ML18282A082. Washington, DC: U.S. Nuclear Regulatory Commission. 2018.

Rodriguez-Marek, A., J. Ake, C. Munson, E. Rathje, S. Stovall, T. Weaver, K. Ulmer, and M. Juckett. "Site Amplification Factors Developed Using SSHAC Guidance." Design Safe-CI. 2021. <https://doi.org/10.17603/ds2-9t3a-kz92>.

**APPENDIX A**  
**PPRP Closure Letter**

## **PPRP Closure Letter for the NRC-Sponsored SSHAC Level 2: Site Response Analysis Study**

This document constitutes a consensus closure letter from the Participatory Peer Review Panel (PPRP, “the Panel”) for the SSHAC (Senior Seismic Hazard Analysis Committee) Level 2: Site Response Analysis Study. The Site Response Analysis Study was carried out following guidance from the SSHAC NUREG-2213<sup>1</sup>. The U.S. Nuclear Regulatory Commission (NRC) sponsored the project and intends to use the results to develop and support technical bases for future updates to regulatory guidance, including regulatory guides to develop performance-based site-specific ground motions at NRC regulated facilities.

### **Summary**

The goal of the study was to apply the SSHAC process to the conduct of site response analyses (SRA) at two example sites (Garner Valley, CA and the Savannah River Site, SC) to develop a consistent, scalable framework that can be applied in future SRA. This framework provides a set of practical tools and methods for future SRA studies, and it will enable practitioners to systematically identify and propagate epistemic uncertainties in SRA data, models, and methods into the assessment of site response at nuclear facilities. The PPRP concludes that the Project Team, including the Technical Integration (TI) Team and the Data Analysis Group, and the PPRP successfully followed and implemented the guidance in NUREG-2213 for a SSHAC Level 2 study.

Specifically:

- All the participants in the study were trained in the SSHAC principles and everyone understood and executed their assigned roles and responsibilities.
- All essential steps of a SSHAC Level 2 process have been followed and documented in the final report, including the enhancement of holding the SRA related workshop that identified key SRA technical issues that were considered and addressed by the SRA TI Team.
- The TI Team, supported by the Data Analysis Group, evaluated available data, models, and methods, including a broad set of alternative proponent positions from the technical community of geological, seismological, and geophysical working in seismic hazard and site response analyses.
- The TI Team integrated these data, models, and methods into seismic site response models that captured the center, body, and range (CBR) of technically defensible interpretations (TDI).
- The technical elements of the SRA models have been defined in sufficient detail to provide confidence that the relevant SRA epistemic uncertainties and aleatory variability have been assessed and quantified.
- The technical bases for the site response models at the two sites were justified and adequately documented in the final report.
- The PPRP was fully engaged throughout the project and was able to provide a thorough and complete review of both the SSHAC processes and the technical bases for the TI Teams’ final models.

---

<sup>1</sup> USNRC, 2018, “Updated Implementation Guidelines for SSHAC Hazard Studies,” United States Nuclear Regulatory Commission, NUREG-2213, Washington, D.C.

Based on these seven points, the PPRP concludes that the final technical report appropriately captures the CBR of TDI, and therefore adequately provides the technical basis for future PSHA studies to incorporate site response within the SSHAC process.

### **Project Plan and Project Organization**

The PPRP notes that a detailed Project and Plan was available at the beginning of the project (delivered to the PPRP on November 18, 2019, PPRP comments provided in January 2020), with a final plan completed in August, 2020 that included PPRP review and edits to address PPRP comments. The Project Plan covers project scope and requirements, project organization, project activities and schedule, control of documents and project processes, management, and details on the project participants. The PPRP believes that the Project Plan significantly contributed to the success of the project, and it facilitated the PPRP's participatory review.

The sponsor for this project is the U. S. Nuclear Regulatory Commission Office of Research. A Project Manager provided overall coordination and responsibility for all organizational and administrative aspects, including liaison with the sponsor (NRC) and the PPRP. The project was also supported by the Data Analysis Group, Resource Experts, and Proponent Experts. The roles and responsibilities of project participants are described in the Project Plan and final report and conform to the SSHAC guidelines.

### **PPRP Organization and Duties**

The PPRP for this project consisted of three members: Dr. John Stamatakos (chair), Mr. Jeff Kimball, and Dr. Dogan Seber. These members collectively meet all requirements in terms of subject area expertise, knowledge of PSHA, and experience from other projects carried out following SSHAC guidance.

As part of the Level 2 process, peer review occurs in a participatory fashion at several stages of the process, rather than only at the end. In the present project, the main PPRP participation consisted of:

- Review the Project Plan.
- Observation of the project Workshop.
- Review of Workshop agendas and review of proposed lists of invited Resource and Proponent Experts.
- Review of Workshop sessions, including providing feedback to the Project Manager and TI Teams in a report at the end the Workshop.
- Attendance by at least one PPRP member at several of the TI Team's weekly Working Meetings, at which informal feedback was given verbally.
- Attendance at the PPRP Briefing, held on July 27, 2021
- Review of the draft Final Report.
- Review of responses to the comments on the draft Final Report to ensure the adequacy of the responses.

The PPRP review has therefore been participatory in that the PPRP has been informed by their observation and participation at all important stages of the process. The PPRP review consisted of ensuring that the SSHAC process was being faithfully followed and that the SRA TI Team was fully

evaluating relevant SRA technical issues and integrating the assessment of these issues into the SRA assessments, and that the technical bases for these decisions were adequately documented.

### Conclusions

The Final Project Report presents the results of the project in detail, and the PPRP concludes that the TI Teams have captured the CBR of TDI for site response analysis. The PPRP hereby formally concurs that issues have been resolved and that the Final Project Report is acceptable as the successful result of the Project.

The PPRP would like to take this opportunity to note the excellence of the work of the Project Manager and the TI Team Lead, which greatly facilitated the efficient execution of the project at all stages.

PPRP

John  
Stamatakos



Digitally signed by John  
Stamatakos  
Date: 2021.10.08 15:56:43  
-04'00'

John Stamatakos (PPRP Chair)



Jeff Kimball (PPRP Member)

Dogan  
Seber



Digitally signed  
by Dogan Seber  
Date: 2021.10.12  
07:25:20 -04'00'

Dogan Seber (PPRP Member)

## **APPENDIX B**

### **PROJECT PLAN, REV 3.**

**Document Located in the NRC's Agencywide Documents Access and Management System (ADAMS). Accession Number ML21320A076**

## **APPENDIX C**

### **REPEATED RANDOM SAMPLING APPROACH**

## Repeated Random Sampling Approach for Developing Total Fractile Hazard Curves

As described in Section 7, rather than combining all the control point hazard curves for the two distributed seismicity sources together with the four possible configurations for the Charleston repeated large magnitude earthquake (RLME), the Technical Integration (TI) Team implemented a repeated random sampling approach to develop total fractile hazard curves for the Savannah River Site (SRS) study site. Figure C-1 shows the 10 Hertz (Hz) hazard curves from the two distributed seismotectonic sources [Extended Continental Crust – Atlantic Margin (ECC-AM) and Paleozoic Extended Zone – Narrow Configuration (PEZ-N)] together with the four alternative Charleston RLME configurations [Charleston Local Source (CLS), Charleston Narrow Source (CNS), Charleston Regional Source - Parallel (CRP), and Charleston Regional Source – Perpendicular (CRR)]. Overlain on each of the sets of hazard curves is the mean hazard for each source (red dashed curves) and the total combined mean hazard (black curve). Because each of the six sources has 8,925 alternative hazard curves, determining the fractiles for the total hazard would necessitate combining 8,925 curves raised to the sixth power to capture all the total possible combinations. Instead, the TI Team developed a random sampling approach that it repeated multiple times to achieve stable estimates of the total fractile hazard curves.

Figures C-2a and C-2b show the 10 Hz hazard curves for ECC-AM and PEZ-N, respectively, each with a red vertical line at a spectral acceleration value of 0.05g. To implement the sampling approach, the TI Team selected a random sample of the annual frequency of exceedance (AFE) values and their associated weights for each spectral acceleration value for each seismic source. For each of the selected samples, the TI Team then added the randomly sampled AFEs together from each source for each spectral acceleration value. After adding the randomly sampled AFEs for the multiple seismic sources, the TI Team ordered the summed AFE values and developed a cumulative distribution function (CDF) based on the combined weights for the summed AFE values. This CDF was then used to estimate the desired fractiles. This process was then repeated multiple times to develop stable estimates of the total fractile hazard curves. Figures C-3a and C-3b show the 5<sup>th</sup> and 16<sup>th</sup> percentiles for the combined sources of ECC-AM and PEZ-N for the 10 Hz spectral acceleration value of 0.05g. Shown on these two plots are the combined AFE percentiles for sample sizes of 100, 500, 1000, 2000, and 5000, as well as all 8,925 AFE values. For the case where the entire set of 8,925 AFEs was selected for each spectral acceleration, the TI Team randomly shuffled the order of the AFEs before combining them with the 8,925 AFEs from the other sources, to mimic the random sampling process used for the other sample sizes. As shown in Figure C-3a, the average percentile value (box) and error bars ( $\pm 1$  sigma) begin to stabilize for the sample size of  $n=1,000$  repeated 10 times. Figures C-4a and C-4b show the same repeated sampling process for the median and mean, while Figures C-5a and C-5b show the results for the 84<sup>th</sup> and 95<sup>th</sup> percentiles. The TI Team used the total mean hazard curve developed from combining the weighted mean hazard curves from each of the sources as a check on the repeated sampling approach. Figure C-4b shows that the repeated sampling approach does converge to the actual total 10 Hz mean AFE value of  $1.4 \times 10^{-3}$  for the combined ECC-AM and PEZ-N sources for a sample size of 1,000 repeated 10 times.

Figures C-6a and C-6b show the 10 Hz total mean and fractile hazard curves for SRS for the two combined distributed seismotectonic sources ECC-AM + PEZ-N and the four combined Charleston RLME configurations (CLS+CNS+CRP+CRR), respectively. Finally, Figure C-7 shows the 10 Hz total mean and fractile hazard curves for SRS after combining all the seismic

sources. For each of the source combinations, the TI Team used a sample size of 1,000 and 10 iterations.

In summary, the TI Team's repeated sampling approach to develop total fractile hazard curves follows the steps outlined below.

1. Randomly sample a vertical slice of AFEs from each source for a given spectral acceleration and frequency
2. Add randomly sampled AFEs from each source to obtain total hazard
3. Develop cumulative distribution for the total hazard after normalizing
4. Determine fractiles from the cumulative distribution
5. Repeat steps 1-4 multiple times
6. Average the fractiles from the multiple iterations
7. Move to next AFE vertical slice

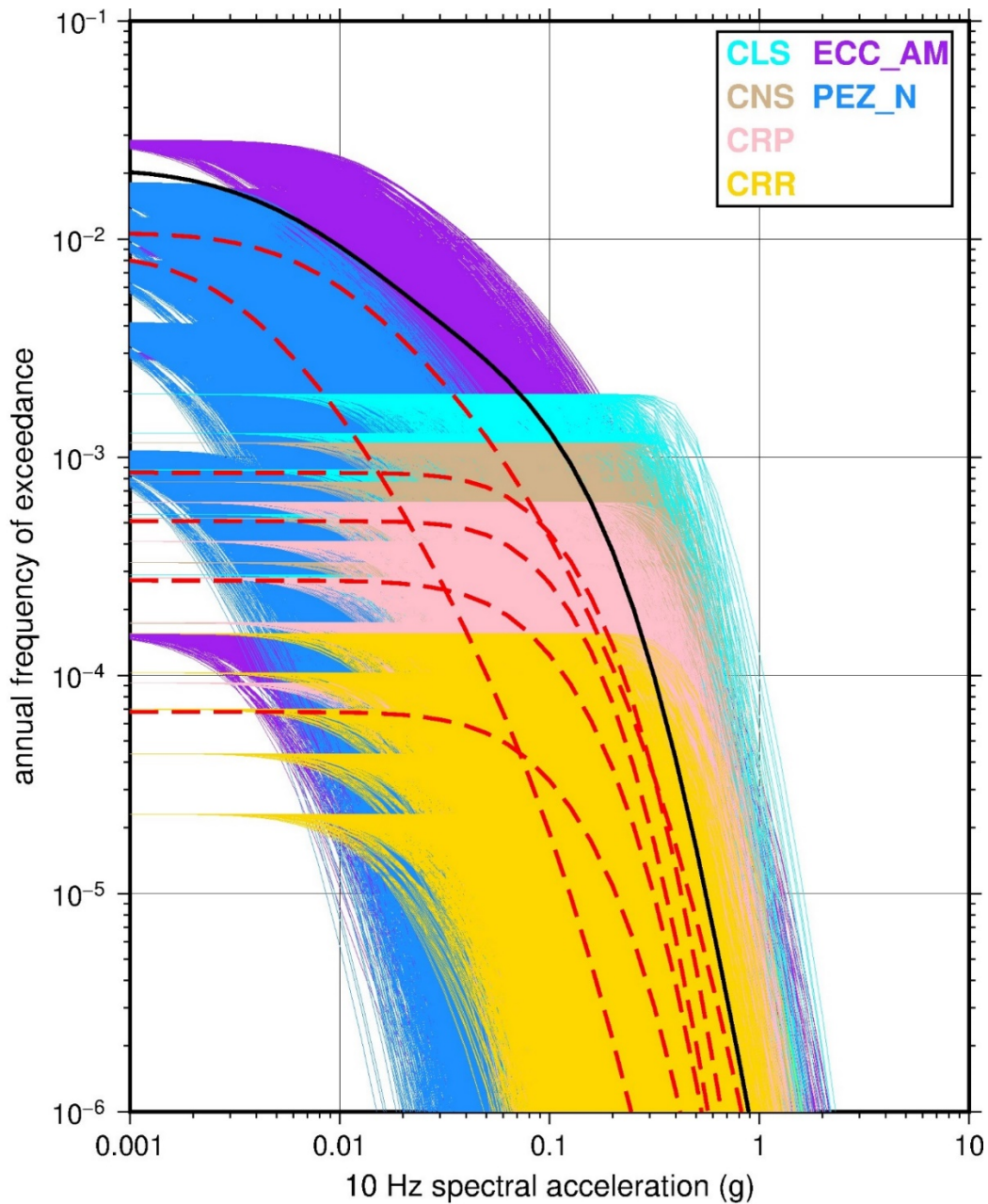


**Figure C-1** Hz hazard curves from the two distributed seismotectonic sources [Extended Continental Crust – Atlantic Margin (ECC-AM) and Paleozoic Extended Zone – Narrow Configuration (PEZ-N)] together with the four alternative Charleston RLME configurations [Charleston Local Source (CLS), Charleston Narrow Source (CNS), Charleston Regional Source - Parallel (CRP), and Charleston Regional Source – Perpendicular (CRR)]. Overlain on each of the sets of hazard curves is the weighted mean hazard for each source (red dashed curves) and the total combined mean hazard (black curve).).

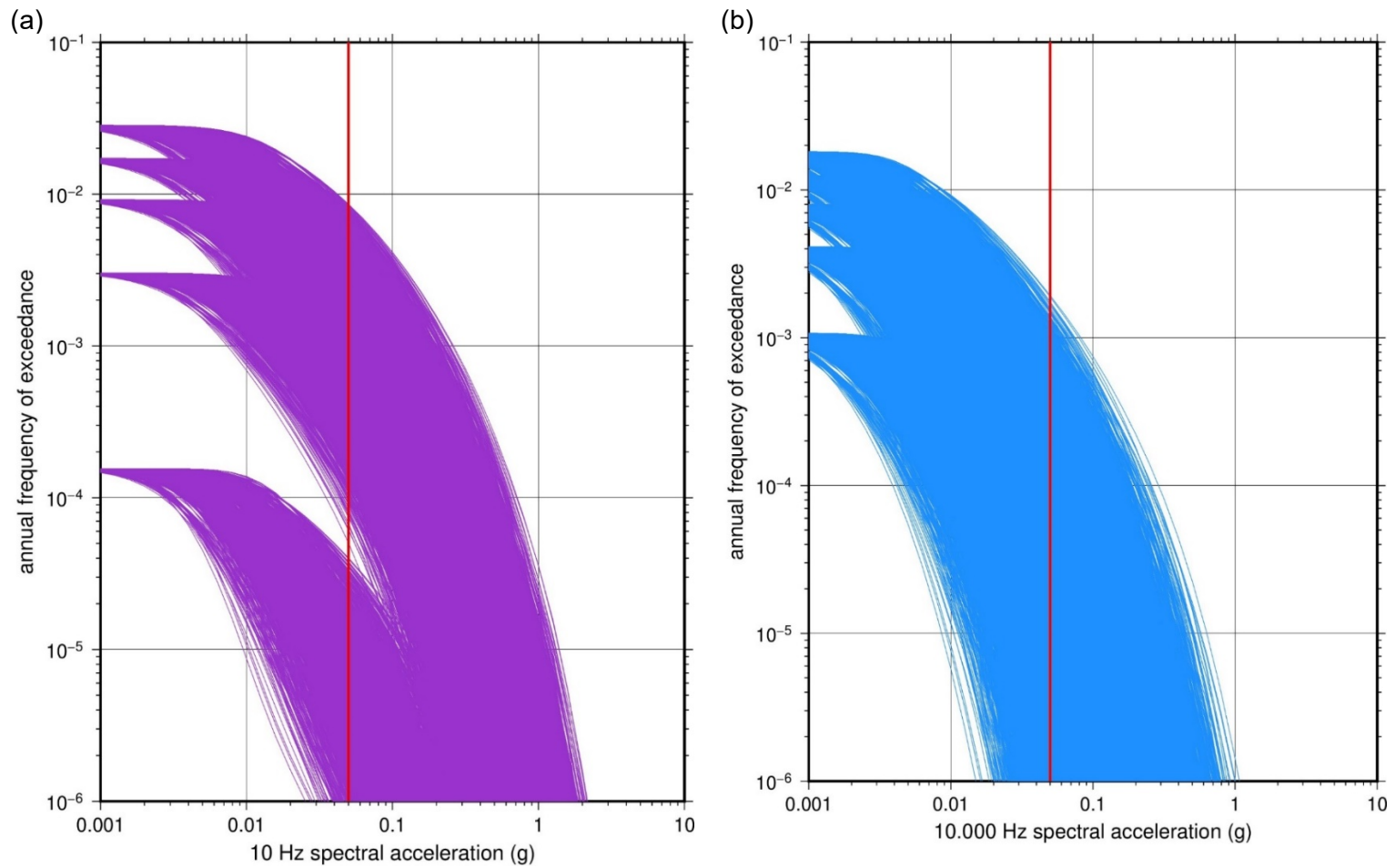
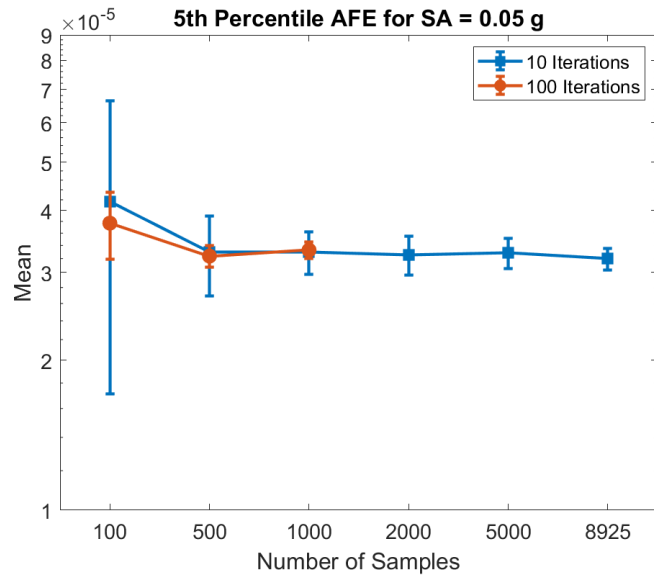


**Figure C-2 (a) 10 Hz hazard curves for ECC-AM (purple curves) with red vertical line at a spectral acceleration value of 0.05g. (b) 10 Hz hazard curves for PEZ-N (blue curves) with red vertical line at a spectral acceleration value of 0.05g.**

(a)



(b)

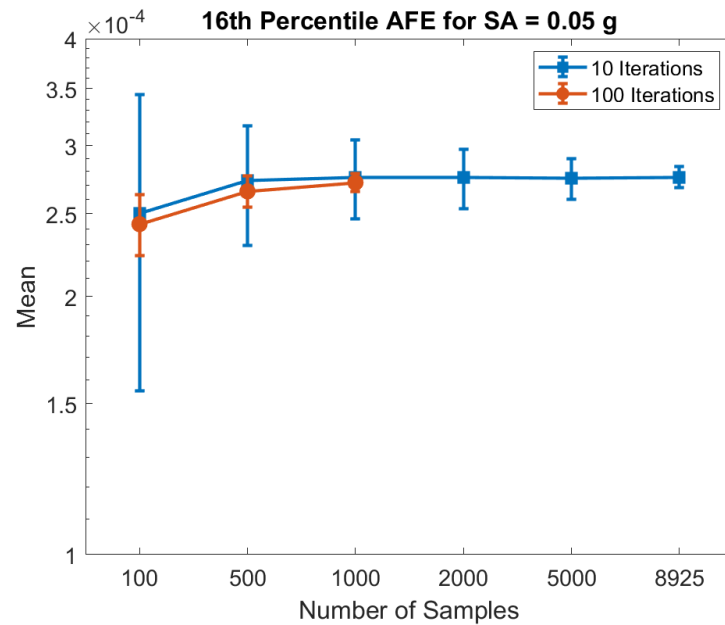


**Figure C-3** (a) Fifth percentile for the combined sources of ECC-AM and PEZ-N for the 10 Hz spectral acceleration value of 0.05g. Combined AFE 5th percentile mean (box) and error bars ( $\pm 1$  sigma) are shown for sample sizes of 100, 500, 1000, 2000, 5000, as well as all 8,925 AFE values for 10 (blue) and 100 (red) iterations. (b) Sixteenth percentile for the combined sources of ECC-AM and PEZ-N for the 10 Hz spectral acceleration value of 0.05g. Combined AFE 16th percentile mean (box) and error bars are shown for sample sizes of 100, 500, 1000, 2000, 5000, as well as all 8,925 AFE values for 10 (blue) and 100 (red) iterations.

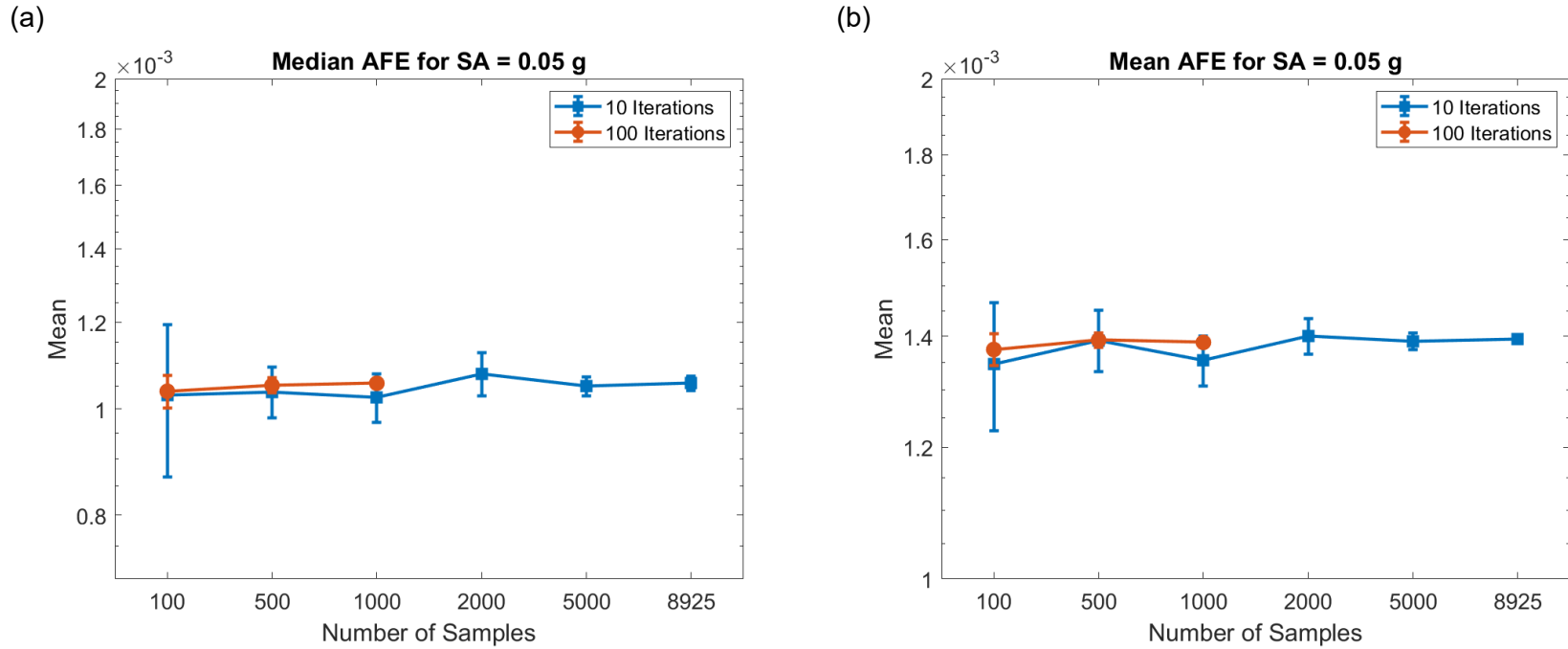
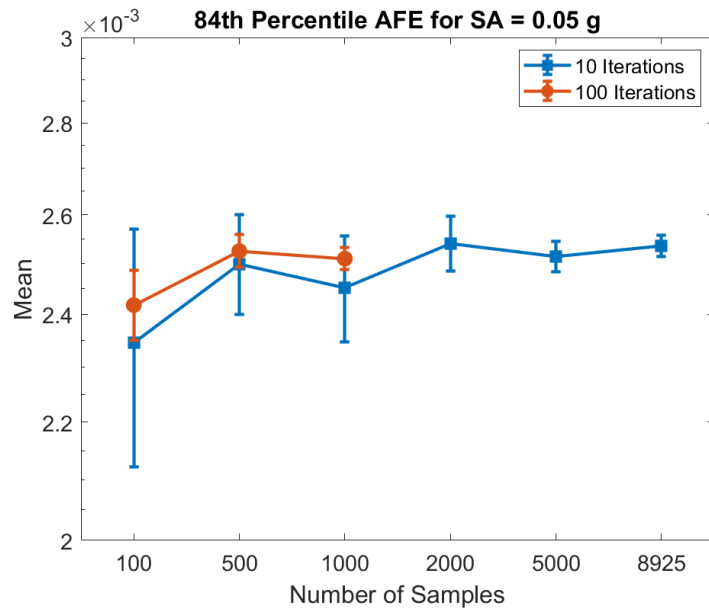


**Figure C-4** (a) Median percentile for the combined sources of ECC-AM and PEZ-N for the 10 Hz spectral acceleration value of 0.05g. Combined AFE median percentile mean (box) and error bars are shown for sample sizes of 100, 500, 1000, 2000, 5000, as well as all 8,925 AFE values for 10 (blue lines) and 100 (red lines) iterations. (b) Mean for the combined sources of ECC-AM and PEZ-N for the 10 Hz spectral acceleration value of 0.05g. Combined AFE mean average (box) and error bars are shown for sample sizes of 100, 500, 1000, 2000, 5000, as well as all 8,925 AFE values for 10 (blue lines) and 100 (red lines) iterations.

(a)



(b)

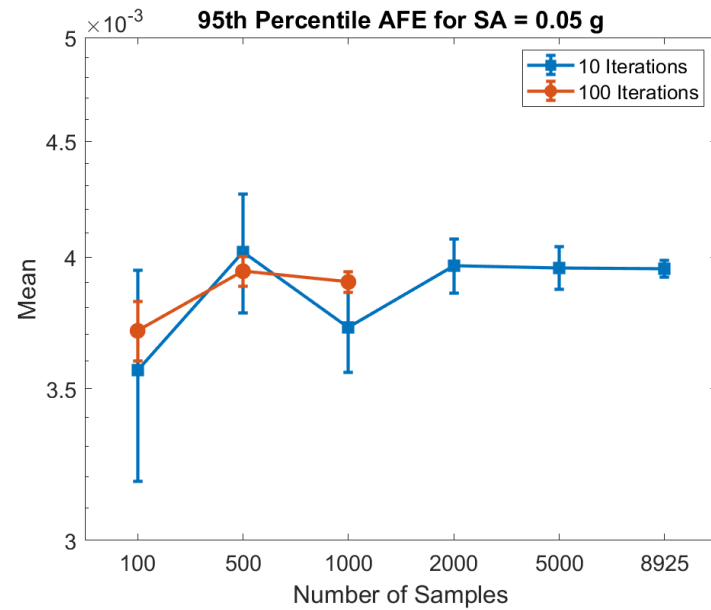


**Figure C-5** (a) Eighty-Fourth percentile for the combined sources of ECC-AM and PEZ-N for the 10 Hz spectral acceleration value of 0.05g. Combined AFE 84<sup>th</sup> percentile mean (box) and error bars are shown for sample sizes of 100, 500, 1000, 2000, 5000, as well as all 8,925 AFE values for 10 (blue lines) and 100 (red lines) iterations. (b) Ninety-Fifth percentile for the combined sources of ECC-AM and PEZ-N for the 10 Hz spectral acceleration value of 0.05g. Combined AFE 95<sup>th</sup> percentile mean (box) and error bars are shown for sample sizes of 100, 500, 1000, 2000, 5000, as well as all 8,925 AFE values for 10 (blue lines) and 100 (red lines) iterations.

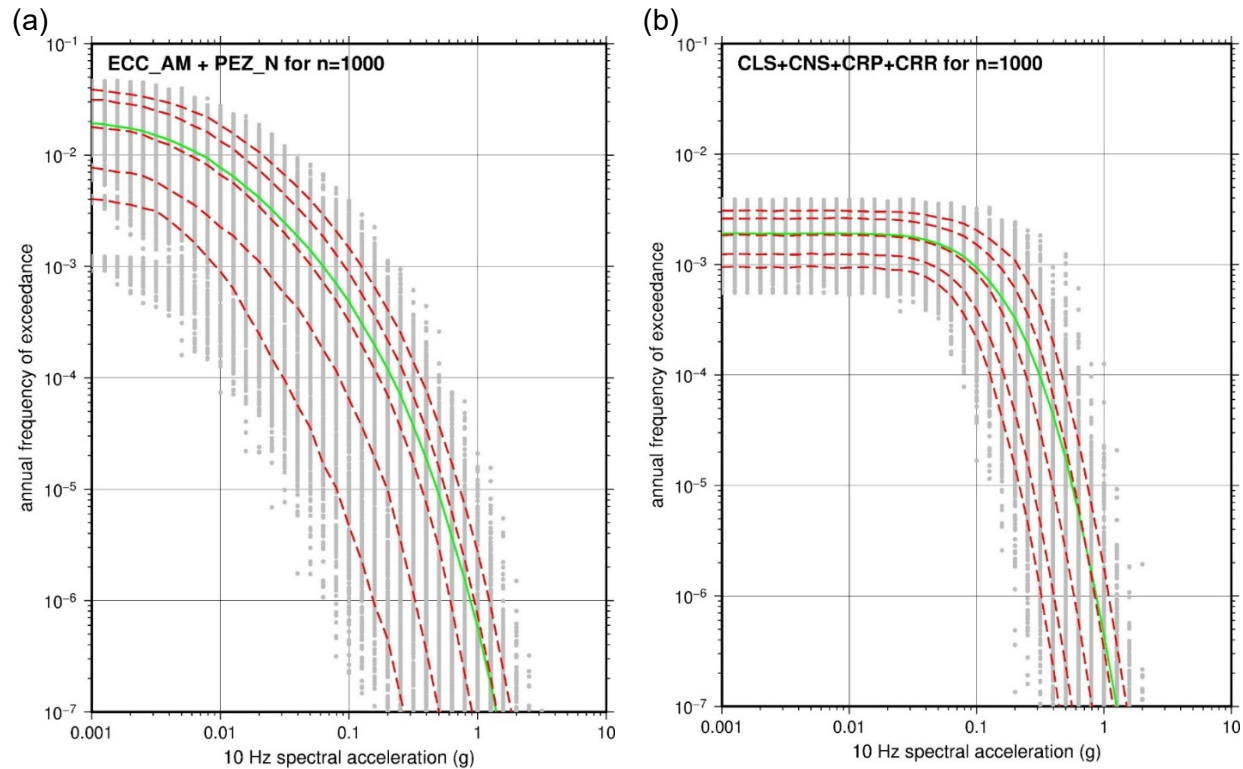


**Figure C-6 (a) 10 Hz total mean (green curve) and fractile (0.05, 0.16, 0.50, 0.84, 0.95) hazard curves (red dashed curve) for SRS for the two combined distributed seismotectonic sources ECC-AM + PEZ-N. Fractile estimates are based on a sample size of 1,000 (gray dots) with 10 iterations. (b) 10 Hz total mean (green curve) and fractile (0.05, 0.16, 0.50, 0.84, 0.95) hazard curves (red dashed curve) for SRS for the four combined Charleston RLME configurations (CLS+CNS+CRP+CRR). Fractile estimates are based on a sample size of 1,000 (gray dots) with 10 iterations.**

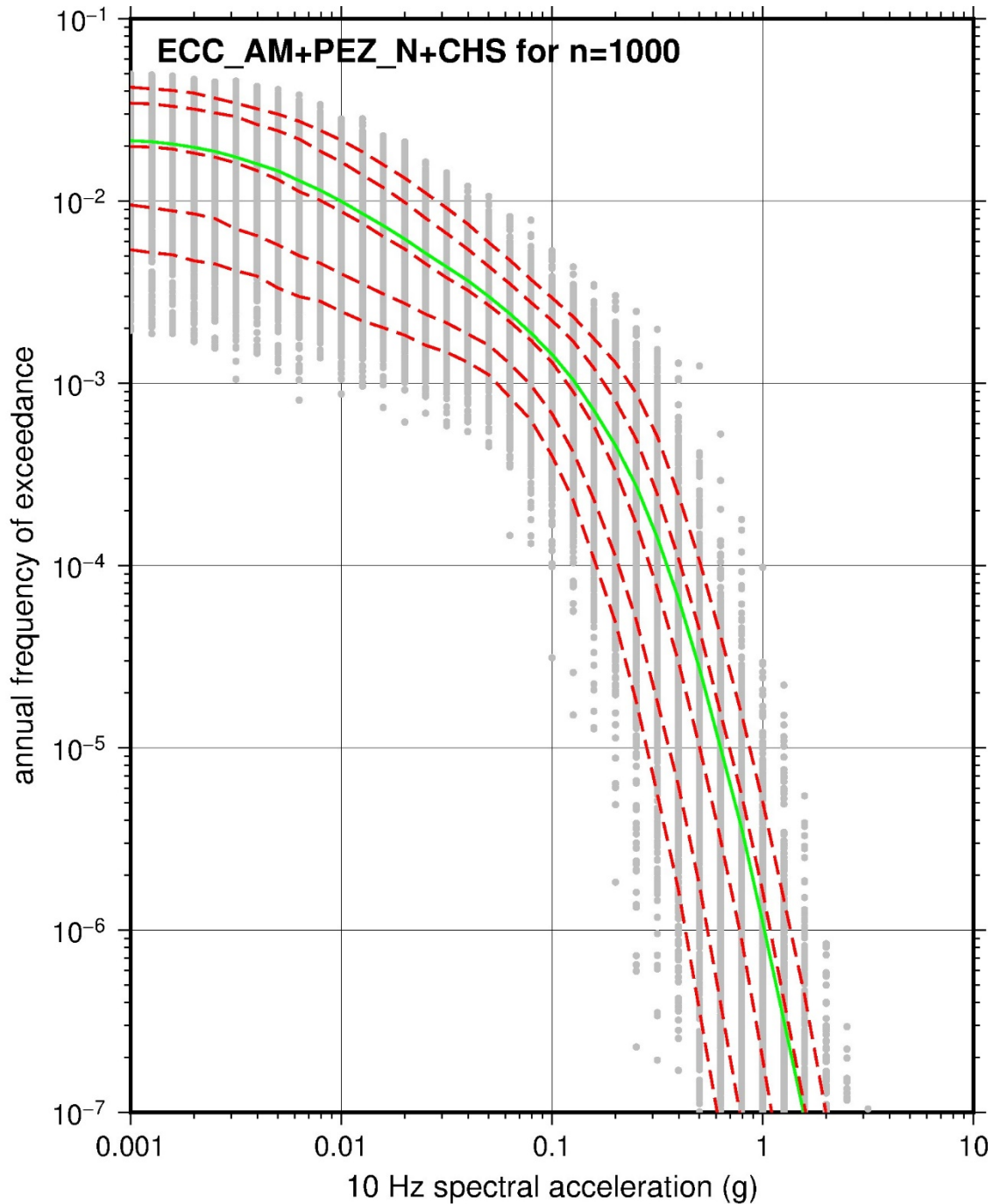


**Figure C-7** 10 Hz total hazard mean (green curve) and fractile (0.05, 0.16, 0.50, 0.84, 0.95) hazard curves (red dashed) for SRS after combining all the seismic sources. Fractile estimates are based on a sample size of 1,000 (gray dots) with 10 iterations.

**APPENDIX D**  
**ESTIMATING KAPPA**

## Estimating Site Kappa ( $\kappa_0$ ) and Its Epistemic Uncertainty From Downhole Array Data

This appendix describes in detail the data and methods used in Section 5.3.3 of this report for estimating site kappa ( $\kappa_0$ ) at the Garner Valley Downhole Array (GVDA) site. The high-frequency spectral decay parameter kappa introduced by Anderson and Hough (1984) and later adjusted to zero-distance by Hough and Anderson (1988) can be used to estimate  $\kappa_0$  and constrain the small-strain damping used in site response analyses (Xu et al., 2020). One approach to estimating  $\kappa_0$ , such as the one used for the Savannah River Site (SRS) study site in this report, is using multiple empirical relationships. The relationships are chosen for their alternative approaches in correlating site properties to  $\kappa_0$ , resulting in a range of  $\kappa_0$  values that is assumed to capture the epistemic uncertainty in  $\kappa_0$ . For the GVDA site, an alternative approach is used to capture the epistemic uncertainty in  $\kappa_0$ ; this approach is based on estimating  $\kappa_0$  from multiple on-site ground motion recordings over alternative frequency bands. The use of alternative frequency bands protects against biased estimates in  $\kappa_0$  and captures the center, body, and range of expected  $\kappa_0$  values at the site. A unique approach to weighting the  $\kappa_0$  for each frequency band is also described. The following sections provide details on the processing of ground motion data and the approaches used in quantifying the epistemic uncertainty in  $\kappa_0$ .

### Ground Motion Data

The Technical Integration (TI) Team extracted ground motion data from the Network for Earthquake Engineering Simulations (NEES) data portal (<http://nees.ucsb.edu/data-portal>). The TI Team required individual ground motions to meet three criteria to be considered reliable for estimating  $\kappa_0$ .

1. The ground motion must be from an earthquake of magnitude 3.5 or greater with a source-to-site distance within 100 kilometers (km).
2. The surface motion's peak ground accelerations (PGA) must not exceed 0.01g in either horizontal component to ensure low-strain linear response at the site.
3. The ground motion is required to have a signal-to-noise (SNR) of at least 3 decibels (dB) in both horizontal components to exclude noise effects.

The TI Team identified 110 surface ground motions that met these criteria. The TI Team considers these motions as candidates for evaluating  $\kappa_0$  and its uncertainty.

### Data Processing

The TI Team applied a series of data processing steps to each horizontal component of candidate surface and downhole ground motions prior to estimating  $\kappa_0$ . First, the Team applied a baseline correction using a 1<sup>st</sup> order polynomial. Then, the Team filtered the motion using a 10<sup>th</sup> order Butterworth bandpass (1 to 50 Hz) to avoid aliasing effects. To avoid inclusion of possible surface waves into the analyses, the Team selected a 5-second data window from the ground motion record beginning 1 second before the S-wave arrival. Similarly, the Team selected a 5 second window from the end of the ground motion record and computed the SNR between the two windows (Figure D-1). If the SNR was 3 dB or higher, the TI Team computed the acceleration Fourier amplitude spectrum (FAS) of the window containing the S-wave.

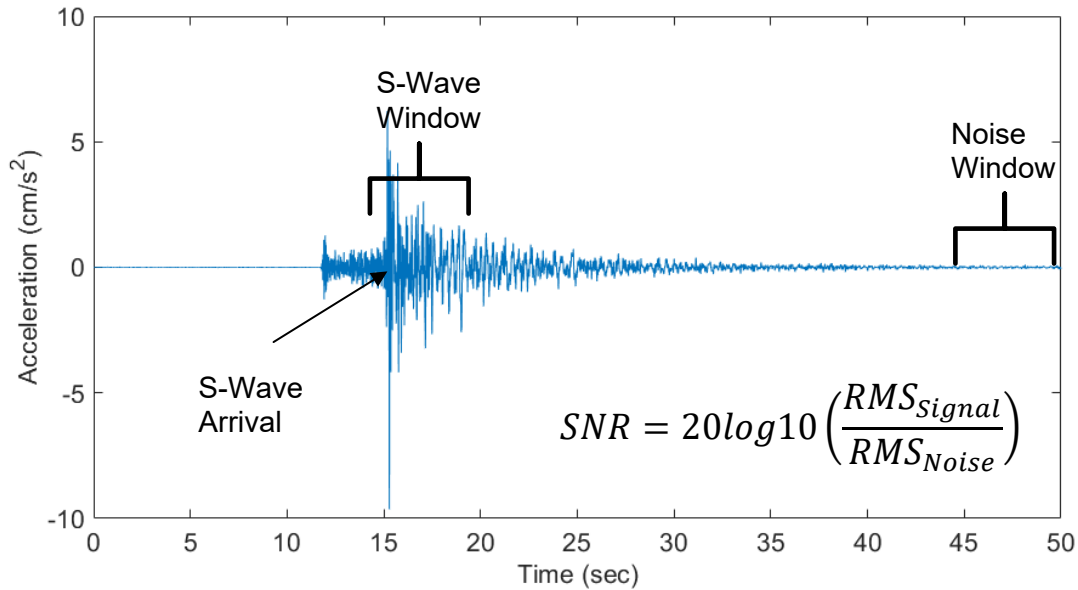


**Figure D-1 Data processing of ground motion data. RMS is the root mean square of the windowed data.**

### Sampling of $\kappa_0$

Anderson and Hough (1984) introduced the factor  $\kappa$  to model the exponential decay of an acceleration FAS as shown in Eq. D-1.

$$A(f) = A_0 \cdot e^{-\pi\kappa f} \quad (\text{Eq. D-1})$$

where  $A_0$  incorporates seismic source and geometrical spreading effects,  $f$  is frequency, and  $\kappa$  is the high frequency spectral decay parameter. Hough and Anderson (1988) observed that if the estimates of  $\kappa$  for various records at a given station are plotted versus epicentral distance ( $R$ ), the resulting plot is a linear relationship that can be written as

$$\kappa = \kappa_0 + \kappa_r R \quad (\text{Eq. D-2})$$

where  $\kappa_0$  is the intercept representing the attenuation attributed to the site-specific geologic materials in the upper few km beneath a site and  $\kappa_r$  is the slope from linear regression on  $\kappa$  values evaluated from ground motions with varying epicentral distance  $R$ . Common practice in evaluating Eq. D-1 is to perform a linear regression over a specified frequency range to determine  $\kappa$  values for individual recorded events. This frequency range is typically chosen to start at a frequency well above the corner frequency and end at a frequency below, where either the FAS begins to turn horizontal or aliasing effects are expected. Initially, the TI Team used a frequency range of 30 Hertz (Hz) (15 Hz to 45 Hz) to evaluate  $\kappa$ . However, as will be discussed later in this appendix, multiple frequency ranges were later evaluated to capture the epistemic uncertainty in  $\kappa_0$ .

For this project, the TI Team used Bayesian regression with Markov Chain Monte Carlo (MCMC) sampling to evaluate  $\kappa$ . For each horizontal component of ground motion, a Bayesian

regression was performed and MCMC methods used to sample the posterior distribution. Using this approach, the TI Team generated 10,000 sampled  $\kappa$  values from each ground motion record to evaluate the statistical properties of  $\kappa$  as a function of epicentral distance (Figure D-2.) The TI Team then randomly selected a  $\kappa$  value from each ground motion record and performed ordinary least squares (OLS) regression to estimate a sample  $\kappa_0$  value. The team repeated this process 10,000 times to produce 10,000  $\kappa_0$  values from which the statistical properties (mean, median, and standard deviation) were evaluated (Figure D-3).

### **Epistemic Uncertainty of $\kappa_0$**

While the above methodology for sampling the distribution of  $\kappa_0$  and quantifying its uncertainty is robust, it contains both aleatory and epistemic uncertainties. The distribution of  $\kappa_0$  contains both record-to-record variability (aleatory), which would be considered as captured by the aleatory component of the ground motion model (GMM), and modeled regression uncertainty (epistemic). In addition, spatial variability on the regional attenuation will result in uncertainty in the  $\kappa_r$  parameter, which will also result in variability in  $\kappa_0$  estimates. The TI Team recognizes the importance of parsing the types of uncertainty to ensure no double counting; however, the TI Team decided that further research on how to appropriately parse these components was needed but out of scope for this project. However, the TI Team identified the frequency band used to compute  $\kappa$  values from the FAS as a significant contributor to epistemic uncertainty in  $\kappa_0$ . Due to the unique characteristics of each measured ground motion, which includes amplification effects and high frequency noise in the FAS, the frequency band over which  $\kappa$  can be evaluated may be different for each record. The TI Team chose to evaluate  $\kappa$  using the process described in the section above but using multiple frequency bands, all of which are within the 15 Hz to 45 Hz range. The TI Team chose a floor of 15 Hz to avoid any influence from site resonances and a ceiling of 45 Hz which is below the Butterworth filter cutoff frequency of 50 Hz. The Team used four frequency ranges to define multiple frequency bands. The four frequency ranges are: 15 Hz, 20 Hz, 25 Hz, and 30 Hz. Estimates of  $\kappa_0$  distributions were made using each frequency band evaluated over a range of starting frequencies. For example, a 15 Hz frequency band can have a starting frequency of 15 Hz and therefore the  $\kappa$  values used to evaluate  $\kappa_r$  and  $\kappa_0$  in Eq. D-2 would be estimated from the 15–30 Hz frequency range of the FAS. Then, a 1 Hz shift in the starting frequency is applied and the  $\kappa$  values used to evaluate  $\kappa_r$  and  $\kappa_0$  in Eq. D-2 would be estimated from the 16–31 Hz frequency range of the FAS. This process is repeated for the 15 Hz frequency band up to a starting frequency of 30 Hz where the frequency band would reach the 45 Hz limit. This process is repeated for all frequency bands resulting in 34 frequency bands for estimating the epistemic uncertainty in  $\kappa_0$ ; 16 bands for the 15 Hz range, 11 bands for the 20 Hz range, 6 bands for the 25 Hz range, and 1 band for the 30 Hz range. Median  $\kappa_0$  values were then obtained from each frequency band's  $\kappa_0$  distribution.

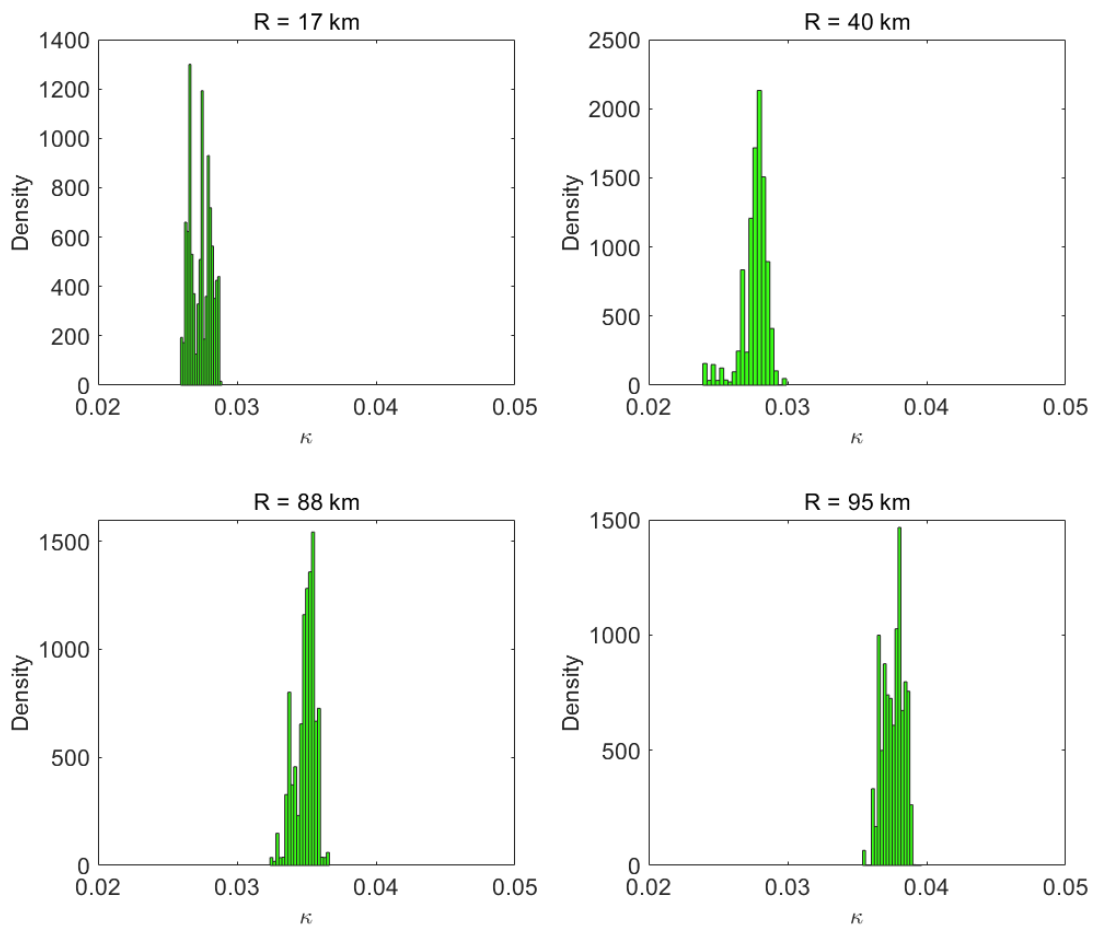


**Figure D-2 Histograms approximating the distribution of  $\kappa$  values for events with varying epicentral distances.**

Initially the TI Team considered weighting the median  $\kappa_0$  values from each frequency band by the inverse of their standard error. This approach tends to weight the  $\kappa_0$  distributions estimated over larger frequency bands higher. However, while investigating  $\kappa_r$  from each frequency band, the TI Team recognized that this approach may not accurately capture the full uncertainty in  $\kappa_0$  estimates. Figure D-4 (top and middle rows) shows a comparison of surface versus downhole [150 meter (m) depth]  $\kappa_r$  computed from a 15 Hz frequency band (20–35 Hz) and a 20 Hz frequency band (25–45 Hz.) If only the inverse of standard error was used as a weighting measure, the surface 20 Hz frequency band would have higher influence on the overall epistemic uncertainty compared to the 15 Hz frequency band. However, comparison of  $\kappa_r$  between surface and downhole motions advocates the need to evaluate some additional uncertainty in  $\kappa_0$  estimates. While  $\kappa_0$  values between surface and downhole recordings should be different,  $\kappa_r$  should be consistent between the surface and downhole. However, Figure D-4 (bottom row) shows that for an individual frequency band,  $\kappa_r$  between the surface and downhole can be quite different, suggesting additional uncertainty in estimated  $\kappa_0$  values.

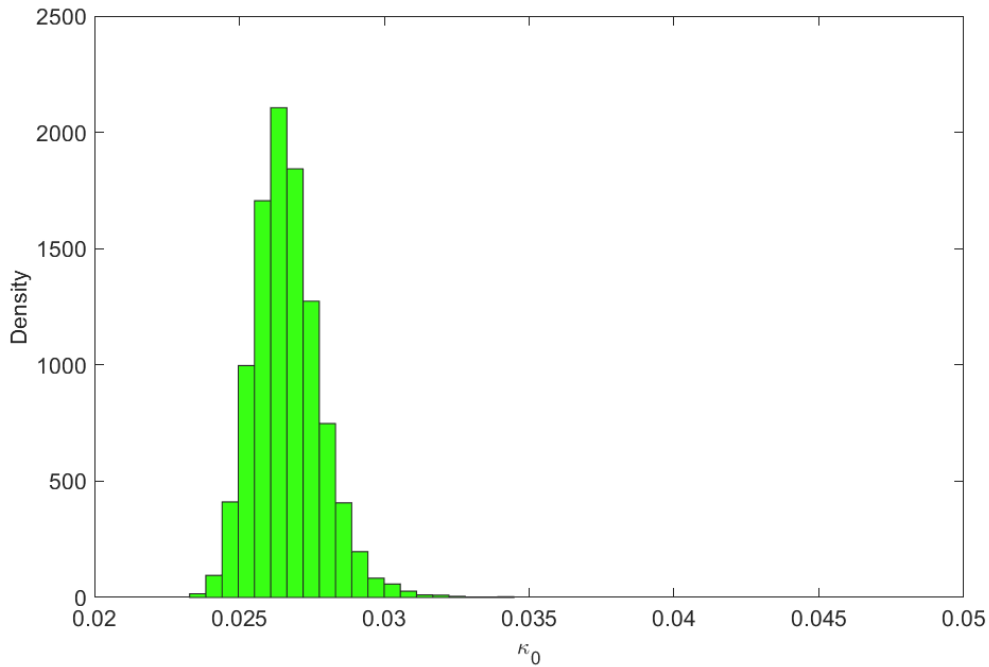


**Figure D-3 Histogram of  $\kappa_0$  values obtained from 10,000 random samples drawn from the  $\kappa$  distributions across all epicentral distances.**

To account for this additional uncertainty, the TI Team defined a fitness function (Eq. D-3) to penalize the  $\kappa_0$  distributions by the degree to which  $\kappa_r$  between the downhole and surface motions differ

$$F_i = \frac{\left| \kappa_{r,i_{Surface}} - \kappa_{r,i_{Downhole}} \right|^{-1}}{\sqrt{SE_i^2(\kappa_{r,i_{Surface}}) + SE_i^2(\kappa_{r,i_{Downhole}})}} \quad (\text{Eq. D-3})$$

where  $\kappa_{r,i_{Surface}}$  is the median  $\kappa_r$  of the surface motion for the  $i^{\text{th}}$  frequency band,  $\kappa_{r,i_{Downhole}}$  is the median  $\kappa_r$  of the downhole motion for the  $i^{\text{th}}$  frequency band,  $SE_i(\kappa_{r,i_{Surface}})$  is the standard error on the surface's median  $\kappa_r$  for the  $i^{\text{th}}$  frequency band, and  $SE_i(\kappa_{r,i_{Downhole}})$  is the standard error on the downhole's median  $\kappa_r$  for the  $i^{\text{th}}$  frequency band. The standard error for the  $i^{\text{th}}$  frequency band is defined as

$$SE_i = \frac{\sigma_{\kappa_{r,i}}}{\sqrt{N * \Delta_{f,i}}} \quad (\text{Eq. D-4})$$

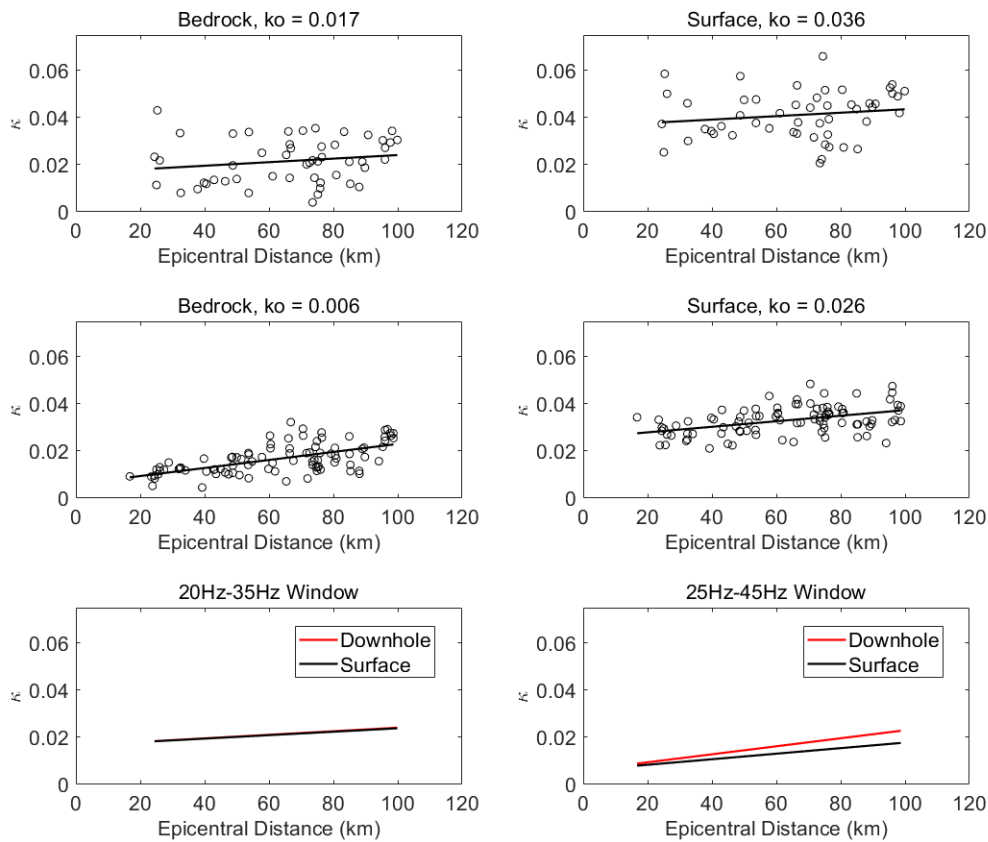


**Figure D-4 Comparison of surface vs downhole  $\kappa_r$  slopes computed from frequency bands of 20 Hz to 35 Hz (top row) and 25 Hz to 45 Hz (middle row) and surface slopes shifted to downhole intercept for better comparison (bottom row)**

where  $\sigma_{\kappa_{r,i}}$  is the standard deviation on  $\kappa_r$  for the  $i^{\text{th}}$  frequency band,  $N$  is the number of ground motions used in regressing  $\kappa_r$ , and  $\Delta_{f,i}$  is the frequency bandwidth used in the regression. The parameter  $N$  was included in the standard error to account for the error associated with the number of ground motion records used for each frequency band. The number of records changes for individual frequency bands due to the TI Team requiring individual ground motions to have larger  $\kappa$  values for surface recordings than those from borehole recordings to be considered reliable.

The results of Eq. D-3 allow for assigning a weighting function to each  $\kappa_0$  distribution

$$W_i = \frac{F_i}{\sum F} \quad (\text{Eq. D-5})$$

where  $W_i$  is the weight applied to the  $\kappa_0$  distribution resulting from the  $i^{\text{th}}$  frequency band. Figure D-5 shows the resulting weights applied to the  $\kappa_0$  distribution for each frequency band with a given starting frequency. The height of each color bar represents the weight applied to that frequency band.

Having median  $\kappa_0$  values with associated weights afforded the TI Team the opportunity to use the approach defined by Miller and Rice (1983) to reduce the set of 34 weighted  $\kappa_0$  distributions to a representative five-point distribution used in the site response logic tree. Figure D-6 shows the cumulative distribution function for the weighted median  $\kappa_0$  values from each  $\kappa_0$  distribution (red line) and the resulting Miller and Rice (1983) five-point distribution values (black dots). The five-point distribution values are also listed in Table 5-5 of this report. The values for  $\kappa_0$  in Figure D-6 show a significant decrease in the uncertainty in  $\kappa_0$  compared to the SRS study site, which uses a range of empirical relationships to define the uncertainty in  $\kappa_0$ . Also, the median value of 0.0266 seconds for  $\kappa_0$  from this study agrees well with the value 0.027 seconds reported by Archuleta et al. (1992) for the GVDA site.

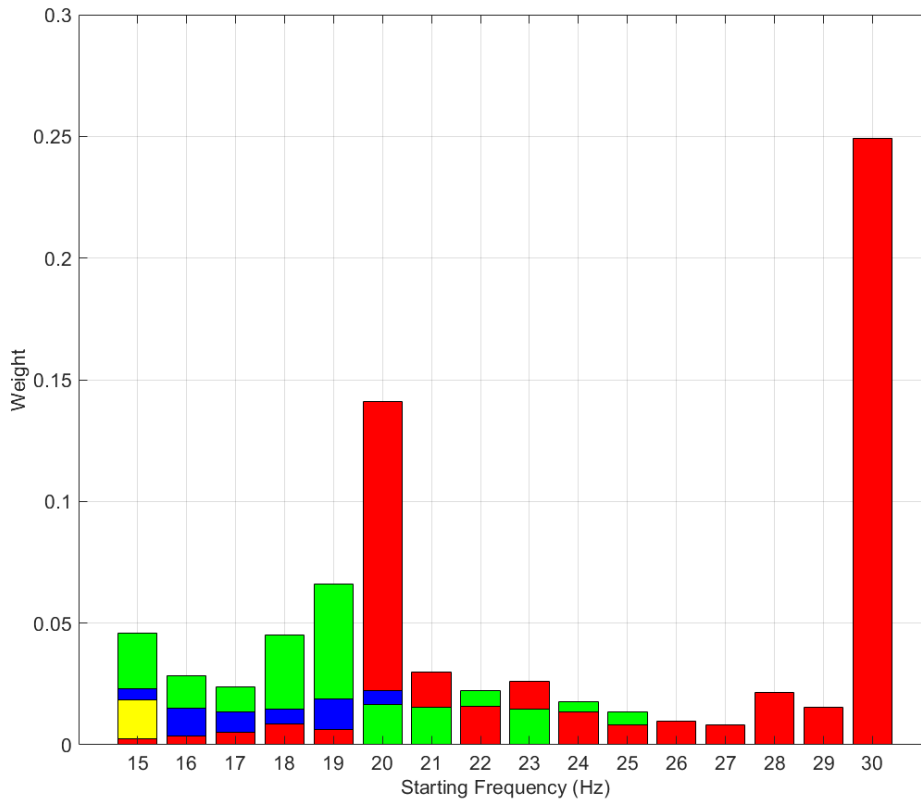


**Figure D-5** Weights applied to the alternative frequency bands: 15 Hz (red, 16 bands), 20 Hz (green, 11 bands), 25 Hz (blue, 6 bands), and 30 Hz (yellow, 1 band). The height of each color bar represents the weight applied to that frequency band with a given starting frequency.

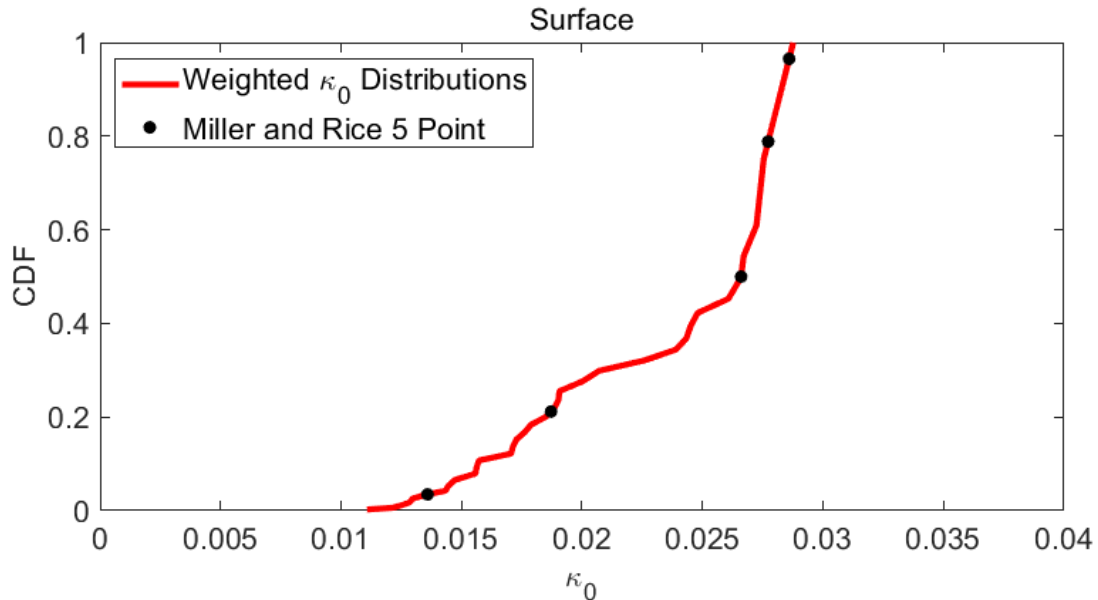


**Figure D-6 Cumulative distribution of weighted  $\kappa_0$  values and representative five-point distribution values from Miller and Rice (1983).**

## References

Anderson, J. G. and S. E. Hough. "A Model for the Shape of the Fourier Amplitude Spectrum of Acceleration at High Frequencies." *Bulletin Seismological Society of America*. Vol. 74. pp. 1969–1993. 1984.

Archuleta, R., S. Seale, P. Sangas, L. Baker, and S. Swain. "Garner Valley Downhole Array of Accelerometers: Instrumentation and Preliminary Data Analysis." *Bulletin of the Seismological Society of America*. Vol. 82, No. 4. pp. 1592–1621. 1992.

Hough, S. E. and J. G. Anderson. "High-Frequency Spectra Observed at Anza, California: Implications of Q Structure." *Bulletin of the Seismological Society of America*. Vol. 78. pp. 692–707. 1988.

Miller, A. C. and T.R. Rice. "Discrete Approximations of Probability Distributions." *Management Science*. Vol. 29, No. 3. pp. 352–362. 1983.

Xu, B., E. Rathje, Y. Hashash, J. Stewart, K. Campbell, and W. Silva. " $\kappa_0$  for Soil Sites: Observations From KiK-Net Sites and Their Use in Constraining Small-Strain Damping Profiles for Site Response Analysis." Earthquake Engineering Research Institute, EERI Vol 36, Issue 1. 2020.